Multi-Instrument Observations of Physical Processes in the Arctic Ionosphere and Derived Applications

Durgonics, Tibor

Publication date:
2017

Document Version
Publisher's PDF, also known as Version of record

Multi-Instrument Observations of Physical Processes in the Arctic Ionosphere and Derived Applications

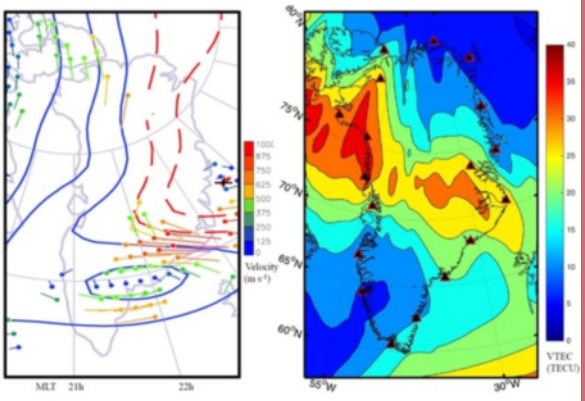

Tibor Durgonics
Ph.D. dissertation
November 3, 2017

Supervisors: Per Høeg and Attila Komjáthy

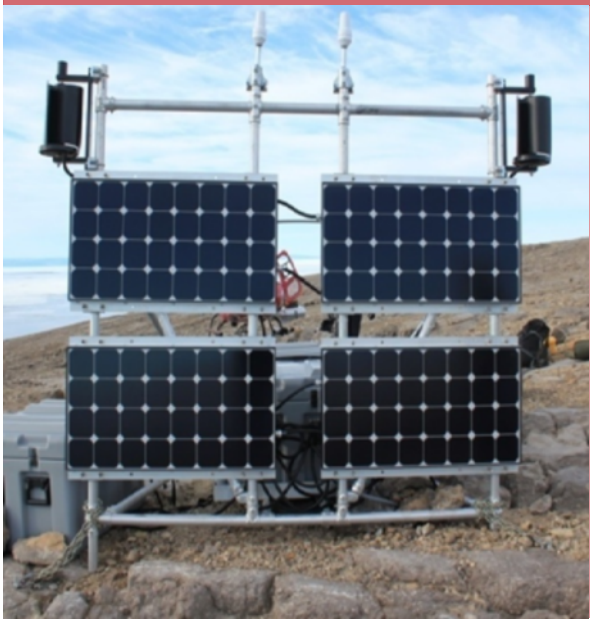

DTU Space
National Space Institute

Multi-Instrument Observations of Physical Processes in the Arctic Ionosphere and Derived Applications

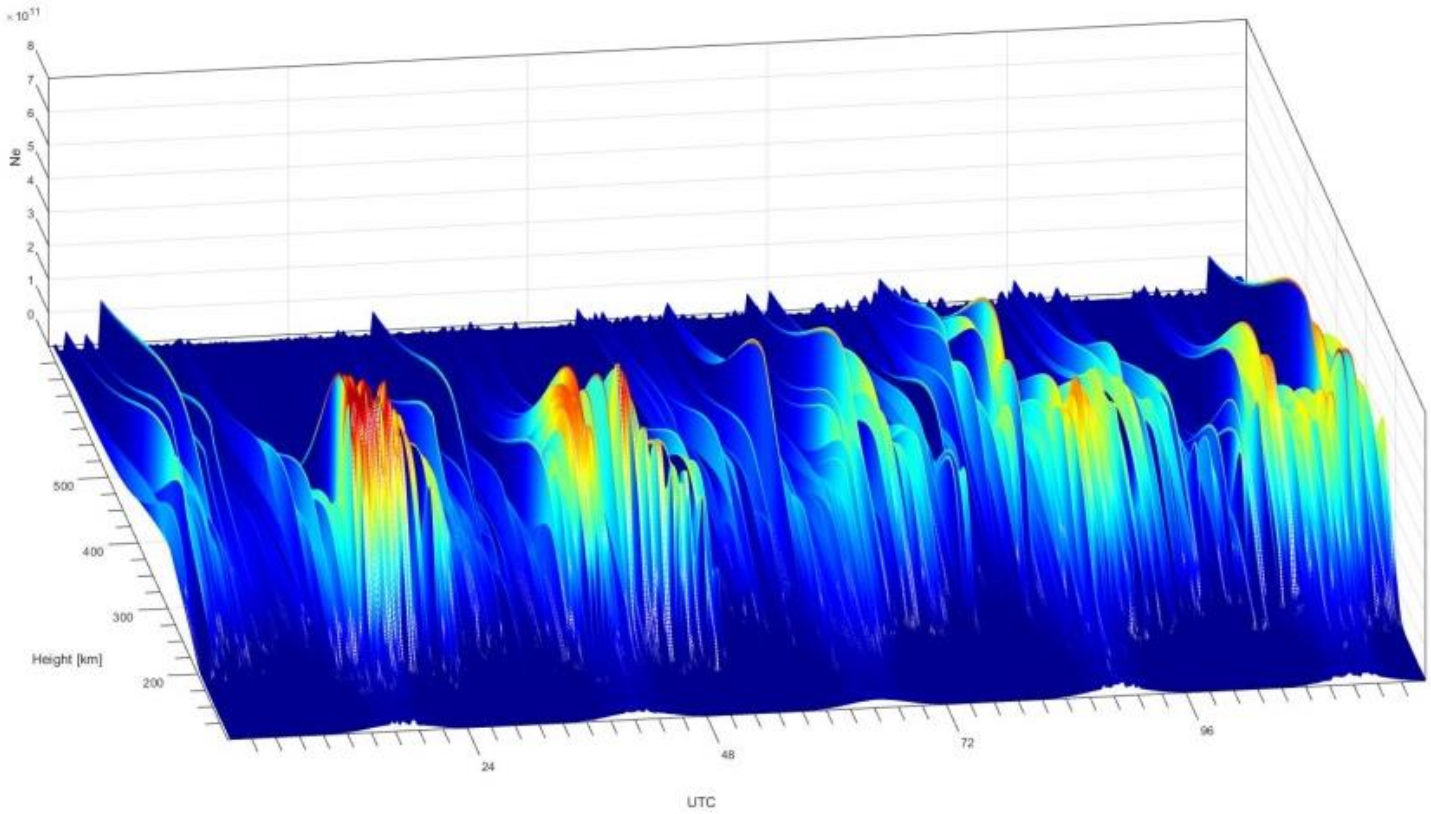

Tibor Durgonics

Ph.D. dissertation

November 3, 2017

Supervisors: Per Høeg and Attila Komjáthy

DTU Space
National Space Institute

Multi-Instrument Observations of Physical Processes in the Arctic Ionosphere and Derived Applications

Undersøgelse af fysiske processer i den arktiske ionosfære baseret på multi-instrument observationer

Tibor Durgonics

National Space Institute, DTU Space

Technical University of Denmark

Kgs. Lyngby, Denmark

This dissertation is submitted for the degree of Doctor of Philosophy on November 3, 2017.

www.space.dtu.dk

"In general, we look for a new law by the following process: First we guess it. Then we – now don't laugh, that's really true. Then we compute the consequences of the guess to see what, if this is right, if this law that we guessed is right, to see what it would imply. And then we compare the computation results to nature, or we say compare to experiment or experience, compare it directly with observations to see if it works. If it disagrees with experiment, it's wrong. In that simple statement is the key to science. It doesn't make any difference how beautiful your guess is, it doesn't make any difference how smart you are, who made the guess, or what his name is. If it disagrees with experiment, it's wrong. That's all there is to it."

- Richard P. Feynman (1918-1988)

Abstract

The ionosphere is the source of the largest errors in satellite-based navigation and positioning, transionospheric radio communications, and certain satellite-based radar remote sensing techniques. A proper understanding of ionospheric dynamics and its coupling with space weather can help mitigate these errors. Specifically, ionospheric electron density and scintillation forecasting would significantly improve reliability of navigation and positioning systems.

This Ph.D. thesis is primarily concerned with the physical processes in the terrestrial Arctic upper atmosphere. Additionally to this, two studies about lower-latitude regimes and a global ionosphere mapping study are also presented. Whenever multi-instrument observations were available, these measurements were combined to obtain a more complete physical description of the underlying processes. All of the studies presented employ the observation-based approach with utilization of GNSS-derived measurements as the primary data source, and the primary subject of the research being the terrestrial atmosphere (the ionized part, the neutral part, or both). The collected measurements are used to construct a model of the underlying physical processes. The complexity of the studied atmospheric processes often required multiple, independent measurements of various physical parameters. These results are then combined such that they complement each other and provide validation.

Some of the important findings of this work include (1) the analysis of an interplanetary coronal mass ejection (ICME) induced negative storm phase at high latitudes in February 2014 exhibited thermospheric O/N_2 decrease due to atmospheric heating, increased ion flow in the topside ionosphere, and an increase in polar patch formation inhibition, all of which lasts for several days. These appear to be general features of these types of geomagnetic storms. (2) During an energetic, mixed high-speed stream (HSS) and ICME-induced storm in March 2015, GPS phase scintillation

was found to be mapped to the poleward side of the westward electrojet and to the edge of the eastward electrojet region. At the same time, the scintillation was largely collocated with fluxes of energetic electron precipitation observed by DMSP satellites, with the exception of a period of pulsating aurora when only very weak currents were observed. (3) Based on measurements employing a space-qualified GPS receiver placed on a mountain at the Haleakala observatory on the Hawaiian island of Maui, it was found that simulated surface-reflection signals and the measured reflection signals were revealing matching spectral structures of the reflected signals that could lead to extraction of parameters of sea surface roughness, surface wind speed, and direction. (4) 4-year long regional electron density observations from Thule, Greenland revealed a series of findings: strong correlation with solar extreme ultraviolet (EUV) spectral irradiance that is related to solar rotation and sunspot numbers, increased electron density variability during equinoxes that is related to the Russell-McPherron effect, and a strong influence of ambipolar diffusion as a function of ionospheric E layer conductivity. (5) The polar cap index rate of change showed significant differences during ICME and HSS-induced storms. This indicates that the energy input into the polar cap occurs at significantly different rates for these two phenomena which results in some differences in the induced geomagnetic storm evolution.

Sammenfatning

En stor fejlkilde i satellitbaseret navigation og positionering skyldes forholdene i ionosfæren. Det samme gør sig gældende i mange anvendelser indenfor radiokommunikation og radar-basserede satellit-remote-sensing metoder. Derfor er en god forståelse af ionosfærens tilstand og dynamik essentiel for at afbøde disse fejl. Varsling af forholdene i ionosfæren vil forbedre pålideligheden af den satellit-baserede navigation og positionering.

Dette ph.d.-studie består af en række eksperimentelle og teoretiske undersøgelser indenfor aeronomi, ionosfære og rumfysik, GNSS målinger af ionosfærens elektrontæthed, GNSS reflektometri, og solvindens interaktion med magnetosfære-ionosfære systemet. Fokus har været på forholdene i den arktiske ioniserede del af den øvre atmosfære. Men også studier af forholdene på lavere breddegrader er behandlet i forbindelse med forståelsen af processerne på lukkede magnetiske kraftlinjer i jordens magnetosfære-ionosfære system.

Formålet med studiet har også været at give indsigt i de måletekniske problemstillinger indenfor satellitnavigation og udnyttelse af GNSS-signaler til bestemmelse af for eksempel forholdene på oceanerne (højder af havoverflader, bølger, ruhed og overfladevind). Derfor har det været en integreret del af studiet at forstå målingerne, der ligger til grund for observationerne. Denne indsigt har været basis for modelleringsresultaterne og teorierne for de observerede fysiske processer. Kompleksiteten i ionosfærens plasmaprocesser har krævet uafhængige multiinstrument og netværksobservationer for at komme til de beskrevne resultater.

Nogle af de vigtige resultater af dette projekt er:

(1) Analysen af en ’interplanetary coronal mass ejection’ (ICME) med en induceret negativ stormfase på høje breddegrader ledte til observationen et fald i ionosfærens O/N_2-indhold

drevet af ’heating’ og øget ion-fluks i den øverste del af ionosfæren. Resultatet af denne proces er en reduceret dannelse af ’polar patches’ (elektrontæthedsforøgelser) i jorden polkappe. En situation, som varer flere dage, og som synes at være en general feature for sådanne magnetiske storme.

(2) GPS fase-fluktuationer er identificeret til at være centreret på den nordlige side af den ’westward electrojet’ og på kanterne til den ’eastward electrojet’ i forbindelse med energetiske ’high-speed streams’ (HSS) og ICME-inducerede magnetiske storme drevet af solvinden. Mens scintillationer i ionosfæren følger den energetiske elektronstråling i ionosfæren langs jordens magnetiske kraftlinjer (observationer fra DMSP satellitterne).

(3) Data fra en rumkvalificeret GPS modtager placeret på Haleakala observatoriet på Hawaii gav mulighed for at differentiere det direkte signal fra det hav-reflekterede signal i spektraldomænet og derved beskrive strukturer i det reflekterede signal som ruhedsparameteren af havet, overfladevinden og dens retning.

(4) En 4-års dataserie af elektrontæthedsobservationer i Thule, Grønland, viste en kraftig korrelation med solens EUV-spektralradians, som også er relateret til solens rotation og solplettallet, større elektrontæthedsvariabilitet ved jævndøgn drevet af Russell-McPherron effekten, og tæt indflydelse af diffusionsprocesserne i ionosfærens E-lag samt dens elektromagnetiske ledningsevene.

(5) Ændringen i ’polar cap index’ i forbindelse med ICME- og HSS-inducerede magnetiske storme er signifikant forskellig. En indikation på at energi-afsætningen i polkappen er forskellig i rum og tid drevet af disse processer på solen. Resultaterne tyder på, at udviklingen af de geomagnetiske storme i ionosfæren udvikler sig forskelligt alt efter hvilken af solprocesserne, der er den dominerede, samt hvilken energiafsætning, der foregår i jordens magnetosfære-ionosfære system fra solvinden.

Acknowledgements

This work has been carried out at the Technical University of Denmark (DTU), DTU Space department under the principal supervision of Per Høeg. During my Ph.D., between July 1, 2014 and July 31, 2017, I spent approximately 9 months at NASA Jet Propulsion Laboratory (JPL) working under the supervision of my Ph.D. co-supervisor Attila Komjathy. The Ph.D. was co-funded by ESA (grant numbers 4000105775/2012/NL/WE and 4000112279/2014/D/MRP) and DTU Space. Additional funds for external research stay and conference participation were granted by the Otto Mønsteds Fond.

Firstly, I would like to thank my principal advisor, Professor Per Høeg, for making this Ph.D. possible for me, and his valuable guidance throughout the years. I was allowed a great deal of intellectual freedom to pursue my own ideas in between the mandatory courses and project works. I also really appreciate allowing me to visit JPL twice and work with my co-supervisor Attila Komjathy, who is a Principal Investigator in JPL's Ionospheric and Atmospheric Remote Sensing (IARS) group. Working there was an unforgettable experience and I feel extremely lucky that I was granted this opportunity. I would also like to express my sincere gratitude to Attila who supported and encouraged me even before he officially became my co-advisor. His vast knowledge and excellent work ethics remain an example to follow. And last but not least Professor Per Knudsen, our geodesy section leader, who was always helpful and supportive and whom I could always count on when academic life got difficult.

Secondly, I would like to thank my colleagues from DTU Space: Hans-Henrik von Benzon, Finn Bo Madsen, Ole Bjerregaard Hansen, Shfaqat Abbas Khan, Karina Nielsen, Lars Stenseng, Susanne Vennerstrøm, and Kristian Pedersen; my colleagues at IARS: Anthony Mannucci, Olga Verkhoglyadova, and Clara Chew. And I'd like to give special thanks to Professor Richard Langley

of University of New Brunswick, who was not officially my advisor, but it sure felt like it at times and I am really grateful for all his help.

I would also like to express my thanks toward my fellow Ph.D. students here at DTU Space with whom we had some good times together: Ioana, Johan, Carlo, Alessandro, Adili, Daniel, Zhao, and Maulik.

And finally, thanks for my family, my wife Rebecca, my son Tibor Gabriel, and my brother Tamás who helped me make it through good and bad times and inspiring me to follow my dreams. I have received invaluable help from Rebecca (who is also a scientist) during the writing and editing of this thesis, and I would like to express my special gratitude to her.

Table of Contents

CHAPTER 1 ..... **1**

INTRODUCTION **1**

1.1 Background and Motivation of the Research 1
1.2 Literature Overview 5
1.3 Overview of the Research 13
1.4 Scientific Approach 20
1.4.1 Fundamentals of the Arctic ExB Convection Patterns *22*
1.4.2 The Solar Photoionization *27*
1.4.3 STEC, VTEC, and MVTEC Calculations *33*
1.4.4 Phase-Based Scintillations: σ_ϕ and ROTI *37*
1.5 Outline of the Dissertation 39

CHAPTER 2 ..... **41**

STUDY 1: DETECTION OF IONOSPHERIC SIGNATURES FROM GPS-DERIVED TOTAL ELECTRON CONTENT MAPS **41**

2.1 Introduction and Relevance of the Paper 41
2.2 Detection of Ionospheric Signatures from GPS-Derived Total Electron Content Maps 42
2.2.1 Study Area and GNSS Resources *45*
2.2.2 GNSS Ground Station Selection *47*
2.2.3 Determination of a Representative GNSS Ground Network Based on GIS *48*
2.2.4 Obtaining TEC Values from Bernese GPS Software 5.0 ..... *51*
2.2.5 Interpolation and Visualization *52*
2.2.6 Spatial Analysis of the GPS ground station Distribution *53*
2.2.7 TEC Map Interpolation *54*
2.2.8 Diurnal and Seasonal Changes in the Ionosphere *55*
2.2.9 Relation to Solar Activity *58*
2.2.10 Possible Relation to Seismic Activity *59*
2.2.11 Discussion *60*

CHAPTER 3 ..... **65**

STUDY 2: MULTIINSTRUMENT OBSERVATIONS OF A GEOMAGNETIC STORM AND ITS EFFECTS ON THE ARCTIC IONOSPHERE: A CASE STUDY OF THE 19 FEBRUARY 2014 STORM **65**

3.1 Introduction and Relevance of the Paper 65
3.2 Multiinstrument observations of a geomagnetic storm and its effects on the Arctic ionosphere: A case study of the 19 February 2014 storm 66
3.2.1 Methods, Instrumentation, and Observations *70*
3.2.1.1 Storm Effect Overview 72
3.2.1.2 Ground-based Measurements and Solar Wind Parameters 73
3.2.1.3 Analysis of Solar Wind Parameters and Geomagnetic Observations 80
3.2.1.4 Spaceborne Observations 82
3.2.1.5 Results: Electron Density Observations 84
3.2.1.6 O/N_2 Composition Changes 87
3.2.1.7 Polar Patch Propagation and Convection 89
3.2.1.8 Ion Composition and Velocity Distribution of Ions in the Topside Ionosphere 90
3.2.2 TEC Variations and Scintillation Characteristics *91*
3.2.3 Discussion *99*
3.2.4 Conclusions *102*

CHAPTER 4 ..... **104**

STUDY 3: GPS PHASE SCINTILALTIONS AT HIGH LATITUDES DURING THE GEOMAGNETIC STORM OF 17–18 MARCH 2015 ..... **104**

4.1 Introduction and Relevance of the Paper 104
4.2 GPS phase scintillation at high latitudes during the geomagnetic storm of 17–18 March 2015 105
4.2.1 Instruments and Techniques *106*
4.2.2 Solar Wind and Geomagnetic Conditions *110*
4.2.3 Ionospheric Irregularities at High Latitudes *111*
4.2.4 GPS Phase Scintillation in Relation to Auroral Currents *120*
4.2.5 Geomagnetic Storm of 17–18 March 2015: Discussion and Summary *128*

CHAPTER 5 ..... **131**

STUDY 4: ANALYSIS OF SATELLITE-BASED NAVIGATION SIGNAL REFLECTOMETRY: SIMULATIONS AND OBSERVATIONS **131**

5.1 Introduction and Relevance of the Paper 131
5.2 Analysis of Satellite-Based Navigation Signal Reflectometry: Simulations and Observations 132
5.2.1 Simulation of a Bistatic Scattering System *134*
5.2.2 Measured and Simulated Results *138*
5.2.3 Conclusions *144*

CHAPTER 6 ..... **146**

MULTI-INSTRUMENT OBSERVATIONS OF SOLAR EUV IRRADIANCE INDUCED IONOSPHERIC VARIATIONS **146**

6.1 Introduction and Relevance of the Research 146
6.2 The Effects of Solar-Rotation-Related Spectral Irradiance Variations on Northern Polar Cap Plasma Number Densities 147
6.2.1 Methods and Observations *149*
6.2.2 Results *153*
6.2.2.1 Interpretation of the MVTEC Time-Series and Related Observations 156
6.2.2.2 Relation of MVTEC Time-Series to Geomagnetic Indices and Digital Ionosonde Measurements 160
6.2.2.3 Dependency of MVTEC Time-Series on Solar Irradiance 166
6.2.2.4 MVTEC Decomposition 169
6.2.3 Discussion *171*
6.2.4 Summary *178*

CHAPTER 7 ..... **180**

CROSS-VALIDATION OF TEC DATA PRODUCTS **180**

7.1 Introduction 180
7.2 Objectives and Approaches of the TEC validation 181
7.3 Data Products for the Cross-Validation 182
7.4 Description of the Geophysical Conditions 183
7.5 Cross-Validation Results 186
7.6 Conclusions and Summary 191

CHAPTER 8 ..... **195**

COMPARISON OF HIGH-LATITUDE IONOSPHERIC PROCESSES DURING HSS AND ICME-INDUCED GEOMAGNETIC STORMS **195**

8.1 Introduction 195
8.2 Observations and Mapping Technique 196
8.3 Comparison of ICME-Induced and HSS-induced Storms 197
8.4 Results 202

8.5 SUMMARY 206
CHAPTER 9 207
CONCLUSIONS AND RECOMMENDATIONS FOR FUTURE WORK 207
9.1 CONCLUSIONS AND RECOMMENDATIONS FOR FUTURE WORK 207
REFERENCES 212
APPENDIX I: AGU'S RADIO SCIENCE JOURNAL COVER PAGE FROM JANUARY 2017 FEATURING ONE OF THE FIGURES (TOP) AND FIGURE CAPTION (BOTTOM) FROM STUDY 2. 250
APPENDIX II: HATCH FILTER SCRIPT (MATLAB) 251
APPENDIX III: STEC CALCULATING SCRIPT (MATLAB) 252
APPENDIX IV: SOLAR RADIO BURST RESULTS 254
IV.1 SOLAR RADIO BURST AND RAY TRACING DURING THE 4 NOVEMBER 2015 EVENT 254
IV.2 Proposed Questions 255
IV.3 Facts about the Airport Base 255
IV.4 Time of Incidence for the Received Erroneous Localizer Signal 255
IV.5 The Sunlit Ionosphere for the Period of November 3-4, 2015 256
IV.6 Raytracing of the Localizer Frequency for Plasma Frequencies from 10 to 15 MHz 256
IV.7 Conclusions of the Ray Tracing Study 256
APPENDIX V: EXTRA FIGURES – SPECTRAL INDICES #1 257
APPENDIX VI: EXTRA FIGURES – SPECTRAL INDICES #2 258
APPENDIX VII: GNET STATIONS (2017) 259
APPENDIX VIII: CRITICAL FREQUENCY PROFILE PLOTS. 260
APPENDIX IX: CONFERENCE PARTICIPATIONS DURING THE PH.D. (FIRST AUTHOR ABSTRACTS ONLY) 263

List of Abbreviations, Acronyms, and Technical Terms

AE	Auroral Electrojet index.
AIM	Arctic Ionospheric Maps.
B	Magnetic field (vector, bold).
CASSIOPE	CAScade, Smallsat and IOnospheric Polar Explorer.
CHAIN	Canadian High Arctic Ionospheric Network.
CIR	Co-rotating Interaction Region.
(I)CME	(Interplanetary) Coronal Mass Ejection.
CODE	Centre for Orbit Determination in Europe.
DCB	Differential Code Bias.
Dst	Disturbance storm time index.
DTU	Technical University of Denmark.
E	Electric field (vector, bold).
Epoch	A specific time when a measurement was made.
e-POP	Enhanced Polar Outflow Probe.
ESA	European Space Agency.
F10.7	F10.7 index is a measure of the solar radio flux per unit frequency at a wavelength of 10.7 cm, near the peak of the observed solar radio emission.
FAC	Field Aligned Current.
FPDM	Horizontally structured F region Plasma Decay Model.
Geospace	The combination of magnetosphere, atmosphere, and ionosphere systems.
GIM	Global Ionosphere Map.
GNET	Greenland GPS Network.
GNSS	Global Navigation Satellite System.
GNSS-R	GNSS Reflectometry.
GNSS-RO	GNSS Radio Occultation.

GPS	Global Positioning System.
HSS	High Speed Stream.
IGS	International GNSS Service.
IMF	Interplanetary Magnetic Field.
IRM	Imaging and Rapid Scanning Ion Mass Spectrometer.
JPL GIM	Jet Propulsion Laboratory's Global Ionosphere Maps.
LEO	Low Earth Orbit.
MHD	Magnetohydrodynamics.
MVTEC	Mean Vertical Total Electron Content.
NASA	National Aeronautics and Space Administration.
NRT	Near Real-Time.
O/N_2	O/N_2 column density ratio.
PCN	Polar Cap (North) Index.
RIM	Regional Ionosphere Map.
ROTI	Rate of TEC Index.
S_4	Intensity Scintillation Index.
SED	Storm Enhanced Density.
SI	Sudden Impulse.
SSI	Spectral Solar Irradiance.
STEC	Slant Total Electron Content.
SuperDARN	Super Dual Auroral Radar Network.
SYM-H	Symmetric Disturbance Index in the Horizontal Dipole Direction.
TEC	Total Electron Content.
TECU	Total Electron Content Unit = 10^{16} electrons/m^2.
TOI	Tongue of Ionization.
TSI	Total Solar Irradiance.
VTEC	Vertical Total Electron Content.
σ_ϕ	Phase Scintillation Index.

CHAPTER 1

INTRODUCTION

1.1 Background and Motivation of the Research

The main focus of this dissertation is the study of the physical processes in the northern high-latitude (or simply Arctic) ionosphere. In addition to the main focus, two further studies are also presented regarding midlatitude ionosphere and neutral atmospheric simulations and observations. This section presents some basic background and the motivation behind these research topics.

Space weather can be defined as "conditions on the sun and in the solar wind, magnetosphere, ionosphere and thermosphere that can influence the performance and reliability of space-borne and ground-based technological systems and can endanger human life or health" (https://sohowww.nascom.nasa.gov/spaceweather/). Space weather concerns a wide array of physical phenomena, of which this dissertation emphasizes those taking place within the combination of the terrestrial magnetosphere, atmosphere, and ionosphere (or briefly geospace), with special emphasis on the ionosphere. These physical phenomena in geospace can negatively influence satellite and ground-based technologies, and potentially even negatively influence our health (astronauts on the International Space Station can be at high risk during increased space weather activity and according to recent studies even people on the ground can experience negative effects [Mavromichalaki et al., 2012]), therefore it is important to gain a better understanding of the

physical processes to be able to mitigate the undesired negative consequences of space weather phenomena.

The main drivers of space weather processes in geospace originate from the sun. For the purposes of this work, the relevant solar originated radiations can be divided into solar irradiance (all wavelengths of electromagnetic (EM) radiation emitted by the sun) and solar wind (corpuscular radiation plus its electromagnetic field). The plasma in the terrestrial ionosphere, as in all known planetary ionospheres, primarily develops through solar-originated photoionization and to a smaller degree through corpuscular radiation from the solar wind. The extreme ultraviolet (EUV) band of the total solar irradiance and all shorter wavelength bands (e.g., x-ray) of the solar EM radiation are responsible for the photoionization process [Unglaub et al., 2011].

The solar wind and the terrestrial ionosphere are among the most extensively studied naturally occurring plasma systems, yet due to their inherent complexities and the complexities of their interactions, the physical description and the modeling of these systems still present significant challenges [Bothmer and Daglis, 2007]. The ionosphere is typically divided naturally into three regimes: the low (equatorial), middle, and high (Arctic and Antarctic) geomagnetic latitudes, each has a number of distinctive and unique physical characteristics [Schunk and Nagy, 2009]. Among these three regimes the high-latitude ionosphere performs a critical role in solar-terrestrial energy transfer processes [Lu et al., 2016], through solar wind-magnetosphere coupling. Above the Arctic and Antarctic regions a portion of the near-Earth solar wind energy is continuously injected into the magnetosphere and through a series of complex processes, is dissipated into the high-latitude ionosphere (which drives a series of ionospheric phenomena, e.g., aurora) [Richmond and Lu, 2000; Fuller-Rowell et al., 1997]. This unique role that the high-latitude magnetosphere and ionosphere play in solar-terrestrial energy transfer processes necessitates and gives motivation to the study of this region, which is the main focus of this thesis.

The impacts of space weather on performance and reliability of space-borne and ground-based technological systems, such as navigation systems and power grid systems, are numerous, and these impacts are expected to grow as technologies further develop in the future (due to, for example, the move toward higher precision navigation systems). Different types of space weather phenomena may impact different technologies. For instance, solar flares can degrade radio communication on earth [Knipp et al., 2016]. Solar energetic particles not only can penetrate and damage satellite electronics, but also endanger astronaut health [Feynman and Gabriel, 2000]. The two most important types of solar wind disturbances that are responsible for causing geomagnetic storms are co-rotating interaction regions (CIRs) and interplanetary coronal mass ejections (ICMEs) [Denton et al., 2006]. The solar counterparts of these phenomena are referred to as coronal holes and coronal mass ejections (CMEs), respectively. CMEs, that are often associated with flares, can propagate into interplanetary space in the form of ICMEs and may eventually trigger geomagnetic storms [Verkhoglyadova et al., 2017], which can induce currents in the ground [Pulkkinen et al., 2005] that may affect power grids and communication cables [Kappenman, 2005]. CIRs originating from coronal holes may also cause geomagnetic storms, somewhat similarly to ICMEs [Tsurutani et al., 2006]. Ionospheric storms caused by ICMEs and CIRs typically develop during these disturbed times and result in degraded Global Navigation Satellite Systems (GNSS) positioning and navigation [Astafyeva et al., 2014]. Atmospheric heating during geomagnetic storms cause atmospheric expansion, and consequently increased drag on certain satellites [Oliveira et al., 2017]. These are just a few examples demonstrating how space weather can impact society.

In this thesis, the emphasis is on GNSS-related space weather impacts. In addition, we also use wide range of ground and satellite-based geophysical measurements that are available from the northern polar cap (e.g., Greenland, Canada, and Alaska) can be employed to study the connection between ICME/CIR characteristics and high-latitude space weather effects. It is widely accepted in

the scientific community that solar wind transients are associated with increased ionospheric scintillations [e.g., Prikryl, 2016]. Recent studies [e.g., Durgonics et al., 2017; Teunissen and Montenbruck, 2017] also show that storm-time heating, including Joule heating, has a large impact on ionospheric plasma density. This is of high importance in GNSS-navigation and positioning. In order to assess, and in the future, forecast GNSS-related space weather impacts, GNSS-derived total electron content (TEC) maps, GNSS-derived phase scintillation measurements, magnetic disturbance measurements obtained from magnetic stations, and in-situ polar-orbiting satellite measurements (CASSIOPE) were employed. By analyzing these measurements, we identified the ionospheric conditions under which GNSS phase scintillations occur, which could lead to the forecast of these events.

In summary, the effects of the solar wind are most prominent in the high-latitude regime of the ionosphere. The polar cap regions serve as major terrestrial sinks for numerous solar and magnetospheric events, including the most energetic solar wind-geospace energy exchange processes. This special connection with the solar wind makes this regime of the ionosphere considerably more complex than at lower latitude regimes. These dynamics of the high-latitude ionosphere can have significant impacts on navigation and positioning in the polar cap. These impacts can only be mitigated by understanding the underlying physical processes. Today, the Arctic is gaining more and more geo-political and geo-economic interest. It is crucial for air and marine traffic, and there is an ongoing competition for the natural resources in this area between the Arctic nations. Anthropogenic climate change is causing rapid warming and melting of ice in the Arctic. This makes areas in the North Polar Region, which potentially holds abundant raw materials, gradually more accessible for cost-effective exploitation and development (www.bmub.bund.de/P2834-1/). Therefore the study of high-latitude ionospheric processes has a greater importance today than ever before.

1.2 Literature Overview

The main focus of this dissertation is the observation-based scientific exploration of Arctic ionospheric physical processes, with the goal of gaining deeper understanding of this complex geophysical system. This section presents a brief historical and literature overview of this area of research.

First, let us define the region that we refer to as the Arctic ionosphere. The Arctic ionosphere is part of the terrestrial ionosphere consisting of two main regions: the northern polar cap [Watson et al., 2016; Brekke, 2013; Schunk and Nagy, 2009] and the northern auroral oval (or auroral zone) [Dashkevich et al, 2017; Serban et al., 2016; Schunk and Nagy, 2009; Gerard and Rusch, 1979]. It is also referred to as the (northern) high-latitude ionosphere. Its equatorward boundary is the imaginary line between open and closed geomagnetic field lines. This boundary is not fixed, but varies as function of solar wind and geomagnetic activity [Schunk and Nagy, 2009]. From modern digital ionosonde observations [Reinisch et al., 2009] it can be determined that the ionization may start around 60 km altitude. The topside does not have such a sharp boundary. From GNSS radio occultation (GNSS-RO) measurements it is clear that there is typically still a measurable electron density at around ~1000 km altitude [Shume et al., 2015; Shume et al., 2017] and this value is what one usually finds in the literature. Above 1000 km there is still ionization (free electrons) but this decreases exponentially as the altitude increases.

To provide an overview of the current state of high-latitude ionospheric research, a brief historical outline of some of the important personalities of science and their contributions are presented, followed by the most recent results in the field, and finally some of the most relevant observations techniques that are available today. The history of modern ionospheric science goes back to the year 1600 when William Gilbert published his book *De Magnete* which stated: "…*the Earth itself is a*

great magnet." This revelation marked the birth of the science of geomagnetism. Other necessary scientific discoveries came much later. In 1839, Carl Friedrich Gauss postulated the existence of the ionosphere, but only in 1901 did Guglielmo Marconi verify it experimentally with his radio signals. Shortly thereafter, , in 1908, Kristian Birkeland hypothesized the existence of auroral currents. The Greek word *plasma* was first used to describe ionized gases in 1927 by Irving Langmuir and Lewi Tonks. In 1940, Hannes Alfvén developed the theory of magnetohydrodynamics (MHD) which models the plasma as a conducting fluid. Since that time, MHD has been applied to a wide variety of natural and laboratory plasmas with success, including the ionospheric plasma. In 1958, James Van Allen discovered the Van Allen radiation belts around earth using satellite data which led to foundation of the field of space plasma physics. Just a bit later, by the 1970s, there was already an extensive scientific discussion of the high-latitude ionosphere [e.g., Richmond and Matsushita, 1975; Brekke et al., 1974].

In 2017, the extent of the relevant literature has become rather extensive; therefore the only studies focused on are those that are closely linked to the material in the thesis. Modern descriptions of Arctic ionosphere processes can be found in, e.g., Liu et al. [2016], Zou et al. [2014], Brekke [2013], Blagoveshchenskii [2013], Schunk and Nagy [2009], Coster et al. [2007]. Studying these ionospheric processes requires a set of observations which are derived from instruments present in the region. Currently the number of available instruments that are able to conduct a wide range of physical measurements about the Arctic ionosphere is steadily increasing. These can be ground-based, low earth orbiting (LEO) satellites, or satellites that orbit above the typical ionospheric altitudes (e.g., GNSS satellites). Three of the currently expanding ground-based GNSS networks are the Canadian High Arctic Ionospheric Network (CHAIN) [Jayachandran et al., 2009], the Canadian GPS Network for Ionosphere Monitoring (CANGIM) installed by University of Calgary [Skone and Hoyle, 2005], and the Greenland GNSS Network (GNET) [Durgonics et al., 2017]. Newer LEO

satellites are the polar orbiting Swarm satellite mini-constellation [Olsen et al., 2016] and the polar orbiting CAScade, Smallsat and IOnospheric Polar Explorer (CASSIOPE) [Yau et al., 2015], which were launched in 2013. Swarm and CASSIOPE provide state of the art in-situ multi-parameter measurements from inside the ionosphere. A new and still not fully operational GNSS constellation is the European Galileo (*https://www.gsc-europa.eu/system-status/Constellation-Information*). TEC is one of the most essential ionospheric observations that will be used in this dissertation, and its calculation is well detailed in several works, e.g., Komjathy [1997], Hernandez-Pajares et al., [2007], Jakowski et al., [2011], Komjathy et al., [2005b], Mendillo [2006], Teunissen and Montenbruck, [2017]. (Note that a basic introduction to TEC and related parameters is presented in Section 1.4.3 and to phase-based scintillation indices in Section 1.4.4.) It requires at least one GNSS satellite and a ground-based or a LEO satellite-based receiver [Hajj and Romans, 1998]. TEC mapping techniques were presented in Mannucci et al., [1998]. Digital ionosonde data can be processed and interpreted as described in Reinisch et al., [2009]. Further independent observational techniques include the Global Ultraviolet Imager (GUVI) which is on board the TIMED spacecraft [Paxton et al., 2004; Prölls, 1995; Verkhoglyadova et al., 2014; Meier et al., 2005; Zhang et al., 2004]. A network of coherent HF radars (SuperDARN) observations are also available and they have been used with relatively low horizontal resolution TEC data [e.g., Thomas et al., 2015; Prikryl et al., 2015c]. The set (or a subset) of observations described above may be utilized to collect measurements of the high-latitude ionosphere and compare these results to existing physical model outputs. This allows for an ongoing validation of these models and further improving them when they cannot be experimentally validated.

A brief summary of relevant studies regarding solar-terrestrial energy transfer processes (with focus on high-latitudes) are presented in this paragraph. Keskinen [1984] and more recently Lu et al. [2016] studied this high-latitude energy input and described this region of the terrestrial ionosphere

as a major sink for a wide range of solar and magnetospheric phenomena. The physical features of the high-latitude ionosphere originate from phenomena such as solar flares, ICMEs/CIRs, radiation belt and wave-particle interactions, and substorms [Keskinen, 1984]. Note that authors working in the field of ionospheric research and closely related topics often refer to ICME simply as CME, e.g., Rodríguez-Zuluaga et al. [2016], Chen et al. [2012]. However, strictly speaking CMEs (similarly to coronal holes) are solar phenomena; and geomagnetic storms are in fact triggered by ICMEs, which are solar wind phenomena. Because of this, the reader should always make sure to identify which phenomenon the authors refer to in a publication.

The electrodynamic coupling between the supersonic and magnetized solar wind and the magnetosphere-ionosphere-thermosphere system is the most crucial process that drives high-latitude plasma convection [Schunk and Nagy, 2009]. (Note that fundamentals of this Arctic **E**x**B** convection patterns are presented in more details in Section 1.4.1.) The interaction of the solar wind with geospace starts as the solar wind encounters Earth's magnetic field and forms the magnetosheath. This interaction subsequently creates the magnetopause [Haaland et al., 2014]; this relatively thin boundary layer separates the geomagnetic field from the interplanetary magnetic field (IMF) via a system of currents that flow in this layer [Lu et al., 2013; Dmitriev et al., 2012; Shue and Chao, 2013]. This separation is however not complete and a fraction of the IMF penetrates the magnetopause and magnetically connects with the terrestrial magnetic field. The region where this connection occurs is called the polar cap. The geomagnetic field lines over this area are referred to as open field lines, and the transition zone between the open and closed field lines is referred to as the auroral oval [Hosokawa et al., 2010].

The physical description of the solar wind plasma (which is the dominant medium in the processes described above) is based on certain assumptions and idealizations in this thesis. The assumptions and the idealized MHD equations are described in more detail in Section 1.4.1. Briefly, the solar

wind plasma is considered to be magnetized, collisionless, and highly conducting, therefore its electric field is governed by the cross product between the solar wind velocity and the IMF. When the IMF has a southward component its interaction with the geomagnetic field over the polar cap will result in a dawn-to-dusk directed electric field. This imposed electric field is mapped along interconnected IMF-geomagnetic field lines onto the polar cap ionosphere. Moreover, the high-latitude ionospheric electric field is mapped down even to the ground. This model was first suggested by Dungey [1961] and later improved upon by, e.g., Park [1976] and Toffoletto and Hill [1989]. This mapped-down electric field at ionospheric altitudes will drive an anti-sunward **E**x**B** plasma drift over the polar cap.

Because an across-the-polar-cap electric field exists, it can be inferred that the transition zone between open and closed field lines is charged, with positive charge on the dawn sector and negative on the dusk sector [Schunk and Nagy, 2009]. These charged sectors of the auroral zone (polar cap boundary) will consequently induce electric fields on the closed field lines near them, and they will have opposite polarity than the polar cap electric field [Stern, 1977]. These opposite-directed electric fields on the closed field lines will also map down to ionospheric altitudes, and consequently cause **E**x**B** plasma drift, but this will be sunward directed. The geomagnetic field lines that separate the oppositely directed electric fields will carry field aligned currents (FACs) that flow between the magnetosphere and ionosphere [Kaufmann et al., 1990]. The FAC flows toward the ionosphere on the dawn side, then along the ionosphere E layer, and then upwards when it reaches the dusk side. Figure 1.1 shows electrostatic potential contours over the northern polar cap in magnetic-latitude local time reference frame [Cousins et al., 2015]. The horizontal flow streamlines coincide with the potential contours when there is only an **E**x**B** drift and the IMF is pointing southward, and thus the convection will take a two-cell shape. As described above there will be an anti-sunward flow over the polar cap and a return flow (opposite direction) along the equatorward

boundary of the polar cap [Oksavik et al., 2010]. The scenario described above was an idealized one, because co-rotational and magnetospheric electric potentials were neglected along with the y-component of the IMF (B_y). Figure 1.1 depicts a real situation where the two-cell structure is deformed by these other influences. Note that there exists also a vertical drift which results from the fact that while **E** is perpendicular to **B**, **B** is typically not vertical even in the polar cap. Therefore, there will be an upward component for the **E**x**B** drift on the day side, and a downward component on the night side [Pedatella et al., 2011]. At times when the IMF points upward there will be a more complex cell pattern in the polar cap compared to the southward pointing IMF when there is a two-cell structure. During these times the over-the-polar-cap convection can be sunward and there can be three, four, or even more cells present. In this work I focus on times and events when the IMF is southward, therefore the more complex upward pointing case will not be further discussed [Le et al., 2002; Watson et al., 2016].

Among the aforementioned polar cap plasma convection phenomena, the most relevant for this work are the polar cap patches and the tongue of ionization (TOI) [Hosokawa et al., 2010; David et al., 2016; Middleton et al., 2005; Zhang et al., 2013]. Polar cap patches are plasma irregularities convected in or around the outer boundary of the polar cap with densities sometimes nearly one order of magnitude higher than the background ionospheric plasma [Liu et al., 2015; Horvath and Lovell, 2011]. One of the relatively early experimental observations of patches was made by Steele and Cogger [1996], who employed optical images of 630 nm emission from drifting F region polar patches from an all-sky imager for a period of 9 hours. They compared the observed ionospheric convection velocity with nearby digital ionosonde measurements and obtained good agreement between the two data sets. The patches can be the result of the breaking up of a tongue of ionization (TOI) structure or generated by precipitation events [Keskinen, 1984]. The exact physical processes that break the TOI into patches are not yet fully understood [Steele and Cogger, 1996], but the

phenomenon has been observed by several authors, e.g., Horvath and Lovell [2015], Middleton et al. [2008]. The TOI forms from midlatitude plasma that is convected across the polar cap as it was described before, thus it can be observed even during winter conditions when the polar cap ionosphere is extremely weak due to low to absent solar photoionization. During geomagnetic storms, solar-produced plasma densities become deposited on the equatorward edge of the midlatitude trough and form so called large storm-enhanced densities (SEDs) [Foster et al., 2004]. The SEDs can subsequently be transported across the polar cap and for the TOI. In Chapter 3, TOIs and TOI segmenting events were reported even during relatively calm conditions and not only during geomagnetic storms.

Although this work focuses on the Arctic ionosphere, it is important to note some of the potential physical similarities, differences (asymmetries), and interhemispheric conjugate effects between the Arctic and Antarctic ionospheres. In Zesta et al. [2016] energy input into the ionosphere-thermosphere system and asymmetries between the northern and southern hemispheres were investigated. It was found that solar wind energy and energy carried by the solar electromagnetic radiation are typically not distributed into the two hemispheres symmetrically. Geometrically speaking, during equinoxes, it can be assumed that the energy inputs into the north and south polar ionospheres are nearly symmetric. On the other hand, the distribution becomes extremely asymmetric during the solstices [Wu et al., 1991]. This geometrical picture is neglecting the orientation and geoeffectiveness of the solar wind, which alone can cause asymmetries even during ideal equinox times [Russell and McPherron, 1973; Lockwood et al. 2016]. Zesta et al. [2016] also found that seasonal illuminational effects were important drivers of interhemispheric asymmetries. The fact that seasonal variations cause dissimilar illumination conditions for the two hemispheres results in asymmetric ionospheric conductivities, and consequently, asymmetric current distribution in the two hemispheres. (Note that brief physical description of the solar photoionization is

presented in Section 1.4.2.) Furthermore, in addition to variability in diurnal and seasonal illumination, the solar cycle also plays a key role in the global TEC due to the crucial dependence of TEC on solar EUV radiation [Chakrabarty et al., 2012]. This effect is superimposed on the diurnal and seasonal variability and can potentially enhance the hemispheric asymmetry near solar maxima. Chapter 6 presents novel observations and analyses regarding the connection between solar EUV and high-latitude TEC. Other phenomena can also significantly affect the asymmetric energy input into the hemispheres, e.g., IMF orientation, terrestrial dipole angle with respect to the rotation axis, local magnetic field configuration, and even atmospheric dynamics. Analogous asymmetries exist in the auroral electrojets that are well correlated with the state of the auroral oval [Zesta et al., 2016].

Finally, it is important to mention the interhemispheric conjugate effects in the ionosphere. The history of research in this area started several decades ago [e.g., Rotwell et al., 1962; Matsushita et al., 1968]. These geomagnetic conjugate points are locations on the opposite hemispheres, but along (or nearby) the same geomagnetic field lines. Particles captured by the geomagnetic field tend to move along the same field lines back-and-forth, therefore these locations, even though they are far apart physically, are linked in a magnetic sense. A relevant conjugate effect study was conducted by Titheridge and Buonsanto [1983], where TEC measurements were collected from a pair of near-conjugate ground stations for a duration of 3 years, and it was observed that TEC values are persistently larger in the northern hemisphere than in the southern hemisphere. Further studies were later performed on conjugate F2 layer critical frequencies with similar results [e.g., Besprozvannaya, 1995; Chasovitin et al., 1987].

Another high-latitude phenomenon is the substorm, which is potentially the most common and well-studied nightside auroral process. Most of the substorm models are typically based on Northern Hemisphere observations and conjugacy is assumed between hemispheres. It was found

that a systematic displacement exists for the substorm onset locations in one hemisphere compared to the other [Ostgaard et al., 2007]. The list of known conjugated effects includes GPS phase scintillations. Studies using phase-based scintillation indices can be found in Chapters 3 and 4 and a similar but interhemispheric study was conducted by Prikryl et al. [2011b] and Morioka et al. [2011] where the focus was on phase scintillation measurements obtained from quasi-conjugate pairs of GPS receivers in the Arctic and Antarctic.

1.3 Overview of the Research

The research presented in this thesis is contained in already published articles (Chapters 2 to 5), articles in preparation for publication (Chapters 6 to 8), with a concluding chapter (Chapter 9). Since the included studies cover a relatively wide area and the topics are not always relate to each other in a scientific sense, this section aims to describe the relationship between them and to create the necessary connections so the thesis can be viewed as one continuous and cohesive work.

A multi-observation-based approach is used in this thesis to conduct a series of studies of ground and satellite-based measurements (except for Chapter 2 which employs only GPS-derived TEC data, Chapter 5 where GPS-derived reflectometry data is compared with simulations, and Chapter 7 in which GNSS-derived TEC maps are cross-validated). The measurements enable the determination of physical parameters and conditions of relevant geophysical meaning for the ionosphere, or in the case of Chapter 5, the neutral atmosphere and ocean surfaces. If it is feasible, the derived parameters are typically validated against each other to filter out biases or measurement artifacts. Next, we examined the data to find patterns and correlations in them; in this step we also interpreted the data in the context of the ionosphere. After interpretation, the results were compared

with existing knowledge and literature. Finally, we suggested hypotheses and logical consequences of the hypotheses based on mathematical models or simulations.

From the aforementioned steps it is apparent that multi-instrument observations played a very important role in this approach. The more instruments (or the more observations from a single instrument) one can employ in a specific study, the more geophysical/physical parameters can typically be derived and used for the understanding of the real physical processes that are occurring. With the inherent complexity of physical processes in the ionosphere, one type of observation is typically insufficient to understand the intricacies of the processes. For instance, Chapter 7 focuses on comparing the most widely used GNSS-derived TEC map products of today and reveals the biases between them. The physical interpretation of these biases will require additional independent methods. GNSS may provide a very convenient line-of-sight integrated electron density (Chapters 2 and 3), or in the case of reflected signals, sea surface parameters information (Chapter 5), but to put that information in context, scintillation data, vertical electron density profiles, electric field maps, plasma convection information, ion composition data, solar wind parameters, (Chapters 3, 4, 6, and 8) and physics-based assimilative models may also be needed in order to obtain a much more complete picture. Such a multi-instrument study is almost always multi-disciplinary. It typically requires the understanding of atmospheric physics, atmospheric chemistry, space plasma physics, electrodynamics, geomagnetism, and geomatics, among other fields. This multi-instrument approach or view was borne out of the body of work discussed here and a number of novel results were achieved by applying it.

Chapter 2 introduces the technical details of how to build a regional ionospheric monitoring network; this also includes specific software suggestions. This specific study was done for midlatitudes, but the information therein can be applied to all latitudes and sectors of Earth. We introduced a simple mathematical method for optimal GNSS ground station selection. This method

is most valuable when, due to technical limitations or other concerns, the inclusion of all available stations is not desired; or it can be employed when setting up a new network to provide ideal spatial distribution for a given region. One of the critical choices that need to be made when setting up ionospheric monitoring for a region is what kind of mapping technique will be used. Finally, as a practical application, diurnal and seasonal TEC time-series are presented for a midlatitude region. In summary, this chapter provides a solid basis for the following chapters which are mostly focused on higher-latitudes and because of this it is presented first. The station selection method and the interpolation techniques were used and improved in the following chapters/studies.

In Chapter 3, a robust multi-instrument study is presented on effects of the 19 February 2014 geomagnetic storm on the Arctic ionosphere. This particular storm was selected for the reason that it had the largest impact on the disturbance storm time (Dst) index in that year. One of the important findings of this study was the several days long negative storm effect following an ICME hit, which is again the subject of Chapters 6 and 8. We show that this negative phase typically starts when there is a sudden positive spike in the PC-index. The sudden PC-index jump indicates a rapid increase in energy input into the polar cap which, via a series of complex atmospheric processes, eventually leads to N_2 upwelling and decreased ionospheric electron density (in Chapter 8 it is shown that there is a similar negative phase after HSS-induced storms as well). The impact of the negative phase and the O/N_2 anomaly is strikingly strong, and since this storm occurred during winter conditions (when there is very limited photoionization in the polar cap), we can observe a depleted ionosphere for several days with very weak polar patch activity. Data obtained from the IRM sensor was used here for the first time in a published research. The analyzed IRM-derived data provided in-situ ion parameters and supported the upwelling hypothesis. The study introduced for the first time the mean vertical total electron content (MVTEC) parameter, which is also employed in Chapters 8 and 10. MVTEC is a special type of mean vertical total electron content (VTEC)

parameter that is capable of capturing large-scale electron density variations over a single GNSS station. As an example of single-instrument, multi-parameter data, we also analyzed rate of TEC index (ROTI) observations in addition to VTEC and MVTEC. ROTI, VTEC, and MVTEC are derived from the very same raw data source, but provide complementary information about the ionosphere. It demonstrated that TEC gradients do not always come with increased scintillations.

Chapter 4 is the second study that focuses on a specific storm, i.e., the geomagnetic storm of 17–18 March 2015. In addition to Greenlandic ground stations, stations from Canada, Alaska, and Russia were also included in the network which provided the GNSS data. This was also a multi-instrumental study using GNSS receivers, HF radars, digital ionosondes, riometers, and magnetometers. It is shown in this chapter how GNSS scintillations shift after the storm commences from the polar cap arcs to the cusp and SED regions. In agreement with the findings in Chapter 3, the main source of scintillations during the storms is TOI and polar patch originated. As the TOI convects over the polar cap it typically breaks down (gets fragmented into) patches. Inside the auroral oval, scintillation was found to be collocated with energetic particle precipitation causing bright auroras, and the EIC maps demonstrate that GPS phase scintillation was collocated with the westward electrojet. In general, the coupling between the solar wind and magnetosphere determines the regions where GPS scintillation will occur at high latitudes. These are typically the following areas: storm-enhanced density region, cusp, polar cap (TOI, polar patches, or sun-aligned arcs), auroral oval, and subauroral polarization streams.

Chapter 5 describes a different application of GNSS transmitted EM waves. This study focuses on GNSS-R techniques and simulations. The field of GNSS-R is developing and its applications are becoming more and more used for atmospheric science, climate science, and altimetry. In this study we introduced a new wave propagator that can be used to simulate GNSS-R signals in the context of reflections from ocean surface reflections. The developed simulator includes detailed models of

the neutral atmosphere and the ionosphere, and the interface between the electromagnetic wave and the ocean. The simulation results were compared against real ocean-reflection measurements where a GPS satellite is the transmitting source. Our short-time Fourier transformation method was able to distinguish between direct and reflected wave fields. The comparison with simulation output shows that the simulated results and the ocean-reflected measurements are in good agreement. The observations were obtained from a field campaign that took place at Haleakala Observatory on the island of Maui (Hawaii, U.S.A.). The summit where the observatory is located is at over 3,050 m in altitude. Surrounded by ocean, this location provides a good location for such a GNSS-R experiment, although ideally the receiver would be on a LEO satellite. We found that with additional work it could be possible to use GNSS-R to determine ocean wave heights, salinity, and other parameters.

In Chapter 6, we identified the physical mechanisms responsible for a series of features that were observed in an ionospheric MVTEC study using 4 years of data. Some of these ionospheric features are described here for the first time. This is also the first study that was conducted for such a long time period in the Arctic polar cap region using GPS satellite signals with such high time-resolution in the data. We found that the high MVTEC variability near the equinoxes is due to the Russel-McPherson effect. The observations reveal an approximately 27-day fluctuation with amplitude of 10-15 TECU in the MVTEC data throughout the studied years which was found to be the result of SSI EUV-related 27-day fluctuations. The fluctuations are more apparent during the summer when the ionosphere is smooth due to the filling-up effect caused by the constant solar photoionization. During the summer (when the F layer cross-field plasma diffusion rate is increased due to an underlying conductive E layer) the MVTEC time-series are significantly less variable than during the winter or equinox times, and this was identified as the consequence of the E layer conductance dependent diffusion model. In the winter the insulating E layer slows the F layer plasma decay rate,

allowing F layer structures to survive significantly longer and thus cause higher variability in MVTEC.

Chapter 7 summarizes an European Space Agency (ESA) validation campaign which was aimed to evaluate various ESA TEC map products. In Chapter 2 and 3 it was noted that the calculated slant vertical total electron content (STEC)/VTEC values always have biases and different kind of errors, thus this uncertainty will propagate into the TEC maps as well. In fact, the mapping process itself will also introduce additional errors which require further studies to assess. Our cross-validation results show that there can be significant differences between various global data products (e.g., ESA- International GNSS Service (IGS)), especially in the equatorial anomaly zone (even on the order of ~30 TECU) which poses an important question: which data product is actually the closest to physical reality? In this study we could not answer that question as that will require additional efforts. Nevertheless, there are times and regions where the data product estimates are very close to each other. We found that the best match was during winter conditions in northern Europe. This good match is due to the poorly developed, mostly featureless ionosphere, which we could call the ionospheric ground state. This ground state appears as a plateau of nearly constant TEC (typically between 2-5 TECU) at high-latitude winter time when solar photoionization is nearly nonexistent and there is no active geomagnetic storm or sub-storm. During this low activity time period the most important factors in TEC calculation are the station and satellite biases. If these are not calculated properly, it is possible to obtain non-physical, negative TEC values. In all the studied data products this was handled well. The worst match occurs along the equatorial anomaly, especially in those areas where ground station coverage is poor. We also found that there is a quite stable bias between ESA and IGS global TEC products in general, which is possibly due to the difference in the aforementioned bias estimations. During geomagnetic storms the bias between products always changes sign, however this interesting phenomenon requires further analysis.

In Chapter 8, a comparison study is presented between ICME-induced and HSS-induced ionospheric storm effects. ICME-induced storms (e.g., Chapter 3) and mixed ICME-HSS-driven storms (e.g., Chapter 4) have been studied in the literature. Pure HSS-driven storms seem to receive less attention due to the fact that the related geomagnetic storm is usually less intense and builds up slower than ICME storms, even though we found that the former typically deposits more energy into the magnetosphere during its whole duration. We also found that even though the PC-index rise is significantly slower during HSS hit and during ICME hit, there is also a negative phase present during the main and recovery phases of the storm that can effectively slow polar patch formation. The exact physical mechanism behind this is still to be identified, but from GUVI and IRM measurements, it was suggested that one of the main factors is probably the N_2 upwelling (Chapter 3) that occurs during the storm. This effect is quite significant during winter conditions (the differences between summer and winter polar cap ionospheres were explored in Chapter 6) and future work should be carried out to obtain and analyze observations during a summer time geomagnetic storm in order to see how a highly conducting E layer affects this process. For more suggestions on future works see Chapter 9.

The presented research topics in Chapters 2 through 8 possess many common aspects. For example, all of them utilize GNSS-transmitted radio signals as the main technological tool to gain additional insights about the atmosphere. In general, ionized and neutral atmospheric species are important to obtain a complete picture of the contributing physical processes. One example of this is in Chapter 3, where a sudden N_2 upwelling significantly affected the ionospheric dynamics at a large scale. Chapter 5, while it does not concern the ionosphere, the study also employs GNSS-based data to determine ocean reflection parameters. In this case the ionized part of the atmosphere was affecting the signals while they were propagating through the ionosphere, but using certain assumptions, this influence was rightfully neglected during this study. Thus Chapter 5 deals solely with neutral

atmospheric medium, which differs from the remaining studies. Because GNSS-R is still an emerging field, with significant scientific and technological potential on Earth as well as on other planets, it was considered relevant to include in this thesis. Furthermore, GNSS-R is one of the three main GNSS applications that is used in atmospheric and surface properties science, these are (1) GNSS tomography (GNSS satellite-ground station), (2) GNSS-RO (GNSS satellite-LEO satellite), and (3) GNSS-R (GNSS satellite-terrestrial surface-LEO satellite or ground station at a high elevation). An additional published study that was not included in this thesis concerned GNSS-RO [Shume et al., 2017]. By utilizing these three techniques, substantial information can be obtained from the terrestrial atmosphere and surface. In this work solar-driven processes were primarily examined, e.g., ionospheric storms, atmospheric heating, and long-term EUV-TEC relations. To get a full picture of these processes, other measurements were often used to complement the GNSS-based measurements. In summary, while the work presented in this thesis can be considered overarching they are all connected by their main tool using GNSS measurements and their object of scientific investigations.

1.4 Scientific Approach

As discussed in Section 1.3, this work builds on a wide range of scientific fields and also on numerous interdisciplinary areas. These include atmospheric physics, atmospheric chemistry, space plasma physics, electrodynamics, geomagnetism, and geomatics. That said, the scientific approach employed in this work always starts with experiments (observations) and is followed by an attempt to identify the best fitting physical or physics-based computational model while always keeping the relevant simplifying assumptions in mind. It is clear that presenting all the required background knowledge in the relevant fields is out of the scope of this dissertation, and it is assumed that the

reader is familiar with them and some of the fundamental studies cited in Section 1.2. However introduction to at least the most essential processes and methods could support the presented studies, therefore a few particularly relevant topics are discussed in this section. These are the following: Section 1.4.1: Fundamentals of the Arctic **E**x**B** Convection Patterns; Section 1.4.2: The Solar photoionization; Section 1.4.3: STEC, VTEC, and MVTEC Calculations; Section 1.4.4: Phase-Based Scintillations: σ_ϕ and ROTI. Note that each presented study (Chapters 2 to 8) also contains a brief description of relevant methodologies, so the topics presented in the following sections can be considered as supporting materials.

Two key phenomena that deposit energy into geospace are the solar wind and solar electromagnetic radiation (solar irradiance). Directly or indirectly, these phenomena power most of the ionospheric processes. The physical description of these two processes is discussed separately due to differences in the physical models in which they are typically described. Section 1.4.1 deals with the solar wind and briefly how the solar wind **E** field gets mapped down to ionospheric altitudes through simplified MHD equations. It presents the polar cap **E**x**B** plasma drift formula and introduces the basic polar cap plasma irregularity nomenclature. This is followed by the description of solar photoionization (Section 1.4.2), which is predominantly responsible for the ionospheric plasma generation. Next, the connection is derived between the irradiance intensity at any neutral density relative to the maximum values. Simplifying assumptions about monochromatic radiation and single-species atmosphere are used. The subsequent discussion (Section 1.4.3) is describes a methodology where three columnar electron density parameters are defined. These three parameters are used throughout the work, therefore they deserve additional discussion. Finally, in Section 1.4.4, a methodology is presented that is similar to Section 1.4.3, but there the frequently used phase-based scintillation indices are defined. Sections 1.4.1 to 1.4.4 together provide additional scientific background relevant for the subsequent chapters.

1.4.1 Fundamentals of the Arctic ExB Convection Patterns

The aim of this section is to provide the reader with a brief overview of the physical processes behind some of the core phenomena discussed in Chapters 3, 4, 6, and 8. The aim is to build up the connection between the solar wind and the magnetosphere and then to describe how the mapped-down **E** field contributes to the polar cap **E**x**B** drift. Note that additional relevant literature to this Section is also presented in Section 1.2.

The solar wind and solar irradiance are the main influences that drive the strongly coupled ionosphere-magnetosphere-atmosphere system. Following the approach of Schunk and Nagy [2009], the solar wind is modeled using the simplified MHD equations. In order to use these simplified equations one has to add several assumptions.

(1) $\rho_c = 0$, i.e., the charge neutrality stands.

(2) $\mathbf{P} = p\mathbf{I}$, so consequently $\nabla\mathbf{P} = \nabla p$, where $\mathbf{P}$ is the pressure tensor, p is the scalar pressure.

(3) $\mathbf{J} = \sigma_e (\mathbf{E} + \mathbf{u} \times \mathbf{B})$, i.e., the simplified Ohm's law stands, where $\mathbf{J}$ is total current density vector, σ_e is the parallel conductivity, $\mathbf{E}$ is the electric field vector, $\mathbf{u}$ average drift velocity vector, and $\mathbf{B}$ is the magnetic field vector.

(4) The energy equation can be simplified into an equation of state. (For more details on this see Schunk and Nagy [2009]).

(5) The ion time scales govern the interactions, i.e., the changes in the plasma are occurring slowly in time so that the displacement current is negligible: $\varepsilon_0 \partial\mathbf{E}/\partial t \approx 0$, where ε_0 is the permittivity of free space.

If the assumptions (1) to (5) are justified, one can write the simplified MHD equations as follows:

$$\frac{\partial \rho}{\partial t} + \boldsymbol{\nabla} (\rho \mathbf{u}) = 0, \tag{1.1}$$

$$\boldsymbol{\nabla} \mathbf{J} = 0, \tag{1.2}$$

$$\rho \frac{D\boldsymbol{u}}{Dt} + \boldsymbol{\nabla} p - \rho \mathbf{G} - \boldsymbol{J} \times \mathbf{B} = 0, \tag{1.3}$$

$$\mathbf{J} = \sigma_{\mathrm{e}} (\mathbf{E} + \mathbf{u} \times \mathbf{B}), \tag{1.4}$$

$$p = \mathrm{C} \rho^{\gamma}, \tag{1.5}$$

where **G** is acceleration vector due to gravity, C is a constant, γ is ratio of specific heats (e.g., γ = 1 for isothermal flow and γ = 5/3 for adiabatic flow), and note that $\frac{D}{Dt} = \frac{\partial}{\partial t} + \boldsymbol{v} \boldsymbol{\nabla}$.

The associated Maxwell equations are given by following equations:

$$\boldsymbol{\nabla} \times \mathbf{E} = -\frac{\partial \boldsymbol{B}}{\partial t}, \tag{1.6}$$

$$\boldsymbol{\nabla} \times \mathbf{B} = \mu_0 \boldsymbol{J}, \tag{1.7}$$

In our simplified physical model, the solar wind is a magnetized, collision-free, and highly-conducting plasma satisfying Equations 1.1 to 1.5. From now on, instead of **u,** $\mathbf{u}_{\mathrm{SW}}$ will be written, where SW stands for solar wind and $\mathbf{u}_{\mathrm{SW}}$ is the solar wind velocity. As the focus is on the high-latitude ionosphere, the concentration is on the region poleward from the open-closed field line boundary, i.e. the polar cap. Equatorward from this imaginary line the field lines are closed. And along this line lies the auroral zone where the field lines are closed but they are *pulled* out into space by the solar wind. These stretched field lines allow for a set of interesting phenomena to occur - some of these are discussed in Chapter 4.

The simplified current density MHD equation (Equation 1.4) shows how the electric field behaves in the solar wind. In the limit of $\sigma_e \rightarrow \infty$ (i.e., highly conducting plasma) Equation (1.4) will take the shape of

$$\mathbf{E} + \mathbf{u} \times \mathbf{B} = 0. \tag{1.8}$$

When only the perpendicular-to-B-component of **u**, denoted by $\mathbf{u}_\perp$, is considered in Equation (1.8) the cross product of Equation (1.8) with **B** yields the **E** × **B** plasma drift velocity formula:

$$\boldsymbol{u}_\perp = \frac{\mathbf{E} \times \mathbf{B}}{B^2} \ . \tag{1.9}$$

Equation (1.9) is one of the fundamental equations used in the understanding of high-latitude ionospheric dynamics. It describes how the plasma convects when there are **E** and **B** fields present. In the next step it will be demonstrated how the high-latitude **E** field gets mapped down from the solar wind **E** field into the ionosphere.

It was shown in Equation (1.8) how the solar wind **E** field behaves. This **E** field is present outside the magnetopause as the solar wind drifts near geospace. (We define geospace as the combination of terrestrial magnetosphere, atmosphere, and ionosphere systems.) Equation (1.8) can be rearranged as

$$\mathbf{E}_{SW} = -\mathbf{u}_{SW} \times \mathbf{B}_{SW} \ . \tag{1.10}$$

$\mathbf{B}_{SW}$ is also called interplanetary magnetic field (IMF) and its vector components are traditionally written as (B_x, B_y, B_z). Spacecraft-derived IMF data is typically presented in geocentric solar ecliptic (GSE) and geocentric solar magnetospheric (GSM) coordinate systems (for a detailed description of these reference frames see, e.g., Lockwood et al. [2016]). In both frames *X* points to the sun and it is parallel to the imaginary line between the sun and the earth. Positive *Z* in GSE points to the north

ecliptic pole, while in GSM it is the projection of earth's dipole axis on GSE YZ plane. And finally, *Y* completes the right-handed coordinate system in both cases. The (B_x, B_y, B_z) components are important solar wind parameters and they can significantly shape high-latitude ionospheric convection systems (Figure 1.1). It is worth noting that the difference between the GSM and GSE coordinate systems can explain the Russell-McPherron effect [Russell and McPherron, 1973], which is discussed in Chapter 6.

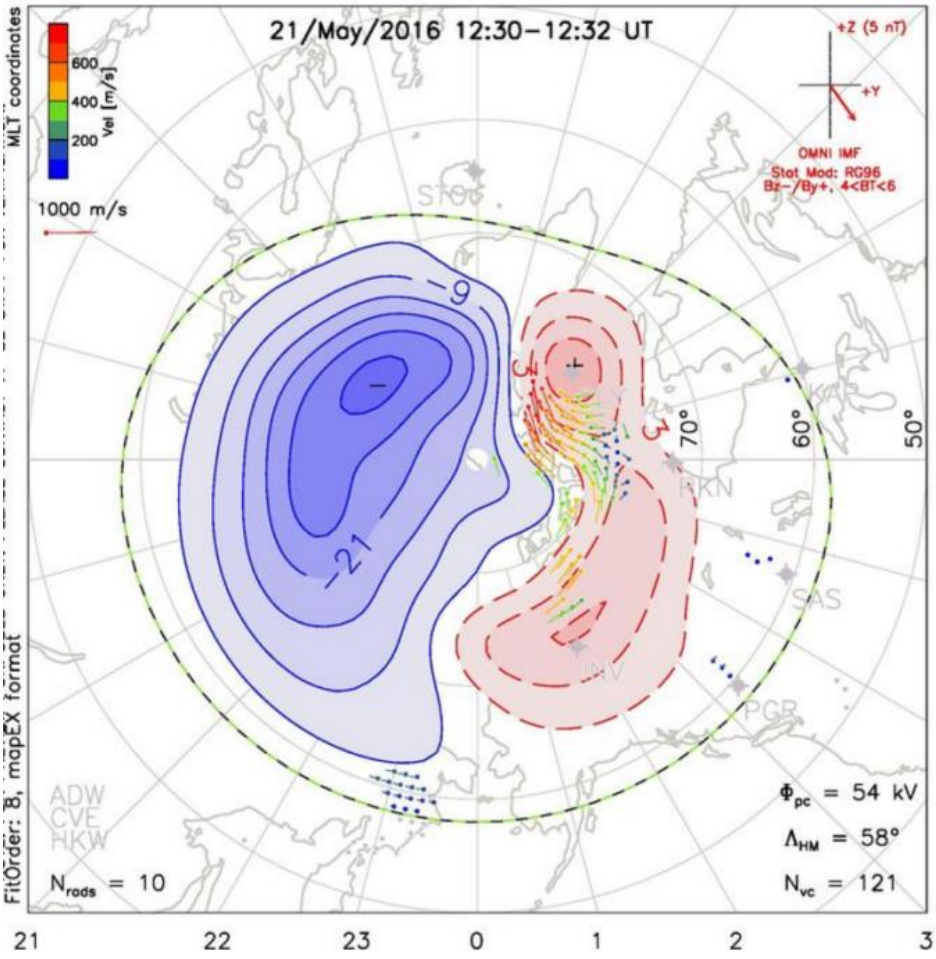

Figure 1.1 An example of a SuperDARN convection map depicting polar cap electric field contours in a magnetic local time (MLT) reference frame and showing the IMF B_y and B_z (right upper corner) components (source http://vt.superdarn.org). The map has the north magnetic pole at the center and extends to a lower boundary at 50°. The direction to the sun is upward (12 MLT). The contours represent ionospheric electrostatic potentials in kilovolts and are parallel to the plasma motion. Plasma velocity vectors are plotted at locations where Doppler velocities are observed.

The main drivers behind the two-cell convection pattern asymmetry are co-rotational effects and the IMF B_y and B_z components.

When B_z is negative (points downward) the solar wind imposes a dawn to dusk directed electric field across the polar cap (see Equation 1.10). Any potential between the highly conductive geomagnetic field lines will map down along said field lines into the ionosphere which will result in an $\mathbf{E} \times \mathbf{B}$ drift (see Equation 1.9). Such ionospheric plasma convection can be seen in Figure 1.1. In an ideal case where $B_y = 0$, a symmetrical double-cell convection pattern would result. In Figure 1.1 B_z is negative and *By* is positive which will distort the shape of the double-cell structure. Note that the across-the-polar-cap convection is antisunward under these circumstances. When B_z is positive the two-cell convection patter typically breaks up and gets distorted into a more complex structure. This more complex pattern may include several cells and turbulence. Additional literature regarding the **E** field mapping is presented in Section 1.2.

There exists an extensive body of work dealing with polar cap plasma convection dynamics. Chapters 3 and 4 further discuss some of the most important aspects. The plasma is typically being convected across the polar cap in the form of so-called polar patches. The convection speed of the polar patches is typically between 300 ms^{-1} to 1 kms^{-1}. Figure 1.1 shows relatively calm geomagnetic conditions where the convection speed is around a few hundred ms^{-1}. Patch number densities are 5 to 10 times more intense than the background ionospheric densities and their horizontal scale-sizes can vary from 200 to 1000 km [Pedersen et al., 2000]. At times, under the same conditions, a tongue of ionization (TOI) structure can be observed instead of individual patches, or the TOI can break up into patches while it convects over the polar cap [Prikryl et al., 2016]. There are a number of further relevant ionospheric phenomena that can be observed at high latitudes or near the equatorward boundary of the open field lines. For instance Foster [1993]

describes the storm-enhanced density plumes (SEDs) as solar-produced F-region ionospheric plasma that is transported sunward and poleward from a source region in middle and low latitudes in the afternoon sector. Consequentially, a latitudinally narrow section of SED and increased TEC is convected toward higher latitudes in the noon sector. For further details about on SEDs, TOI, and polar patches see, e.g., Coster et al.[2007]; Zou et al., [2014]; Liu et al., [2016]; and Pedersen [2000].

1.4.2 The Solar Photoionization

The aim of this section is to provide the reader with brief overview of the physical processes behind some of the core phenomena discussed in Chapters 2 and 6.

Solar extreme ultraviolet (EUV) radiation is part of the electromagnetic spectrum, specifically between 124 nm and 10 nm wavelengths. EUV and electron precipitation are among the most important sources of input energy into the Arctic ionosphere [Schunk and Nagy, 2009]. In this section contributions and relevant effects of EUV will be discussed. Before proceeding and describing the physical principles, a set of simplifying assumptions is first presented in order to make the derivation clearer.

(1) Instead of the whole EUV band, it is assumed that the solar radiation is monochromatic, i.e., λ is the wavelength and $I(\lambda, z)$ is the intensity, where z is the altitude.

(2) The ionosphere (and the atmosphere) consists of a single species. The density of this species decreases exponentially with z:

$$n = n_0 \exp(-z/H), \tag{1.11}$$

where n_0 is the density at the reference height z_0 (typically at z_0 = 0) and H is the characteristic length (scale height).

(3) The surface of the earth is a plane and the atmosphere is horizontally layered.

(4) The atmosphere is in hydrostatic equilibrium.

Following the approach in Brekke [2013], the equation for the monochromatic radiation passing through an infinitesimal part (*ds*) of the atmosphere can be written:

$$\frac{dI}{ds} = -n\sigma I, \tag{1.12}$$

where σ is the cross-section (probability) of ionizing an atmospheric particle per m^2. For each unit of energy, as a consequence of the ionization, there will be a number (ionization efficiency or *C*) of new free electrons present. That is:

$$q = C\sigma nI\frac{dI}{ds}. \tag{1.13}$$

For atomic species C = 1. In this model we assumed that the ionosphere only consist of O atoms. To find the maximum of the product *nI* we may write:

$$\frac{dq}{ds} = -C\sigma\left(I\frac{dn}{ds} + n\frac{dI}{ds}\right) = 0, \tag{1.14}$$

$$\frac{1}{n_{max}}\left(\frac{dn}{ds}\right)_{max} + \frac{1}{I_{max}}\left(\frac{dI}{ds}\right)_{max} = 0. \tag{1.15}$$

At this step it is proper to incorporate the zenith angle (χ) of the radiation into the equations. The zenith angle is conveniently defined as:

$$ds = -\frac{dz}{\cos(\chi)}, \tag{1.16}$$

and consequently

$$\frac{1}{n}\frac{dn}{ds} = -\frac{1}{n}\frac{dn}{dz}\cos(\chi)\ . \tag{1.17}$$

Plugging *n* from (1.11) into (1.17) yields:

$$\frac{1}{n}\frac{dn}{ds} = \frac{\cos(\chi)}{H}. \tag{1.18}$$

Equation (1.18) is valid for any *s* distance,, but for the specific case of production maximum, , (1.18) becomes:

$$\frac{1}{n_{max}}\left(\frac{dn}{ds}\right)_{max} = \frac{\cos(\chi)}{H}\ . \tag{1.19}$$

Taking Equation (1.12) at this maximum yields:

$$\frac{1}{I_{max}}\left(\frac{dI}{ds}\right)_{max} = -\sigma n_{max}. \tag{1.20}$$

Plugging Equations (1.19) and (1.20) into (1.15) results in:

$$\frac{\cos(\chi)}{H} - \sigma n_{max} = 0, \tag{1.21}$$

and thus

$$\sigma n_{max} H\sec(\chi) = 1, \tag{1.22}$$

where

$$\sec(\chi) = \frac{1}{\cos(\chi)}\ . \tag{1.23}$$

It is known (for example from Brekke [2013]) that if an atmosphere has constant scale height (see also assumption (2) in this section) the following equation stands:

$$n_0 H = \mathcal{N}\,, \tag{1.24}$$

where $\mathcal{N}$ is the total number of neutrals between infinity and the reference height (per unit area). For the specific case of maximum ionization height, (1.24) takes the following form:

$$n_{max} H = \mathcal{N}_{max}. \tag{1.25}$$

Plugging (1.25) into (1.22) yields:

$$\sigma \mathcal{N}_{max} \sec(\chi) = 1. \tag{1.26}$$

Inserting (1.16) into (1.12) and results in the following steps:

$$\frac{1}{I}\frac{dI}{ds} = -\frac{1}{I}\frac{dI}{dz}\cos(\chi) = -\sigma n = -\sigma n_0 exp\left(-\frac{z}{H}\right)$$

$$\frac{dI}{I} = \sigma n_0 exp\left(-\frac{z}{H}\right)\sec(\chi)dz$$

$$\int_{I_\infty}^{I} \frac{dI}{I} = \sigma n_0 \sec(\chi) \int_{\infty}^{z} exp\left(-\frac{z}{H}\right) dz$$

and finally:

$$\ln\frac{I}{I_\infty} = -\sigma n H \sec(\chi). \tag{1.27}$$

Taking Equation (1.27) at the maximum ionization height yields:

$$\ln\frac{I_{max}}{I_\infty} = -\sigma n_{max} H \sec(\chi) = -1 \tag{1.28}$$

and

$$I_{max} = \frac{I_\infty}{e}\,. \tag{1.29}$$

The meaning of Equation (1.29) is clear: the original intensity of the radiation decreases with a factor of $\frac{1}{e}$ at the height of the maximum production. Observational determination of the maximum production height is possible with, e.g., ionosondes [Reinisch et al., 2009] or GNSS-RO [Hernández-Pajares et al., 2017; Hajj and Romans, 1998; Fjeldbo et al., 1971; Fjeldbo and Eshleman, 1969].

The general expression of Equation (1.29) can be derived as follows:

$$I = I_{\infty}\exp\big(-\sigma nH\sec(\chi)\big) = I_{\infty}\exp(-\tau),$$

where $\tau = \sigma nH\sec(\chi)$, which is called optical depth. τ_{max} is the optical depth at the maximum production altitude:

$$\tau_{max} = \sigma n_{max}H\sec(\chi) = \sigma n_0\exp\left(-\frac{z_{max}}{H}\right)H\sec(\chi) = 1$$

and thus

$$\exp\left(\frac{z_{max}}{H}\right) = \sigma n_0 H\sec(\chi).$$

For the case of $\chi = 0°$:

$$\exp\left(\frac{z_{max,0}}{H}\right) = \sigma n_0 H \tag{1.30}$$

and thus

$$\exp\left(\frac{z_{max}}{H}\right) = \exp\left(\frac{z_{max,0}}{H}\right)\sec(\chi)$$

and finally (1.31) can be derived :

$$\frac{z_{max}}{H} = \frac{z_{max,0}}{H} + \ln[\sec(\chi)]. \tag{1.31}$$

Equation (1.31) describes the relationship between the height of the maximum ion production and zenith angle. Maximum production height is lowest when the sun is in the zenith ($z_{max,0}$). Equation (1.31) is particularly important in the polar ionosphere due to the typical solar radiation incident angles at these latitudes. The ionosphere is often modeled as a thin-shell single-layer 2D surface at the maximum ionization height [Komjathy, 1997], but as it is clear from (1.31), the single-layer height is never constant even in this largely simplified model. For the Arctic ionosphere we used an empirically determined 350 km single-layer height (see, e.g., Chapter 3). Note that in the literature we use the following conventions: $n_{max} = N_mF_2$ and $z_{max} = h_mF_2$, where F_2 denotes the F_2 layer of the ionosphere.

Combining (1.27) and (1.28) with (1.26):

$$\mathrm{Ln}\frac{I}{I_{max}} = -(n - n_{max})\sigma H\sec(\chi) = \left(1 - \frac{n}{n_{max}}\right),$$

and

$$\frac{I}{I_{max}} = \exp\left(1 - \frac{n}{n_{max}}\right) \tag{1.32}$$

Equation (1.32) provides the connection between the intensity at any neutral density relative to the maximum values.

In this section it was assumed that the radiation is monochromatic and that there is only one atmospheric species present. Clearly, the terrestrial atmosphere contains multiple species, such as O, N_2, O_2, N, NO, H, He, etc. The dominant species around the heights where the ionization reaches its maximum (also called ionospheric F layer) is atomic O with the first ionization energy of V_p = 13.61 eV (λ = 91.1 nm):

$$O + h\upsilon \rightarrow O^+ + e^- \tag{1.33}$$

Thus only photons with wavelengths shorter than $\frac{hc}{V_p}$ can ionize O, which means only EUV or shorter wavelengths from the solar irradiation can participate in this process. For a multi-species multi-frequency model the above equations will take a more complex form [Brekke, 2013].

1.4.3 STEC, VTEC, and MVTEC Calculations

In this dissertation we employ three types of total electron content (TEC) parameters: slant TEC (STEC), vertical TEC (VTEC), and mean VTEC (MVTEC). Figure 1.2 shows the simplified geometry for STEC and VTEC calculation.

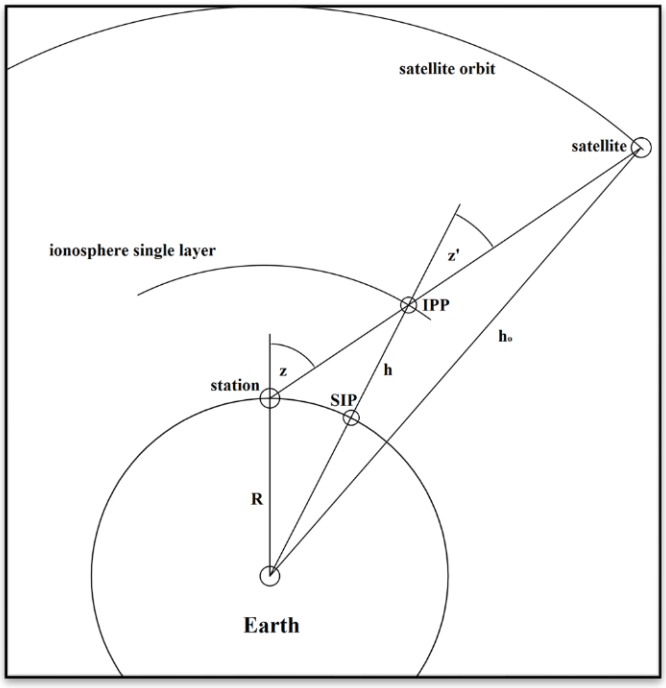

Figure 1.2 Schematics of STEC and VTEC geometry. The satellite is a seelcted GNSS satellite and the station on earth's surface can represent any selected GNSS receiver. The ionosphere single layer (shell) height is typically set at the h_mF_2 peak density height, denoted by h. The line connecting the station with the satellite (line-of-sight) intersects the single layer height at the ionospheric piercing point (IPP). The orthogonal projection of the IPP coordinates onto earth's

surface gives the sub-ionospheric point (SIP) coordinates. The angle z between zenith and the satellite's visible location is called satellite zenith angle.

A software application called Arctic Ionospheric Maps (AIM) was developed in this dissertation [Durgonics et al., 2017]. AIM is capable of calculating all the three aforementioned TEC types and mapping them in planar 2D space using the *natural neighbor interpolation* method. Although AIM has Arctic in its name, it has been also successfully applied for midlatitude ionospheric monitoring in Denmark (*http://www.spaceweather.space.dtu.dk/Forskning/GPS*). In this section we describe how AIM is used to compute TEC maps. AIM is not yet fully complete as it still relies on a small number of external data products, e.g., precise orbit data and satellite differential code biases (DCBs) (details on DCB determination can be found in, e.g., Hernandez-Pajares et al. [2007] and Komjathy [1997]). The first TEC parameter that AIM calculates is the STEC (see Appendix III). This provides the number of free electrons along the signal path between a GNSS satellite and a ground receiver for a 1 m^2 column. The unit for TEC is TEC unit (TECU), 1 TECU equals 10^{16} electrons in 1 m^2 cross section. TEC is sometimes also referred to as the columnar electron density.

In Figure 1.2, the ionosphere single-layer (see also Section 1.4) is represented with an infinitesimally thin sphere; however AIM treats the single layer as a rotational ellipsoid. IPP (ionospheric pierce point) is the point where the signal path crosses the single-layer shell and SIP is the sub-ionospheric point. The GNSS receivers on the ground are capable of measuring a set of observables related to the transmitted GNSS satellite signal. P_1, C_1, and P_2 are code observables; the index indicates the GPS frequency they belong to. L_1 and L_2 are the phase observables for the first and second GPS frequencies, respectively. These observables can be obtained directly from GNSS receivers. Among these, AIM uses the code observables (P_1 or C_1 and P_2) and the phase observables (L_1, L_2) to compute STEC [Misra and Enge, 2011]. AIM assumes the GPS geometry-free

combinations of phase and code (L_I, P_I) for each satellite-receiver pair as described by Hernandez-Pajares et al. [2007]. The code observables are then smoothed with hatch-filter (Appendix II) [Hatch, 1982] and corrected for DCB_{sat} and DCB_{rec}:

$$STEC = L_I - \langle L_I - P_I \rangle - DCB_{sat} - DCB_{rec} \tag{1.34}$$

where the angle brackets symbolize the mean value calculated for a continuous arc of observations, (which was performed by hatch-filtering), and DCBs are differential code biases, which are inter-frequency biases resulting from the receiver hardware. STEC unavoidably incorporates elevation angle dependence (See Figure 1.2): the lower the elevation-angle of a satellite, the longer its path inside the ionosphere. To correct for this, AIM has a 10 degree elevation cutoff angle and uses the following mapping function:

$$VTEC = STEC\sqrt{1 - \left[\frac{\rho_l \cos(\alpha)}{\rho_l + h_s}\right]^2}. \tag{1.35}$$

where ρ_l is local earth curvature at the receiver station, α is the elevation angle, and h_s is the ionospheric single layer height (350 km) [Jakowski et al., 2011]. The obtained VTEC is typically used for time-series analysis and 2D TEC mapping.

AIM is also capable of calculating MVTEC values from GNSS observations. The geometry of MVTEC can be seen in Figure 1.3.

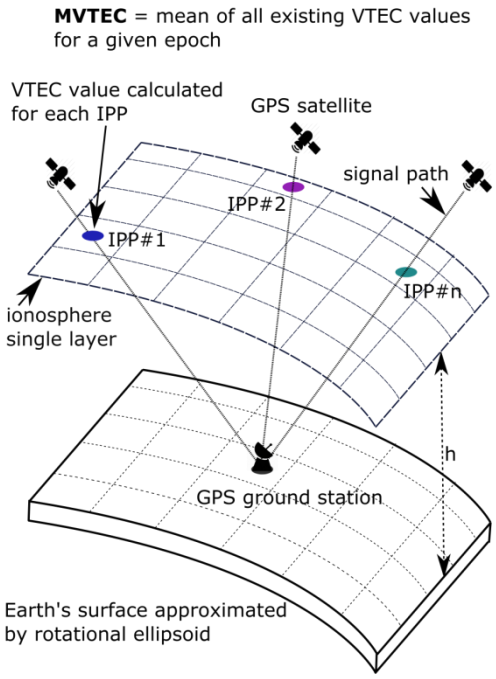

Figure 1.3 Schematics of MVTEC geometry. MVTEC is the mean of all the VTEC values at a given epoch. Since IPP locations can be geographically far from each other, this parameter typically averages values over a large area.

During undisturbed times in any epoch, a typical modern GNSS ground station is capable of observing around ~12 GPS satellites in the polar cap. This equals to ~12 IPP locations and a VTEC value for each IPP. The IPPs can be quite far away from each other - in Chapter 6 the reader will see the area the IPPs can cover for a single station. The outer boundary of this area is close to an oval shape, therefore the whole area is referred to as an *IPP oval*. A single ground receiver can only obtain information inside its IPP oval, but inside this large area the ionosphere can be quite varied. When the signal path crosses polar patches, the observed VTEC values can increase significantly compared to the ionospheric background density. This makes it difficult to observe large scale phenomena above the station. For this reason MVTEC was introduced, which is calculated as the mean of all the observed VTEC values for a single station (Figure 1.3). MVTEC can be thought of

as a low pass filter that will remove small scale disturbances and can be visualized as a smoothed single ionospheric density layer above the station.

1.4.4 Phase-Based Scintillations: σ_ϕ and ROTI

It is known from the works of, e.g., Pi et al. [2013], Rino [1979], Bhattacharyya et al. [2000] and Kersley et al. [1988] that amplitude scintillations (S_4) are not well-suited for high-latitude ionospheric studies due to the phenomenon called Fresnel filtering. By definition S_4 is calculated as:

$$S_4 = \sqrt{\frac{\langle I^2 \rangle - \langle I \rangle^2}{\langle I \rangle^2}} \,. \tag{1.36}$$

S_4 is typically determined for a 60-second data segment. On the other hand, the phase scintillation index (σ_ϕ) is generally considered ideal and it is widely used in this region. By definition σ_ϕ is calculated as:

$$\sigma_\phi = \sqrt{\frac{1}{N}\sum_i (\phi_i)^2} \,, \tag{1.37}$$

where ϕ is the differential phase (see, e.g., Rino [1979]). Another phase-based scintillation index is the rate of TEC index (ROTI) which is calculated from the rate of TEC (ROT) parameter as shown in Equation (3.1). ROT is in TECU/min units, t and Δt are the time at a certain epoch and the sampling rate in minutes respectively. ROTI is the detrended standard deviation of ROT over N epochs, as shown in Equation (3.2), which is calculated using 1-minute running window [Pi et al., 2013; Jacobsen, 2014; Durgonics et al., 2017].

Pi et al. [2013] states that when measuring ionospheric irregularities, the resulting S_4, σ_ϕ,, and ROTI observations are in fact correlated, but this correlation is not linear. This non-linearity can take an extreme form in the Arctic when S_4 is largely rendered ineffective due to Fresnel filtering. In general, the correlation means that ROTI is a good occurrence indicator for both S_4, σ_ϕ scintillations; however the measured magnitudes will have a non-linear dependence. It is also important to be aware of some inherent limitations that ROTI has compared to S_4 and σ_ϕ. For ROTI to be able to distinguish electron density fluctuations inside irregularities, the phase screen approximation needs to be valid [Bhattacharyya et al., 2000]. This approximation may fail when there are significant fluctuations inside an irregularity layer (e.g., inside a TOI). Conversely, σ_ϕ will still be able to track these fluctuations inside a thick layer [Bhattacharyya et al., 2000]. Unfortunately, due to technical and infrastructural limitations, there exist high-latitude GNSS networks where only geodetic receivers are installed and in that case ROTI is the only technically viable way to measure scintillations [Durgonics et al., 2017].

1.5 Outline of the Dissertation

This work consists of published studies (Chapters 2, 3, 4, and 5) and research that are in progress and aimed for later publications (Chapters 6, 7, and 8). Additional chapters are included to provide context and describe the connection between Chapters 2-8. The dissertation is organized as follows:

Chapter 1 This is the introductory chapter. Its aim is to give a brief overview of the most relevant articles in the field and describe structure of the dissertation. Furthermore, it gives an overview of some important high-latitude physical processes, equations, and relevant data types.

Chapter 2 (Study 1) Essential aspects of GNSS ground network distributions, TEC mapping techniques, and interpolation methods.

Chapter 3 (Study 2) A complex multi-instrumental case study analysis of a specific ionospheric storm.

Chapter 4 (Study 3) A second multi-instrumental case study focusing on scintillation structures.

Chapter 5 (Study 4) Comparison of observations with simulation results for ocean reflected GNSS signals.

Chapter 6 A 4-year long regional electron density study, in which the various features are analyzed and linked to existing physical models.

Chapter 7 Results and conclusions of an ESA TEC cross-validation campaign.

Chapter 8 A comparison study between HSS and ICME induced storms.

Chapter 9 Summarizes the results and suggests future research recommendations.

The published papers present in Chapters 2-5 are the following:

I. **Durgonics, T.**, G. Prates, and M. Berrocoso (2014), *Detection of ionospheric signatures from GPS-derived total electron content maps*, Journal of Geodetic Science, Vol. 4, Issue 1, doi:10.2478/jogs-2014-0011.

II. **Durgonics, T.**, A. Komjathy, O. Verkhoglyadova, E. B. Shume, H.-H. Benzon, A. J. Mannucci, M. D. Butala, P. Høeg, and R. B. Langley (2017), *Multiinstrument observations of a geomagnetic storm and its effects on the Arctic ionosphere: A case study of the 19 February 2014 storm*, Radio Sci., 52, doi:10.1002/2016RS006106.

III. Prikryl, R. Ghoddousi-Fard, J. M. Weygand, A. Viljanen, M. Connors, D. W. Danskin, P. T. Jayachandran, K. S. Jacobsen, Y. L. Andalsvik, E. G. Thomas, J. M. Ruohoniemi, **T. Durgonics**, K. Oksavik, Y. Zhang, E. Spanswick, M. Aquino, and V. Sreeja (2016), *GPS phase scintillation at high latitudes during the geomagnetic storm of 17–18 March 2015*, J. Geophys. Res. Space Physics, 121, 10,448–10,465, doi:10.1002/2016JA023171.

IV. Benzon, H-H., P. Hoeg, and **T. Durgonics** (2016), *Analysis of Satellite-Based Navigation Signal Reflectometry: Simulations and Observations*, IEEE Journal of Selected Topics in Applied Earth Observations and Remote Sensing, 9(10), doi:10.1109/JSTARS.2015.2510667.

CHAPTER 2

Published as: *Durgonics, T., G. Prates, and M. Berrocoso (2014), Detection of ionospheric signatures from GPS-derived total electron content maps, Journal of Geodetic Science, Vol. 4, Issue 1, doi:10.2478/jogs-2014-0011.*

STUDY 1: DETECTION OF IONOSPHERIC SIGNATURES FROM GPS-DERIVED TOTAL ELECTRON CONTENT MAPS

2.1 Introduction and Relevance of the Paper

The processing of measurement data from satellite constellations such as Global Navigation Satellite Systems (GNSS), including the well-known Global Positioning System (GPS), have been successfully applied to virtually all areas of geophysical sciences. In this work, a method is described where Geographical Information Systems (GIS) are employed to build hourly ionospheric Total Electron Content (TEC) maps for 2011 over the southern Iberian Peninsula. The maps used GPS-derived geometry-free linear combinations attained from station data from the Algarve, Alentejo (Portugal), Andalusia, Murcia and Valencia (Spain) regions. Following the construction of the ionospheric maps, it was possible to relate these results to natural phenomena. The observed phenomena included diurnal and seasonal variations: daytime TEC maxima, nighttime TEC peaks, summer TEC value decreases, and spring and fall TEC maxima. After validation of these periodic phenomena, detection of non-periodic changes, such as solar fares and tectonic interactions with the

ionosphere were attempted. The results showed a TEC increase following a selected solar flare event and a potential TEC build-up prior to the 2011 Lorca earthquake. Further studies could open up the possibility of building early warning systems. The presented methods, based on available software packages, are also of value in monitoring the effect of the ionosphere on radio signals, satellite and mobile communication, power grids, and for accurate GNSS navigation.

2.2 Detection of Ionospheric Signatures from GPS-Derived Total Electron Content Maps

The ionosphere is the subject of extensive scientific research mainly due to the fact that it affects the propagation of electromagnetic (EM) signals. Thus its presence must be taken into account whenever a satellite is sending radio signals through the atmosphere, and it is important to consider for radio communication and navigation systems in general. Today it is not only possible to correct for ionospheric refraction, but also to build ionospheric maps by computing the delay (or advance in the case of carrier phase) it causes in the GNSS signal, allowing GNSS-derived data to be used for model building. The ionosphere can be mapped regionally or globally, depending on the study area and the available ground GNSS stations. Prior literature such as in Camargo et al., [2000], Georgiadou [1994], Leick [1995], Orús et al., [2003], Ping et al., [2002 and 2003], and Taylor et al., [2006] provides a comprehensive theoretical background for GPS derived ionospheric TEC modeling. Jin et al., [2011] argue that GPS satellites are capable of providing even more accurate detection of ionospheric parameters than traditional ionospheric detection methods such as ionosondes, scatter radars, topside sounders, onboard satellites, and in situ rockets, and at a cheaper user cost. Additionally, they developed a piece of software called Regional Ionospheric Mapping and Tomography (RIMT), which can monitor 2D TEC and map 3D ionospheric electron density

distribution using GPS measurements. Having up to 1 Hz GNSS data availability, high temporal resolution mapping can be carried out. Orús et al., [2003] and Ping et al., [2003], used data from regional and global GPS networks which were utilized to build Global Ionospheric Maps (GIMs) and Regional Ionospheric Maps (RIMs) over Europe and Japan.

Studies concerning specific ionospheric behavior above the study area of southern Iberia have not yet been conducted. However, the technological background exists for such research because Spain and Portugal support networks of permanent GNSS stations.

One potential application of ionospheric mapping is the detection of earthquake signatures and other natural phenomena. The most seismologically active areas of the Iberian Peninsula are located in southern Iberia [Gibbons et al., 2003], more specifically along the Baetic System (Andalusia and Murcia, Spain), and between the Goringe seamount and Cape Saint Vincent (Algarve, Portugal). These regions are also the most hazardous, especially along their coastline (due to possible tsunami event). During the year 2011, the time span of the data applied in the present work, there were two noteworthy seismic events inside the study area. The more energetic of these two occurred in southern Spain, later named the 2011 Lorca earthquake. This was a moderate magnitude $5.1M_W$ shallow-focus 1 km event on May 11, 2011 at 06:47:25 local time. Its coordinates were 37.699°N 1.673°W, 50 km southwest of Murcia, situated near a major fault, the Alhama de Murcia fault. Ouzounov et al. [2011] retrospectively analyzed spatial and temporal variations of physical parameters, such as GPS derived TEC, of the $M_W = 9$ Tohoku Japanese earthquake of March 11, 2011. They could characterize the state of the ionosphere several days before the onset of the seismic event. The GPS-derived TEC values indicated an increase in electron density which had reached its maximum 3 days before the earthquake. They had found a positive correlation between the ionospheric anomalies and the Tohoku earthquake. Perrone et al. [2009] conducted research regarding Italian earthquakes, including the April 6, 2009 earthquake in L'Aquila. They

investigated whether evidence for an ionospheric precursor can be found. Although they only considered 6.0> M_W> 5.5 events, which are significantly less energetic than the Tohoku earthquake, empirical dependencies for the seismo-ionospheric disturbances relating to the earthquake magnitude and the epicenter distance were obtained and they were shown to be similar to the ones obtained for the Tohoku earthquake. They concluded that the similarity of these processes in different parts of the world suggests a uniformity of the processes during the earthquake preparation period both for powerful and moderate earthquakes.

Lognonné et al. [2009] argue that tsunami waves propagating across long distances in the open ocean can induce atmospheric gravity waves by dynamic coupling at the surface, and thus can be detected from TEC measurements. In that work, ionospheric TEC monitoring of Europe, California, and Japan was used for several investigations, in addition to the study of post-seismic signals. It is important to keep in mind that all of these studies were performed using post-processing data. Earthquake forecast, as a scientific method, is still far from being accepted by the scientific community and there are significant doubts that it can ever be done reliably. Nevertheless, TEC monitoring, as it was demonstrated by the aforementioned articles, shows promising and important results.

As one final example of an application of ionospheric mapping, Jin et al. [2011] describe a case study of GPS ionospheric mapping and tomography in a geomagnetic storm caused by a coronal mass ejection (CME) associated with an M 3.2 flare. They conclude that a strong increase can be shown in the ionospheric peak density during the storm, although they suggest further investigations. Thus great potential also exists for detecting solar effects from GNSS-derived ionospheric TEC models. The present work describes a series of techniques that can be employed to build ionospheric maps, TEC time-series, and also describes a number of attempts to link these maps with other environmental variables.

There are two primary goals in this work. Firstly, this study aims to develop a GIS application which is able to build ionospheric maps from GNSS-derived TEC values, and to demonstrate how these vary in time above the selected study area. Daily, monthly, and seasonal changes of 2011 were studied. It is crucial to understand what natural phenomena can affect GNSS accuracy, how they affect it, and what can be done to compensate for these errors. These can be partially achieved by building accurate ionospheric models. It is worth noting that solar fares that disturb the ionosphere can cause position errors in GPS-based navigation systems, such as the Wide Area Augmentation System (WAAS), as large as 50 meters if no corrections are applied. This can present an extreme hazard for aerial and other navigation systems (Hofmann-Wellenhof, 1994). Secondly, the results of this work can assist atmospheric and geophysical scientists to better understand the regional behavior of the ionosphere. A number of global and regional ionospheric mapping projects already exist, as described above, but this is the first study that concentrates specifically on the southern Iberian Peninsula.

2.2.1 Study Area and GNSS Resources

The study area is located in the southern portion of the Iberian Peninsula (Figure 2.1). *Rede Nacional de Estações Permanentes* is a Portuguese public GNSS data service for real-time positioning, maintained by the Portuguese *Direção Geral do Território*, that also makes GNSS data available for post-processing in Receiver INdependent Exchange (RINEX) format files. It consists of dozens of GNSS stations evenly distributed in Portugal. These stations collect GNSS data continuously, broadcast corrections in real time for those using the code and/or phase Differential-GNSS techniques. In Spain there are different GNSS data services for real-time positioning for every region that also provide GNSS data for post-processing. Thus the RINEX data files had to be

collected separately from the *Red Andaluza de Posicionamiento* maintained by the Spanish Junta de Andalucia, *Red de Estaciones de Referencia* GPS de Murcia maintained by the Spanish Comunidad Autónoma de la Región de Murcia, and *Red de Estaciones de Referencia* GNSS de Valencia maintained by the Spanish *Generalitat Valenciana*. For the purposes of this work the GNSS data was collected from four distinct regions: southern Portugal containing 6 selected GNSS stations, Andalusia containing 12 stations, Murcia containing 5 stations, and Valencia containing 2 stations. Figure 4.2 shows the distribution of all stations involved in this work.

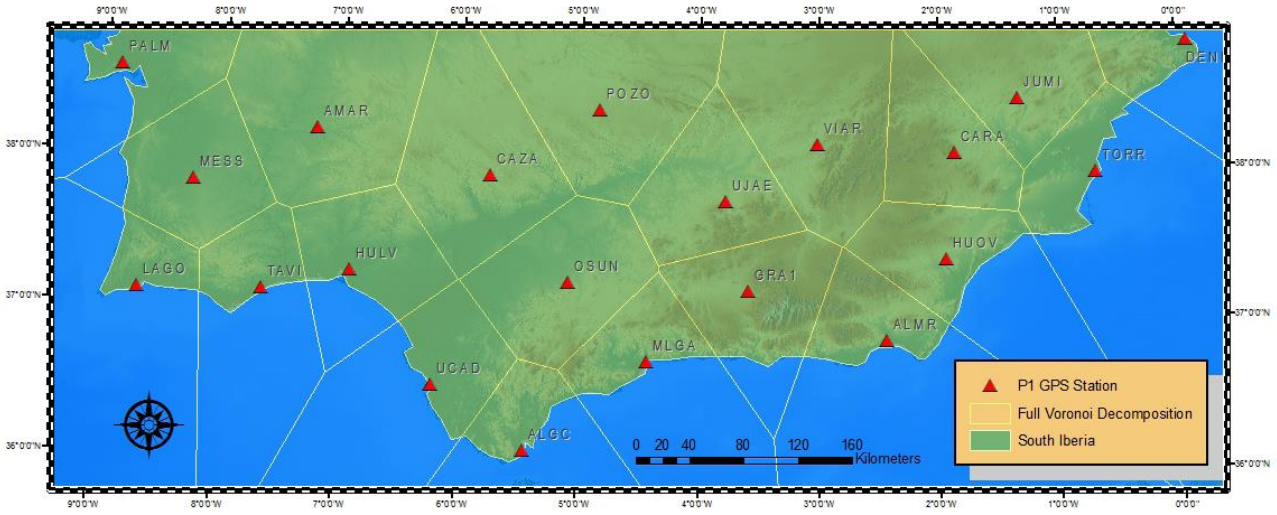

Figure 2.1 The study region overlaid with the Voronoi-decomposition of the study area using the selected stations as sites. Note that on this map only the Priority 1 (P1) stations are considered. P1 stations had good enough quality data to be included in the TEC map building, while P2 stations had to be rejected.

2.2.2 GNSS Ground Station Selection

After selection of GNSS ground stations in the study area, RINEX data files were collected with 30 second sampling rates. The four regions of the study area contain a relatively high density of permanent GPS stations, but they belong to four different networks. Typically they are less than 100 km from each other; in some areas this is as short as 30-60 km. Due to the large amount of data storage, computing power, and computing time that TEC map computing requires, selection of a representative sub-network was required. This was done by selecting no more than 2 stations closer than approximately 60 km from each other, and with no geographical point further than 90 km from a station. The network should be as uniform as possible and dense enough that the interpolation between the intersection points of the lines between receivers and satellites with the ionospheric layer, ionospheric pierce points (IPPs), provide acceptable values, and also taking into account that the line-of-sight TEC data quality is proportional to $1/\sin(\varepsilon)$, where ε is the elevation angle above horizon, thus the highest quality probing is accomplished near the stations zenith. There should also be stations near the boundary of the study area. The scheme that was used is shown in Figure 2.1, with station selections in Table 2.1. This consists of a total of 25 stations. Although not completely ideal (up to a 118 km exists between two stations, while two other stations are 62 km from each other), this was the most optimal network that could be created from the available stations. The GIS analysis of the GNSS ground station network was performed in ArcGIS (version 9.3; ESRI Inc., Redlands, CA, *http://www.esri.com*). Precise station antenna coordinates are typically provided by the GNSS network data processing - these coordinates can be entered one by one into a point geometry shapefile, resulting in the map shown in Figure 2.1. An additional coastline contour (polygon geometry) shape file was also created. Based on this station shapefile and the coastline contour shapefile various spatial analyses can be conducted. Note the Priority column in Table 2.1.

Priority 2 stations had to be eliminated from the final subnetwork mainly due to occasional deficient and/or sporadic RINEX data provided by these stations.

2.2.3 Determination of a Representative GNSS Ground Network Based on GIS

One of the basic assumptions behind our GNSS network selection was that an ideal GNSS monitoring network should consist of uniformly distributed ground stations with stations at least 60 km from each other. This 60 km distance is double the maximal baseline (30 km) between a single station and a mobile receiver inside which the ionospheric errors are considered still acceptable (during normal ionospheric circumstances), so the relative TEC error will be in the range of 1 to 2% [Astafyeva et al., 2008]. However, twice that distance was allowed, considering the probing locations are the IPPs for each receiver-satellite line-of-sight. For higher space and time resolution, it is necessary to process the data from more GNSS stations; however this is not always possible due to limitations in data processing and limitations in the availability of stations.

In order to mathematically describe the requirements for an optimal network, geostatistical methods can be applied to determine the best possible combination of stations. At each epoch, the maximum number of measurements equals the number of GNSS stations multiplied by the number of visible satellites from all stations. The ionospheric TEC values outside the measurement points can be estimated by interpolation. The GNSS stations situated in the study area are permanent stations operated by various institutes and companies independent of this work. Therefore the approach to mathematically describe, evaluate, and identify the optimal sampling scheme for this irregular structure was to first decompose the study area through Voronoi tessellation (Figure 2.1) [Atsuyuki et al., 2000]. In this analysis, there are n stations (Table 2.1) with appropriate geographic coordinates, that is $s_1, s_2, \ldots, s_n$, and each station/site s_i has its corresponding Voronoi cell C_i. C_i

contains all the points in the study area which are closer to s_i than to any other station, s_j, and where $i \neq j$ (Boots, 1986). Paláncz et al. [2006] have stated that the area of a Voronoi polygon generated by a site may be considered as the Region of Attraction (RA) of this site, simply because these points are closer to the measurements of this station than to any other. Therefore, it is expected that more accurate TEC mapping will be achieved for smaller polygon areas and less accurate mapping for larger ones.

St.#	4-ID	Site Name	Region	Priority	Latitude	Longitude
1	TAVI	Tavira	Algarve (P)	1	37º 07' 56.29112" N	7º 38' 27.27793" W
2	BENA	Benafim	Algarve (P)	2	37º 13' 56.53192" N	8º 07' 36.10238" W
3	LAGO	Lagos	Algarve (P)	1	37º 05' 56.16677" N	8º 40' 06.16780" W
4	PALM	Palmela	Lisboa (P)	1	38º 34' 17.26707" N	8º 54' 12.42132" W
5	AMAR	Amareleja	Alentejo (P)	1	38º 12' 31.30250" N	7º 13' 40.37843" W
6	MESS	Messejana	Alentejo (P)	1	37º 50' 04.65669" N	8º 14' 40.88909" W
7	HULV	Huelva	Andalusia (S)	1	37º 16' 49.0240" N	6º 54' 48.7581" W
8	CAZA	Cazalla de la Sierra	Andalusia (S)	1	37º 56' 16.3534" N	5º 45' 35.2118" W
9	UCAD	Univ. de Cádiz	Andalusia (S)	1	36º 31' 54.0048" N	6º 12' 37.7919" W
10	MLGA	Málaga	Andalusia (S)	1	36º 42' 56.1481" N	4º 26' 7.4766" W
11	ALGC	Algeciras	Andalusia (S)	1	36º 6' 39.7483" N	5º 26' 39.0368" W
12	GRA1	Granada	Andalusia (S)	1	37º 11' 23.6392" N	3º 35' 47.0601" W
13	HUOV	Huercal-Overa	Andalusia (S)	1	37º 24' 5.6154" N	1º 56' 31.6490" W
14	VIAR	V. del Arzobispo	Andalusia (S)	1	38º 10' 3.4985" N	3º 0' 44.9163" W
15	POZO	Pozoblanco	Andalusia (S)	1	38º 23' 0.4796" N	4º 50' 57.5901" W
16	OSUN	Osuna	Andalusia (S)	1	37º 13' 56.3221" N	5º 5' 42.6110" W
17	UJAE	Univ. de Jaén	Andalusia (S)	1	37º 47' 15.9386" N	3º 46' 54.2186" W
18	ALMR	Almería	Andalusia (S)	1	36º 51' 45.6004" N	2º 26 ' 27.1690" W
19	MURC	Murcia	Murcia (S)	2	37º 59' 31,78546" N	1º 07' 28,86841" W
20	JUMI	Jumilla	Murcia (S)	2	38º 28' 16,38635" N	1º 19' 37,77497" W
21	MAZA	Mazarrón	Murcia (S)	2	37º 35' 36,38537" N	1º 18' 37,785" W
22	CARA	Caravaca	Murcia (S)	1	38º 06 '52,49750" N	1º 52' 07,12029" W
23	LORC	Lorca	Murcia (S)	2	37º 39 '14,00121" N	1º 41' 12,38662" W
24	TORR	Torrevieja	Valencia (S)	1	37º 58' 31.1290" N	0º 40' 51.1905" W
25	DENI	Dénia	Valencia (S)	1	38º 50' 5.1992" N	0º 6' 13.1815" E

Table 2.1 The complete stations list. Including 4-character station names and other relevant information. "P" stands for Portuguese and "S" for Spanish stations. The data continuity of the Priority 2 stations was sporadic for the selected days; therefore they were eliminated from the final processing.

It is now possible to rephrase the first assumption of this section by stating that if stations are uniformly distributed, each RA would have equal area. The area of these polygons presents us with

the possibility to obtain statistics that are representative of the sampling scheme [Dubois, 2000]. For instance, isolated stations will have larger corresponding polygon surfaces. The distribution of the GNSS stations in the study area is non-uniform and denser than it was described in the beginning of this section. It is desired that the RA of the optimal sub-network have a homogeneous distribution and relatively low standard deviation. Dubois [2000] has recommended an additional measure that takes into account the distance of each station to its nearest neighbor and the surface of the Voronoi polygon. Let S_V be the surface of the Voronoi polygon belonging to s_i station and S_m the mean polygon surface defined as:

$$S_m = \frac{S_{total}}{n} \ , \tag{2.1}$$

where S_{total} is the area of the whole study region and n is the number of Voronoi polygons in it. N_i^{d} is defined as the distance between a site and its nearest neighbor. Using these variables, a quantity (for each station/polygon) called Coeffcient of Representativity (CR) can be defined:

$$CR = \frac{S_V}{S_m}\frac{\left(N_i^d\right)^2}{S_m} = S_V \frac{\left(N_i^d\right)^2}{{S_m}^2} \, . \tag{2.2}$$

In an ideal case CR = 1. CR > 1 means that the station is isolated (i.e. it is relatively far from the other stations), while CR < 1 means that the station is close to a neighboring station (Paláncz et al. 2006). It can be concluded that the statistics of the polygon surface areas and the CR values provide tools to determine the regularity of a given sampling scheme. The CR should help identifying under-sampled areas [Dubois, 2000].

ArcGIS software was utilized to aid this geostatistical analysis. During the station distribution analysis the polygon areas had to be determined and the ArcToolbox/Analysis Tools set was employed, resulting in the RA. Additionally, the CR was calculated based on the nearest neighbor

station. A Matlab (version 2010a; MathWorks, *http://www.mathworks.com*) script was written to compute and plot the statistics of the values acquired through the geospatial analyses.

2.2.4 Obtaining TEC Values from Bernese GPS Software 5.0

Bernese GPS Software (version 5.0; Astronomical Institute, University of Bern, *http://www.bernese.unibe.ch/*) can build three types of ionospheric models based on spherical harmonic expansions. These are global, regional, and station specific. For the purpose of this work the regional model was selected. For the processing strategy, precise point positioning (PPP) was selected, which is a special case of zero-difference processing. The main purpose of performing PPP in Bernese using GPS observations from a number of stationary ground receivers is to obtain a set of station coordinates at a cm resolution level. From these PPP results the extraction of TEC information is possible. As opposed to other processing strategies, the satellite clock corrections are not estimated but are assumed to be known. They are introduced in the processing together with orbit information and Earth orientation parameters. These parameters can be obtained from the International GNSS Service (IGS) database. The parameters left to estimate are station clock corrections, coordinates, and troposphere parameters. The parameter estimation is done sequentially by executing a user-defined list of Bernese scripts. These scripts employ data reading, reprocessing, conversion, synchronizing, and parameter estimation. Ultimately, the PPP solutions are computed, and optionally, ionospheric models can be generated [Dach et al., 2007]. The quality of the introduced information should be as good as possible for PPP, as all errors directly propagate to the position of the station. The regional TEC model may be written as:

$$TEC(\beta, s) = \sum_{n=0}^{n_{max}} \sum_{m=0}^{n} P_{nm}\,(\sin\beta)(a_{nm} cos\, ms - b_{nm} \sin ms)\,, \qquad (2.3)$$

where is the geographic latitude of the intersection point of the line receiver–satellite with the ionospheric layer (this point is called ionospheric pierce point (IPP)); *s* is the sun-fixed longitude of the IPP; n_{max} is the maximum degree of the spherical harmonic expansion, P_{nm} are the normalized associated Legendre functions of degree *n* and order *m* based on a normalization function, and a_{nm} and b_{nm} are the unknown TEC coefficients of the spherical harmonics, i.e. the regional ionosphere model parameters to be estimated [Dach et al., 2007]. We used the phase observables for the geometry-free linear combination (L4) to estimate the ionosphere. A 10 degree cutoff-angle and *1/sin(ε)* elevation-dependent weighting were selected. The type of the temporal modeling was static employing the geomagnetic reference frame. After PPP processing, the IONosphere map EXchange format (IONEX) files can be obtained [Schaer et al., 1998]. The TEC map section contains coordinates and values in TEC units (TECU); the root-mean-square error (RMS) map section contains the RMS values for each location. Dach et al., [2007] recommends degree and order values around n=6 and m=6 for regional modeling. After running test processes with several degree and order values, n=5 and m=5 were selected. This was due to the facts that with the selected GNSS network, the higher values did not reveal additional ionospheric structures, but the processing time was increased significantly. The data files were processed from the selected stations for a 450 km single layer height. Latitudes were between 35° and 40°, with 0.5° steps, and longitudes were between 12° W and 2° E, with 0.5° steps.

2.2.5 Interpolation and Visualization

Interpolation algorithms estimate the value at a given location as a weighted sum of data values at surrounding locations, with weights assigned according to functions that give a decreasing weight with increasing separation distance [Cressie, 1990]. In order to process the interpolation in ArcGIS

and Surfer (version 9; Golden Software, *https: //www.ssg-surfer.com/*), the TEC values and their corresponding time parameters and coordinates were read from the IONEX les and transformed into an XYZ array using a custom MATLAB script, which was then imported into ArcGIS or Surfer. Once all the epochs were imported into ArcGIS or Surfer, the interpolations were made using inverse distance weighted (IDW), kriging, natural neighbor, spline, and trend methods [Davis, 1975]. All methods were tested, and the kriging method was chosen (see Section 2.2.7).

ArcGIS was used for calculating interpolation statistics, and Surfer was used for visualization. Composite images were first created in MATLAB using a reference image consisting of the first epoch or day of the series, and images from the remaining epochs or days. The reference image values (layer or data matrix) were subtracted from the referent image values using pixel-by-pixel subtraction.

2.2.6 Spatial Analysis of the GPS ground station Distribution

The vertical TEC (VTEC) value is estimated in the IPP from the line-of-sight (integrated) TEC. Since these IPPs can be above sub-ionospheric points (SIPs) outside the study area, the ionosphere can be mapped beyond the area delineated in Figure 2.1, as long as the elevation angle is not smaller than 15° [Dach et al. 2007]. However, it is still desired that the GNSS sub-network be uniformly distributed. In order to obtain ideal GNSS station coverage we require that none of the 30 km buffers around each GNSS station intersect another 30 km buffer (an unnecessarily dense distribution), and that the areas not covered by 60 km buffers be minimized. Additionally, difficulties are presented by polygons extending over the ocean/sea, therefore the coastline is artificially extended by a 30 km buffer zone. This new delimitation provides a reduced study area but an extended virtual land surface over which more reliable results are expected.

In Section 2.2.1, CR was defined to provide an additional statistical measure about a GNSS network distribution based on Voronoi polygon areas, but also taking nearest station distances into account. Performing the RA and the CR calculations with the help of GIS, it is now possible to visualize the computed CR results for each polygon (Figure 2.2).

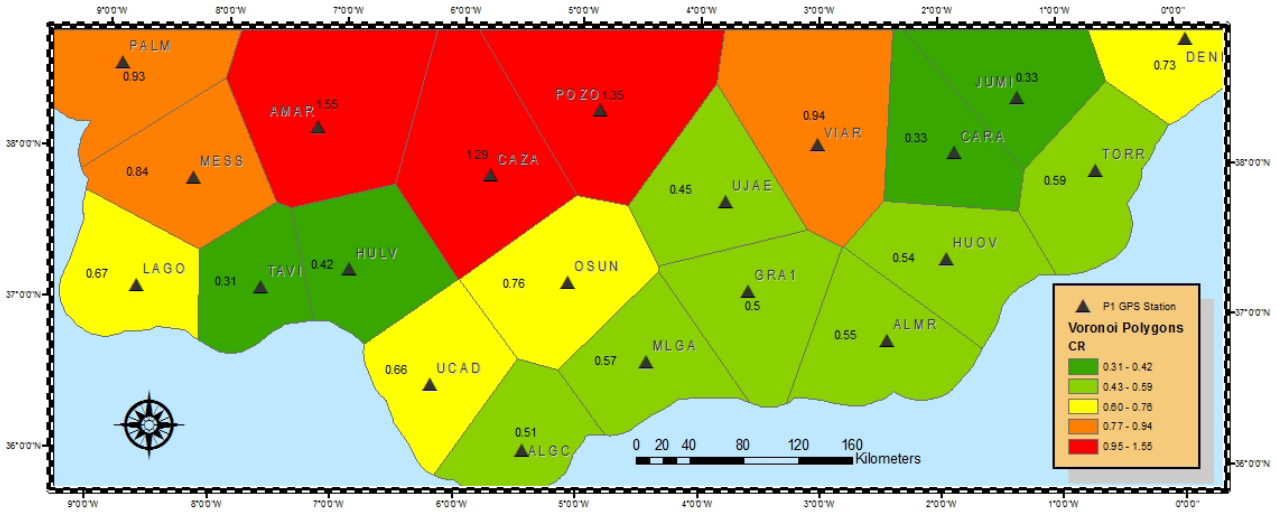

Figure 2.2 Computed CR values (see Equation (2.2)) visualized for each station. Green and yellow cells belong to clustered stations while red ones belong to isolated stations.

2.2.7 TEC Map Interpolation

TEC values and their RMS were obtained from Bernese GPS 5.0 software as described in Section 2.2.4. Typical RMS values are in the range of *0.1 - 0.2 TECU*, which corresponds to about *1%* of the corresponding TEC values. Various interpolation methods were tested, which are illustrated in Figure 2.3, with the TEC values shown on the z-axis. It can be visually observed that kriging and natural neighbor interpolation do not contain visible artifacts and that they are not over-smoothing the topography. Therefore they are optimal methods for our TEC data. Statistical measures were also used to mathematically assess the different interpolation methods. RMS deviation values can

be seen in Table 2.2. RMS deviation is the standard deviation of the residuals between interpolated values and estimated values. Kriging interpolation has the lowest RMS deviation value; therefore it was selected as the interpolation method in the remainder of this study.

	IDW(p=2)	IDW(p=3)	Kriging	Natural Neighbor	Spline	Trend
RMS deviation	0.0760	0.0600	0.0462	0.0463	0.0627	0.1755

Table 2.2 RMS deviations. The visual comparison of different interpolation techniques shown in Figure 2.3. Specific values are based on a particular epoch; however they are representative of the entirety of the data. Kriging interpolation has the best results.

2.2.8 Diurnal and Seasonal Changes in the Ionosphere

Not all ionospheric layers are affected equally by solar radiation. Because this work uses a single layer model, these effects and others are all integrated into a 2D surface above the study area (at an altitude of 450 km), thus representing a superimposition of the different layers. It is expected that the TEC maps are providing insights into specific ionospheric temporal characteristics and quantitative relationships with influencing factors [Afraimovich et al., 2009]. Based on Komjathy [1997], it is expected that there will be constant nonzero ionospheric TEC values from at least the D layer, even during nighttime, due to excitation by cosmic radiation. Since the E layer is strongly dependent on the zenith angle of the Sun, there is also an expected additional diurnal variation component. Furthermore, F_1 is expected to add short term changes which are only present during day time. The global spatial distribution of the F_2 layer also reveals a fundamental geomagnetic dependence [Komjathy, 1997], which could indicate that this layer is affected by seismo-ionospheric coupling. To investigate diurnal and seasonal ionospheric variations over southern

Iberia, average TEC values over the study area for 1 hour increments were determined. In Figure 2.4, hourly average TEC values and daily average TEC values are shown for every 15th day of 2011 (±2 days when station data was of poor quality or missing). Diurnal changes are apparent, with a noon peak, a night peak, and a possible secondary daytime peak. Maximum TEC values peak around April to May (day 100 to 130) and in September to November (day 266 to 326). Maximum vales are lowest in the winter, and are also reduced during the Summer months.

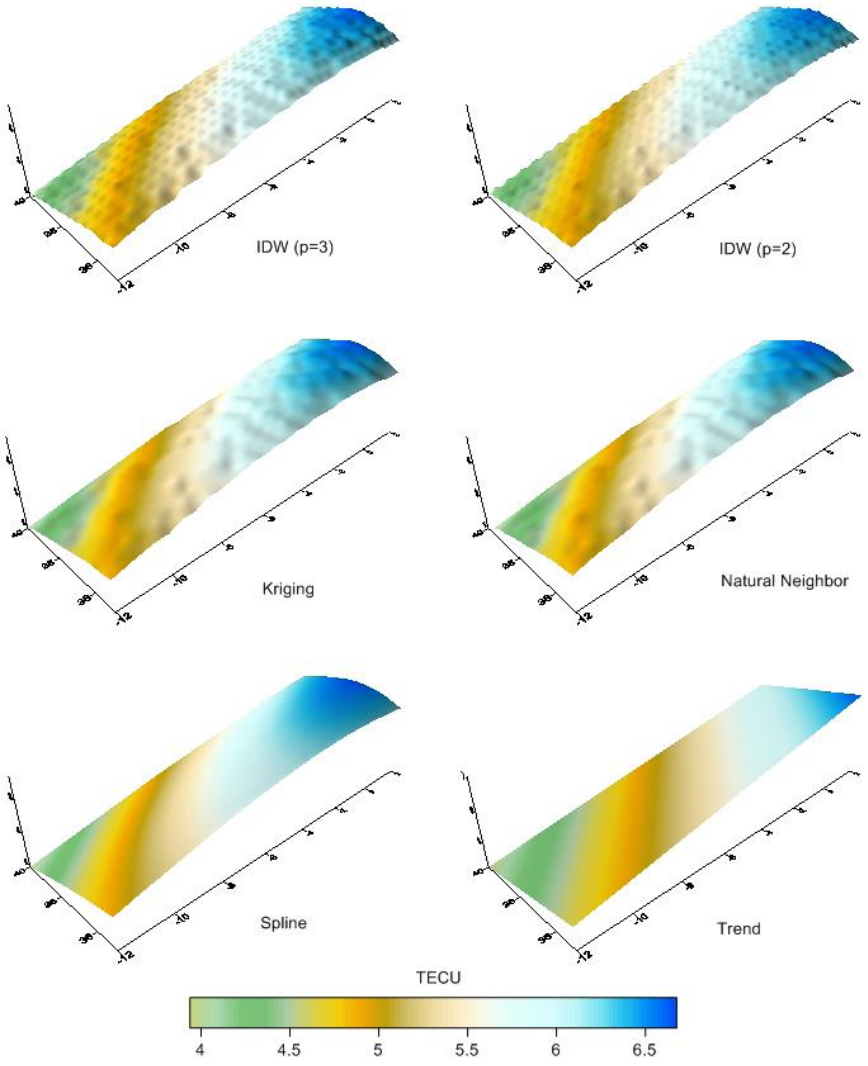

Figure 2.3 Comparison of interpolation methods visualized in Surfer. TEC values are indicated both by a color scale and as values on the z-axis. Inverse Distance Weighted (IDW) with two powers (p = 2 and p = 3) show artifacts which are related to the grid in the IONEX files. These artifacts make it practically impossible to study small scale changes

and variations. Spline interpolation results in an over-smoothed surface. Trend interpolation only displays the inclination and general properties of the TEC model. Kriging and natural neighbor visually provide the most details about small scale variations.

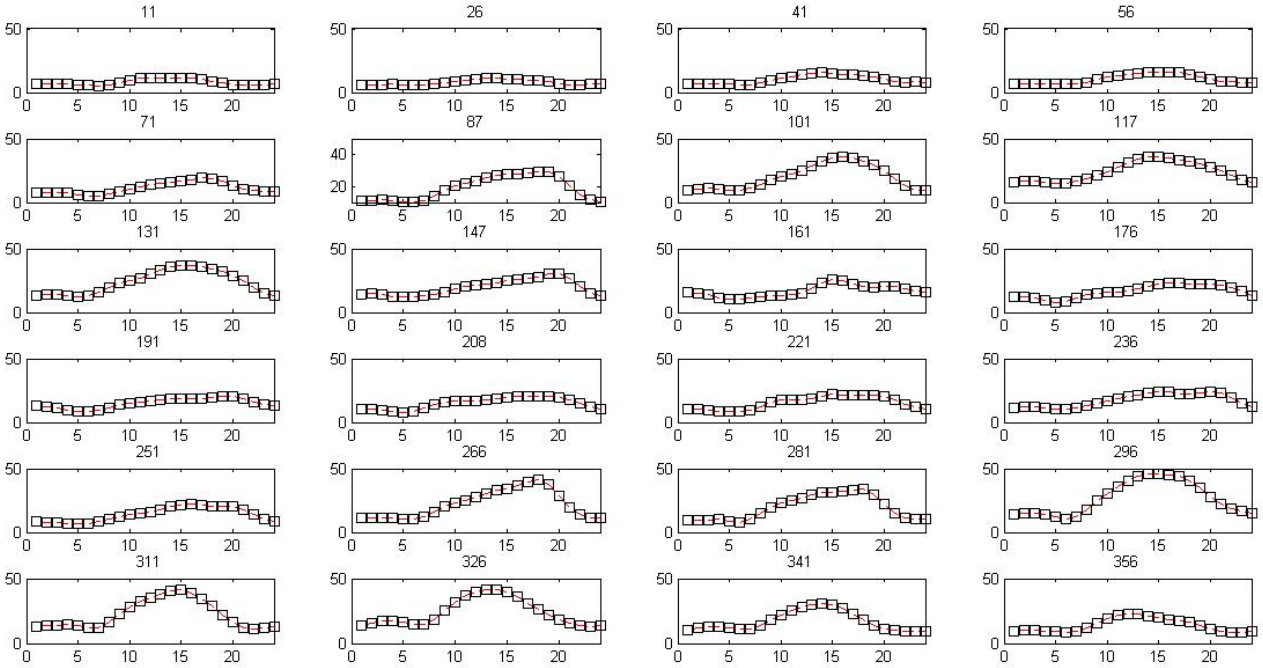

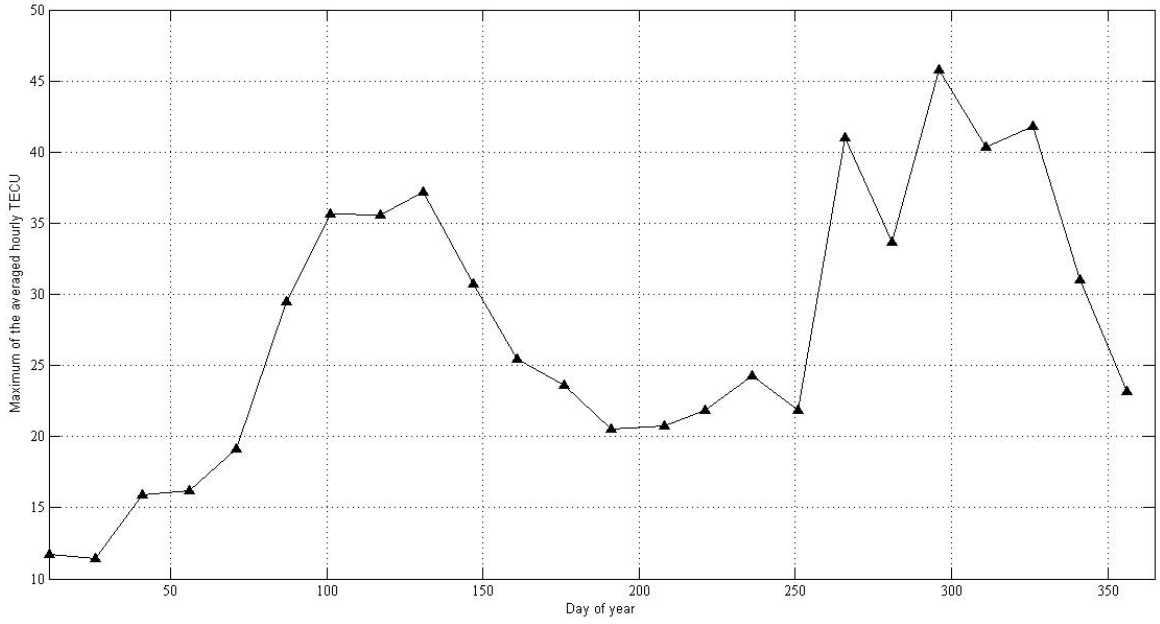

Figure 2.4 (Top) Diurnal changes of hourly averaged TEC values. The x-axis shows the hours of the day, the y-axis is the TEC value in TECU, and the numbers above each plot represent the day of the year. Diurnal variations are clearly

apparent. **(Bottom)** Daily average TEC values for 2011. Seasonal peaks in Spring (April through early May) and Fall (September to November) are apparent.

2.2.9 Relation to Solar Activity

A solar fare is an eruption on the Sun that occurs when energy stored in twisted magnetic fields is suddenly released. Flares produce a burst of radiation across the electromagnetic spectrum, from radio waves to X-rays and gamma rays. Solar fares are divided into classes, the most powerful of which are the X-class fares. There were two X-class fares during 2011, one of which is denoted X 6.9 which occurred on August 9, 2011. Figure 2.5 displays the hourly averaged TEC values over the study area from August 10th through August 12th with the corresponding hourly averaged TEC values from August 9th subtracted from each value. These days were selected because a coronal mass ejection is expected to reach Earth within one to four days. During the 72 hour period, large TEC maxima were observed centered around hour 20 and hour 45.

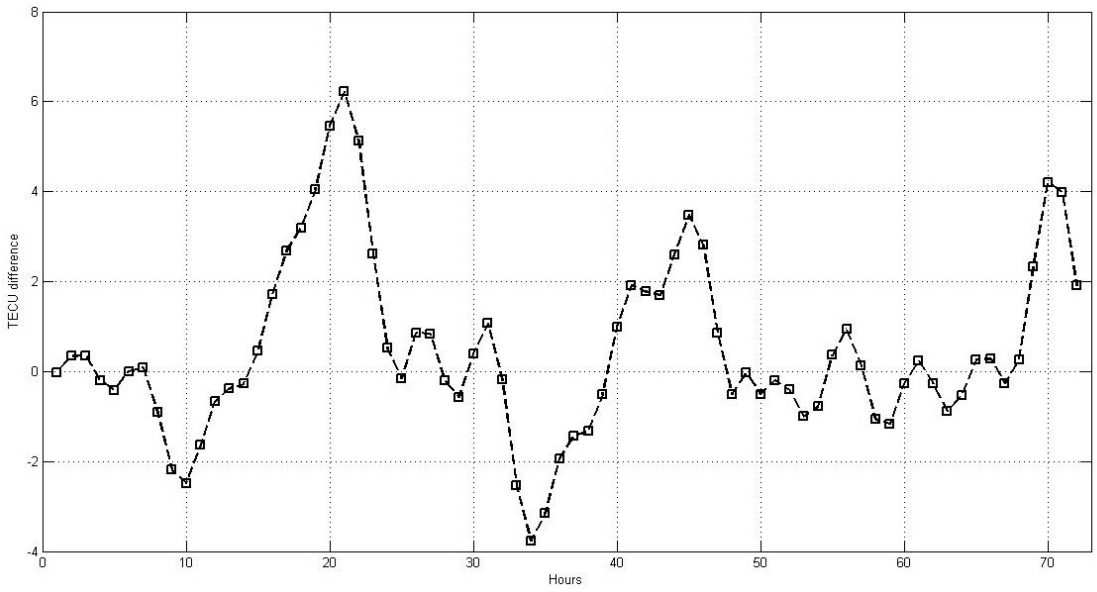

Figure 2.5 Hourly average TEC value differences between the second, third, and fourth day of the solar event beginning August 9, 2011, and the first day. The closer the TEC value is to zero, the smaller the difference between that epoch and the same epoch on the first day.

2.2.10 Possible Relation to Seismic Activity

TEC maps were analyzed in an attempt to detect a precursor or an ionospheric anomaly prior to the May 11, 2011 Lorca earthquake. Data from five days before the earthquake to three days after the earthquake were processed. To better quantify any unusual activity, Figure 2.6 displays the hourly averaged TEC values over the study area from May 7th through May 14th, with the corresponding hourly averaged TEC values from May 6th subtracted from each value. To subtract out any longer-term trend in the data, a cubic polynomial equation was determined to reasonably fit to the data, and the residuals are depicted. An unusually large residual is observed beginning at 80 hours, approximately 30 hours before the earthquake.

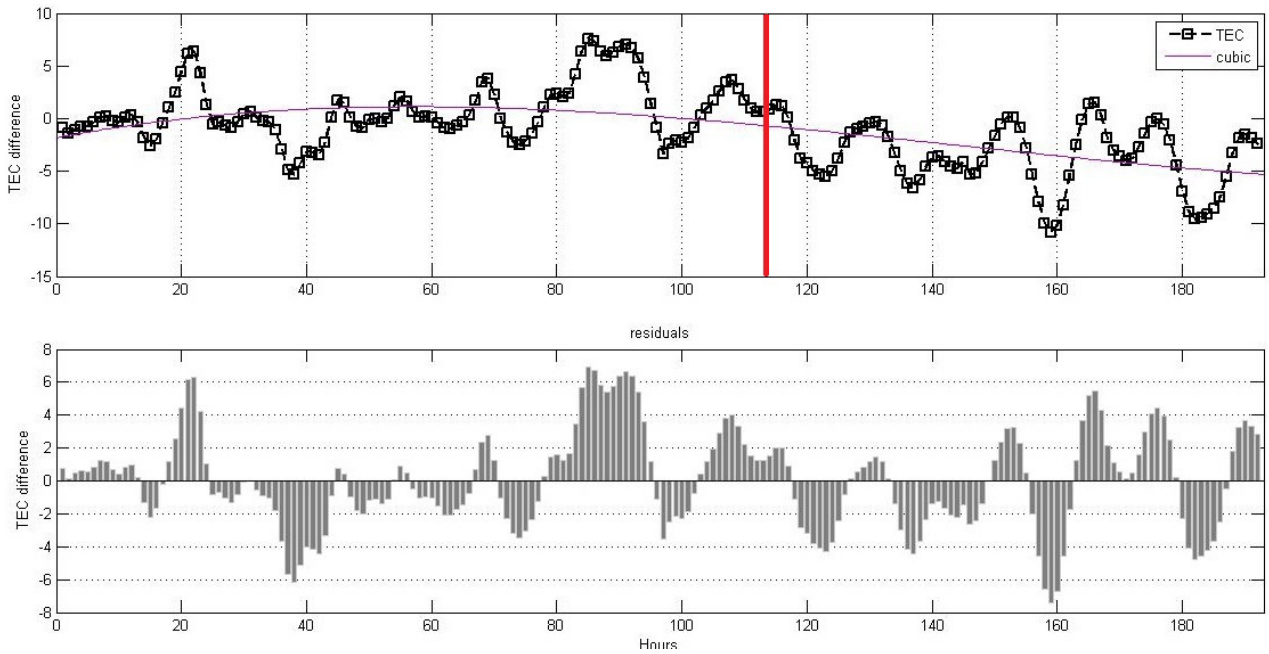

Figure 2.6 (Top) Hourly averaged TEC value differences for the second to ninth days (May 7th through May 9th) around the May 11th, 2011 Lorca earthquake, with the hourly averaged TEC values from May 6th subtracted from the data. The vertical red line indicates the time of the earthquake. The TEC differences reveal a longer-term trend that is best fit with a cubic polynomial function. **(Bottom)** TEC value residuals are about the fitted curve. An anomalously large residual peak is observed approximately 30 hours prior to the time of the earthquake.

Unusually high TEC values are observed over the study area one day before the earthquake. Also from this data, composite maps for the same epoch were constructed by subtracting out the TEC values from May 6th in order to compare local variations (Figure 2.7). Note that due to the very ne resolution, each map in Figure 2.7 employs a different color scale. On the day of the earthquake and one day after, a large negative TEC anomaly is observed over the epicenter. Such negative anomalies have been observed in multiple other studies around the time of other earthquakes [Pulinets et al., 2004].

2.2.11 Discussion

In the first part of this study, a methodology was presented for selecting an optimal GNSS sub-network in order to obtain GPS-derived data for TEC mapping. We can conclude, after analyzing Figure 2.2, that an acceptable, regular GNSS ground network has been selected. All but four isolated stations are border stations of the sub-network. One possibility to improve station distribution uniformity would be to include GNSS stations from another network north of the study area. As a final validation of the selected GNSS network, one can analyze the RMS maps provided in each IONEX file. These values are in the range of 0.1 TECU in most files and higher values only exist if there is a problem with a station data for a given day. This GNSS station selection methodology for ionospheric TEC mapping could be expanded or employed for different areas of Earth using the same techniques and principles. Problems may arise when it is applied on island-like geography or coastal areas, where uniformity cannot be guaranteed due to geographic constraints. At high latitudes and near the equatorial region there exist other ionospheric phenomena that require further studies, e.g. scintillations (see for instance Takashi et al., [2014]). This work is limited to the midlatitude ionosphere. Interpolated data were analyzed statistically (Table 2.2) and

visually (Figure 2.3). In this case, the only two viable interpolation methods based on statistical measures were kriging and natural neighbor. Most importantly, the RMS deviation values were the lowest when using kriging and natural neighbor, with kriging being slightly lower. Once the optimal interpolation was found, the next step was to construct ionospheric maps and time series.

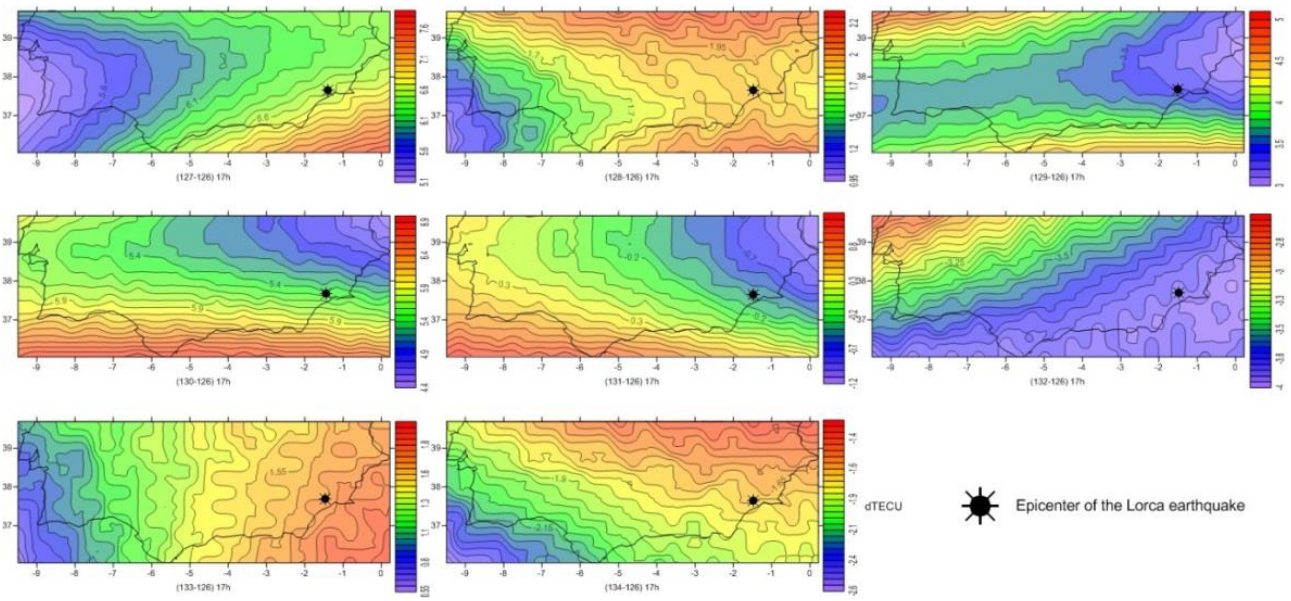

Figure 2.7 Composite maps of TEC differences of the 17:00 (UTC) epoch for May 7th through 14th with the same epoch from May 6th subtracted out. Values can be negative due to the subtraction. Due to the very fine value resolution each map has its own color scale shown to the right of each map.

In the second part of the study, TEC models were built using the selected GNSS sub-network in order to study seasonal and diurnal changes, and also to study how a selected coronal mass ejection (CME) and earthquake affected the ionosphere over the study area. The results suggest that the seasonal variability of TEC shows a semiannual cycle with higher values near the equinox and lower values near the solstice. This would be expected due to changes in the incidence angle of sunlight resulting in variations in excitation of the ionosphere from solar radiation. Similar observations were made by Huang et al. [2006]. It is also notable that the yearly cycle in Figure 2.4

does not return to its initial value (from 12 TECU to 24 TECU). This suggests that there is a correlation between the averaged TEC values and sunspot number progression (11-Year Solar Cycle), as solar activity increased until 2013 within Solar Cycle 24. Diurnal changes were also observed, with the daytime peak beginning when the solar terminator reaches the study area. During the nighttime the TEC value contours are nearly in horizontal lines (east-west or 90° azimuth), but as the terminator enters the area they can reach an azimuth of 45° or sometimes even down to 0° (north-south or vertical lines). TEC values rise rapidly during the day and only begin to drop during the late afternoon. This is an expected behavior since the E layer is almost entirely dependent on solar activity and the zenith angle of the Sun. Therefore these changes are likely reflecting variations in the E layer. Note that the E layer can practically vanish during the night; therefore the expected observation was a sudden decrease in TEC values after sunset and a constant low until sunrise. Contrarily, a nighttime peak was observed. This was consistent with previous studies such as in Horvath et al. [2000] and Huang et al. [2006]. Midlatitude nighttime TEC increases have been attributed to anomalous increases in the F_2 region [Horvath et al., 2000]. The physical processes underlying its formation are still not properly understood. It has been shown that solar activity largely controls seasonal and diurnal cyclic TEC variability. But other ionospheric disturbances can also lead to considerable day-today variations in TEC. One of the sources of these disturbances is CMEs. In this work, the most energetic solar fare of 2011 was investigated. It was found that the effect of the CME on the ionosphere can be identified in the TEC data. The strongest influence (a peak with a maximum of 7 TECU above the August 8 value) was on the day following the CME (August 9) at around 21:00 (UTC) hours, with even the third and the fourth day showing approximately +4 TECU maximum anomalies. In addition to the positive peaks, there were two negative peaks that were 3 to 4 TECU below the August 8 value for the same hour. It should be noted that these values may not be the real maximum and minimum anomalies due to the 1 hour

time resolution, thus any short-term variation in TEC could remain undetected. The results show that the maximum values occur at different times every day after the solar are event and eventually diminish.

Finally, a connection was attempted to be made between TEC trends and the 2011 Lorca earthquake. An attempted was made to find a correlation between the seismic event and ionospheric anomalies appearing prior to or after its occurrence. The interaction between earthquakes and ionospheric disturbances has been studied for many years [Pulinets et al. 2004]. Ionospheric disturbances following major earthquakes have been detected using GPS-derived TEC maps [Pulinets et al. 2004]. At the same time, the existence of ionospheric precursors is still not widely accepted by the scientific community. Therefore, the present study focused on days both before and after the Lorca earthquake. The reference day was May 6th and the last processed day was May 14th. Each of the nine processed days demonstrated typical diurnal variations, although a secondary daytime peak was less apparent on the day of the earthquake and the day after. The daily maximum value was the highest the day before the earthquake, and then dropped significantly the following days. An hourly average difference analysis (Figure 2.6) showed cyclic positive/negative fluctuations. The highest residuals are the day before the earthquake, with a maximum of approximately 8 TECU. This positive anomaly lasted for nearly 20 hours; however there is also a negative anomaly on May 8. As a comparison, Ouzounov et al. [2011] observed that TEC values reached their maximum 3 days before the Tohoku earthquake. In order to verify that these anomalies are not triggered by solar activity, NOAA solar event reports were analyzed for May 7, May 8, and May 9, and no significant solar activity was reported, likely excluding solar fares as a cause of the positive anomaly. Figure 2.7 reveals the 2D structure of the local ionospheric anomalies. Such images provide a good sense of the constantly changing spatial structure of the ionosphere above the study area. While solar flare interactions with the ionosphere were unlikely,

there are still other possible sources for such anomalies which cannot be excluded as yet. Prior results suggest that because phenomena other than solar activity, such as magnetic processes, predominantly affect nighttime midlatitude TEC [Horvath et al. 2000], potentially improved precursor detection could be achieved by concentrating only on the nighttime peak.

Furthermore, a more detailed study analyzing the correlation of TEC with sunspot numbers should be carried out in order to eliminate this effect. The time resolution also should be increased from the current 1 hour to a much smaller time interval, possibly even down to 30 seconds.

CHAPTER 3

Published as: *Durgonics, T., A. Komjathy, O. Verkhoglyadova, E. B. Shume, H.-H. Benzon, A. J. Mannucci, M. D. Butala, P. Høeg, and R. B. Langley (2017), Multiinstrument observations of a geomagnetic storm and its effects on the Arctic ionosphere: A case study of the 19 February 2014 storm, Radio Sci., 52, doi:10.1002/2016RS006106.*

STUDY 2: MULTIINSTRUMENT OBSERVATIONS OF A GEOMAGNETIC STORM AND ITS EFFECTS ON THE ARCTIC IONOSPHERE: A CASE STUDY OF THE 19 FEBRUARY 2014 STORM

3.1 Introduction and Relevance of the Paper

We present a multiinstrumented approach for the analysis of the Arctic ionosphere during the 19 February 2014 highly complex, multiphase geomagnetic storm, which had the largest impact on the disturbance storm-time index that year. The geomagnetic storm was the result of two powerful Earth-directed coronal mass ejections (CMEs). It produced a strong long lasting negative storm phase over Greenland with a dominant energy input in the polar cap. We employed global navigation satellite system (GNSS) networks, geomagnetic observatories, and a specific ionosonde station in Greenland. We complemented the approach with spaceborne measurements in order to map the state and variability of the Arctic ionosphere. In situ observations from the Canadian CASSIOPE (CAScade, Smallsat and Ionospheric Polar Explorer) satellite's ion mass spectrometer were used to derive ion flow data from the polar cap top side ionosphere during the event. Our

research specifically found that (1) thermospheric O/N_2 measurements demonstrated significantly lower values over the Greenland sector than prior to the storm time. (2) An increased ion flow in the topside ionosphere was observed during the negative storm phase. (3) Negative storm phase was a direct consequence of energy input into the polar cap. (4) Polar patch formation was significantly decreased during the negative storm phase. This paper addresses the physical processes that can be responsible for this ionospheric storm development in the northern high latitudes. We conclude that ionospheric heating due to the CME's energy input caused changes in the polar atmosphere resulting in N_e upwelling, which was the major factor in high-latitude ionosphere dynamics for this storm.

3.2 Multiinstrument observations of a geomagnetic storm and its effects on the Arctic ionosphere: A case study of the 19 February 2014 storm

In this paper we focus on ionospheric storm disturbances in the Arctic ionosphere. The impact of geomagnetic storms on the ionosphere and the underlying first principles behind these physical and chemical processes have been discussed by numerous authors, including, e.g., Rodger et al. [1992], Buonsanto [1999], and Blagoveshchenskii [2013]. Nevertheless, the precise geophysical background behind this complex system is still not completely understood [e.g., Lastovicka, 2002]. Coronal mass ejections (CMEs) and other manifestations of solar activity can trigger magnetospheric storms that may cause global or regional geomagnetic disturbances impacting the ionosphere. These effects will result in changes in the regular (e.g., diurnal and seasonal) ionospheric processes [e.g., Blagoveshchenskii, 2013; Durgonics et al., 2014].

Interaction between a CME and the magnetosphere often starts with the arrival of a shock wave in near-Earth space. On Earth's surface the outset of such interaction is seen as the sudden impulse

(SI), which can be detected using, for example, geomagnetic field horizontal (H) component measurements collected by magnetometers. There is a set of well-established indices to identify the early stages of these interactions including the global disturbance storm time (Dst) index [e.g., Anderson et al., 2005; Le et al., 2004; Blagoveshchenskii ,2013] or the regional auroral electrojet (AE) index which is derived from auroral region magnetic stations and the polar cap north (PCN) index computed from a near-pole single magnetic station (details on the indices can be found in, e.g., Wei et al. [2009] and Vennerstrøm et al. [1991]). A sudden decrease in the Dst values typically indicates a change in the globally symmetric and asymmetric (partial) components of the ring current suggesting a global geomagnetic event [Liemohn et al., 2001]. Once such an event is identified, the local state of the geomagnetic field can be observed using data from the individual magnetic observatories in the Arctic region. The localized measurements can provide additional insights into the electromagnetic response to storm input, since the Dst is derived from a global network of stations with local information content no longer overtly present. These observed magnetic disturbances indicate dependence on the quasi-dipole (QD) coordinates [Emmert et al., 2010].

Ionospheric storms caused by geomagnetic activity can be observed using total electron content (TEC) scintillations based on global navigation satellite systems (GNSSes) observations, ionosonde observations, and other independent measurements of the ionospheric plasma [Pi et al., 1997]. The locations of a subset of GNSS stations used in this research, and a sample TEC map generated from the observed data is shown in Figure 3.1. Blagoveshchenskii [2013] and Schunk and Nagy [2009] described a set of variables to define the state of the ionosphere during storm time conditions. These variables include season, local time, solar activity, storm onset time (or time since storm onset time), storm intensity, prestorm state, and QD latitude. Additionally, ionospheric processes have to be considered along with processes of other regions of the geo-space environment such as

thermospheric circulation, neutral and ion composition changes, gravity waves, acoustic waves, chemical composition, variations in the electric and magnetic fields, and other couplings with the magnetosphere and neutral atmosphere [Heelis, 1982; Khazanov, 2011]. During such an ionospheric storm, there can be both positive and negative TEC anomalies (also known as phases) due to storm effects of different scales. The durations of the positive and negative phases typically exhibit a clear latitudinal dependence (i.e., at higher latitudes the negative phase is prolonged) and seasonal dependence (i.e., negative storms are more pronounced in the winter) [Mendillo, 2006; Mendillo and Klobuchar, 2006]. These phases are apparent in electron density (N_e) variations in the F_2 layer (N_mF_2) and the changes in F_2 peak height (h_mF_2) [Buonsanto, 1999]. In addition to electron density observations (describing the spatial distribution of the free electrons), ionospheric scintillation measurements can also be carried out to provide complementary statistics about irregular structures in the ionosphere, which are often accompanied by rapid signal phase fluctuations. This could be of particular interest in regions where polar patches are present [Prikryl et al., 2015]. A comparison of such N_e and scintillations in the Arctic region is performed in this paper, followed by analyses of the results with particular attention to distinguishing between plasma gradients due to solar ionization and patches. Rate of TEC index (ROTI) will be presented as a surrogate indicator of ionospheric structure variations [Pi et al., 2013].

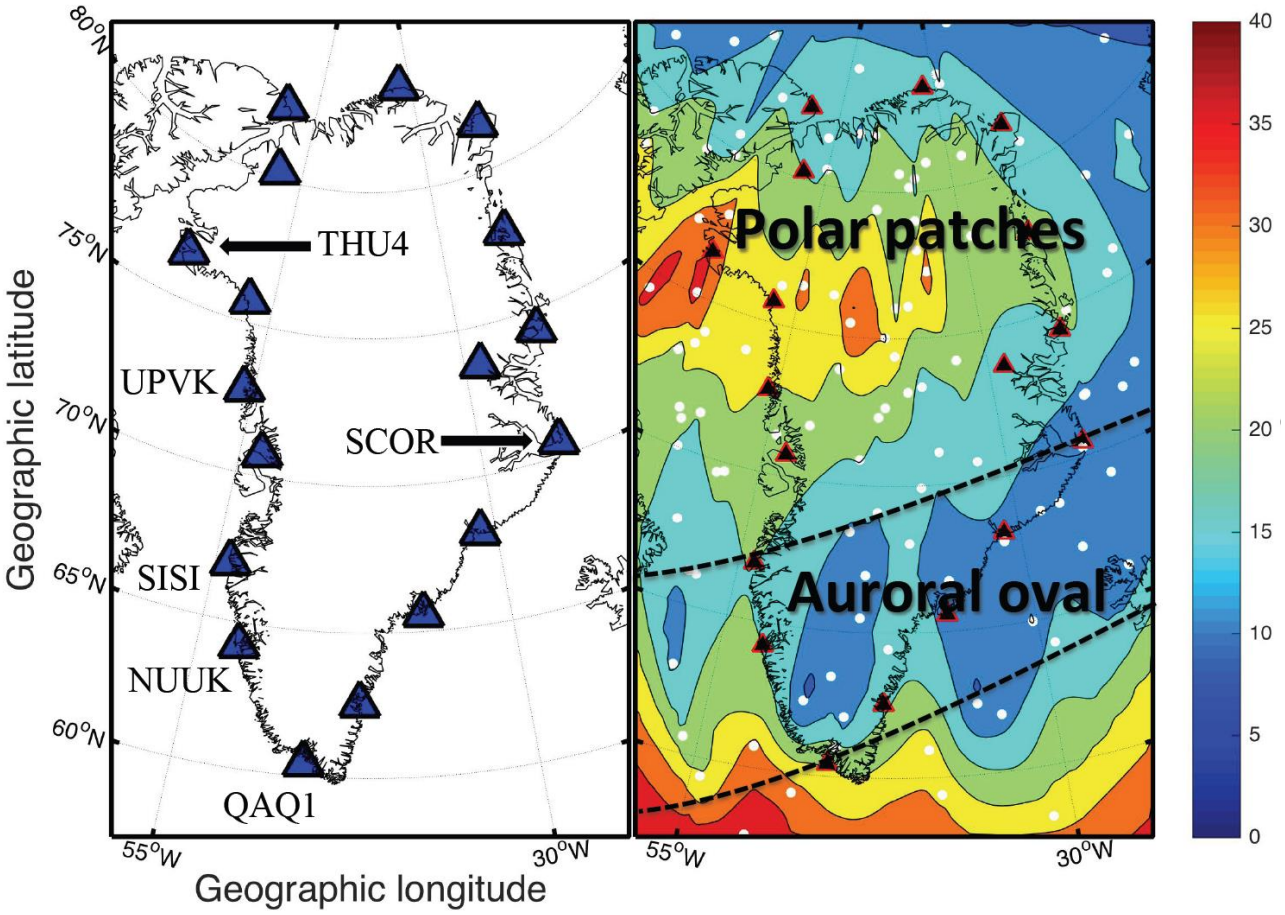

Figure 3.1 (left) Map of Greenland with blue triangles marking the locations of a subset of GNET GNSS stations that has been used to generate the VTEC maps in this study. Six out of the 18 stations were specifically labeled so their locations will be easily identified in later figures. Legend for the station codes are as follows: Nuuk (NUUK), Qaqortoq (QAQ1), Scorebysund (SCOR), Sisimiut (SISI), Thule (THU4), and Upernavik (UPVK). Note that the Thule ionosonde station is collocated with the Thule GNSS station for all practical purposes. **(right)** An example for VTEC map over Greenland at 19:15:00 (UTC), 18 February 2014, the day before the CME impact. The VTEC values at the ionospheric pierce points are denoted with white circles. The mapping was performed by employing the commonly used natural neighbor interpolation scheme to estimate values using the IPP values. The map clearly demonstrates local ionospheric structures [see, e.g., Rodger et al., 1992] and polar patches. Due to the experimental setup auroral-E ionization (AEI) is not clearly apparent in this figure (for further details on AEI detection see Coker et al. [1995]). The auroral oval boundaries for this particular time are taken from The Johns Hopkins University Auroral Particles and Imagery website (*http://sd-www.jhuapl.edu/Aurora/ovation/ovation_display.html*).

The purpose of the research is to observe and interpret the processes in the Arctic ionosphere, which are caused by CME-driven storm of 19 February 2014. During the course of this ionospheric storm the Dst index dropped to its lowest value of -95 nT in all 2014; additionally, the related geomagnetic storm was highly complex. Therefore, we selected this specific event for our case study. For details on this specific storm see E. J. Rigler (unpublished data, 2014) available from the U.S. Geological Survey (*http://geomag.usgs.gov/storm/storm18.php*). In this research we investigate storm effects in ionospheric TEC and the vertical N_e and use scintillations during storm time as a key diagnostic tool. The paper is organized as follows: Section 3.2.1 describes the storm effects of the 19 February 2014 ionospheric storm and the utilized methodology and instrumentation. In section 3.2.2 we elaborate on the specific observation types and measurements. Section 3.2.3 introduces a scintillation index that originates from the same observations as TEC and may be combined with electron density results; this approach is able to provide further insights into temporal variations of the ionosphere and its smaller scale structure. In section 3.2.4 we provide a summary for the research and draw conclusions in order to ascertain geophysical insights into the observed phenomena.

3.2.1 Methods, Instrumentation, and Observations

In this section and the following sub-sections we describe the storm effects, followed by an overview of the methodology, the instruments used, and the results of the different observations employed in the study. We start with the solar wind para-meters and induced geomagnetic variations. This is followed by an analysis of electron density observationsand related neutral gas composition changes. Lastly, supporting data derived from TEC mapping, the Super Dual Auroral

Radar Network (SuperDARN), and the CASSIOPE (CAScade, Smallsat and IOnospheric Polar Explorer) satellite ion mass spectrometer are presented.

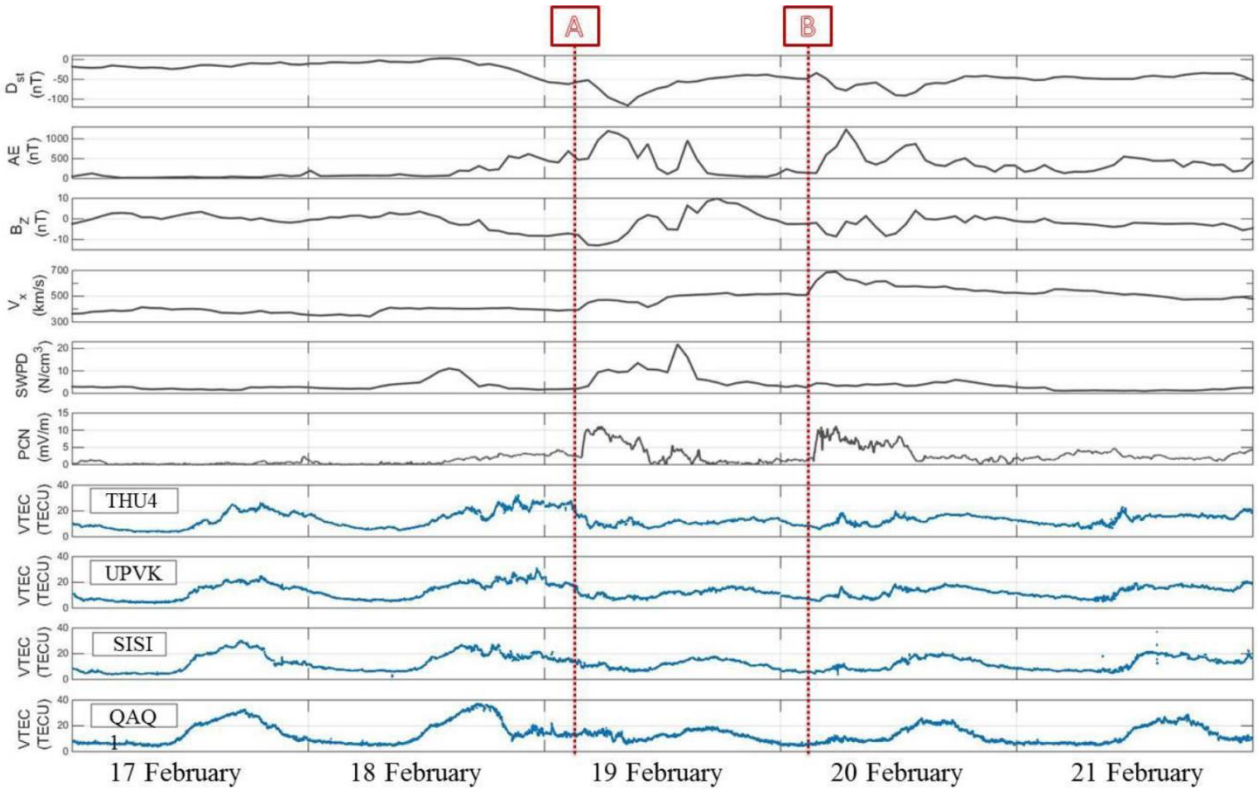

Figure 3.2 Near-Earth solar wind, interplanetary magnetic field (IMF), and plasma parameters shown in addition to the computed MVTEC using four Greenlandic GNSS stations on 17–21 February 2014: **(first panel)** Dst index, **(second panel)** AE index, **(third panel)** IMF B_z component, **(fourth panel)** Operating Missions as Nodes on the Internet (OMNI) solar wind velocity x component, **(fifth panel)** OMNI solar wind proton density, **(sixth panel)** PC north index, and **(seventh to tenth panels)** MVTEC values in order of decreasing station geographic latitude: Thule (77°28000″N, 69°13050″W), Upernavik (72°47013″N, 56°08050″W), Sisimiut (66°56020″N, 53°40020″W),and Qaqortoq (60°43020″N, 46°02024″W). The red dashed lines mark the approximate times when the first (A) and second (B) CME-induced effects were detected inthe observations.

3.2.1.1 Storm Effect Overview

At northern latitudes the auroral zone (or auroral oval) is typically located between 10 and 20° from the geo-magnetic pole and it is 3 to 6° wide. Its location and width normally depend on the actual geomagnetic activity. The auroral zone expands and becomes wider during geomagnetic storms and subsequently contracts as the storm subsides [Feldstein, 1986]. Poleward from the auroral oval lies the polar cap region, where the geo-magnetic field lines are open and extend into space. Figures 3.2–3.4 give an overview of the 19 November 2014 storm effects over Greenland. Figure 3.2 demonstrates how the solar wind parameters and vertical TEC (VTEC) values evolved over time (from 17 to 21 November 2014; for more details, see section 3.2.1.2). Figure 3.2 shows a clear separation between polar cap stations and auroral oval stations described below. Station Qaqortoq (QAQ1) indicates a strong negative storm phase onset on 18 February with the AE index concurrently showing an increased activity. AE indicates the strength of the auroral electrojet, and it increases when the B_z and Dst begins to decrease around 14:00 UTC on 18 February. The solar wind proton density also shows activity at this time, ~10 cm^{-3}, and then it diminishes and only shows increased values again when the first CME impacts [Ghamry et al., 2016]. Station Sisimiut (SISI) can be under either the polar cap or the auroral oval, depending on geomagnetic and storm conditions. Figures 3.2 (sixth panel) and 3.2 (ninth panel) show that the ionosphere above Sisimiut appears to be more similar to Qaqortoq than the other two stations at higher latitudes. The ionosphere over Upernavik and Thule, on the other hand, demonstrates clear polar-cap-like behavior, showing an abrupt TEC decrease while the PC index displays a sudden large energy input into the polar cap region coinciding with the first CME impact around 03:00 UTC on 19 February. After that time all stations exhibit negative storm effects with diminished TEC values for several days. For a comprehensive analysis of the solar wind parameters during the 19 February 2014 storm see Ghamry et al. [2016].

3.2.1.2 Ground-based Measurements and Solar Wind Parameters

Greenland's GNSS ground stations present a unique opportunity to observe the high-latitude ionosphere. Due to Greenland's unique location the ground-based GNSS measurements will cover regions representing the polar cap and auroral oval of the ionosphere providing a complete latitudinal profile of the Arctic iono-sphere. GNSS ionospheric pierce points (IPPs) can be acquired ranging approximately from 55 to 90° northern geographic latitudes and 10 to 80° western longitudes. Measurements used in this work consist of 1 s, 15 s, and 30 s sampling interval using GNSS observations acquired from the Greenland GPS Network (GNET) permanent ground stations located along the Greenland coastline; see F. B. Madsen (unpublished data, 2013)available from the Technical University of Denmark (*http://www.polar.dtu.dk/english/Research/Facilities/GNET*). The geodetic GNSS receivers are capable of tracking several observables, such as pseudorange observables (P1 or C1 and P2), phase observables (L1 and L2), and carrier-to-noise density ratios (S1 and S2). We calculated TEC and related parameters using two independent methods and validated them against each other. The first method utilized the Jet Propulsion Laboratory's Global Ionospheric Maps (JPL GIMs); for details on JPL GIM see, e.g., Vergados et al. [2016] and Mannucci et al. [1998]. The second method was developed atthe Technical University of Denmark's Space Department (DTU Space) and known as Arctic Ionospheric Map (AIM) with an overview of the processing steps described in the following section. The GPS geometry-free combinations of phase and pseudorange (LI, PI) were calculated for each satellite-receiver pair as described by, e.g., Hernandez-Pajares et al. [2007]. The pseudorange observables were smoothed using a Hatch-filter approach [Hatch, 1982] and corrected for satellite and receiver differential code biases (DCBs). The TEC calculation has included the DCB values; for details see the equations in Hernandez-Pajares et al. [2007]. These slant TEC (STEC) measurements exhibit a pronounced elevation angle dependence since at different satellite elevation angles the length of the signal path

through the ionosphere increases with lower elevation angles [Hernandez-Pajares et al., 2007]. To account for this effect an elevation-angle-dependent scaling scheme was applied in addition to a 10° elevation cutoff angle to minimize the effects of multipath error at low elevation angles. Both the type of weighting functions and the elevation cut-off angles were selected after evaluating several different options. Various *1/cosine*-type weighting functions (or mapping functions) are commonly found in the literature. We adopt the standard thin-shell mapping function [e.g., Jakowski et al., 2011; see also Mannucci et al., 1999, and references therein]. Due to geography, a large number of the GNSS stations used in this work are capable of receiving signals directly from intercept-ing the polar cap region. On the other hand, the southernmost Greenland stations were actually located at midlatitudes.

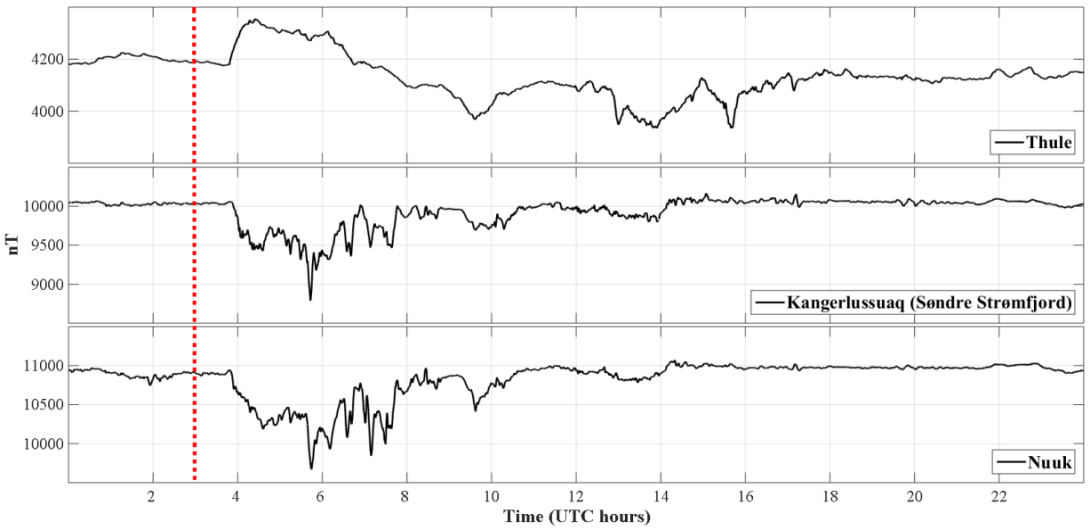

Figure 3.3 The 1 Hz vector variometer measurements from Greenlandic ground stations of the magnetic field vector north component on 19 February 2014. Thule is the northernmost and Nuuk is the southernmost station among the three indicated in the figure. The USGS National Geomagnetism website estimated that the first CME reached the Earth's magnetopause around 03:00 UTC (marked by the vertical red dotted line). Among these three stations the Nuuk magnetic north component indicated the first changes, then ~10 s later they were observed at Kangerlussuaq, and finally ~100 s later they were observed at Thule. The timing accuracy of the instruments is ±2 s. The local ground magnetic response was delayed by almost 1 h compared to the Dst drop.

STEC and VTEC values are typically given in TEC unit (TECU, 1 TECU = 10^{16}el m^{-2}). One TECU is defined as 1016electrons in 1 m^2 cross-section column along the signal path. The computed TECU values serve as a basis for our interpolation and two-dimensional (2-D) TEC mapping. The data point locations for the interpolation are the geographic coordinates where the signal path pierces the single-layer model thin shell (this is a rotational ellipsoid in AIM and sphere in GIM) that represents the ionosphere, also known as IPPs. The IPPs form a 2-Dirregular grid. During the storm days the number of IPPs over Greenland was typically between 150 and 200 at each measurement epoch, depending on the number of receivers tracking and ionospheric conditions. During high scintillation phases with storm time periods, the number of available IPPs is typically lower due to the increased number of cycle slips, which typically deteriorates data quality. Short satellite arcs are often impacted by carrier-phase cycle slips, and depending on the size and location of the phase breaks, often the short arcs need to be discarded by the data processing software. Any VTEC values between ionospheric observations at IPP locations have to be estimated using an interpolation scheme. In this work we applied a natural neighbor interpolation scheme [Sibson, 1981]. For further details on VTEC interpolation and mapping see Durgonics et al. [2014]. The 2-D TEC map color scales are consistent throughout the work to allow comparisons among different figures. In addition to the 2-D VTEC maps in this research we also employ VTEC time series to obtain an overview of ionospheric diurnal variability locally, in the vicinity of agiven station. At any one epoch, the mean VTEC (MVTEC) is calculated as the mean of all the VTEC values obtained from individual data points for a single station. Furthermore, a 10° elevation cutoff angle was applied throughout, and so low elevation angle satellites are removed to minimize error sources such as multipath and to decrease the noise level. In our approach we used the same weight for each satellite. In addition, MVTEC represents a smoothed ionospheric single-layer surface over the given station while its standard deviation indicates how uniformly the ionosphere tends to behave in that

region. The GNSS instruments employed in this work also allow us to study ionospheric scintillations via ROTI. Scintillation indices typically quantify temporal variances of the signal phase and amplitude caused by variations in index of refraction along the signal path. The refractive index is a function of N_e. Therefore, scintillation indicates the presence of electron density gradients. During disturbed times ionospheric scintillations can be severe. The scintillations and their characteristics vary as a function of amplitude, phase, polarization, and angle of arrival of the signal [Maini and Agrawal, 2011]. ROTI is a suitable occurrence indicator for L-band ionospheric scintillations, and for the current work it may have advantages over the traditional scintillation indices, i.e., phase scintillation (σ_φ) and amplitude scintillation (S_4) indices. ROT and ROTI can be computed from the same data source as TEC using L1 and L2, the corresponding wavelengths ($\lambda_{1,2}$), and frequencies ($f_{1,2}$) using the following equations:

$$ROT(t) = \frac{L_I(t) - L_I(t-\Delta t)}{40.3\ 10^{16}\ \Delta t\ (\frac{1}{f_1^2} - \frac{1}{f_2^2})}\ , \tag{3.1}$$

where ROT is in TECU/min units and t and Δt are the time at any epoch in minutes and the sampling interval (1 s in present work), respectively. ROTI is the detrended standard deviation of ROT over N epochs, i.e.,

$$ROTI(t) = \sqrt{\frac{1}{N}\sum_{t-N}^{t}(ROT(t'-N) - \overline{ROT})^2}\ , \tag{3.2}$$

which is calculated using a 1 min running window [e.g., Pi et al., 2013; Jacobsen, 2014]. GNET consists of geodetic GNSS receivers that produce data well-suited for ROTI calculation. This is not the case for the traditional indices (i.e., σ_φ and S_4) that are typically derived from single frequency phase and power measurements at high cadence (50 Hz or higher) and are usually better handled by specialized ionospheric receivers. Although the relationship between the magnitudes of ROTI and σ_φ is not linear, according to Pi et al.[2013], ROTI is very well correlated with σ_φ, which is the

prominent scintillation index used in the Arctic region [Pi et al., 1997, 2013]. This is due to the fact that at these latitudes, the high-speed plasma convection suppresses S_4 due to the Fresnel filtering effect, while σ_φ remains independent of the Fresnel zone size [Mushini et al., 2014 and Kersley et al., 1998]. This analysis seems to break down when the plasma irregularity scales become larger than Fresnel scales for strong turbulence cases. In addition, the minimum detectable plasma irregularity scale size depends on the sampling rate of the receiver. According to typical SuperDARN data (to be discussed subsequently), relative plasma drifts are of the order of 1000 m/s in the polar cap region, which in theory requires at least 1 Hz sampling rate to detect 1 km size irregularities. Fo rmore details, see Virginia Tech SuperDARN (unpublished data, 2014) available from the Virginia Tech Data Inventory (*http://vt.superdarn.org/tiki-index.php?page=Data+Inventory*). The ROTI results presented in this work are generated from 1 Hz sampled data (i.e., N = 60). There exist certain limitations to the applicability of ROTI, which have to be considered when interpreting ROTI results. Bhattacharyya et al. [2000] describes in detail that the phase screen approximation should be valid. This limitation does not hold for example for σ_φ. The limitations essentially mean that thick layers of irregularities might not be tracked sufficiently by ROTI.

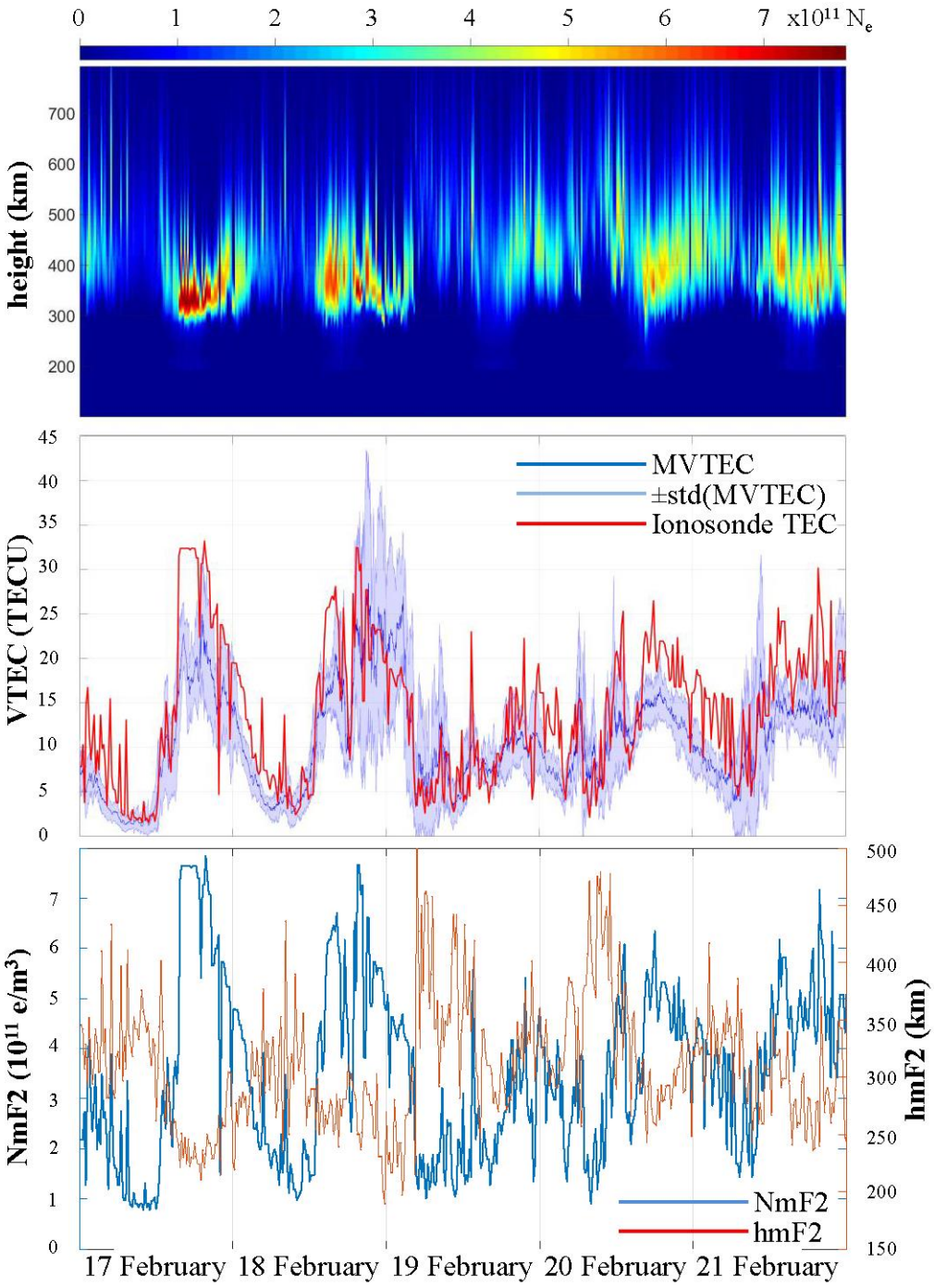

Figure 3.4 (top) Ionogram-derived profiles showing 5 days of ionospheric vertical N_e distributions observed by a digital ionosonde located at Thule. The measurements were collected at every 15 min. The N_e distributions show that the principal ionized region is the F layer with h_mF_2 typically around 300 km. **(middle)** MVTEC time series above Thule during the same days as shown in the top image (dark blue line) with the standard deviation of the MVTEC (light blue shading) and the ionosonde-derived TEC (red line). The diurnal ionization cycle in the F layer was disrupted after

the first CME arrival. The TEC recovery occurs for several days similarly to the Dst (ring current) recovery (Figure 3.2). **(bottom)** N_mF_2 and h_mF_2 timeseries demonstrating negative correlation.

Further ground-based measurements using ionograms and related ionosonde observations were acquired from the Greenlandic Thule ionosonde (Digisonde) station. This station collects measurements every 15 min. The TEC provides integrated N_e values that can be mapped onto a horizontal geographic 2-D surface, and the ionosonde data were used to determine the vertical 1-D N_e distributions over the ground station. These two measurements may be considered completely independent of each other. Additional ground-based measurements were acquired from a network of coherent HF radars (SuperDARN). It operates by continuously observing line-of-sight velocities, backscatter power, and spectral width from ~10 m scale plasma irregularities in the ionosphere. SuperDARN data have been successfully used in combination with relatively low horizontal resolution TEC data in previous studies [e.g., Thomas et al., 2015; Prikryl et al., 2015]. The higher-resolution TEC data available from GNET in combination with SuperDARN convection maps presented in this work potentially allow for an improved monitoring of polar cap patches and their time evolution in the Greenland sector.

Our method to identify time periods with disturbed ionospheric conditions was based on Dst, AE, and PCN indices (for a detailed comparison of these indices see, e.g., Vennerstrøm et al. [1991]) and geomagnetic horizontal north component measurements (see Figure 3.3). Preliminary identification of the beginning of CME-induced geomagnetic storms can be done through analysis of Dst data by detecting significantly negative peaks. On 18 February, Dst heads toward a temporary minimum of -70 nT while AE rises significantly (Figure 3.2), both classical signatures of a storm main phase [Blagoveshchenskii, 2013; Tsurutani and Gonzalez, 1997; Gonzalez et al., 1994]. High-resolution local magnetic data were acquired (magnetic H component measurements)

from the Greenlandic network of magnetic stations, with relevant magnetic measurements shown in Figure 3.3. Some of the magnetic stations are in close proximity to GNSS stations and at some locations to ionosondes as well (e.g., Thule).

At this point it is worth pointing out that the sudden PCN rises on 19 and 20 February (near the red dotted lines A and B in Figure 3.2 (sixth panel)) coinciding with observed MVTEC depletions in the data of polar cap GNSS stations in Thule and Upernavik (Figures 3.2, seventh panel, and 3.2, eighth panel). The same electron density depletions may be less noticeable for auroral oval stations in Sisimiut and Qaqortoq (Figures 3.2, ninth panel, and 3.2, tenth panel). More on the electron density observations can be found in section 3.2.1.5.

The ground-based magnetic instruments consist of 1 Hz sampling rate capable vector variometers. The local magnetic coordinate system is oriented along local magnetic north and east at the time of the vector variometer instrument setup and adjusted every year. In Figure 3.3, the horizontal north component changes are shown for 19 February 2014.

3.2.1.3 Analysis of Solar Wind Parameters and Geomagnetic Observations

The storm was highly complex and had multiple main and recovery phases resulting from a series of Earth-directed CMEs (see *http://geomag.usgs.gov/storm/storm18.php* and Ghamry et al. [2016] for details). As shown in Section 3.2.1.2, Dst, AE, and PCN are all geomagnetic indices but there are also fundamental differences among them. For a more complete discussion see, e.g., Vennerstrøm et al. [1991]. The local magnetometer measurements shown in Figure 3.3 are more comparable to PCN and AE while Dst is sensitive to the ring current, which exists due to larger-scale (global) magnetospheric convection patterns. This fundamental difference has to be taken into

account when interpreting and comparing local, regional, and global indices, such as ones discussed before in Section 3.2.1.2.

The magnetic disturbances in Figure 3.3 indicate an approximately 1 h propagation-based delay compared to the disturbance in the Dst. There appears to be an additional delay, with the disturbance propagating from south to north direction (there is a ~110 s delay between Nuuk and Thule). Note that the magnetic measurements (local north component and Dst) are only applied as indicators of storm activity. There are several other phenomena occurring simultaneously that may also affect the geomagnetic field measurements including the ionosphere currents induced ground currents. The magnetic field north component sudden drop seems significant at stations Kangerlussuaq (located approximately 130 km east of Sisimiut; see Figure 3.1) and Nuuk, and they appear to show a very similar pattern in the Dst drop (compare Figures 3.2 and 3.3). The local recovery is, however, significantly faster than the Dst recovery. This was expected due to the fact that Dst is sensitive to significantly larger-scale convection patterns than regional and local indices. While both stations registered he north component values at approximately 14:00 UTC, the Dst took several days to fully recover. During the same time, the observed magnetic north component at Thule demonstrated a significant increase in early onset rather than a decrease. This positive response was delayed by approximately 100 s compared to station Kangerlussuaq and after approximately 6 h values of ~200 nT below the quiet level were observed (see Figure 3.3).

The Dst (shown in Figure 3.2) exhibited only a small main phase when the first CME's effect was observed, around 03:00 UTC on 19 February. Observed UTC times of the CME launch and the estimated times when the CMEs reached Earth's magnetopause were obtained from the U.S. Geological Survey (USGS) National Geomagnetism website (*http://geomag.usgs.gov/storm/storm18.php*).

The Dst index eventually decreased by in excess of 100 nT. This was followed by a recovery phase, during which the Dst nearly recovered by about 50% of its earlier minimum in ~10 h. The second CME's effect was detectable shortly after 03:00 UTC on 20 February. This was followed by a much slower recovery phase lasting about 3 days. The local magnetic H component anomaly observed from local Greenlandic stations (Figure 3.3) showed an approximately 1–2 h delay compared to the lowest Dst peak. However, the negative peaks also appeared in the local observations. One exception is for the magnetic data at station Thule, which in fact showed a positive magnetic H component anomaly during these events.

3.2.1.4 Spaceborne Observations

In addition to ground-based observations and solar wind parameters two spaceborne measurement types were analyzed to better understand the physical processes responsible for the observed storm effects. The first instrument is the Global Ultraviolet Imager (GUVI) on board the TIMED spacecraft providing global measurements of the far ultraviolet dayglow intensity [Paxton et al., 2004]. The observations allow the determination of atmospheric O/N_2 concentration changes that affect the level of ionization in the upper atmosphere. During storm conditions, the column density ratio $\Sigma[O/N_2]$ tends to decrease at high latitudes [e.g., Prölls,1995; Verkhoglyadova et al., 2014; Meier et al., 2005; Zhang et al., 2004]. We analyzed GUVI O/N_2 ratios for two quiet days before the first CME, the day of the first CME hit, and for three additional days during the nega-tive storm phase. The negative O/N_2 anomaly following the CME onset would indicate that the TEC negative storm may have resulted from atmospheric composition changes.

The second spaceborne measurement type was collected by the e-POP (Enhanced Polar Outflow Probe) instrument on board the Canadian CASSIOPE (CAScade, Smallsat and IOnospheric Polar

Explorer) satellite. e-POP is a suite of eight scientific instruments that were designed to measure physical parameters related to space weather. CASSIOPE was inserted in a low-Earth polar orbit, and at the time of the storm, it had a ~325 km perigee and ~1456 km apogee. Its orbit inclination was 80.995° [Yau and James, 2015]. All data presented here from CASSIOPE observations were measured along near-perigee passes in the Arctic region. We used measurements from one of the eight instruments of e-POP, specifically the Imaging and Rapid Scanning Ion Mass Spectrometer (IRM). The IRM is a low-energy ion spectrograph, capable of measuring the energy, mass, and direction of arrival of incident ions in two- and three-dimensional scans in the energy range 1–100 eV/q, over ±180° pitch angle, and ±60° in azimuth angle, where q is the elementary charge. The instrument performs an entire 2-D sample of the local ion population in 1/100 s, for an imaging rate of 100 Hz. For a detailed description of IRM instrumentation, measurement techniques, and data products see Yau et al. [2015]. During the observation window used in this work e-POP was in default mode, designated as "addressed mode" or AM. This mode normally generates data that are pairs of pixel address and time of flight. For the purpose of this work we utilized the following data sets for IRM. They included TOF (time of flight) bin counts, angle-dependent pixel counts (360° along pitch angle), and skin current. TOF is in units of bin periods each corresponding to 40 ns. The IRM instrument operates semiautonomously gathering measurements in the form of detected anode pixel hits and respective TOF. The IRM pixel data consist of 16 bit values representing 6 bits identifying pixels and 10 bits representing the corresponding TOF for the detected pixel. Measured sensor skin current is also reported in the data packets together with the main instrument data [Yau et al., 2015].

3.2.1.5 Results: Electron Density Observations

Figure 3.4 shows the evolution of ionosonde-derived vertical N_e profiles (including the relation between their peak heights and integrated N_e values) and mean VTEC (MVTEC) time series during the 19 February 2014 geomagnetic storm over station Thule (THU4) in Greenland. These two observations provide the foundation to analyze the polar ionosphere dynamics during the storm. Due to the nature of the ground-based ionosonde measurements the topside ionosphere needs to be modeled to obtain a full vertical profile resulting in our case modeled topside using a fitted Chapman profile. Following this top-side modeling the ionosonde electron density profile can be translated into VTEC in TECUs directly over the station. This is done by integrating the ionosonde profile which is also given along a 1 m^2 column similarly to the definition of the TEC. The major source of differences between ionosonde-derived TEC and GNSS-TEC (Figure 3.4, middle) originates from the inaccuracies in the topside modeling.

On 17 and18 November, the typical diurnal enhancements were building up in the F_2 layer, which was interrupted by the storm after 03:00 UTC on 19 November in the polar cap region and earlier in the auroral region. The diurnal variation during 18 November was barely distinguishable from typical diurnal activity of this particular season (or on 17 November), except for an apparent 3–5 TECU positive enhancement. This is just slightly above the TEC uncertainty, which is ±2.8 TECU for the AIM. AIM outputs result on an irregular grid; therefore, its spatial resolution depends directly on the IPP distribution, and its temporal resolution equals the sampling rate of the GNSS data. The main source of this error seemed to result from the stations' differential code bias (DCB) estimations. The JPL GIM uncertainties are at the two TEC level in middle and high latitudes and about 3 TECU for low-latitude regions [Komjathy et al., 2005a, 2005b]. The DCBs have lower uncertainties as GIM is estimating biases once a day assuming that receiver and satellite differential

biases will not change over the course of 1 day. GIM uses Gauss-Markov Kalman filter taking advantage of persistence in the solar geomagnetic reference frame constraining DCBs biases when separating hardware-related biases and elevation-angle-dependent ionospheric delays [Vergados et al., 2016; Komjathy, 1997]. GIM has a 1° by 1° native spatial resolution and a 15 min temporal resolution. Positive enhancement (phase), which builds up once the disturbance has arrived, was typically observed in the investigated events during 2014. This phenomenon is described in more details in, e.g., Mendillo [2006]. It may also appear in midlatitudes, for instance, as shown in Durgonics et al. [2014]. However due to the TEC error it cannot be fully confirmed without more precise measurements to be collected. The h_mF_2 turned out to be approximately 20–40 km higher during 18 February compared to 17 February. Shortly after 03:00 UTC (~ midnight local time) on 19 February when the first shock arrived, there was a sudden drop in the TEC values, which was also apparent in the ionogram as a sharp contrast line. h_mF_2 became abruptly elevated by about ~150 km. Several hours later, during local daytime, following this, the F region showed significant depletions, the TEC fell to ~7 TECU, and subsequently, h_mF_2 was elevated abruptly by about ~150 km. Several hours later, during local daytime, the F region showed significant depletions. The TEC values fell to ~7 TECU where values of 20–25 TECU had been more typical. This period can clearly be observed in the ionogram plot shown in Figure 3.4. The diurnal variations only resumed after 16:00 UTC on 20 February; however, the daily maximum values only reached a level of approximately ~10 TECU less than during calm days in this season. Furthermore, there was a gradual increase in the TEC values on 20 and 21 February. The daily TEC minima during the ionosphere recovery phase did not decrease compared to the calm day values, and yet they showed an apparent, slight (~2 TECU) increase, which falls within the error bar. Dst was gradually recovering in a somewhat similar fashion to the TEC (Figure 3.2). The ionosonde-derived VTEC is well correlated with GNSS TEC, but it shows a clear positive bias. This offset requires further

studies, but it is possibly due to the topside model estimation of the ionosonde profiles and GNSS DCB estimation errors. N_mF_2 and h_mF_2 demonstrate a weak negative correlation amounting to -0.6.

In order to further investigate the Arctic ionospheric N_e changes induced by CMEs we identified five further noteworthy (peak Dst < -65 nT) geomagnetic storms during 2014, and we analyzed two similarly prominent storms via the same methodology that we applied to the 19 February 2014 event. The 12 April 2014 and the12 September 2014 events (the dates indicate the day when the Dst minimum occurred) resulted in very similar ionospheric storm effects; all three solar events triggered analogous disturbances in the ionosphere. The analyzed high-latitude ionospheric storms exhibited the following common characteristics (see Figure 3.4): (1) during the geomagnetic storm initial phase the regional TEC increased by ~3 to 5 TECU (just above the uncertainty level) compared to the previous calm periods and (2) during the main phase, if it was not followed by a fast recovery phase (e.g., in Figure 3.4, during the second half of 19 February), the F layer was disrupted and the decreased ionization resulted in -10 to -20 TECU anomalies which lasted for days. When there was a fast Dst recovery phase (which is driven by the B_z component turning positive) during the several-days-long main recovery period, it resulted in a sudden increase in F layer ionizations of about ~5 TECU for a short time (2–3 h). Multiple sudden increases can be observed from 19 to 21 February. The long recovery period of the ionosphere is regional (it is present in the polar cap and the auroral oval, although their development is somewhat different see Figure 3.2) and lasts for days. Although it is the dominant factor in the regional TEC, there are still subregional inhomogeneities present (Figure 3.2).

3.2.1.6 O/N_2 Composition Changes

The column density ratio $\Sigma[O/N_2]$ maps (for more details, and technical background on the column density ratio maps, see, e.g., Prölls [1995]) for six consecutive days are shown in Figure 3.5. 17 February 2014 showed typical values over the extended study area followed by a slight decrease on 18 February 2014. On the day of the storm N_2 upwelling occurred over a large area mostly covering latitudes above 50°. Details of the physical mechanism of atmospheric upwelling can be found in, e.g., Prölls [1995].

O/N_2 ratios decreased to ~0.2–0.3. The negative anomaly lasted for several days recovering slowly to typical values prior to the disturbance (~0.7). Figure 3.6 displays global longitudinal slices of the GUVI-derived maps along 73° latitude with Greenland located approximately between 30 and 60° west longitude. Typical values prior to the storm event were around 0.7 to 0.8. On the day of the storm the values decreased to ~0.3. The recovery period lasted for several days similarly to the TEC recovery (Figure 3.5).

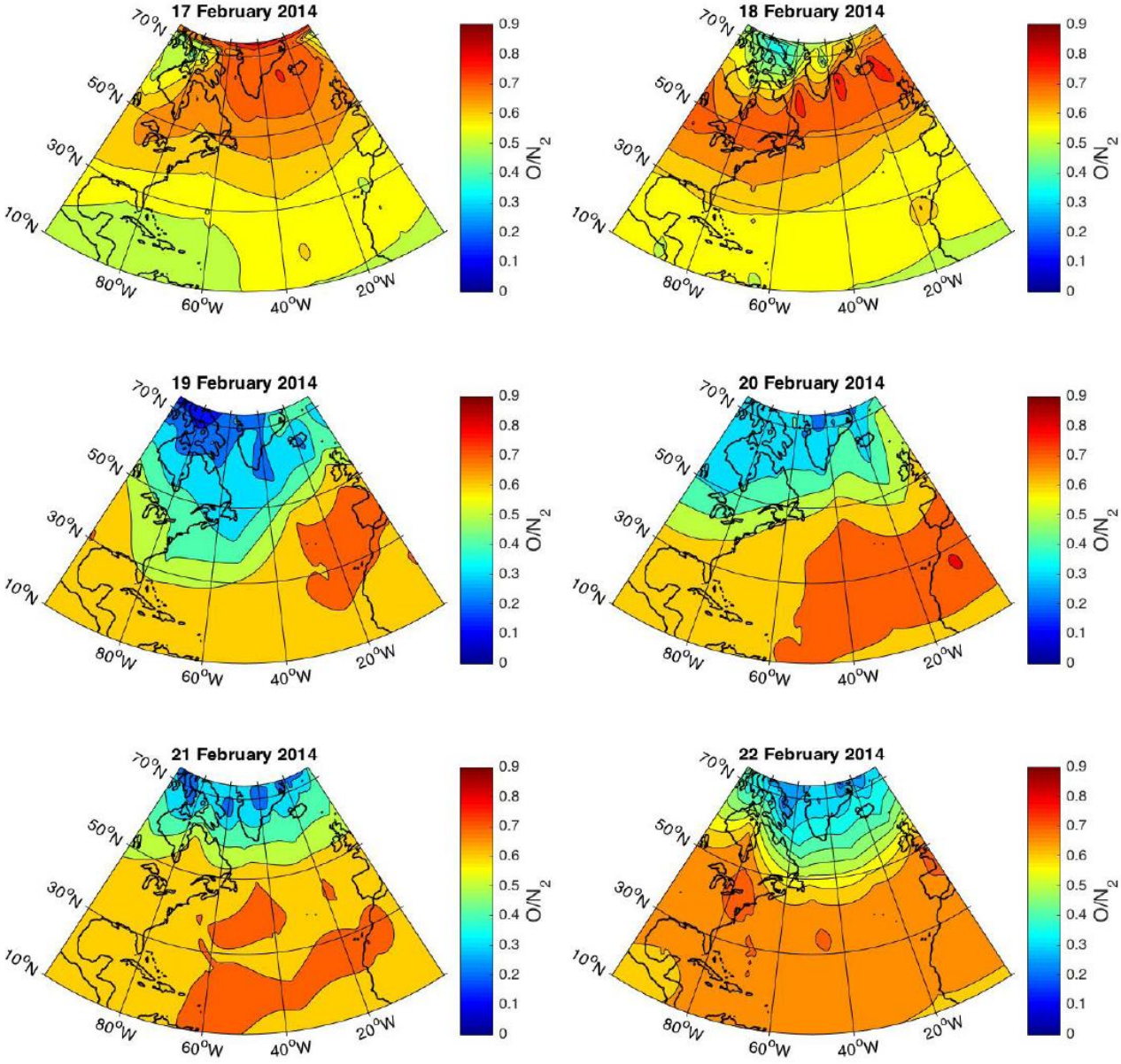

Figure 3.5 O/N_2 ratio maps demonstrating composition changes during the 6 days we investigated. The first CME hit on 19 February and the second on 20 February. The northernmost slice of these maps is shown in Figure 3.6.

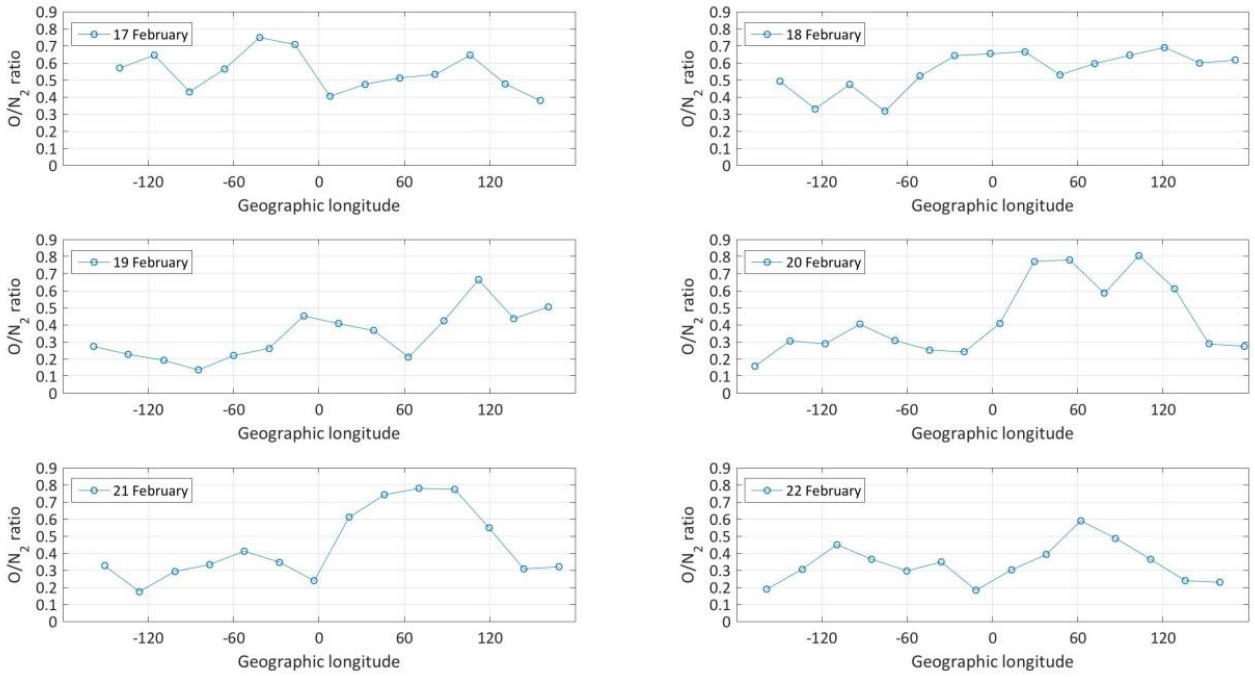

Figure 3.6 Longitudinal profiles demonstrating O/N_2 ratios (unitless) along 73° north latitude. The first CME hit on 19 February and the second on 20 February.

3.2.1.7 Polar Patch Propagation and Convection

Figure 3.7 shows collocated convection and contours of magnetospheric electric field potentials from SuperDARN and GNSS-derived VTEC at 23:30 UTC on 18 February 2014.

Comparison of Figures 3.7 (left) and 3.7 (right) demonstrates that TEC values tend to be low in stagnation zones (Figure 3.7, left), where drift speed is low and high where the antisunward plasma drift is dominant. The antisunward direction can be determined by the magnetic local time values in Figure 3.7 (left). Figure 3.8 shows time evolution of polar cap patches during a 30 min time interval [Rodger et al., 1992].

Velocity magnitudes calculated from features in the TEC data appear to be in good agreement with SuperDARN magnitudes. The observed polar cap patches shown in Figure 3.8 are typically propagating with velocities between 500 and 1000 m/s. During this period, the B_z component was negative (Figure 3.2) and the antisunward cross polar cap convection seemed dominant in the region. The TEC mapping reveals connected patch structures and individual patches drifting in lower electron density regions, as well.

3.2.1.8 Ion Composition and Velocity Distribution of Ions in the Topside Ionosphere

Topside sounding of ion physical properties was feasible using the IRM sensor on e-POP. The altitudes of CASSIOPE were between 350 and 650 km in the Arctic region when taking the measurements. IRM is capable of distinguishing between the five most abundant ion species in the topside ionosphere including H+, He+, N+, O+, and NO+. An important parameter that affects the pixel and TOF separation of the IRM instrument data is the hemispherical electrostatic analyzer inner dome bias voltage (VSA) [Yau et al., 2015]. Due to the fact that the highest-energy ions arrive at the outermost portion of the detector the energy range of the detected ions depends primarily on VSA. For a detailed description of the detector geometry and voltages interested readers are referred to Yau et al. [2015]. The VSA value can be set between 0 and -353 V. By using different values one can achieve different separations between the detection of the aforementioned ion species. Time of flight versus time (TOF-t) and energy angle versus time (EA-t) measurements are shown during four different passes in Figure 3.9.

3.2.2 TEC Variations and Scintillation Characteristics

TEC and ROTI results derived in this work originate from using the same type of observations. GNET consists of well-distributed, high-quality geodetic GNSS receivers along the Greenland coast. The geodetic receivers readily measure the L1 and L2 phase observables at high accuracy, which allows the calculation of ROTI (see equation (3.2)) without any modification to the receiver. As described in section 3.2.1.2, S_4 values remain low under polar region conditions, but σ_ϕ remains unaffected. Nevertheless, we found that the internal hardware and firmware setup of the geodetic receivers make σ_ϕ a less than ideal choice to select as an index to characterize ionospheric activity, while our ROTI results are comparable to the values found in the literature. The majority of the receivers operate at 1/30 Hz sampling rate, but a subset of them is capable of 1 Hz and 50 Hz modes, as well. Other researchers have shown [e.g., Jacobsen, 2014; Pi et al., 2013] and confirmed by modern, continuous observations (e.g., SuperDARN) that the plasma convection velocity magnitude in the polar region can reach 1000 m/s or even higher speeds. This is approximately an order of magnitude larger than plasma drift speeds measured at low latitudes. Therefore, to be able to detect kilometer-size irregularities via ROTI, a minimum 1 Hz sample data rate may be needed. For the purposes of TEC mapping 1/30 Hz data appear tobe sufficient; therefore, the TEC we computed utilized that sampling rate. The data used in this work for ROTI calculation were sampled at 1 Hz.

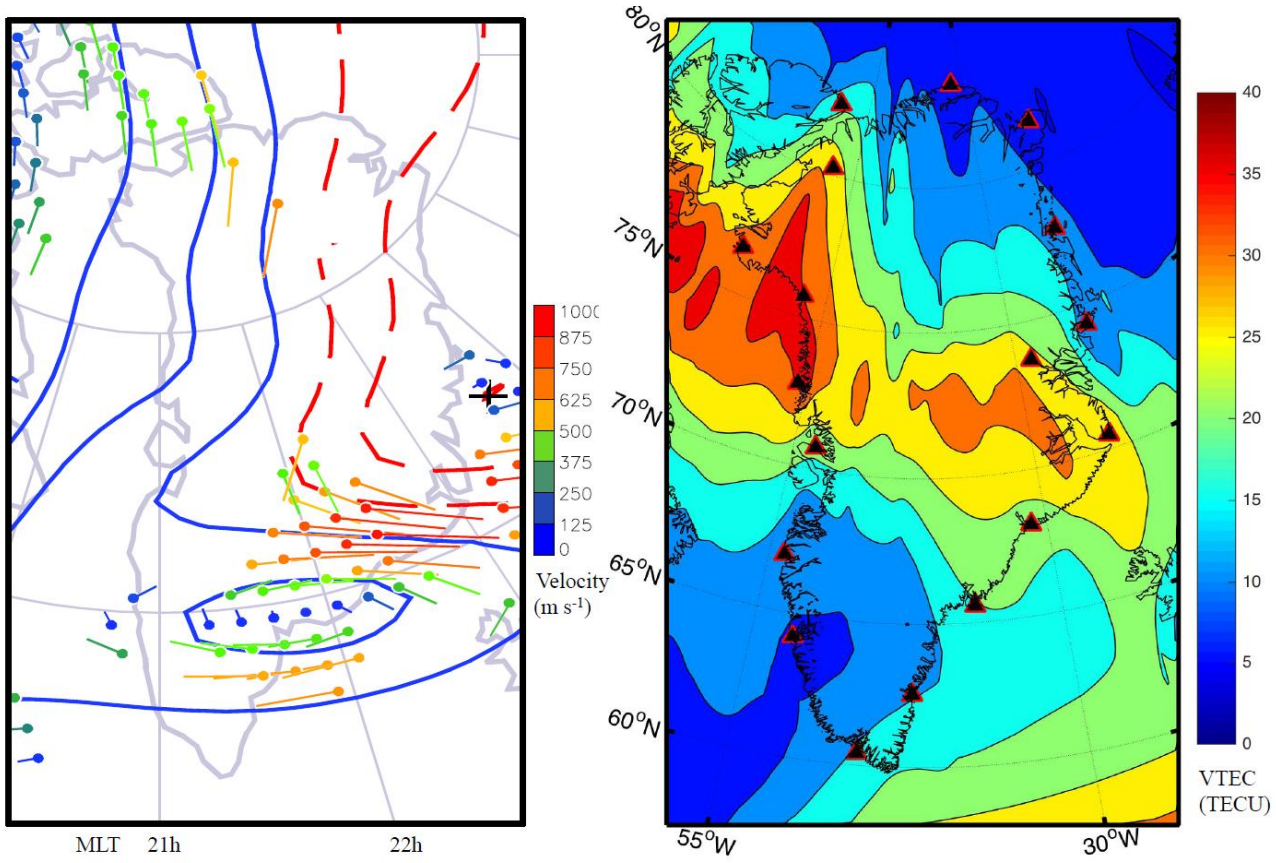

Figure 3.7 (left) SuperDARN drift velocities and contours of magnetospheric electric field potentials shown at 23:30 UTC on 18 February 2014 based on SuperDARN. The region between the two-cell convection pattern is located over Greenland (between red and blue potential contours). Antisunward convection of midlatitude-originated plasma is drifting over the polar cap there (when B_z points downward as shown in Figure 3.2). The closed blue contour surrounds a stagnation zone that results in increased plasma decay; compare this area with the same location on Figure 5.7 (right). **(right)** VTEC map covering the same geographical extent as Figure 3.7 (left). It was derived using 18 GNSS stations (black triangles with red edge) in Greenland. The interpolation is made from approximately 200 IPPs. The figure clearly shows connected but nonuniform patches near the intercell, antisunward convection zone.

Figure 3.4 illustrates the N_e variations over time for the entire 5 day period calculated using ground stations in Thule. Note that in Thule during this time of year the days are only approximately 4 h long (when the Sun is above the horizon) and plasma transported by convection from midlatitudes

may contribute significantly to diurnal N_e variations. The subregional differences in behavior of Greenlandic polar cap TEC variations can be observed in Figures 3.2 and 3.8. The northernmost station, in Figure 3.2, is Thule, and the southernmost station is Qaqortoq. Although there are common characteristics for each station's time series (Figures 3.2, sixth panel, and 3.2, ninth panel) the 19 February ionospheric storm developed somewhat differently in the different subregions. The largest diurnal TEC peak was shown by the Qaqortoq station (Figure 3.2, ninth panel) data on 18 February. The daily enhancement maximum is gradually decreasing as we compared even higher latitudes, with Upernavik and Thule exhibiting the lowest values deep insidethe polar cap. According to The Johns Hopkins University's Auroral Particles and Imagery Display website (see unpublished data 2014; *http://sd-www.jhuapl.edu/Aurora/ovation/ovation_display.html*), on this day Qaqortoq was deep under the auroral oval and Sisimiut was under the poleward edge of it. The 18 February diurnal cycle of ionization was interrupted at Qaqortoq and Sisimiut, when the MVTEC suddenly dropped to ~10–15 TECU from ~30 TECU. At the same time Dst and AE exhibited increased geomagnetic activities, but the PCN index remained virtually unaffected. Starting about the same time, approximately19:00 UTC, we detected significantly increased scintillations.

The JPL GIM software was slightly modified to process GPS data. This was a consequence of a large number of cycle slips in the raw data, which resulted in too small arc sizes followed by data being discarded by the GIM algorithm. While due to certain geophysical processes the F region was significantly depleted (discussed later in this work) after this time (see Figure 3.4) according to SuperDARN data the convection of plasma patches driven by the growing over-the-pole electric field remained strong. The patches propagating in the otherwise depleted ionosphere caused the significant increase in ROTI scintillations. Other researchers have proposed that TEC measurements alone are not sufficient to identify the gradients leading to scintillating conditions [e.g., Alfonsi et al., 2011], while other studies [e.g., Doherty et al., 2004] suggest that TEC gradients and

scintillations often appear together. Our results demonstrate that there is no simple correlation between TEC gradients and ROTI during the storm days. Figure 3.10 shows typical behavior of TEC and ROTI along a single satellite IPP arc. Figure 3.10 (top) portrays TEC gradient due to solar ionization. Superimposed on this enhancement are fluctuations of different scales and after around 14:30 UTC the TEC shows a plateau. Comparing Figure 3.10 (top) with Figure 3.10 (bottom middle) it is clear that ROTI is not sensitive to regular solar ionization (in fact solar ionization tends to fill up less dense plasma regions around patches and decrease scintillations [e.g., Vickrey and Kelley, 1982; Basu et al., 1985, 1988]), but it increases significantly when the signal path intersects drifting plasma patches. Figure 3.10 (bottom row) shows the development and structure of these patches. They become significant around 13:30 UTC and clear the area with nearby IPPs by around 15:30 UTC when the IPP is near the eastern edge of the map.

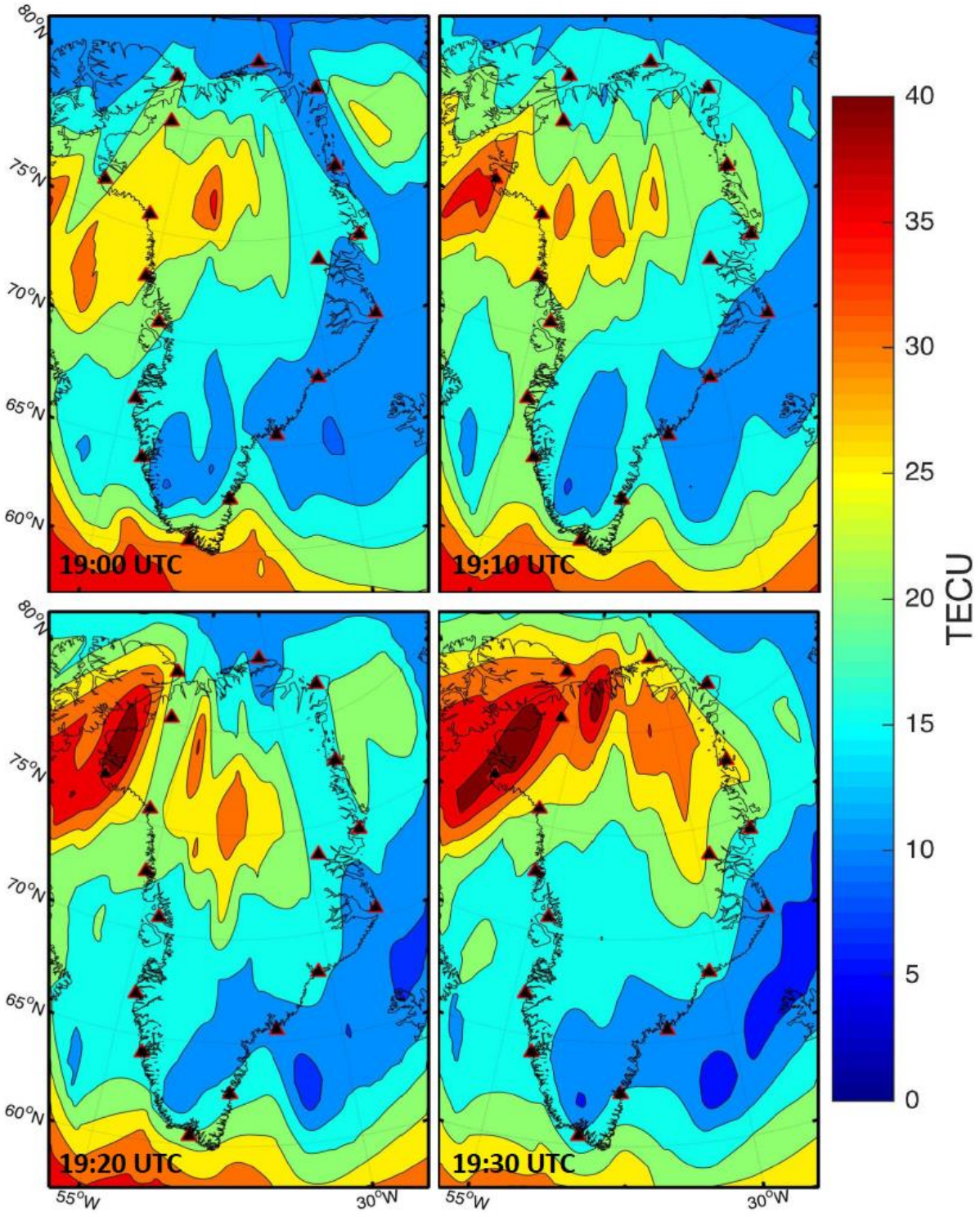

Figure 3.8 Polar patch structure progression over time shown from 19:00 to 19:30 UTC on 18 February 2014. The panels represent 10 min increments. The negative TEC anomaly along 65° latitude lies between the polar cap convection zones and the midlatitude ionosphere.

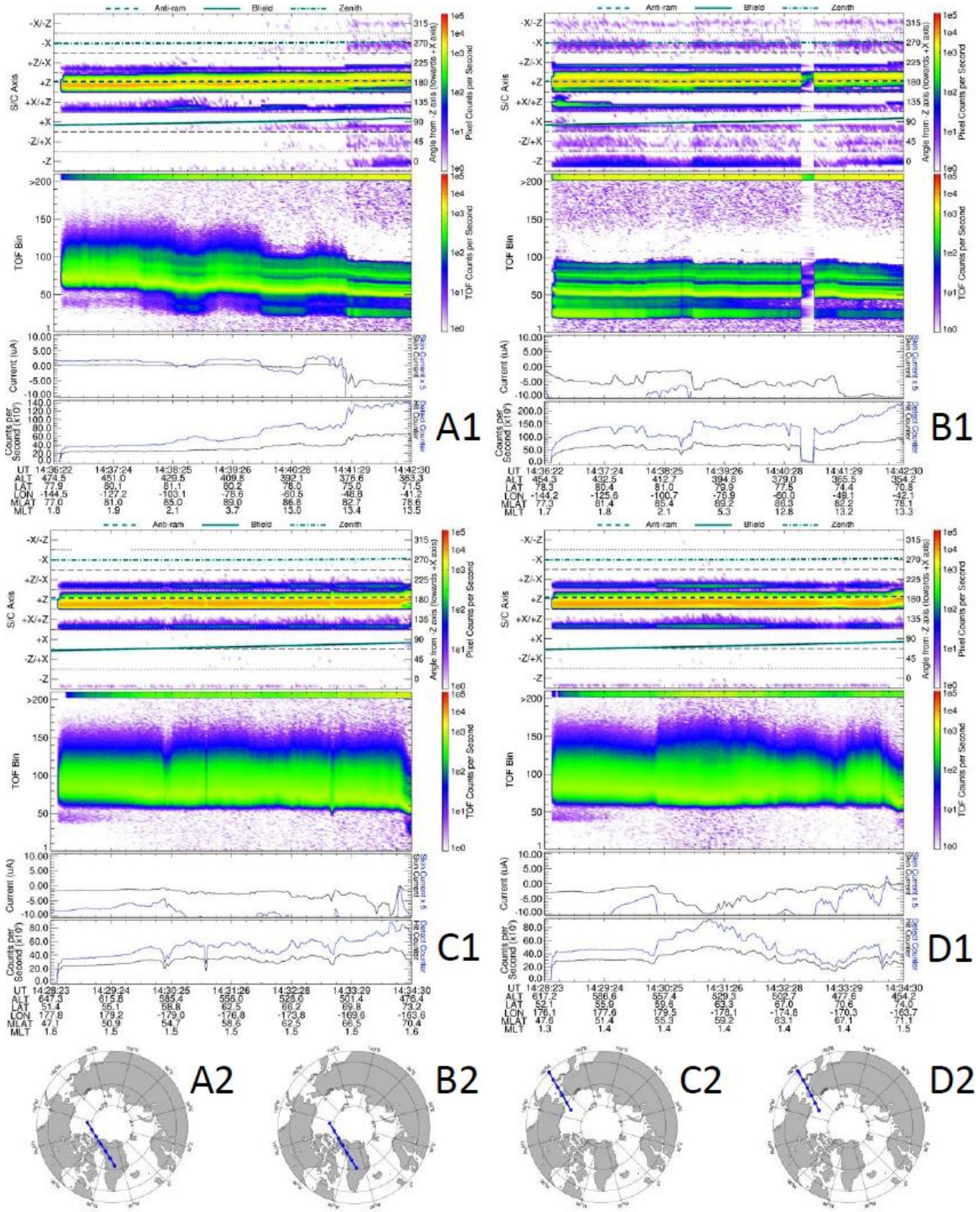

Figure 5.3 Measurements acquired from four different CASSIOPE passes. A2, B2, C2, and D2 are the ground-tracks referring to the measurements of A1, B1, C1, and D1, respectively. A1 was observed on 17 February, B1 was on 18

February, C1 was on 19 February, and D1 was on 20 February 2014 during near-perigee passes. The spacecraft **(S/C) Axis** panels show the EA-t spectrograms of averaged ion count rate in the order of pixel sectors and pixel radii within the pixel sector. Antiram, magnetic field, and zenith directions are depicted by dashed, continuous, and dotted lines, respectively. The **TOF Bin** panel shows the TOF-t spectrogram of the ion count rate. Both at bias voltage of VSA ≈ -176 V. The **Current** panel shows the measured skin current in μA and the **Counts per Second** panel shows the total ion count measured by the detector per second [Yau et al., 2015]. The ground tracks of passes A and B are in Greenland, while C and D are also in the Arctic region at approximately the same latitudes but on the opposite side of the magnetic pole. Unfortunately, other well-collocated passes were not available during this storm event. During all four passes the antiram pixel sector indicated the highest ion count rate, meaning ions were arriving predominantly from the ram direction. Since each of the passes occurred during early afternoon UTC the satellite was flying against the antisunward convection at a relatively low angle each time. The TOF Bin panels on the 19 and 20 show higher values than on the 17 and 18 which indicate the occurrence of heavier (molecular) ion species.

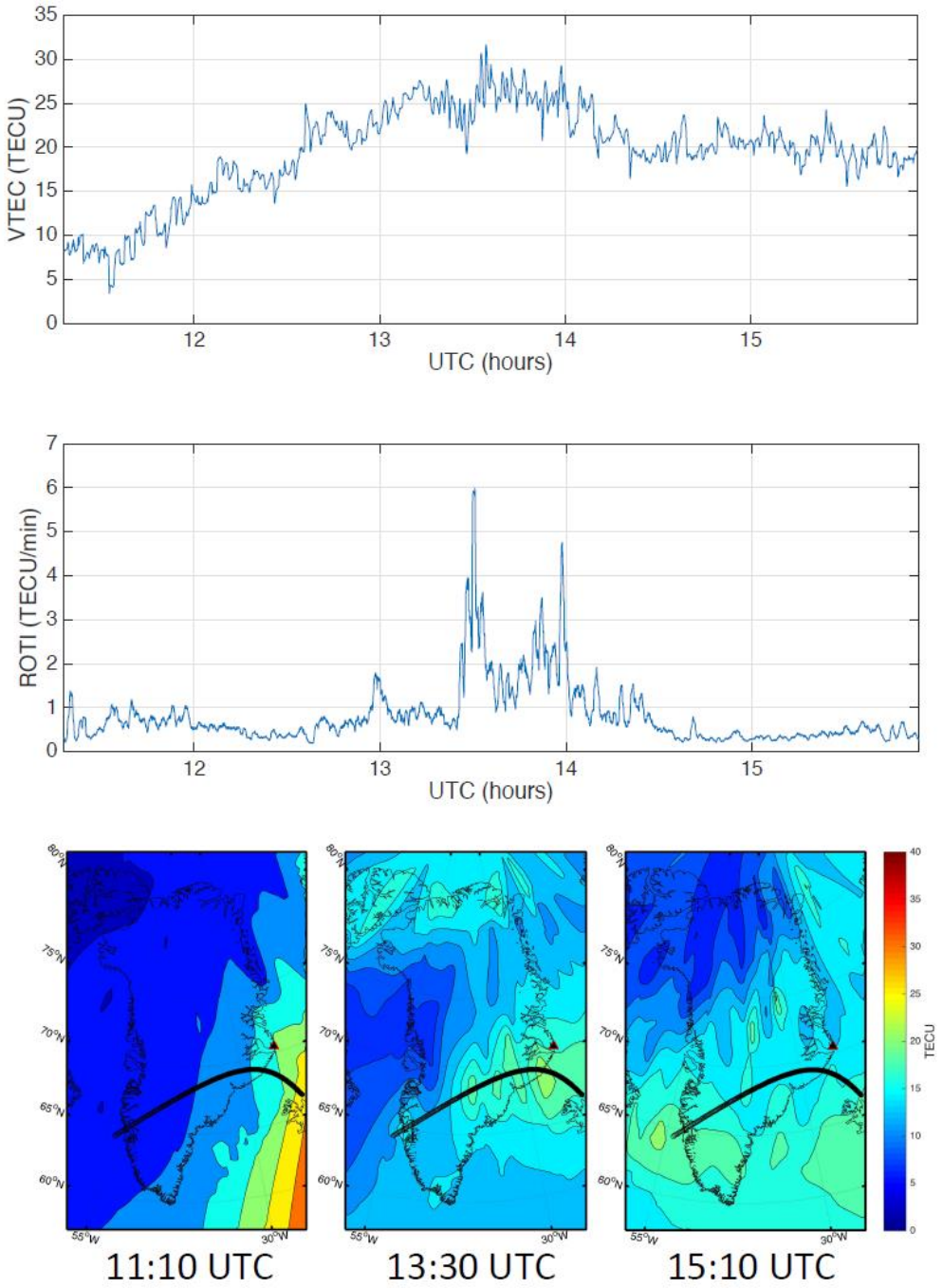

Figure 3.10 (top) PRN 05 (SVN 50) GPS satellite single-arc (the acronyms stand for psuedorandom noise and space vehicle number respectively), bias-free VTEC values on 19 February 2014. Derived from Scoresbysund station data (its location ismarked with black triangle on Figure 3.10 (bottom)). **(middle)** ROTI calculated for the same satellite arc. **(bottom)** Three 2-D TEC maps for the same day as Figures 3.10 (top) and 10 (middle). We used data from all 18 stations (see Figure 3.1) at different UTC times. The thick black line is the IPP arc for this satellite for the time span presented in Figures 3.10 (top) and 3.10 (middle).

3.2.3 Discussion

In this research we combined multiinstrument observations to investigate geophysical processes prevalent during the 19 February 2014 CME-driven geomagnetic storm in the Arctic region. We observed only one relatively small SI associated with the storm. The AE index was rising steadily starting on 18 February in association with the B_z turning southward and the Dst index decreasing until the second part of 19 February. The short recovery phase was interrupted by the arrival of a second CME, approximately 24 h after the first one. The changes in the solar wind parameters before the first CME arrival mostly affected latitudes south of the auroral oval (Figure 3.2). Energy input into the polar cap region was indicated by the sudden increase in PCN index during the early hours on 19 and 20 February. The suggested beginning of the negative storm phase occurred at the same time when the PCN index rose abruptly after 03:00 UTC on 19 February indicating that it occurred in connection with the energy input into the magnetosphere [see also Vennerstrøm et al.,1991]. The fact that this happened during local nighttime makes the pinpointing of the beginning of the negative phase more difficult; to suggest that there is a negative phase, the TEC decrease has to be observed during daytime hours when the ionosphere is well developed. There is a clear difference between the ionospheric behavior over polar cap and auroral stations. Results seen in Figure 3.3 further support this finding; in fact, the magnetic H component has a different direction at Thule than that at the auroral stations of Kangerlussuaq and Nuuk. This implies that the Pedersen currents appear to flow in opposite directions above polar and auroral regions.

Rodger et al. [1992] summarized the most relevant geophysical processes that take part in high-latitude and midlatitude ionospheric structure formation. In our work, we employed a similar approach and proposed a likely geophysical explanation for the observed negative storm phase. According to Prölls et al. [1991] and Rodger et al. [1992] the formations of positive storm effects

are likely caused by traveling atmospheric disturbances, change in the large-scale circulation of the thermospheric wind, penetration electric field, and equatorward shift of the auroral oval (ionization ring). Negative storm effects (e.g., depletions) are caused by agitation of the neutral gas composition and equatorward shift of the high-latitude trough region. From Figure 3.4 (top) we can conclude that the observed ionospheric storm effects take place in the F layer. Based on Figure 3.4 we suggest that at least in the polar cap, the effects of precipitation on electron density are minor.

According to Davies [1990] and Matuura [1972], the auroral heating during such a storm changes the atmospheric circulation that subsequently changes the composition of the neutral atmosphere, resulting in a decrease in the plasma production rate. Since this heating occurs at the bottom side of the F region (it is caused by the Pedersen current at high latitudes; see Brekke [2013]), it will erode this region and consequently will cause depletion while increasing the h_mF_2 height (Figure 3.4). Figure 3.4 (top) also illustrates that the ionization in the polar cap during this storm occurred overwhelmingly in the F_2 region. During times when the F layer was vastly depleted (the ionization was prohibited by some process or processes) the TEC values only fluctuated around 5 to 10 TECU. Therefore, the F_2 layer continuity equation (3.2) can function as a starting point for the physical interpretation [Rodger et al., 1992]:

$$\frac{dN_e}{dt} = q - \beta N_e - N_e \nabla \boldsymbol{V}^{\perp} - \nabla(N_e \boldsymbol{V}^{\parallel}), \tag{3.3}$$

where t is time; q is the production rate; βN_e is the loss rate; and $\boldsymbol{V}^{\perp}$ and $\boldsymbol{V}^{\parallel}$ are the perpendicular and parallel components of the bulk plasma velocity, respectively, with respect to the geomagnetic field. We argue that the loss-rate term on the right-hand side of equation (3.2) was mainly responsible for the negative storm phase, which was caused by N_2 upwelling as a result of a sudden change in the large-scale circulation of the thermospheric wind. These circulation changes cause regional or global atmospheric composition changes, and equatorward shift of the auroral oval, which are well-

known occurrences during geomagnetic storms [Schunk and Nagy, 2009], as shown in Figure 3.9. The long-term (several days long) negative effect following the negative Dst peak occurs when the local horizontal variations of velocity or ionization (this can be approximated by $N_e\nabla\bullet\mathbf{V}^{\perp}$ due to the high-latitude location) cause change in the plasma production processes, loss processes, or plasma transport (equation (3.3)). Additionally, different time histories of regions of plasmas adjacent to each other may also cause decrease in N_e [e.g., Giraud and Petit, 1978]. The present argument is supported by the apparent anomaly in the column-integrated O/N_2 ratio measurements (meaning N_2 upwelling) as seen in Figures 3.5 and 3.6. In response to large energy input at the polar cap region dayside midlatitude, high-density plasma convects into this region at F region altitudes, and currents and electric field potential are increasing, which results in increased electron, ion, and neutral species temperatures due to Joule heating [Schunk and Nagy, 2009], which is demonstrated by Figure 3.9. The aforementioned plasma convection across the polar cap is shown in Figure 3.7, where SuperDARN HF radar network data are compared to high-resolution VTEC data. A continuous, but nonuniform density channel of plasma (tongue of ionization or TOI) is clearly visible, which is spatially collocated with the highest plasma velocities. The TOI eventually breaks down to polar patches as shown in Figures 3.7 and 3.8. In the regions where the plasma is near stationary (Figure 3.7, left) N_e densities decrease as plasma decay is accelerated.

As a consequence of ionospheric heating, N_2 upwelling (also supported by the computational model of Richmond and Matsushita [1975]) is occurring, which increases the loss rate term in equation (3.2). The decreased O/N_2 and heating-induced meridional neutral winds [Richmond and Matsushita, 1975] over Greenland may last for days inhibiting normal photoionization. The three most important heating mechan-isms are Joule heating, ion heating, and auroral heating [Deng et al., 2008]. Heating will result in higher temperatures and thermal expansion, which will increase molecular species upwelling and plasma diffusion. The observation that the h_mF_2 suddenly shifted

to higher altitude (by ~100–150 km), just as the CME-magnetosphere interaction started (Figures 3.2 and 3.4), supports this argument. The time scales of Joule heating are on the order of minutes; thus, they can be responsible for the sudden decrease in TEC after the initial phase. As a consequence of this, the equatorward edge of the Arctic region again becomes part of the plasmasphere, and long-term plasma densities in the plasmasphere will govern it. In order to be able to more precisely characterize and determine the atmospheric and geomagnetic processes responsible for the observed anomalies, additional observations were analyzed. IRM results from measurements during four CASSIOPE passes are shown in Figure 3.9. The TOF bin panels indicate that the satellite encountered more massive species after the storm (C1 and D1) than before (A1 and B1). Molecular ion species, such as NO+, are detected at larger TOF bin values [Yau et al., 2015]. These were only negligible before the storm day. The main ion drift direction was antisunward during each day. Weak ion outflows were detected before the storm and virtually no ion outflow after the storm. The more massive ion presence in the topside ionosphere after the storm indicates possible upwelling.

3.2.4 Conclusions

GNSS-derived TEC and ionosonde N_e observations show negative storm effects for several days following the energy input into the polar magnetosphere by two consecutive CMEs. TEC depletion commencements seem to coincide with PCN enhancements (Figure 3.2).

We found that the energy input was mostly a polar cap phenomenon (based on PCN changes in Figure 3.2),and it did not correlate with Dst and AE indices, which began forming disturbances several hours earlier, and they would potentially indicate auroral or even lower latitude phenomena (Figures 3.2 and 3.3).

During the negative storm phase an atmospheric negative O/N_2 ratio anomaly was observed using GUVI data, which indicated N_2 upwelling and thermospheric wind changes. Ionospheric heating due to the CME's energy input during CME-driven geomagnetic activity can cause these changes in the polar atmosphere (Figures 3.4 and 3.6). Polar cap patch propagation and evolution tend to follow the expected convection patterns during negative B_z periods over the polar cap (Figures 3.7 and 3.8).

Topside sounding of ion densities and velocities using the IRM sensor showed an increase in heavier ion species during the negative storm phase following the commencement of the CME-magnetosphere interaction that seems to support the suggested heat-induced N_2 upwelling mechanism. Results from the particle detector also revealed that the topside ionosphere seems to follow the convection directions that are expected during the course of the interplanetary magnetic field (IMF) *z* component turning southward (Figure 3.9).

Lastly, our investigations of the ROTI scintillations and comparisons with TEC maps revealed that strong scintillations mainly resulted from moving patches in the polar cap while the direct solar ionization does not appear to have had a significant influence (Figure 3.10). A natural way to continue this research is to explore the power law structure of the ROTI and TEC spectra. There are indications from previous studies, e.g., Kersley et al. [1998], that the Fresnel-frequency and the high-frequency (roll-off) slope (or sometimes slopes) of these spectra depend on the irregularity structure and drift speed. In addition to investigating the ROTI and TEC spectra, wavelet analyses could also provide a further approach to continue this research and explore the energies present in the different scale-sizes of plasma irregularities.

CHAPTER 4

Published as: *Prikryl, R. Ghoddousi-Fard, J. M. Weygand, A. Viljanen, M. Connors, D. W. Danskin, P. T. Jayachandran, K. S. Jacobsen, Y. L. Andalsvik, E. G. Thomas, J. M. Ruohoniemi, T. Durgonics, K. Oksavik, Y. Zhang, E. Spanswick, M. Aquino, and V. Sreeja (2016), GPS phase scintillation at high latitudes during the geomagnetic storm of 17–18 March 2015, J. Geophys. Res. Space Physics, 121, 10,448–10,465, doi:10.1002/2016JA023171.*

STUDY 3: GPS PHASE SCINTILALTIONS AT HIGH LATITUDES DURING THE GEOMAGNETIC STORM OF 17–18 MARCH 2015

4.1 Introduction and Relevance of the Paper

The geomagnetic storm of 17–18 March 2015 was caused by the impacts of a coronal mass ejection and a high-speed plasma stream from a coronal hole. The high-latitude ionosphere dynamics is studied using arrays of ground-based instruments including GPS receivers, HF radars, ionosondes, riometers, and magnetometers. The phase scintillation index is computed for signals sampled at a rate of up to 100 Hz by specialized GPS scintillation receivers supplemented by the phase scintillation proxy index obtained from geodetic-quality GPS data sampled at 1 Hz. In the context of solar wind coupling to the magnetosphere-ionosphere system, it is shown that GPS phase scintillation is primarily enhanced in the cusp, the tongue of ionization that is broken into patches drawn into the polar cap from the dayside storm-enhanced plasma density, and in the auroral oval. In this paper we examine the relation between the scintillation and auroral electrojet currents observed by arrays of ground-based magnetometers as well as energetic particle precipitation

observed by the DMSP satellites. Equivalent ionospheric currents are obtained from ground magnetometer data using the spherical elementary currents systems technique that has been applied over the ground magnetometer networks in North America and North Europe. The GPS phase scintillation is mapped to the poleward side of strong westward electrojet and to the edge of the eastward electrojet region. Also, the scintillation was generally collocated with fluxes of energetic electron precipitation observed by DMSP satellites with the exception of a period of pulsating aurora when only very weak currents were observed.

4.2 GPS phase scintillation at high latitudes during the geomagnetic storm of 17–18 March 2015

Ionospheric irregularities cause rapid fluctuations of radio wave amplitude and phase called scintillation that can degrade GPS positional accuracy and affect the performance of radio communication and navigation systems [Skone and de Jong, 2000; Aquino et al., 2007; Kintner et al., 2007; Jacobsen and Dähnn, 2014; Jacobsen and Andalsvik, 2016]. The total electron content (TEC) as observed by GPS becomes particularly disturbed during geomagnetic storms caused by the impacts of interplanetary coronal mass ejections (ICMEs) compounded by high-speed plasma streams from coronal holes. In the context of solar wind coupling to the magnetosphere-ionosphere system, it has been shown that GPS phase scintillation is primarily enhanced in the cusp, where a tongue of ionization (TOI) is broken into patches and is drawn into the polar cap from the dayside storm-enhanced plasma density (SED) [Aarons, 1997; Aarons et al., 2000; Basu et al., 1987, 1995, 1998; Spogli et al., 2009; Li et al., 2010; Prikryl et al., 2011a, 2011b, 2014, 2015a, 2015b; Moen et al., 2013; Sreeja and Aquino, 2014; van der Meeren et al., 2014; Jin et al., 2015; Oksavik et al., 2015]. In the auroral oval, GPS scintillation has been observed during energetic particle

precipitation events, substorms, and pseudo-breakups [Skone et al., 2008; Kinrade et al., 2013; Prikryl et al., 2013a, 2013b] and correlated with ground magnetic field perturbations [Skone and Cannon, 1999; Prikryl et al., 2011a; Ghoddousi-Fard et al., 2015]. The present paper focuses on the GPS phase scintillation in relation to the auroral electrojets as observed in the North American and North European sectors during this geomagnetic storm.

4.2.1 Instruments and Techniques

In the Canadian Arctic, the GPS phase and amplitude scintillation is monitored by the Canadian High Arctic Ionospheric Network (CHAIN) consisting of GPS Ionospheric Scintillation and TEC Monitors (GISTMs) that are configured to record the power and phase of the L1 signal at a 50 Hz sampling rate. The original CHAIN [Jayachandran et al., 2009] consisted of NovAtel GSV4004B receivers that are capable of tracking up to 10 GPS signals at the L1 frequency (1575.42 MHz) and the L2 frequency (1227.6 MHz). Starting in 2014, CHAIN has been expanded by adding new stations equipped with Septentrio PolaRxS multi-GNSS (Global Navigation Satellite Systems) receivers capable of tracking up to 30 satellites including GPS, GLONASS, and Galileo.

In the European sector, the Norwegian Mapping Authority (NMA) operates 10 GISTMs and a dense nationwide network of about 185 1 Hz geodetic receivers. In the Svalbard region, the Birkeland Centre for Space Science operates four NovAtel GPStation-6 multi-GNSS receivers at Ny-Ålesund, Longyearbyen, Hopen, and Bjørnøya [Oksavik et al., 2015; van der Meeren et al., 2015]. The receivers track signals from GPS (L1/L2/L2C/L5), GLONASS (L1/L2), and Galileo (E1/E5a/E5b/Alt-BOC). Scintillation indices σ_ϕ and S_4, based on standard deviation of phase and amplitude over 60 s intervals, are output from the receiver. Only GPS/L1/L2 signals are used in the present paper. The receivers also provide the TEC and rate of TEC Index (ROTI) (not used in this

study). Raw data of the amplitude and phase are available at a 50 Hz resolution. Additional GSV4004B and Septentrio PolaRxS receivers are operated in Norway, Cyprus and in the UK by the Nottingham Geospatial Institute (NGI) of the University of Nottingham.

At the Canadian Geodetic Survey of Natural Resources Canada about 150 globally distributed 1 Hz GPS stations (mostly those of the RT-IGS network with additional stations over Canadian region) are used in near real time to derive, among other statistics and products [Ghoddousi-Fard et al., 2011; Ghoddousi-Fard and Lahaye, 2016], L1-L2 interfrequency phase rate variations by means of mapped-to-zenith standard deviation of delta phase rate (sDPR) over 30 s. For further details we refer the reader to Ghoddousi-Fard et al. [2013]. The Technical University of Denmark, National Space Institute (DTU Space) contributed high-rate GPS receivers of the Greenland GPS Network (GNET). GNET consists of 62 GPS stations (11 of these samples at 1 Hz) that are distributed around the Greenland inland ice. GPS receivers sampling at a 1 Hz rate complement the GISTMs by providing the sDPR proxy scintillation index.

The Super Dual Auroral Radar Network (SuperDARN) [Greenwald et al., 1995; Chisham et al., 2007] is used to map ionospheric convection in the Northern Hemisphere. The TEC data downloaded from Madrigal, an upper atmospheric science database at Haystack Observatory (*http://madrigal.haystack.mit.edu/madrigal/*), are used to make GPS TEC maps [Thomas et al., 2013] that are also available online (*http://vt.superdarn.org*).

Equivalent ionospheric currents (EICs) are obtained from ground magnetometer data using the spherical elementary currents systems (SECS) technique developed by Amm and Viljanen [1999] that has been applied over the entire North American ground magnetometer network by Weygand et al. [2011]. The SECS technique defines elementary divergence-free and curl-free current systems. The divergence-free system with currents that flow entirely within the ionosphere causes a magnetic

field on the ground. The curl-free system whose divergences represent the currents normal to the ionosphere produces no field below the ionosphere [Laundal et al., 2015]. For this study the SEC method calculates the divergence-free currents and from those the spherical elementary current amplitudes are obtained. The SECS method also makes it possible to roughly estimate field-aligned currents under the assumption of no conductance gradients perpendicular to the ionospheric electric field [Weygand and Wing, 2016]. While the EICs/SECS maps were inferred at the minimum resolution of the magnetometer database (10 s), in this paper we use data decimated to 60 s.

Figure 4.1 shows the various GNSS receivers as well as the arrays of magnetometers including those operated by the Natural Resources Canada, the Canadian Array for Real-time Investigations of Magnetic Activity (CARISMA) [Mann et al., 2008] of the Canadian GeoSpace Monitoring (CGSM) program [Liu, 2005], the Geophysical Institute Magnetometer Array (GIMA) (*www.asf.alaska.edu/magnetometer/*), the Greenland array operated by Technical University of Denmark (*www.space.dtu.dk*), and IMAGE (*http://space.fmi.fi/image/*).

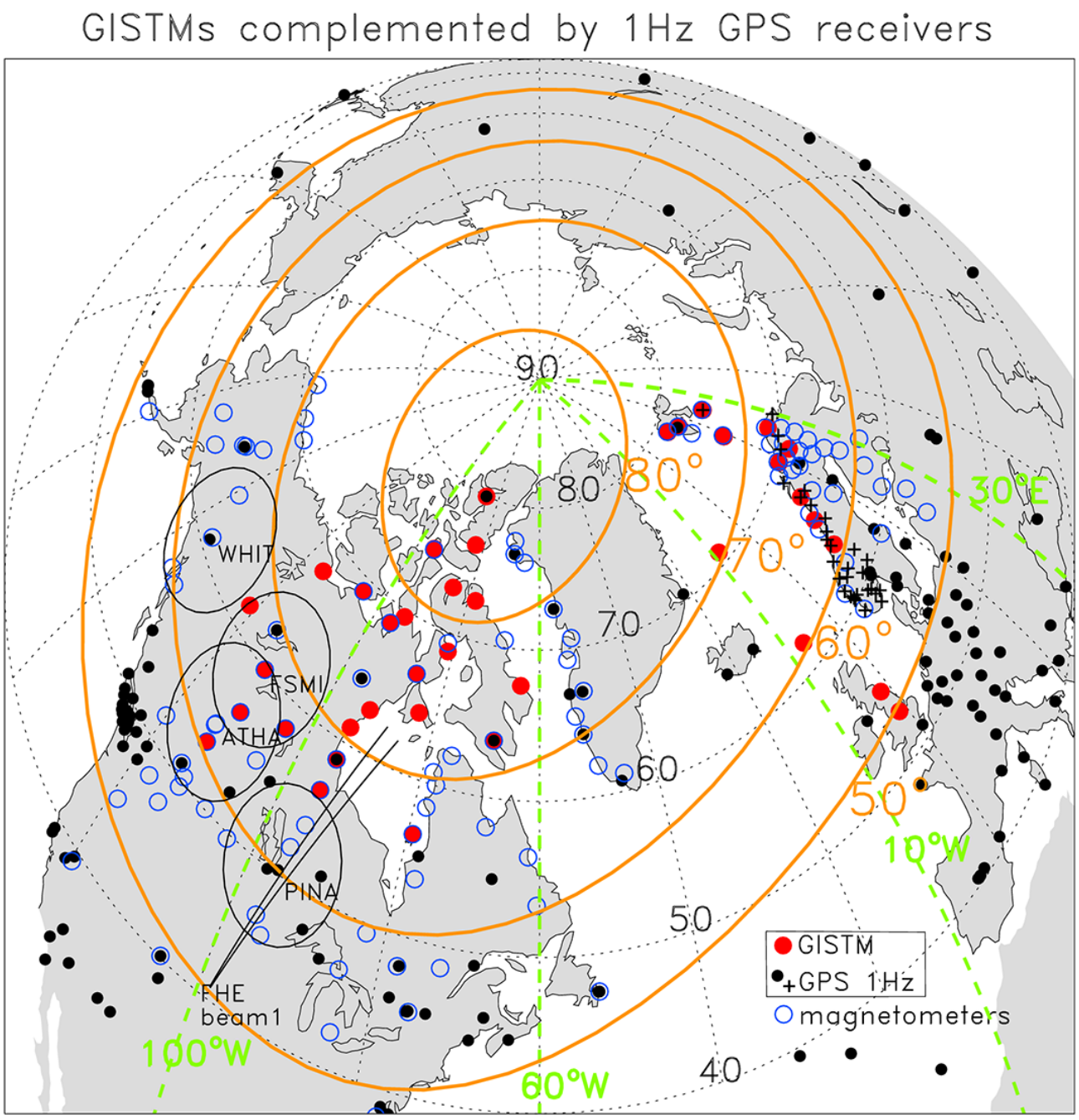

Figure 4.1 The Canadian High Arctic Ionospheric Network (CHAIN) complemented by GISTMs in the North European sector and GPS receivers recording at a sampling rate of 1 Hz. Red dots show locations of specialized scintillation receivers (GISTMs). Black dots show locations of 1 Hz GPS receivers, mainly from IGS and GNET. Black crosses show a fraction of 1 Hz receivers that are a part of the NMA network. Ground magnetometers used to obtain EICs are shown as blue open circles. The AACGM latitudes 50°, 60°, 70°, and 80°, in yellow, are superposed over the geographic grid. The dashed green lines delineate two 40° wide longitude sectors discussed in the text. Field of views of four THEMIS ASIs and beam 1 of the SuperDARN Fort Hays East radar are shown.

The Defense Meteorological Satellite Program (DMSP) satellites provided particle data to support the scintillation study. The DMSP particle detectors were designed by the Dave Hardy of Air Force Research Laboratory, and data are obtained from the Johns Hopkins University Applied Research Laboratory (http://sd-www.jhuapl.edu/Aurora/). Data from a special sensor ultraviolet scanning imager (SSUSI) onboard the DMSP F16 and F17 satellites (*http://sd-www.jhuapl.edu/Aurora/*) were used to produce partial images of the auroral oval [Paxton et al., 2002; Zhang and Paxton, 2008].

The ground-based all-sky imager (ASI) stations support the NASA Time History of Events and Macroscale Interactions during Substorms (THEMIS) project [Mende et al., 2008]. Figure 4.1 shows field of views of four ASIs.

4.2.2 Solar Wind and Geomagnetic Conditions

An interplanetary coronal mass ejection (ICME) ahead of a high-speed plasma stream from a coronal hole led to a geo-effective configuration in the solar wind [Kataoka et al., 2015] that resulted in a severe geomagnetic storm on 17–18 March 2015. In agreement with the conclusions by Kamide and Kusano [2015], Kataoka et al. [2015] pointed out that the storm involved a two-step development, the first driven by the southward IMF in the compressed sheath region, and the second driven by the southward IMF in the magnetic cloud. During this day the Kp index reached a value of 8 and the auroral electrojet (AE) index exceeded 2000 nT. Figures 4.2a–4.2f show, from top to bottom, 1 min averages of the solar wind velocity, Vsw, the IMF components B_y and B_z, total magnitude, B, proton density, np, and temperature, Tp, from the OMNI data set projected to the subsolar bow shock. The upstream interplanetary (IP) shock is indicated by the vertical dotted line at 04:45 UT. The IMF B_z initially turned strongly northward (corresponding to positive excursion in

SYM-H, signaling initial phase of the storm) and then sharply southward, remaining mostly southward for the rest of the day as the storm intensified. Figure 4.2g shows the hourly occurrence of phase scintillation ($\sigma_\phi > 0.1$ rad) observed by CHAIN, while Figure 4.2h shows provisional geomagnetic indices. The AE index peaked at 2298 nT at 13:58 UT and SYM-H dipped to −234 nT at 22:47 UT.

4.2.3 Ionospheric Irregularities at High Latitudes

The ROTI measured by more than 2500 GNSS receivers [Cherniak et al., 2015] revealed considerable dynamics of ionospheric irregularities on a global scale. Significant increases in the intensity of irregularities in the polar cap of both hemispheres were associated with the formation and evolution of SED/TOI and polar patches. In the Northern Hemisphere, a band of intense auroral ionospheric irregularities that expanded equatorward beyond ~45°N of geographic latitude was associated with processes related to enhanced auroral particle precipitation [Cherniak et al., 2015]. Jacobsen and Andalsvik [2016] studied the irregularities in the TEC in relation to the auroral electrojet currents during the geomagnetic storm of 17–18 March 2015. They showed that the most intense disturbances of GNSS signals characterized by ROTI occurred on the poleward side of poleward moving current regions over North Europe.

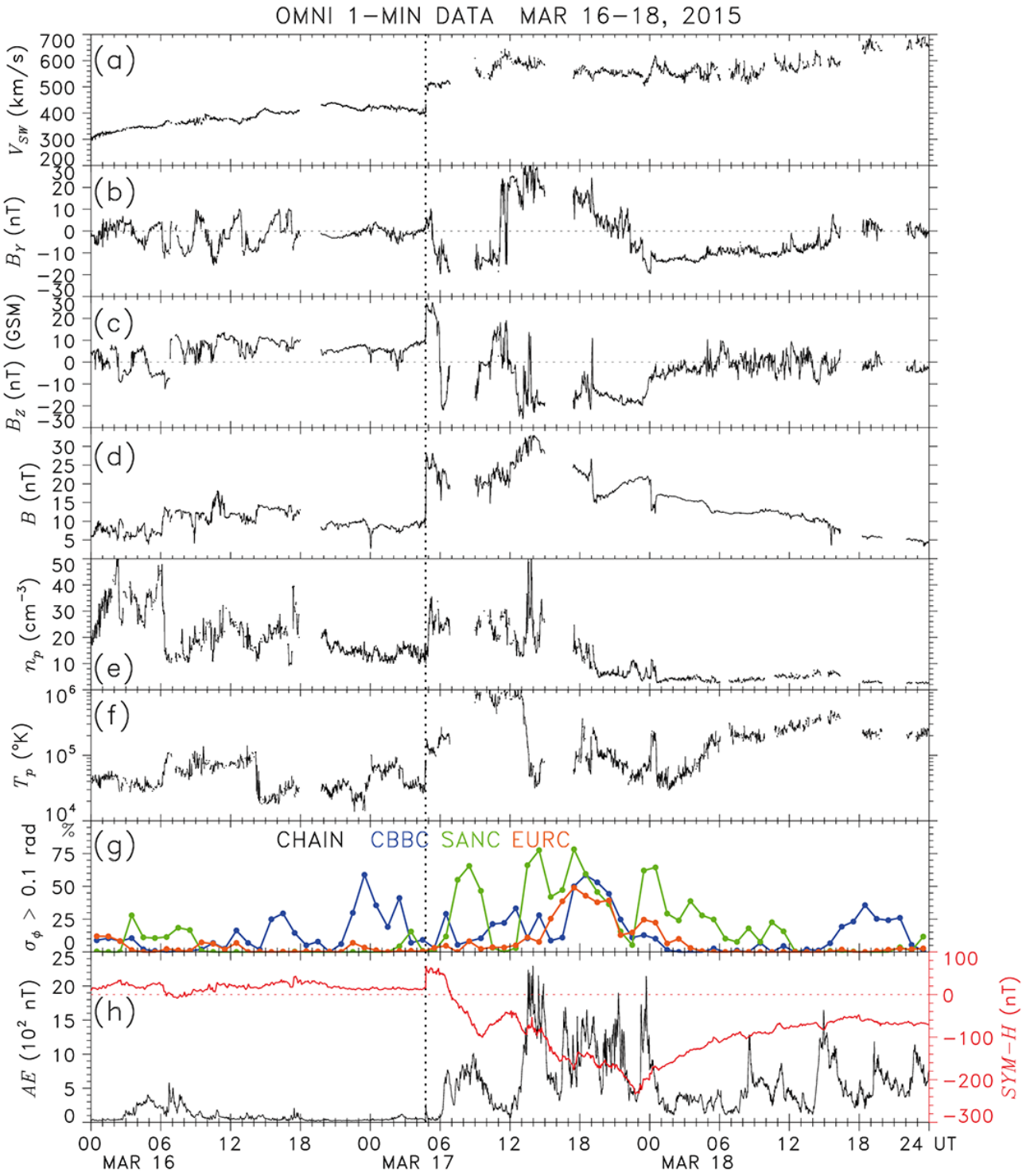

Figure 4.2 (a–f) The solar wind data from the 5 min OMNI data set from 16 to 18 March 2015. **(g)** The hourly occurrence of phase scintillation ($\sigma_\phi > 0.1$ rad) observed by CHAIN in Cambridge Bay (CBBC), Eureka (EURC) and Sanikiluaq (SANC), and **(h)** provisional geomagnetic indices AE and SYM-H are also shown. An interplanetary shock is shown by vertical dotted line.

The hourly occurrences of phase scintillation with $\sigma_\phi > 0.1$ radians that are shown in Figure 4.2g for CHAIN stations at Eureka (EURC), Cambridge Bay (CBBC), and Sanikiluaq (SANC) approximately represent the central polar cap, cusp, and auroral zone, respectively. Scintillation is often observed in CBBC even during geomagnetically less disturbed conditions, either in the cusp or in a contracted auroral oval. The onset of GPS phase scintillation in the expanded auroral oval followed the southward turning of the IMF about 2 h after the IP shock (shown in dotted vertical line) that was associated with a strong northward IMF. Several hours later, after 12:00 UT, under the influence of the magnetic cloud that was characterized by a decrease in proton temperature (Figure 4.2f) and strong southward IMF, the GPS scintillation occurrence increased in the auroral zone, cusp, and the central polar cap.

Figures 4.3a and 4.3b show the occurrence of phase scintillation above comparable thresholds [Prikryl et al., 2013a] of $\sigma_\phi > 0.1$ rad or sDPR > 2 mm/s as a function of the Altitude Adjusted Corrected Geomagnetic (AACGM) latitude and magnetic local time (MLT) before and during the geomagnetic storm, respectively. Assuming an ionospheric pierce point (IPP) height of 350 km, the scintillation occurrence is defined as $100 \times N(\sigma_\phi > 0.1) / N_{tot}$, where N is the number of cases when phase scintillation index exceeded a given threshold and *Ntot* is the total number of data points with IPPs in the bin of 0.25 h MLT × 1° AACGM latitude. Boundaries of the Feldstein statistical auroral oval [Holzworth and Meng, 1975] for quiet and disturbed conditions are shown in Figures 4.3a and 4.3b, respectively. In Figure 4.3a, the data for all available GISTMs combined with 1 Hz GPS receivers from 04:00 UT on 16 March to 03:59 UT on 17 March are used to show 24 h in MLT before the storm, when the IMF was pointing northward. As a result, scintillation was confined within the polar cap and small auroral oval. In Figure 4.3b, the scintillation data from 04:00 UT on 17 March to 03:59 UT on 18 March are used to show 24 h in MLT. During the storm, scintillation occurrence was strongly enhanced on the dayside in the cusp and SED region, a source of TOI

plasma fragmented into patches that were drawn into the polar cap. The IMF B_y was initially dawnward (negative) for several hours before it switched to duskward at ~11:00 UT. As a result, TOI entry was initially through the cusp in the prenoon sector, from where a duskward and antisunward convection pulled a fragmented TOI into the polar cap.

Figure 4.4a shows SuperDARN convection and potential maps at 09:10 UT on 17 March during southward and dawnward IMF. After a period of a strong southward IMF the convection zone expanded significantly. The Heppner-Maynard (H-M) boundary [Imber et al., 2013] moved to 50° of the AACGM latitude. The convection intensified with a potential difference across the polar cap of $\Phi_{PC} = 79$ kV. The IPPs at 350 km (black dots) with $\sigma_\phi > 0.1$ rad and sDPR > 2 mm/s mapped to the cusp and the dawn convection cell, particularly in the midnight and postmidnight sector. At this time there was very sparse GPS data coverage of the dusk cell except around the noon near the cusp. To avoid crowding of IPPs over Scandinavia, only 33 NMA 1 Hz GPS receivers evenly covering Norway (Figure 4.1) are used in Figures 6.4 and 6.6. However, the whole data set for 185 NMA stations is used in Figures 4.3 and 4.12.

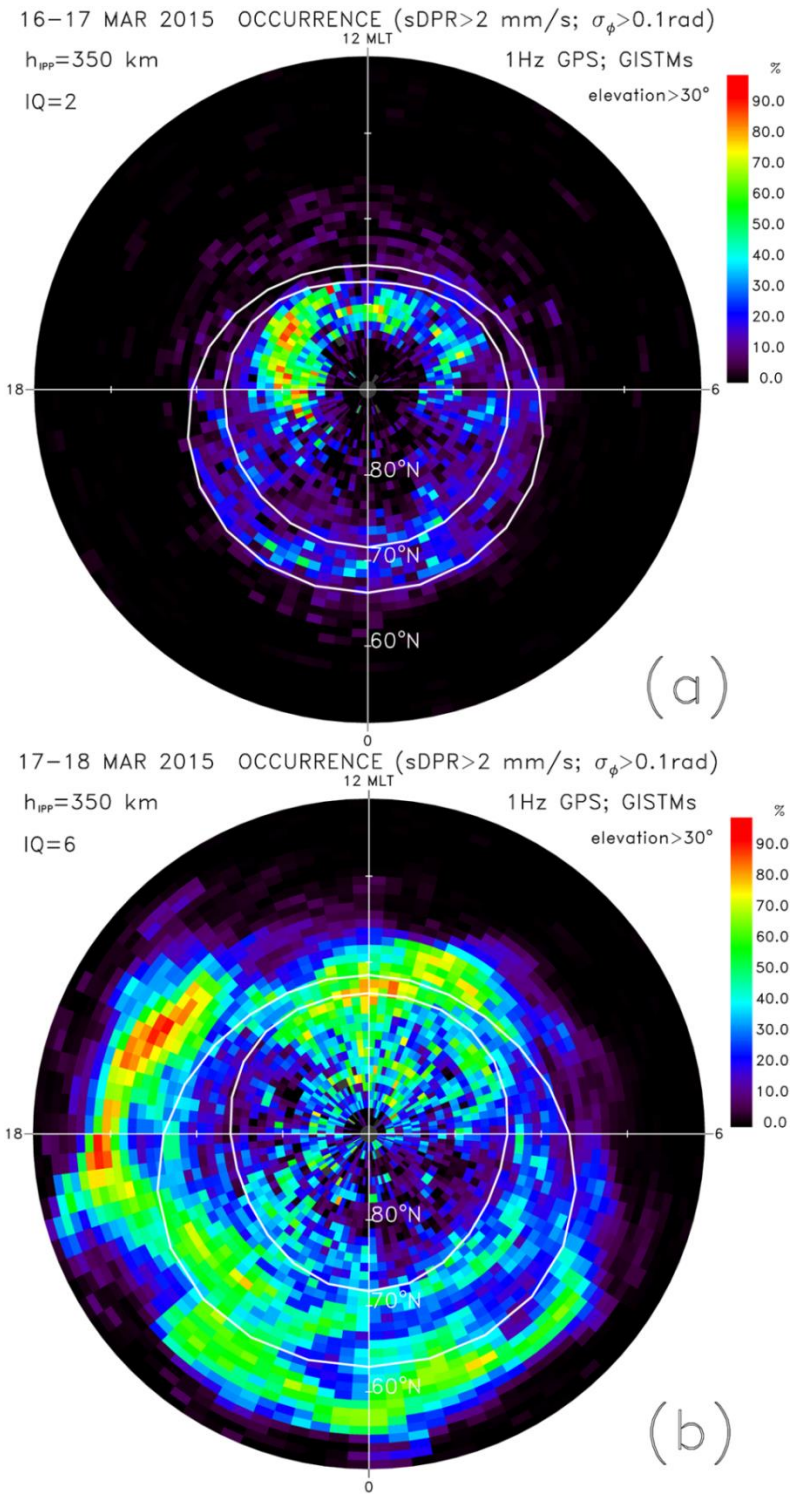

Figure 4.3 The phase scintillation occurrence of $\sigma_\phi > 0.1$ rad or sDPR > 2 mm/s for CHAIN combined with 1 Hz GPS receivers for data from **(a)** 04:00 UT on 16 March to 03:59 UT on 17 March and **(b)** 04:00 UT on 17 March to 03:59 UT on 18 March 2015. The scintillation occurrence is mapped in coordinates of AACGM latitude and MLT. Boundaries of the statistical auroral oval are shown.

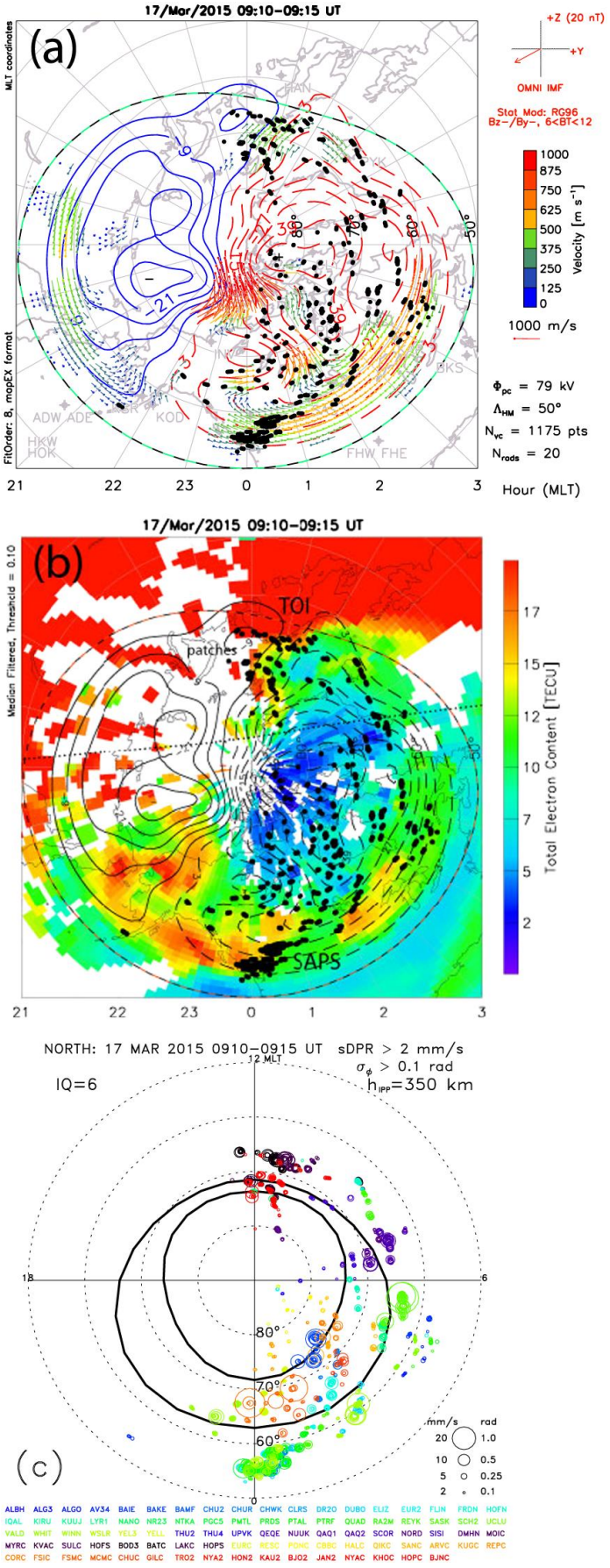

Figure 4.4 (a) SuperDARN convection and potential maps showing expanded convection zone and **(b)** the 5 min median-filtered TEC mapped in coordinates of AACGM latitude and MLT at 09:10 UT on 17 March. In Figures 4a and 4b IPPs with $\sigma_\phi > 0.1$ rad or sDPR > 2 mm/s are superposed (black dots). **(c)** The same IPPs are shown as circles that are sized proportionally to σ_ϕ and sDPR values. Individual stations and their code names are distinguished by color. The IPPs for the IGS 1 Hz GPS receivers are shown in blue, cyan, and green, followed by GNET in dark blue and purple, and the NMA 1 Hz receiver array in black. CHAIN is shown in yellow and orange, and the European GISTMs in red.

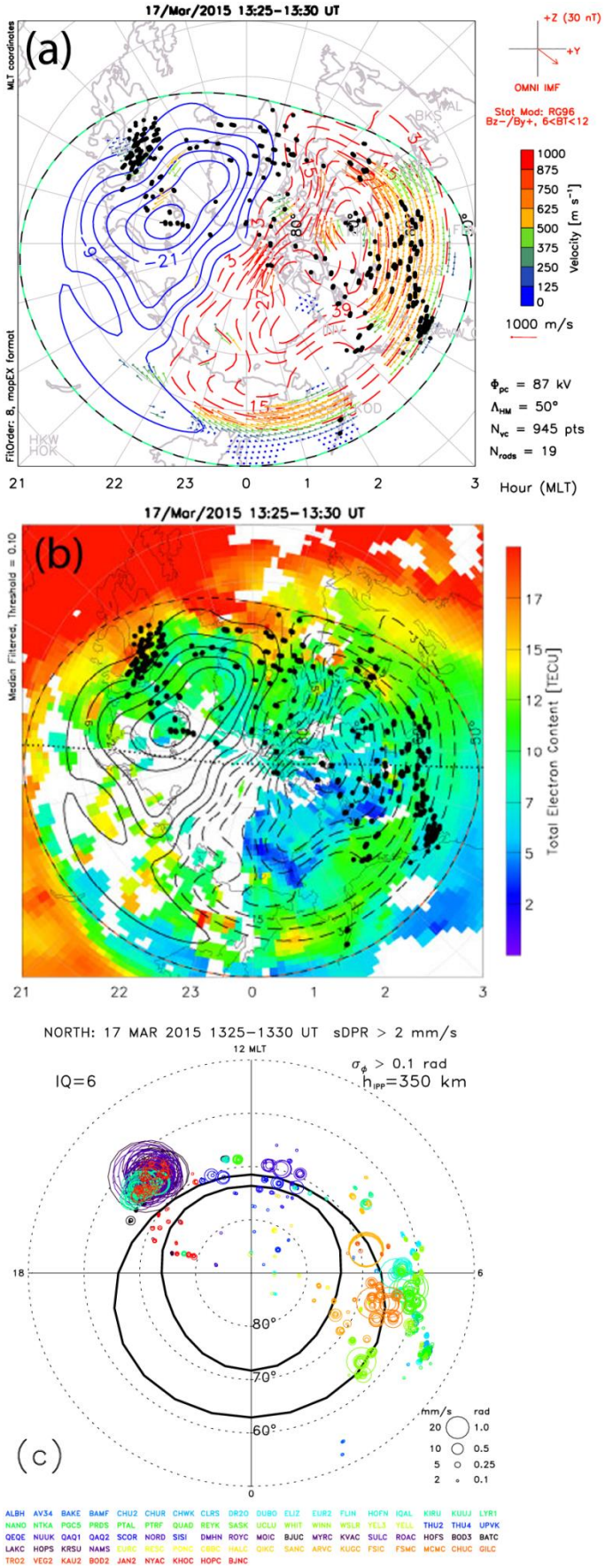

Figure 4.5 (a) SuperDARN convection and potential maps showing an expanded convection zone and **(b)** the 5 min median-filtered TEC mapped in coordinates of AACGM latitude and MLT at 13:25 UT on 17 March. In Figures 6.5a and 6.5b IPPs with $\sigma_\phi > 0.1$ rad or sDPR > 2 mm/s are superposed (black dots). **(c)** The same IPPs are shown as circles that are sized proportionally to σΦ and sDPR values.

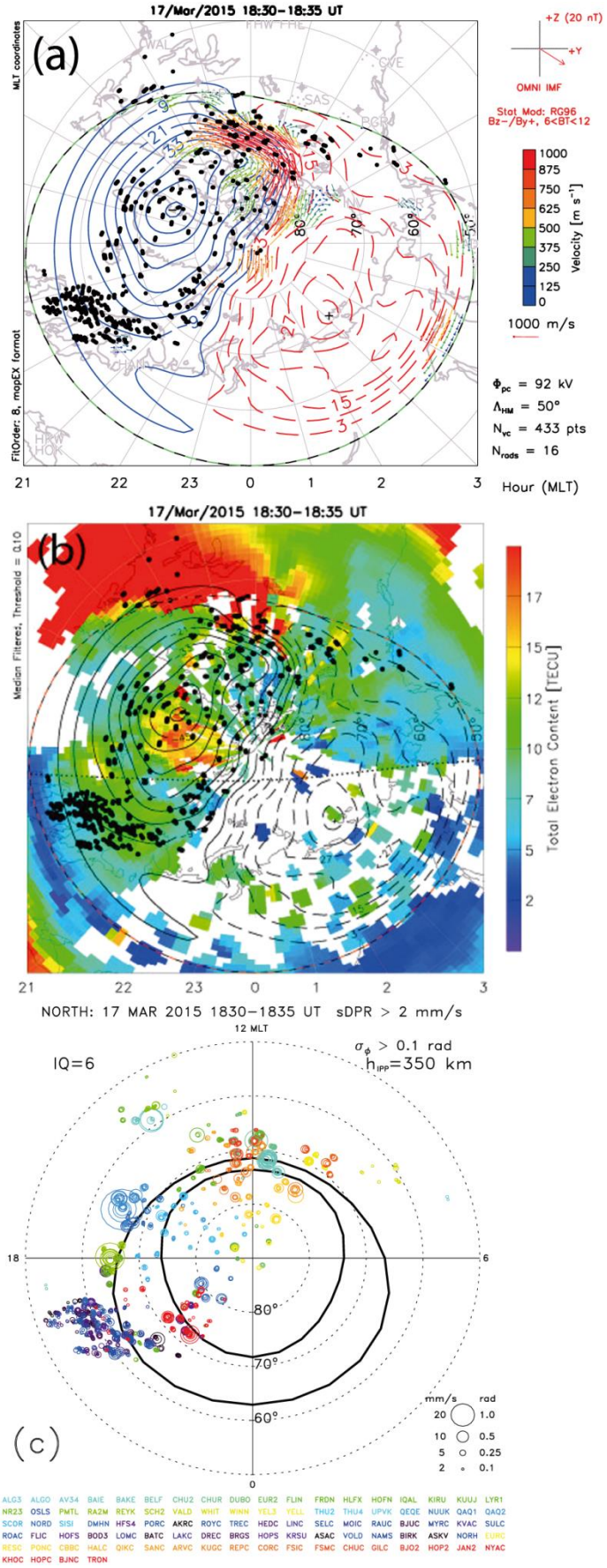

Figure 4.6 The same as Figure 6.4 but at 18:00 UT on 17 March.

Figure 4.4b shows 5 min median-filtered TEC maps overlaid with the electrostatic potential contours and IPPs for cases of phase scintillation $\sigma_\phi > 0.1$ rad and sDPR > 2 mm/s. The dotted line shows the solar terminator at an F region height. The map shows enhanced TEC in the nightside auroral oval poleward of a depleted TEC in the main trough centered at about 50° AACGM latitude. The IPPs with the highest level of scintillation are located just poleward of the enhanced TEC and the return convection in the postmidnight sector. Figure 4.4c shows the IPPs by scaled circles to indicate scintillation intensity. We refer to threshold values shown in the legend to approximately define weak ($\sigma_\phi < 0.25$ rad; sDPR < 5 mm/s), moderate ($0.25 < \sigma_\phi < 0.5$ rad; 5 < sDPR < 10 mm/s), and strong ($\sigma_\phi > 0.5$ rad; sDPR > 10 mm/s) scintillation. At the lowest latitude near the main trough around midnight, a dense cloud of IPPs is collocated with a subauroral polarization stream (SAPS) [Prikryl et al., 2015c]. At this time, only a weak to moderate scintillation is observed on the dayside where it is collocated with a fragmented TOI drawn through the cusp from high TEC in the SED region in the prenoon sector. Also, weak to moderate scintillation is observed in the nightside of polar cap.

After the IMF B_y reversed polarity to duskward (positive) the cusp shifted to the postnoon sector (Figure 4.5). At this time, then TOI was drawn from high TEC in the postnoon SED region (Figure 4.5b). Moderate scintillation was collocated with the TOI but quite strong scintillation was observed at the poleward edge of the SED at ~15:00 MLT (Figure 4.5c). In the central polar cap, only weak scintillation was observed. In the auroral zone, strong scintillation was collocated with intense return convection in the dawn convection cell.

At 18:30 UT on 17 March (Figure 4.6), duskward and antisunward convection on the dayside intensified drawing copious patches into the polar cap. Moderate to strong scintillation was observed at the poleward edge of the SED region, in the cusp and collocated with TOI fragmented into patches. Further poleward in the polar cap, the scintillation level was reduced, although it was

enhanced in the nightside polar cap, where antisunward convection is expected to carry polar cap patches toward the nightside auroral oval. In the dusk auroral zone, scintillation was strong but no convection was observed due to a lack of radar backscatter from F region irregularities. Finally, weak scintillation extended to subauroral latitudes down to 50° AACGM latitude near the poleward edge of the main trough at 19-20 MLT.

4.2.4 GPS Phase Scintillation in Relation to Auroral Currents

In this section we apply the SECS technique to obtain horizontal equivalent currents and the vertical current amplitudes from an array of ground magnetometers seeking a comparison with GPS phase scintillation occurrence in relation with EICs. For the inversion technique we use ground magnetometer data from 77 stations in the North American sector (11 stations in western Greenland). Following Weygand et al. [2011], for each of these stations the quiet-time background from March 2015 is subtracted from the measured field to give the disturbance component which determines the EICs. To calculate the quiet-time background, intervals of relatively smooth magnetometer data (varying in length from an hour to a whole day) are selected with an automated routine from the B_x and B_y components for nearly every day over a 3 month period. These intervals are then averaged together and smoothed to create one 24 h quiet-time background interval. Typically, the quiet-time backgrounds are as smooth as, or smoother than, the average of the five quietest days per month. See Weygand et al. [2011] for more details on the derivation of the quiet-time background.

Figure 4.7a shows a horizontal EIC mapped at 09:10 UT to be compared with Figure 4.4. At this time, strong westward electrojet currents are seen across the continent between about 50 and 60° geographic latitude from southern Greenland to Alaska. At high latitudes poleward of ~65°

geographic latitude, eastward EICs appear to dominate. However, the magnetometer coverage is poor around 120°W poleward of ~65°N as well as on the east coast around 60°W from Labrador to Baffin Island to place much weight on the inversion results there. The westward electrojet pattern compares reasonably well with the dawn convection cell shown in AACGM coordinates (Figure 4.4a). The westward electrojet approximately traces a dividing line between regions of up and down Jz currents shown in Figure 4.7b. As shown by Weygand and Wing, [2016] these up and down SECS currents indicate the regions 1 and 2 currents, respectively. The boundary between the regions 1 and 2 currents helps to identify the approximate location of the particle precipitation region [Weygand and Wing, 2016; and references therein].

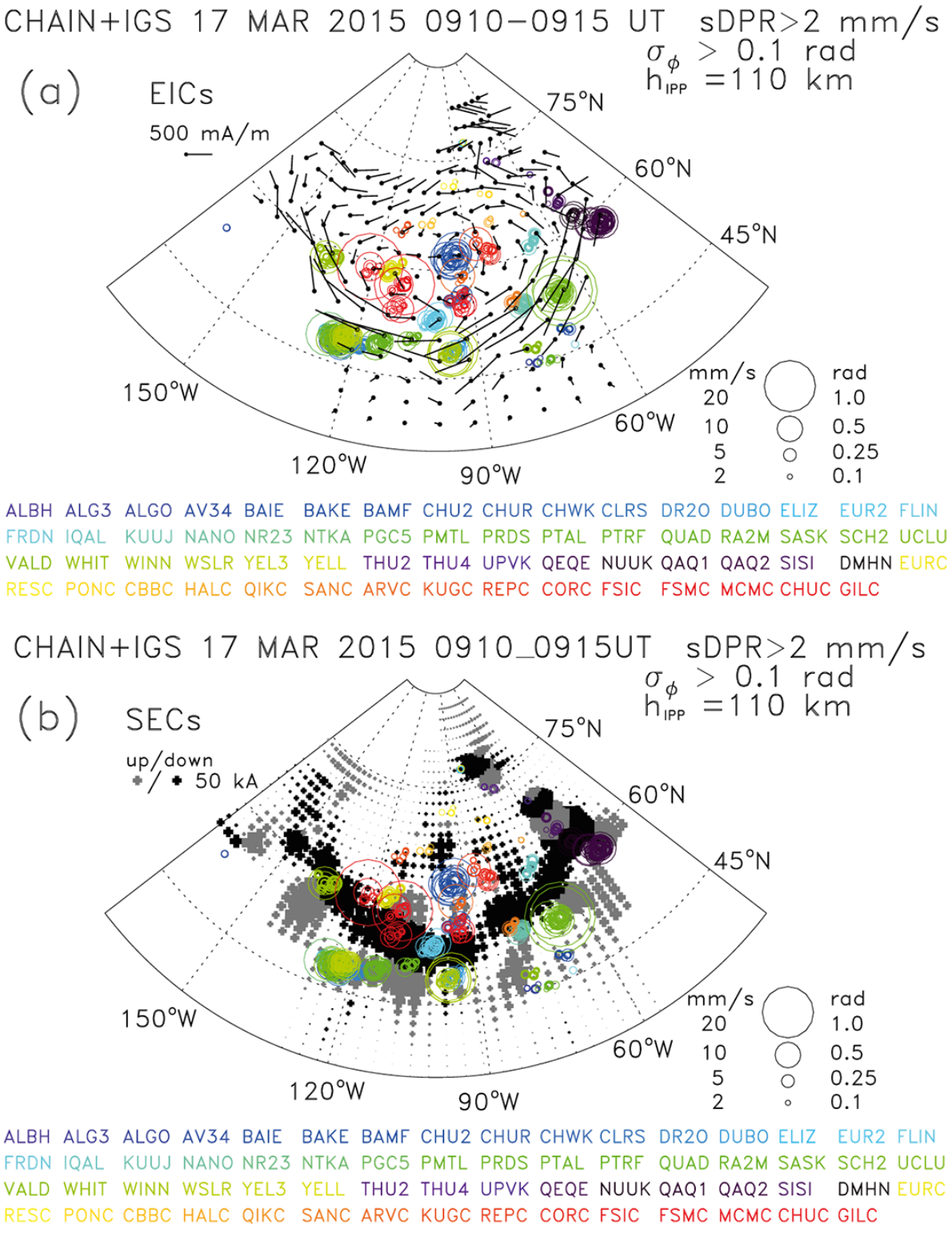

Figure 4.7 (a) Horizontal equivalent ionospheric currents (EICs) and **(b)** vertical current amplitudes (SECS) observed over North America on 17 March 2015 at 09:10 UT. Ionospheric pierce points where $\sigma_\phi > 0.1$ rad or sDPR > 2 mm/s are superposed as circles color coded by stations and sized proportionally to $_{\sigma\phi}$ and sDPR values.

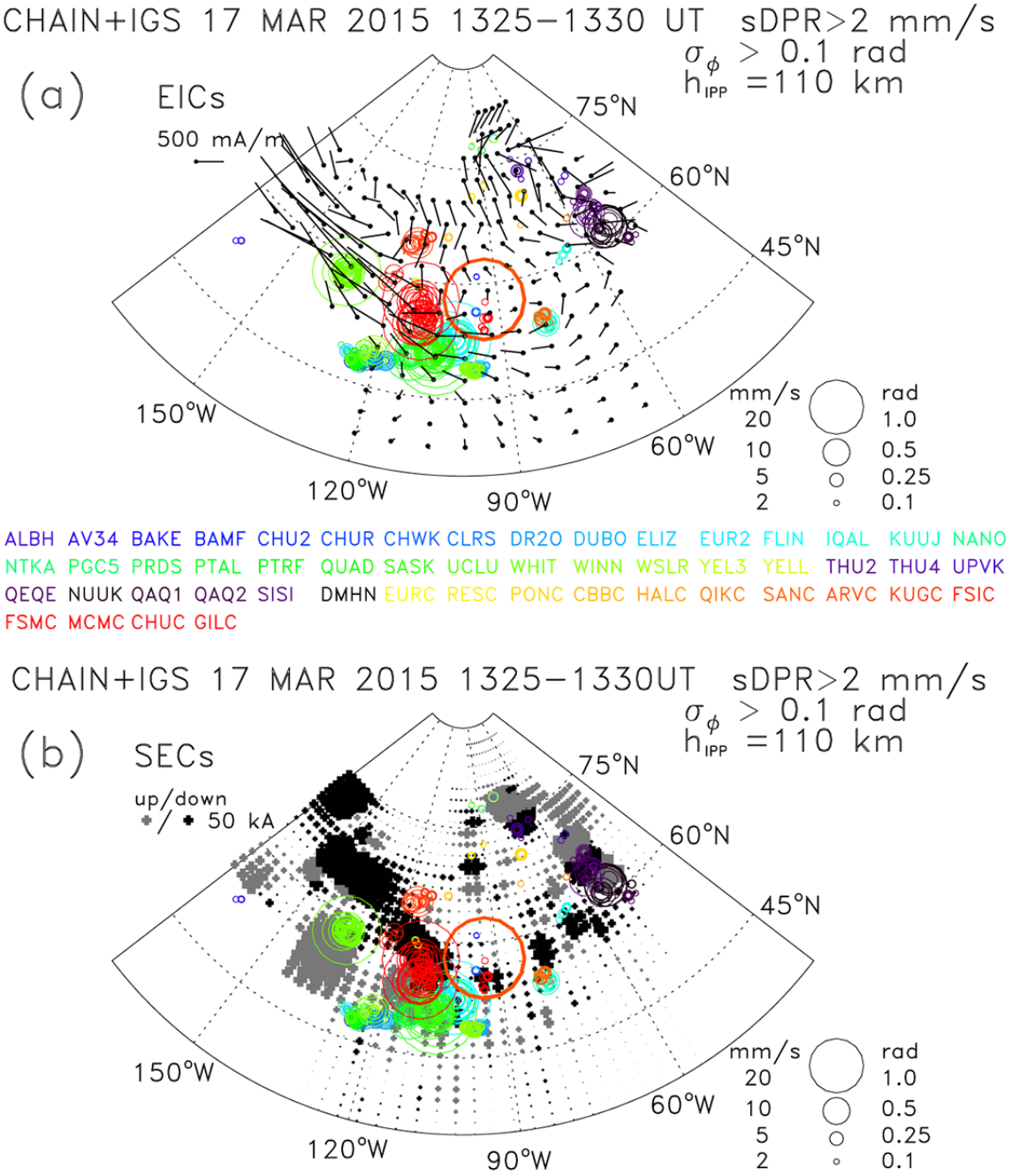

Figure 4.8 The same as Figure 6.7 except at 13:25–13:30 UT.

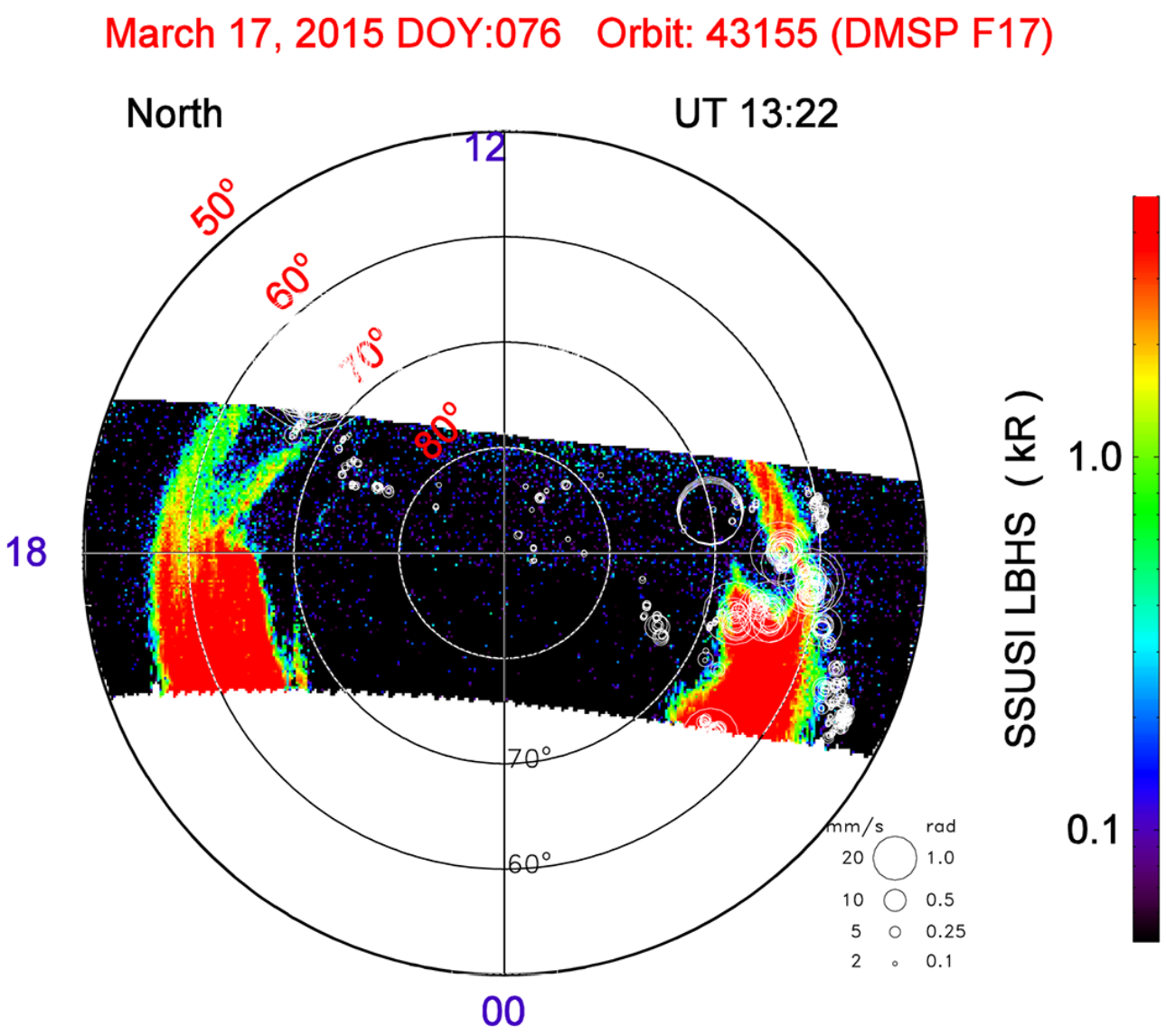

Figure 4.9 SSUSI (DMSP F17) auroral image scans mapped as a function of AACGM latitude and MLT. Scintillation IPPs are shown as white open circles that are scaled by the scintillation intensity.

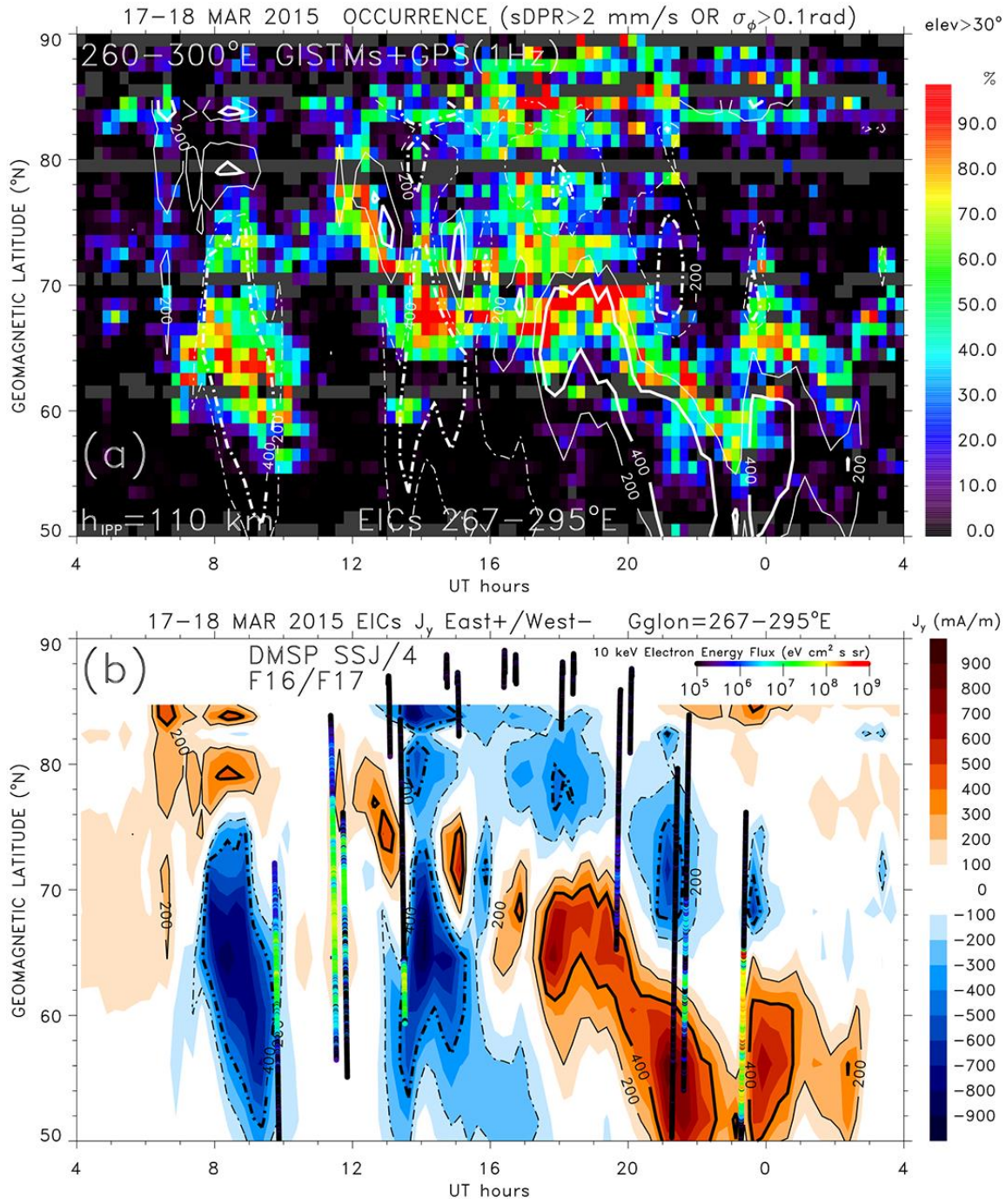

Figure 4.10 (a) The phase scintillation occurrence of $\sigma_\phi > 0.1$ rad or sDPR > 2 mm/s as a function of AAGCM latitude and UT for CHAIN combined with 1 Hz GPS receivers for data from 04:00 UT on 17 March to 03:59 UT on 18 March 2015. Contour plots of the westward and eastward equivalent ionospheric currents are shown in white broken and solid lines, respectively. **(b)** Westward and eastward equivalent ionospheric currents are highlighted in blue and brown shades. Superposed are tracks of DMSP F16 and F17 satellites that crossed the longitude sector between 260° and 300°. The tracks are color coded with observed energy flux of 10 keV electrons.

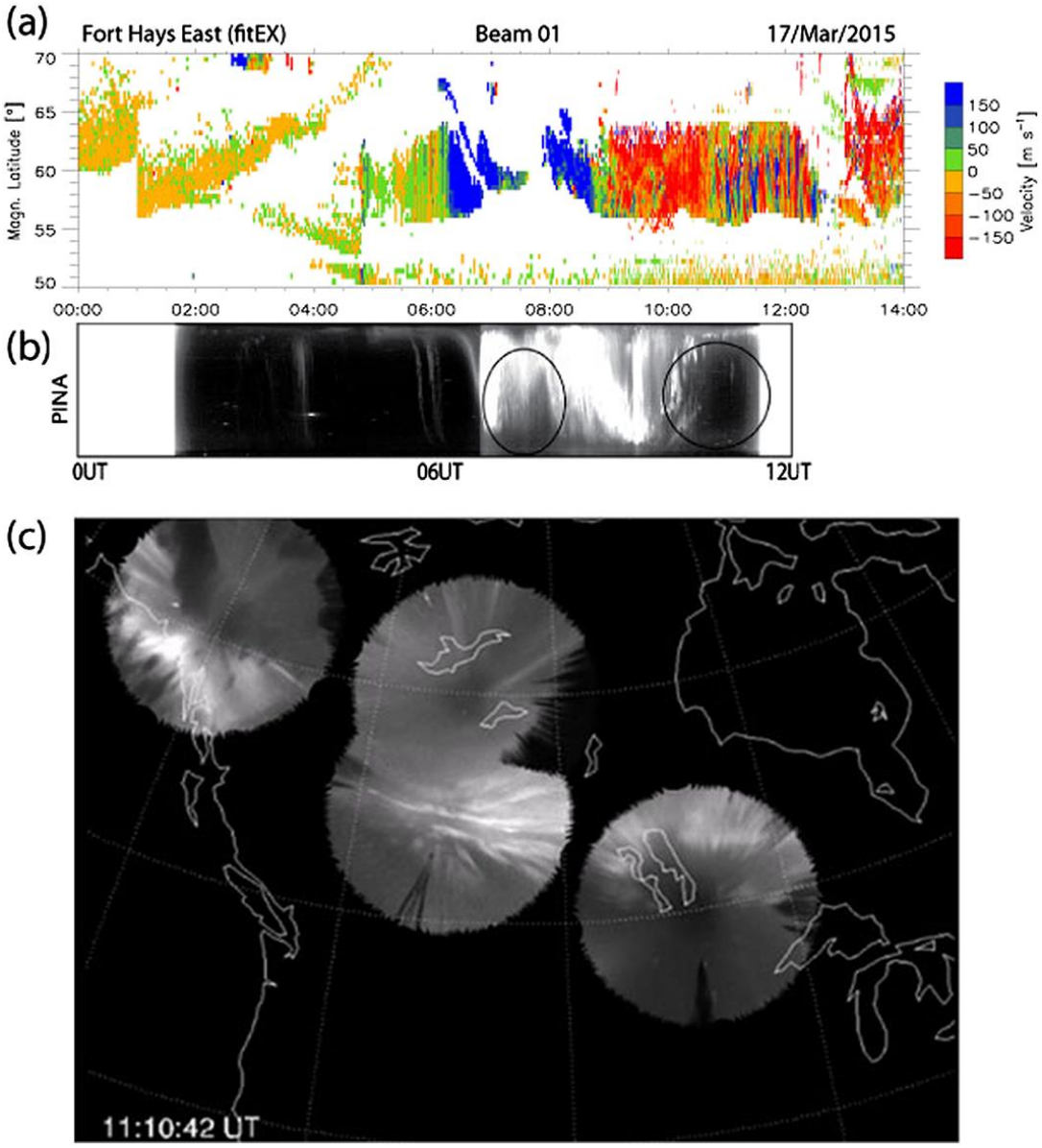

Figure 4.11 (a) Fort Hays East radar line-of-sight velocity for beam 1. **(b)** Keogram of aurora observed by THEMIS ASI in Pinawa with circles approximately indicating occurrence of pulsating aurora. **(c)** THEMIS all-sky imagers showing pulsating aurora at 11:10 UT.

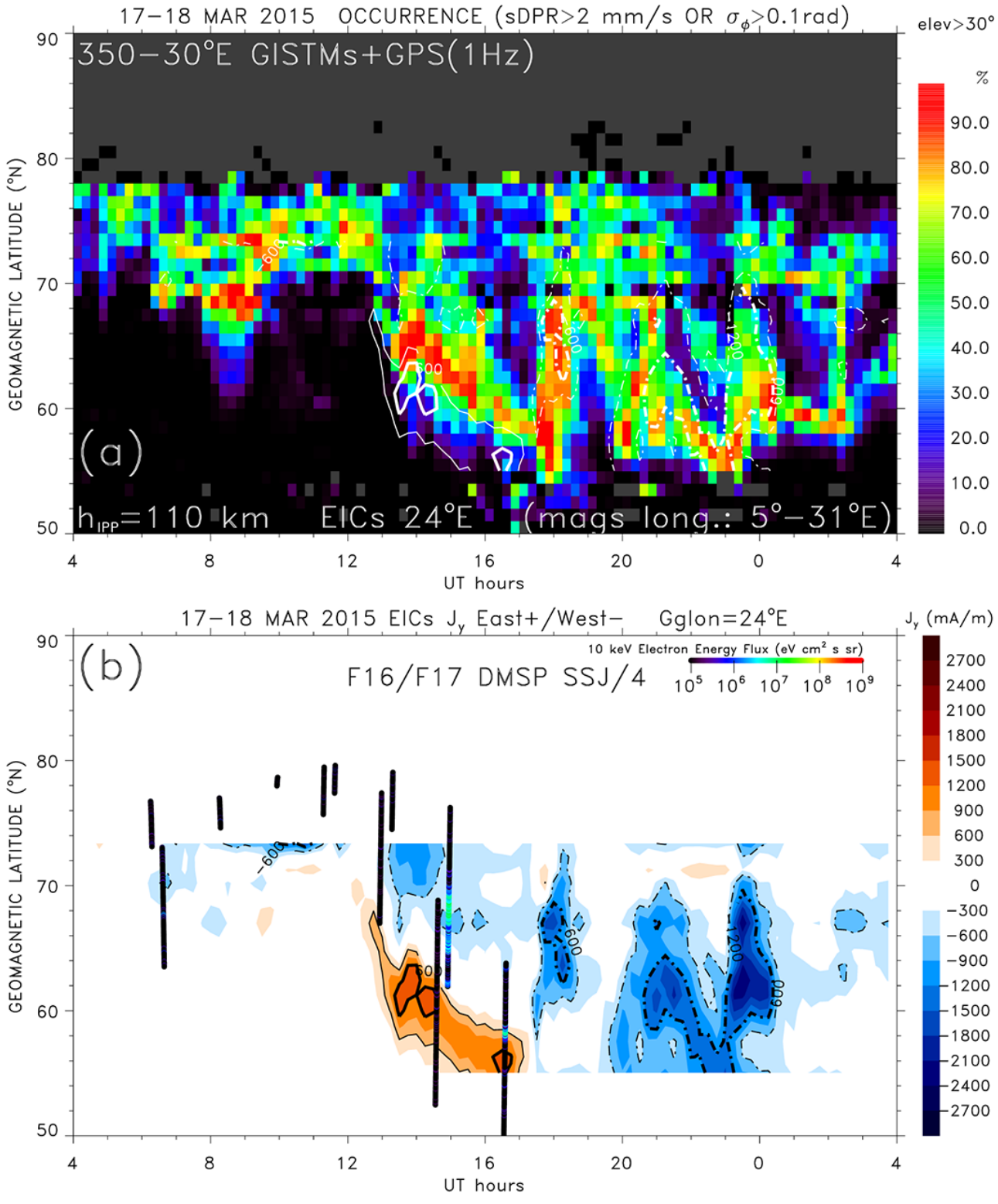

Figure 4.12 The same as Figure 6.10 except for **(a)** the scintillation longitude sector between 350° and 30° and **(b)** the EICs for the longitude 24°.

4.2.5 Geomagnetic Storm of 17–18 March 2015: Discussion and Summary

The solar wind coupling to the magnetosphere-ionosphere system results in a highly structured and dynamic high-latitude ionosphere causing GPS scintillation. On 16 March, the day prior to the storm, the GPS scintillation that was largely confined to the polar cap was caused by Sun-aligned polar cap arcs that are a consequence of northward IMF (Figure 4.2c) [Prikryl et al., 2015a]. In contrast, during the storm when the B_z was southward, scintillation occurrence was strongly enhanced in the cusp and SED regions. In the polar cap, the scintillation was caused by TOI fragmented into patches. Because the IMF B_y controls the dawn-dusk asymmetry of ionospheric convection, the scintillation occurrence band associated with TOI spans the polar cap from the postnoon to postmidnight sector for IMF $B_y < 0$ and from the postmidnight to postnoon sector for IMF $B_y > 0$ [Prikryl et al., 2015c]. The scintillation occurrence on the dayside and in the polar cap, as shown in Figure 4.3b, was a superposition of the two states that were discussed in details for two storms by the latter authors. The IMF B_y was initially dawnward (<0) for several hours before it switched to duskward (>0) at ~11:00 UT and thus TOI/patches entry switched from initially prenoon cusp (Figure 4.4) to postnoon cusp (Figures 4.5 and 4.6). As a result, the scintillation occurrence map, as a function of MLT (Figure 4.3b), shows a composite of the two states resulting in an approximate symmetry about the noon of the dayside scintillation occurrence in the cusp and polar cap.

It is common to approximate the ionosphere as a relatively thin phase-changing shell at 350 km altitude to map the scintillation IPPs and this is quite appropriate with polar cap patches. However, the altitude of GPS scintillation-generating irregularities is often difficult to determine. It is expected that scintillation is caused by F region irregularities at low latitudes where the processes of irregularity generation differ from those at high latitudes. At low latitudes, particularly near the

equatorial ionization anomaly, the scintillation-causing irregularities with scale sizes of a few hundreds of meters are generated by large F region structures (plasma bubbles) and form after sunset [Sreeja et al., 2011; de Paula et al., 2015]. In contrast, at high latitudes, scintillation-causing irregularities can be produced by a variety of auroral and polar cap phenomena, including cusp dynamics, auroral particle precipitation, auroral blobs, and polar cap patches [Moen et al., 2013; van der Meeren et al., 2014, 2015; Oksavik et al., 2015] that produce scintillation-causing irregularities at different altitudes. For example, in the case of particle precipitation with different energy causing emissions 557.7 and 630.0 nm, the GPS IPPs have been projected to 150 and 250 km altitudes on the mapped green 557.7 nm and red 630.0 nm emissions, respectively [van der Meeren et al., 2014, 2015]. Other studies used slightly different altitudes.

In the brief survey of scintillation-causing irregularities in the context of ionospheric signatures of solar wind coupling (Figures 4.3 to 4.6) we assumed an IPP height of 350 km. This may be appropriate for density patches in the polar cap, the cusp, and the density gradients at the poleward edge of SED region. However, in the auroral oval, scintillation is found collocated with energetic particle precipitation causing bright auroras that maximize at much lower altitudes. In section 4.2 (Figures 4.7 to 4.12), we examine the relation between the scintillation occurrence and the ionospheric currents (auroral electrojets and field-aligned currents) as well as auroral precipitation, and thus, we assume IPPs at 110 km. It has been shown that ionospheric irregularities produced by auroral electrojet electric field peak around this altitude [Pfaff et al., 1984; Kelly, 1989]

The maps of EICs (Figures 6.7a and 6.8a) show that GPS phase scintillation is collocated with the westward electrojet currents with the strongest scintillation mapping to the poleward side of strong westward EICs. In relation to vertical current amplitudes (Figures 4.7b and 4.8b) strong scintillation maps to vertical upward or downward Jz currents, or near the reversal boundaries between downward and upward Jz. As it would be expected, these are the regions where strong aurora

caused by energetic particle precipitation occurs. For the same time interval, scintillation is found to be collocated with UV aurora observed by DMSP satellites (Figure 4.9).

Focusing on two 40° longitude sectors with the best coverage by GPS receivers centered about 280°E and 10° longitudes, 15 min averaged EICs and phase scintillation occurrence maps are compared in Figures 4.10 and 4.12. It is found that scintillation occurrence in the auroral zone is collocated with the westward electrojet currents, particularly on the poleward side and with the poleward edge of the eastward electrojet current region. In addition, it is noted that, in general, the energetic electron fluxes observed by DMSP satellites are elevated near the poleward edges of the westward or eastward electrojets, where scintillation occurrence is also elevated. The exception is a 1 h interval between 11:00 and 12:00 UT when no scintillation and very weak EICs (<200 mA/m) were present, yet large fluxes of energetic particles were observed. It is found that during this interval strong pulsating auroras were observed by THEMIS ground-based all-sky imagers and ULF waves were observed by midlatitude SuperDARN radars.

In summary, GPS scintillation regions at high latitudes, namely, storm-enhanced density, cusp, polar cap with polar patches or Sun-aligned arcs, auroral oval, and subauroral polarization streams are largely determined by coupling between the solar wind and magnetosphere. In relation to auroral electrojet currents, scintillation maps to strong EICs, particularly to the poleward side of the westward electrojet and to the poleward edge of the eastward electrojet current region. Scintillation was collocated with energetic electron precipitation regions and aurora observed by DMSP satellites with the exception of a period of pulsating aurora and ULF waves, when large fluxes of energetic particles but very weak EICs were observed.

CHAPTER 5

Published as: *Benzon, H-H., P. Hoeg, and T. Durgonics (2016), Analysis of Satellite-Based Navigation Signal Reflectometry: Simulations and Observations, IEEE Journal of Selected Topics in Applied Earth Observations and Remote Sensing, 9(10), doi:10.1109/JSTARS.2015.2510667.*

STUDY 4: ANALYSIS OF SATELLITE-BASED NAVIGATION SIGNAL REFLECTOMETRY: SIMULATIONS AND OBSERVATIONS

5.1 Introduction and Relevance of the Paper

A new wave propagator that can be used to simulate global navigation satellite systems reflected signals from ocean surfaces is presented. The wave propagator simulates the characteristics of a bistatic scattering system. Simulated GPS ocean surface reflections will be presented and discussed based on different ocean characteristics. The spectra of the simulated surface reflections are analyzed, and the results from the simulations are compared to measured GPS surface reflections. The measurements were performed using a space-qualified GPS receiver placed on a mountain at the Haleakala observatory on the Hawaiian island of Maui. The GPS receiver was during the experiments running in an open-loop configuration. The analysis of both the simulated surface-reflection signals and the measured reflection signals will in general reveal spectral structures of the reflected signals that can lead to extraction of sea surface roughness, surface wind speed, and direction.

5.2 Analysis of Satellite-Based Navigation Signal Reflectometry: Simulations and Observations

Global navigation satellite system (GNSS) coherent and incoherent reflected signals have the potential to enable derivation of large-scale parameters of ocean and ice surfaces, such as barotropic variability, eddy currents and fronts, Rossby waves, coastal upwelling, mean ocean surface heights, and patterns of the general ocean circulation. In the reflection zone, the measurements may enable determination of parameters such as sea surface roughness, winds, water-wave heights and tilts from a spectral analysis of the reflection measurements. Previous measurements' campaigns from mountain tops, airplanes, and satellites have shown results leading to some of these parameters (see Cardellach et al. [2004], Cardellach et al. [2011], Rius et al. [2002]). Upcoming international satellite missions, such as the American CYGNSS, COSMIC-2, and the European/American GEROS on the International Space Station, have underlined the need for simulation studies highlighting the assumptions for the data retrievals and the precision, and the accuracy of such measurements (see Ruf [2013], Fong et al. [2014], Wickert [2014]).

Simulations play an important part in the preparation for new satellite missions and in the development of new measurement techniques. Forward simulation of the measured signals has often been used in an end-to-end simulator tool to develop the retrieval algorithms. The retrieval algorithms are used in the calculations of the geophysical parameters. The forward simulations have been used in a number of different scientific areas such as in the field of radio occultation. Here, retrieval algorithms that can resolve the geophysical parameters in the presence of multipath were developed using radio-occultation simulations that included this effect (see Jensen et al. [2003] and Benzon and Syndergaard [2013]).

This paper introduces a wave propagator that can be used to simulate GNSS-reflected signals from ocean surfaces. The wave propagator simulates the characteristics of a bistatic scattering system, where the transmitted wave from a GPS satellite is detected by a GPS receiver (in the study placed on a mountain) after the wave has been reflected by the ocean surface. Wave propagation simulation tools as presented in this paper can be used in planned upcoming American and European satellite missions, where characteristics of the ocean are retrieved from reflection measurements.

The theory of propagation of microwaves in the atmosphere is well established, and methods for propagation modeling range from ray tracing to numerical solutions to the wave equation. Besides ray tracing, there are propagation methods that use mode theory [Wait, 1963] and a finite difference solution to the parabolic equation (see Kerr [1951] and Tatarskii [1961]). The presented propagator is based on the solution of the parabolic equation. The parabolic equation in our simulator is solved using the split-step sine transformation. The Earth's surface is modeled with the use of an impedance model. This impedance concept gives an accurate lower boundary condition in the determination of the electromagnetic field, and makes it possible to simulate reflections and the effects of transitions between different media (see Kuttler and Dockery [1991]). A semi-isotropic Phillips spectrum is used to represent the air–sea interaction (see Phillips [1957]).

The theory of propagation of microwaves in the atmosphere is well established, and methods for propagation modeling range from ray tracing to numerical solutions to the wave equation. Besides ray tracing, there are propagation methods that use mode theory [Wait, 1963] and a finite difference solution to the parabolic equation (see Kerr [1951] and Tatarskii [1961]). The presented propagator is based on the solution of the parabolic equation. The parabolic equation in our simulator is solved using the split-step sine transformation. The Earth's surface is modeled with the use of an impedance model. This impedance concept gives an accurate lower boundary condition in the

determination of the electromagnetic field, and makes it possible to simulate reflections and the effects of transitions between different media (see Kuttler and Dockery [1991]). A semi-isotropic Phillips spectrum is used to represent the air–sea interaction (see Phillips [1957]). This paper is organized as follows. A description of the simulation of the bistatic scattering system is followed by a comparison between simulated and measured GNSS ocean-reflected signals. These sections are followed by a section containing the conclusion.

5.2.1 Simulation of a Bistatic Scattering System

The electromagnetic wave transmitted from a GPS satellite is reflected in the ocean and received using a GPS receiver placed on a high point on the ground. See the schematic drawing in Figure 5.1. The wave propagation from the specular reflection point to the receiver is performed using the Fourier split-step solution to the parabolic equation approximating the two-dimensional (2D) wave equation. The initial field along a vertical line placed at the specular reflection point is calculated from the ocean-scattering coefficients.

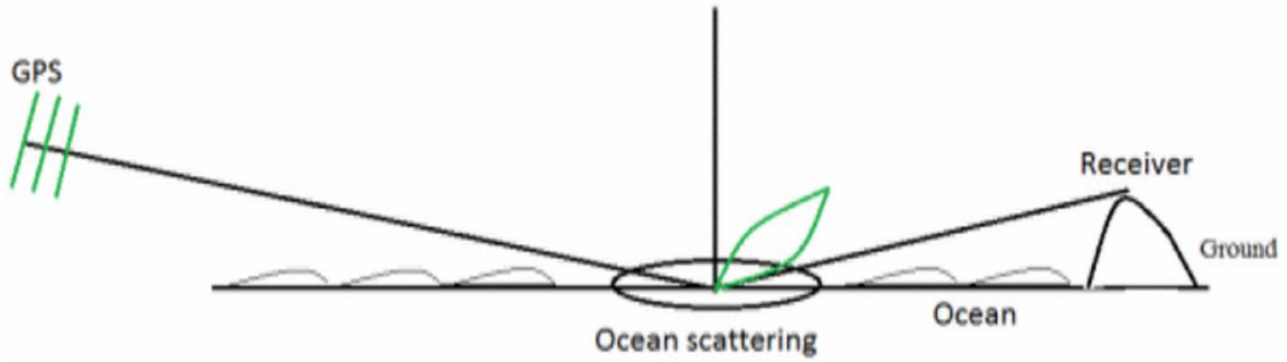

Figure 5.1 Wave originating from the GPS satellite is reflected in the ocean and received by the GPS receiver.

The parabolic equation in our simulator is solved using the split-step sine transformation, where the earth surface is modeled using impedance (see Collins [1992], Barclay [2003], Bole et al. [2005]). This impedance concept gives an accurate lower boundary condition in the determination of the electromagnetic field. The split-step/sine transform solution for the outgoing parabolic equation is given by

$$u(x+\Delta x, y) = e^{ik(n-1)\Delta x} S^{-1}\left\{ e^{ik\Delta x\left(\sqrt{1-\frac{\pi^2 p^2}{k^2}}-1\right)} S\left[u(x,y)\right]\right\} \qquad (5.1)$$

Here, u is the electromagnetic field value and n is the refractive index. The latter is a complex parameter due to absorption at a number of high frequencies. S represents the sine transformation, k is the wave number, and Formula is the spatial frequency. The sine transform is implemented using fast Fourier transforms (FFTs); this significantly increases the execution speed of the propagator (see Press et al. [1992]). Spatial frequencies are used in the Fourier transform calculations. The spatial frequency is a measure of how often sinusoidal components of the field repeat per unit of the distance. The split-step/sine transform solution can be thought of as a field propagating through a number of phase screens. The distance between the screens is Δx. The field propagates along the positive x-axis, and the screens are all orthogonal to the x-axis. Equation 5.1 is not exact; however, it is a good approximation provided the variations of n remain slows on the scale of a wavelength. The primary limitations of this technique are that the backscattered field is neglected, and in the forward direction, the field is only correct for propagation angles below a limit determined by the wavelength and number of calculation points on the screens. However, for the current study, this limitation is not considered to have any measurable impact on the results. The electromagnetic field at the GPS receiver calculated as a function of time is the sum of the direct and reflected wave fields. In our simulator, this field can be represented as the amplitude and phase as a function of

time or the corresponding in-phase and quadrature (I–Q) components as a function of time (see Benzon and Hoeg [2015]). Detailed models for both the neutral atmosphere and the ionosphere are included in the simulations. The ionosphere is modeled using the NeQuick model (see Nava et al. [2008]). Using these models, e.g., it is possible to simulate multipaths in the neutral atmosphere and scintillations in the ionosphere with the correct setting of a number of parameters. The interface between the electromagnetic wave and the ocean is handled using the concept of impedance for rough surfaces and the mixed Fourier transformation (see Kuttler [1991]). The discrete Fourier transformations make it necessary to extend the needed maximum altitude and truncate the field at the upper boundary to prevent artificial reflections from the boundary. This truncation is in our propagator accomplished with the use of a Hanning window or a region containing perfectly matched layers. The below equation shows how the rough surface impedance Formula can be calculated as a function of the smooth surface impedance δ_0

$$\delta = \sin(\theta)\frac{(1+\rho)\delta_0 + (1-\rho)\sin(\theta)}{(1-\rho)\delta_0 + (1+\rho)\sin(\theta)} \tag{5.2}$$

Values of the smooth-surface impedance can be found in the literature for different materials, radio wave frequencies, and polarizations (see Haynes [2012]). θ is the grazing angle (the angle between the wave-propagation direction and the ground) and ρ is the roughness reduction factor. The roughness reduction factor can be expressed as a function of the Rayleigh roughness parameter γ using the following equation:

$$\rho = I_0\left(\frac{\gamma^2}{2}\right)e^{\frac{-\gamma^2}{2}} \tag{5.3}$$

where I_0 is the modified Bessel function of the first kind and of order 0, while the Rayleigh roughness parameter is given by the following equation:

$$\gamma = 2kh\sin(\theta) \tag{5.4}$$

Here, *k* is a wave number of the electromagnetic wave, while *h* is the root-mean-square (rms) height of the ocean-water waves. If a number of assumptions are met, it is possible to relate the rms of the ocean water heights to the wind speed. A detailed analysis of this subject can be found in Beckmann and Spizzchino [1987]. Another forward model can be found in Zavorotny and Voronovich [2000]. A thorough description of the calculation of the time-delayed scattered signal power in the ocean from the GPS radio wave is presented in this paper. This model is based on a bistatic radar equation derived using the geometric limit of the Kirchhoff approximation. The model presented here and the model in Zavorotny and Voronovich [2000] are both based on approximations to Maxwell's equations, and the results for the scattered power are expected to give similar results. An analytical model of bistatic reflections can be found in Pavelyev [2011].

A well-developed sea, forced by a wind speed *U*, can generate a Phillips wave spectrum. The Phillips spectrum is calculated as the Fourier transformation of the correlation function for the ocean wave heights, and here, the rms of the ocean wave heights *h* is proportional to the square of the wind speed *U* as seen in the following equation:

$$h = 0.0051\frac{s^2}{m}U^2 \tag{5.5}$$

Based on the geometry of the positions of the GPS satellite and the GPS receiver and through use of (5.2)–(5.5), it is possible to calculate the rough-surface impedance from the wind speeds. It is a common practice to define the sea state from the value of the wind speed and the water-wave height calculated using (5.5). Normally, sea states numbered from 1 to 5 correspond to wind speeds from 5.14 to 14.01 m/s, with a wind speed step-size of 2.58 m/s. The rms height values for the water waves will, in accordance with (5.5), lie in an interval between 0.135 and 1.0 m. The sea state 0 is

associated with no winds and consequently no water waves. These sea states and the corresponding values for wave heights were used to set up the simulations in the later sections.

The wave propagator presented in this section was used in the following sections, where the wave propagation simulations are compared to real GPS receiver measurements.

5.2.2 Measured and Simulated Results

The presented wave propagator is here employed to simulate the signal collected at a GPS receiver placed on a mountain top. The electromagnetic field at the antenna of the GPS receiver is composed of both a direct wave from the GPS satellite and an ocean reflected wave.

Measurements have been performed using a space-qualified European GPS receiver (RUAG) placed on a mountain at the Haleakala observatory on the Hawaiian island of Maui (see Olsen [2005]). The GPS receiver at the mountain top had a clear view toward the ocean. The receiver was running in an open-loop configuration during the measurement campaign, and the simulations were performed using a setup that is comparable to the measurements.

A large number of measurements were performed during the measurement campaign. The GPS receiver is capable of tracking a large number of satellites at the same time. The amplitude and phases of the received GPS signal are measured as a function of time. The power-density spectrum of the I–Q signal for a raising GPS satellite is seen in Figure 5.2 (top). The GPS receiver ran in an open-loop configuration corresponding to a sampling frequency of 1000 Hz. The slope of the spectrum can be seen from the red line, which was calculated as a best-fit to the measured values. From Figure 5.2, it can be seen that the spectrum becomes noisier from around 20 Hz. The short-time Fourier transform has been applied to the measured I–Q signal, and the result is presented in

Figure 5.2 (bottom). The short-time Fourier transformation is also called the spectrogram. A Fourier transformation is here successively applied to a small time window of the total time signal (see Boashash [2003]). A Hann window was imposed on the data in the small time windows. The length of the windows was chosen to be in the order of 1 s. The spectrogram is given as a function of the elevation angle between the GPS receiver and the transmitting satellite. This elevation angle is a linear function of time during the measurement. It is seen from this figure that the elevation angle starts at negative values. This corresponds to the positions of the GPS satellite that is below the local horizon.

The short-time Fourier transformation reveals important information. This can be seen in Figure 5.2 (bottom), where the values of the short-time Fourier transformation are presented by different colors (see Beyerle and Hocke [2001] and Beyerle et al. [2002]). The frequencies of the direct and reflected waves are a little different. The lower red ray in the plot can be interpreted as the direct wave between the GPS satellite and the GPS receiver, while the upper ray can be interpreted as the reflected wave.

A simulation has been performed that mimics the measured data, and the results are presented in Figure 5.3. The GPS L1 frequency is used both in the simulations and for the measured data. The wave propagator is initialized using the scattered field in the ocean from the GPS wave. This field is calculated from the scattering coefficients shown in Figure 5.3 (top). These coefficients have been calculated for scattering angles between 0° and 90° using the well-known bistatic scattering from a single-scale random surface model (see Beckmann and Spizzchino [1987]).

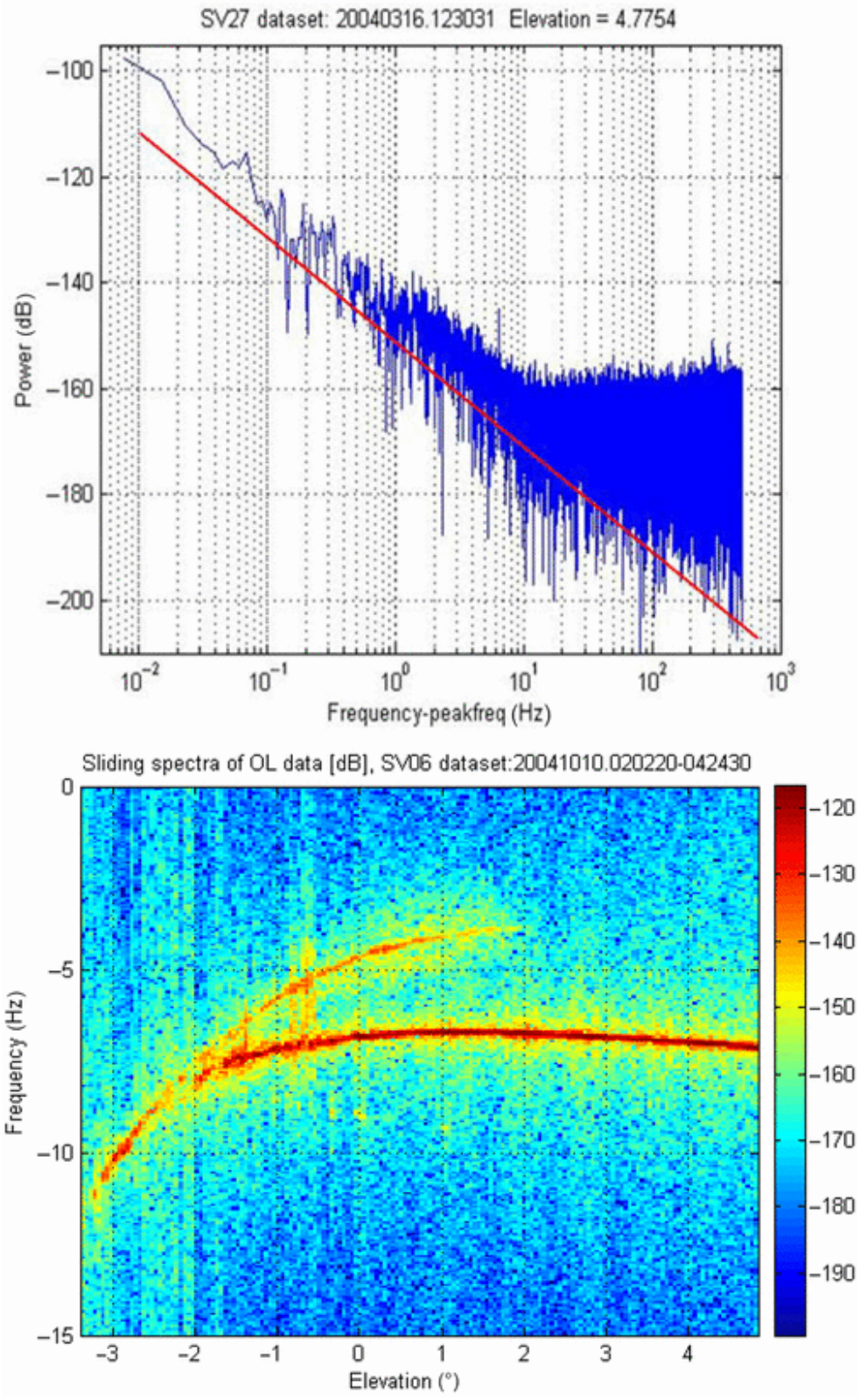

Figure 5.2 (top) Measured power density spectrum. **(bottom)** Spectrogram of the measured data. Signs of the direct wave field (the lower red ray) and the reflected wave field (the upper red ray) can be seen in the plot.

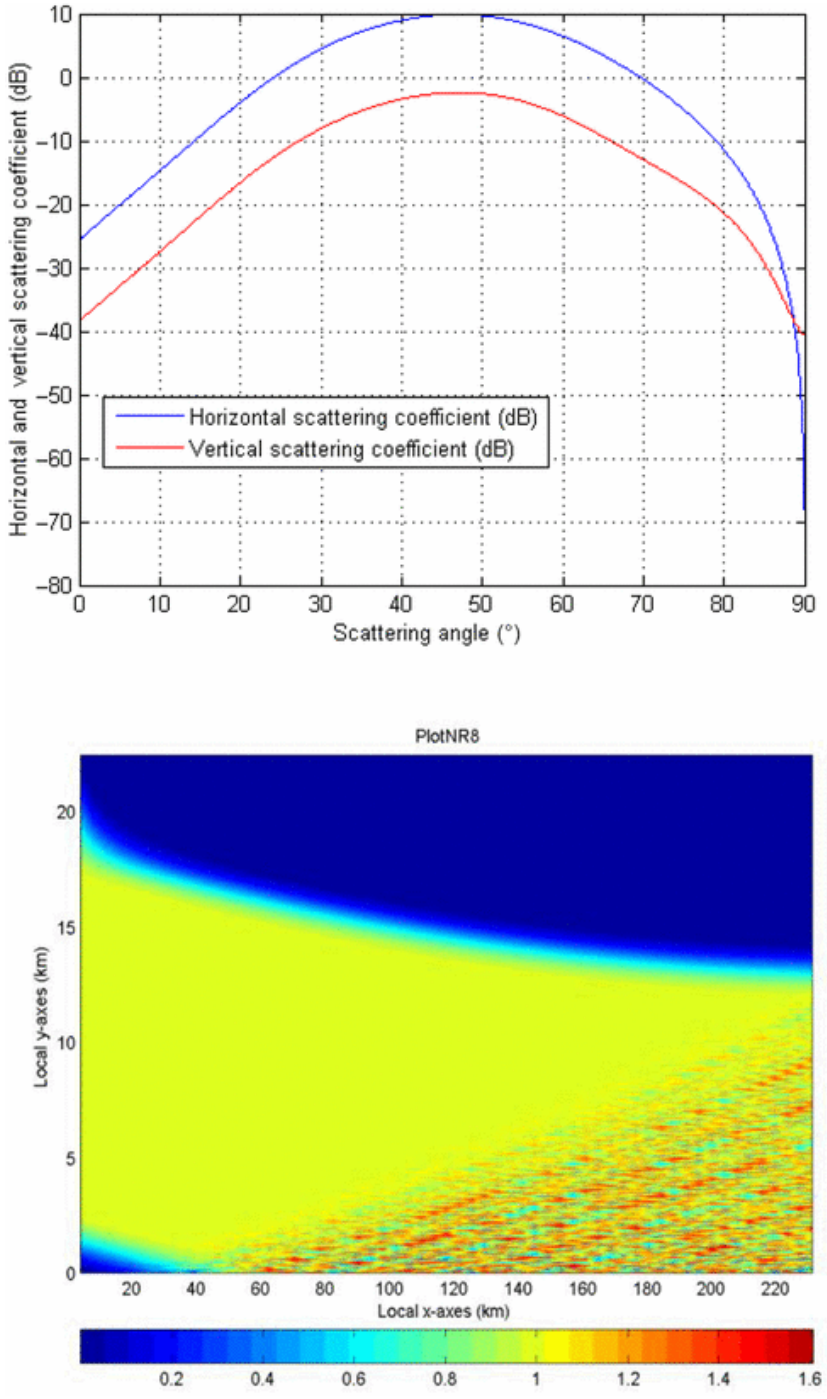

Figure 5.3 (top) Ocean scattering coefficients. These coefficients are used to calculate the initial field for the wave propagation. **(bottom)** In this plot, the x-axis represents the range in a local Cartesian coordinate system placed on the earth surface, while the y-axis represents the height above the sea surface. The colors represent the amplitude of sum of the direct and reflected field as a function of range along the earth surface and height.

Figure 5.3 (bottom) shows the field along the phase screens for a distance of approximate 220 km along the earth surface. The total field after the specular reflection point is the sum of the direct and reflected field. The sum of the two fields is seen on the right side of the plot. The results of applying the wave propagator presented above are seen below using the same type of plots as presented above for the measured data. The calculations have been performed for an rms ocean wave height of 0.13 m corresponding to a wind speed of 5 m/s. The power density spectrum of the simulated I–Q signal is seen in Figure 5.4 (top), while the short-time Fourier transform for the simulated signal is shown in Figure 5.4 (bottom). It is seen that both of these figures show the same characteristics as the figures for the measured data. The power density spectrum for the measured data is noisier than the simulated spectrum, as expected. The simulated spectrum can be fitted very precisely with a function *W* given by

$$W = \frac{\sqrt{(4/(\pi\ f_0))}}{(1+(f/f_0)^2)}. \tag{5.6}$$

Here, *b* is a function of the parameters used in the simulation and Formula is the frequency. The black curve in Figure 5.4 (top) shows this fit for a value of Formula equal to 0.3. This model is similar to the spectrum model found in [Ungan and Johnson, 2000]. The spectrogram for the simulated signal again shows signs of both a reflected wave (upper yellow ray) and a direct electromagnetic wave (lower dark yellow ray). The simulated reflected signal is a little weaker than the direct signal, but it is present throughout the event. This is not the case for the measurement where the reflected signal disappears for high elevation angles. It can be assumed that the disappearance of the reflected component in Figure 5.2 (bottom panel) for elevation angles larger than about 2° is caused by the increasing path difference between direct and reflected component.

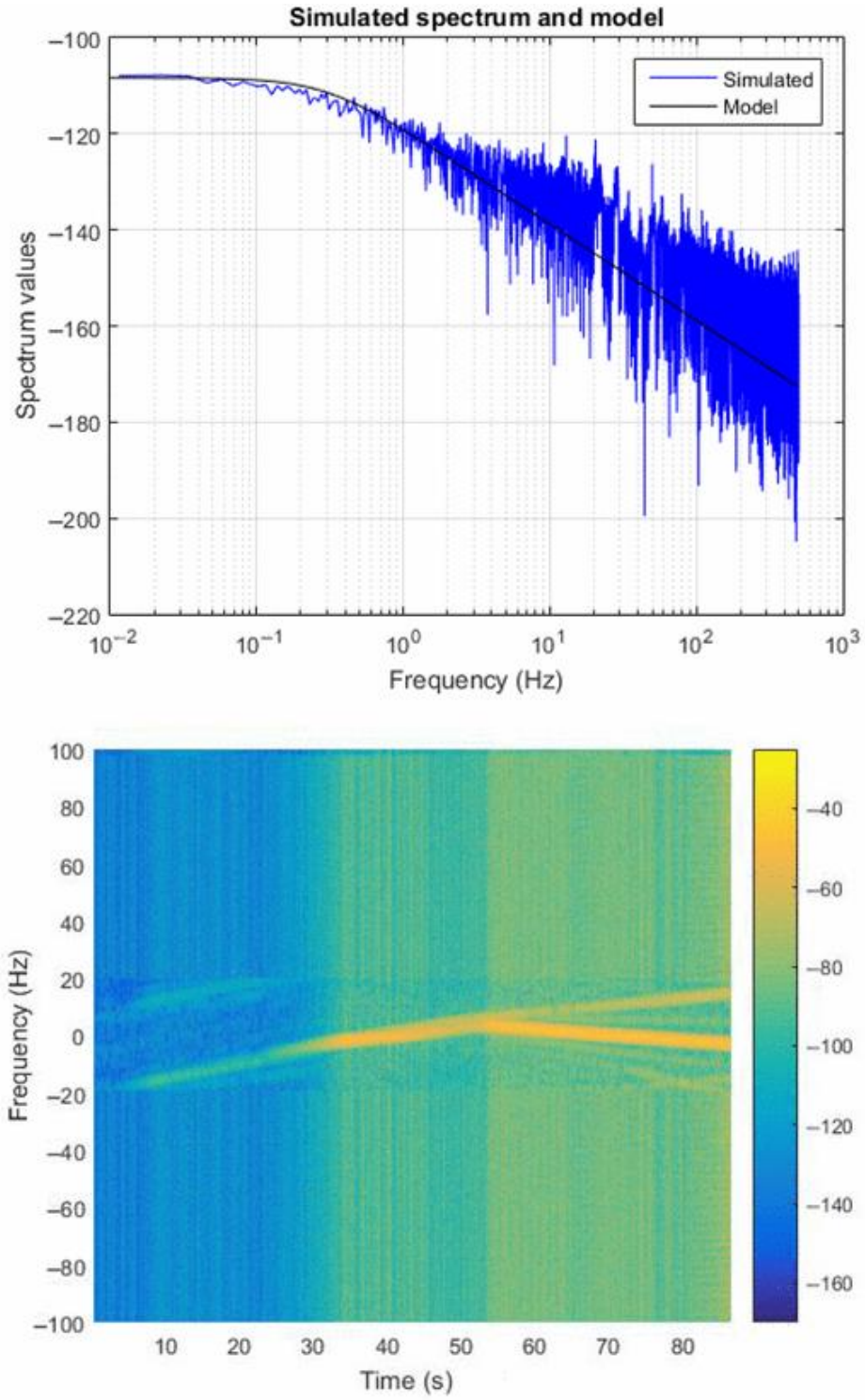

Figure 5.4 (top) Spectrum of the simulated signal collected at the receiver. The black line is a fit to the spectrum. **(bottom)** Spectrogram of the simulated signal collected at the receiver. Signs of the direct wave field (the lower dark yellow ray) and the reflected wave field (the upper yellow ray) can be seen.

When this difference exceeds one chip length (300 m for C/A code modulation), the reflected component has moved too far in the delay space to be detectable. The wave propagator used in this study does not include the effects of code modulation. Thus, the reflected component remains visible in the spectrogram in Figure 5.4 (bottom panel). The *ray artifacts* observed in a number of places in the spectrogram for the simulated data are caused by the periodicity in the discrete short-time Fourier transformations. It should, however, be noted that the simulation setup only mimics and is not identical to the real measurement setup due to a number of assumptions made to perform the simulations.

5.2.3 Conclusions

The field of reflectometry, where the GNSS system is used as the transmitting source, is a relatively new field with a great potential for retrieval of new and precise geophysical parameters such as wave height and salinity. This great potential can also be seen from the relatively large number of satellite missions that are in a planning stage. It is therefore important to have the necessary tools to perform the appropriate simulations and algorithms that can be used to perform the retrieval of a number of important geophysical parameters. The presented wave propagator for a bistatic scattering system is capable of performing some of these tasks. This simulator includes detailed models of both the neutral atmosphere and the ionosphere. The interface between the electromagnetic wave and the ocean has also been modeled in great detail in our simulator. Simulations of ocean-surface reflection measurements have been presented in this paper, and the results have been compared against real ocean-reflection measurements where a GPS satellite is the transmitting source. This comparison shows that the simulator results and the results based on the ocean-reflected measurements are similar. In the future, it would be beneficial to have even better

models. The semi-isotropic Phillips spectrum used here to represent the air–sea interaction is a relatively simple model. More accurate models should be developed, thus making the relationship between wind speed and ocean-wave heights more accurate. It should also be mentioned that the relations for the smooth and rough impedances given in this paper are approximations to more general expressions. Such models are currently being investigated, and they will later be implemented in our wave propagation tool. A large measurement campaign could be used to verify the simulation models in greater detail, where standard GPS receivers and phase-delay mapping receivers placed on unmanned drones or airplanes are used to collect measurements at different locations under different geophysical conditions. This measurement campaign would also collect useful information that could be used in upcoming satellite missions.

CHAPTER 6

MULTI-INSTRUMENT OBSERVATIONS OF SOLAR EUV IRRADIANCE INDUCED IONOSPHERIC VARIATIONS

6.1 Introduction and Relevance of the Research

This research is a work in progress and is planned to be published in the future; as a consequence it is not marked as *Study* (which indicates published articles) but it is still significant enough to deserve its own chapter in this dissertation.

In the previous chapters, results have been presented about a wide variety of regional and sub-regional geophysical phenomena in the Arctic ionosphere (e.g., tongue of ionization, polar patch propagation). Related TEC and scintillation measurements were discussed, but the scope was typically limited to a specific geomagnetic storm and these were therefore mostly short-term studies. A logical follow-on is to investigate the long-term changes at larger scales. At these time-scales (months to years), the effects of geomagnetic storms are negligible for nearly all practical considerations. In order to eliminate local disturbances and be able to assess large-scale TEC variations, MVTEC [Durgonics et al., 2017] was selected as a measure of mean electron content over a large area (diameter of thousands kilometers) at a certain epoch. The station (Thule) location

was selected to minimize auroral oval and midlatitude *noise* in the data set (Figure 6.1). At these spatial and temporal scales, climatological TEC effects are being observed in the polar cap ionosphere. The main drivers behind the variations are the sun, the solar wind, and magnetospheric reconnections [Watson et al, 2016; Prikryl et al., 2015; Chakrabarty et al., 2012].

6.2 The Effects of Solar-Rotation-Related Spectral Irradiance Variations on Northern Polar Cap Plasma Number Densities

In this study, new findings are presented on sub-seasonal GNSS-TEC variations observed in the northern polar cap ionosphere during the most active four years of Solar Cycle 24. In order to understand these variations, the F_2 layer continuity equation (Equation 3.3), which is valid for the polar cap ionosphere, must be considered. On the right hand side of Equation 3.3, the first two terms describe the ion production and loss. The main driver behind the production term is the solar irradiation, while the loss is related to some types of ion-electron recombination processes. The third and the fourth terms in Equation 3.3 are related to plasma redistribution (plasma motion).

At large scales, ion production is mainly driven by photo-ionization or particle precipitation. Long-term variations in total and spectral solar irradiance have been previously studied in a number of works [e.g., Yeo et al. 2014; Willson and Hudson, 1991]. From the total solar irradiance spectrum, only those spectral irradiance wavelengths that are capable of ionizing relevant atmospheric species, e.g., O, N, N_2, and H, are here considered. These wavelength bands are the extreme ultraviolet (EUV) and X-ray fluxes. The solar EUV flux correlates very well with the F10.7 solar radio flux index [Brekke, 2013; Chen et al., 2011], which is a radio frequency that can penetrate Earth's atmosphere and be observed on the ground. On the other hand there are time periods when the F10.7 solar radio flux correlation with solar EUV may be less significant, especially around solar

minimums [Chen et al., 2011]. While the F.10 solar radio flux is simpler to measure, the solar EUV flux can only be effectively measured from spacecraft. However, solar EUV fluxis what directly ionizes relevant atmospheric species, , thus it serves as a more direct measurement of the cause of TEC variations.

The third and the fourth term on the right-hand side of Equation (3.3) describe plasma convection. A number of existing studies describe the physical processes underlying ionospheric plasma convection, including Watson et al. [2016], Prikryl et al. [2015], Jayachandran et al. [2011], Kullen et al. [2008], Ruohoniemi and Greenwald [2005], and Russell and McPherron [1973]. These physical processes were also derived in Section 1.3. In the polar cap ionosphere, which is the focus of this work, the plasma is in constant motion driven by **E**x**B** drift, where the E-field configuration depends fundamentally on the solar wind parameters in proximity of geospace, but is also affected by, for example, interactions with the neutral atmosphere. One of the consequences of **E**x**B** drift is the unique feature of the polar cap ionosphere called tongue of ionization (TOI), observed in TEC maps in Foster et al. [2005] and Durgonics et al. [2017], among others. The TOI consists of plasma convected from midlatitude dayside over the polar cap into the night sector. The TOI can also break down into isolated plasma irregularities (polar patches) during its movement over the polar cap. These patches travel with plasma convection speeds that are usually larger than lower latitude plasma, which can be larger than 10 times the typical equatorial values [Jacobsen, 2014]. Polar cap patch generation, structure, and decay have been previously described in several studies, such as Prikryl et al. [2015], Hosokawa et al. [2011], MacDougall and Jayachandran [2007], Moen et al. [2007], Pedersen et al. [2000], Basu et al. [1994], Kivanç and Heelis [1998], and Basu et al. [1985].

The last remaining term in Equation (3.3) is related to ion loss. The only relevant loss process for the polar cap that is considered in this study is a specific plasma decay process described by Vickrey and Kelley [1982]. In this process, certain F region irregularity scale sizes decay faster if a

highly conducting E region is present via cross-field plasma diffusion, resulting in fundamentally different TEC variations during different seasons.

The sum of all the terms in Equation (3.3) thus far described is equal to the change in electron/ion density with time [Rodger et al., 1992; Vickrey and Kelley, 1982]. This can be measured, for example, by using ground-based GNSS-TEC observations. In this work, ground-based GNSS-TEC measurements complemented by digital ionosonde measurements were employed. GNSS-TEC values are typically computed from data acquired from networks of ground stations. These networks can be global [e.g., Komjathy et al., 2005a] or regional [e.g., Durgonics et al., 2014]; examples of regional high-latitude GNSS-networks are e.g., the Greenland GPS Network (GNET) [Durgonics et al., 2017] and the Canadian CHAIN [e.g., Prikryl et al., 2016]. Long-term deep polar cap, single-station-derived mean vertical TEC (MVTEC) observations from Thule (Figure 6.1) were here employed to study the influence of solar EUV irradiance and seasonal variations (due to the varying angle of Earth's rotational axis relative to the Sun in the Greenland sector) on the ionospheric electron density.

6.2.1 Methods and Observations

The GNSS ground-station employed in this study is located at the Thule Air base, in northwestern Greenland (76.53°N, 68.78°W) (Figure 6.1). This ground-station was one of the first operational permanent GNSS receivers in the network that is now called GNET. Receivers with 4-character IDs THU2 and THU3 were installed in 1998. THU4, a third receiver, was added in 2010. Thule is a scientifically significant location for a number of reasons. Firstly, it is located in the deep polar cap region which is a region containing open geomagnetic flux tubes [Wild et al., 2004]. The ionized part of the upper atmosphere over this region is also referred to as the high-latitude ionosphere

when the auroral oval, which is the boundary region between open and closed flux tubes and lies equatorward from the polar cap, is also included. Secondly, a large number of observations were conducted from other ground-based instruments located at Thule [e.g., Basu et al., 1985 and 1994]. This allows for comparison of collocated measurements between this study and others.

Basu et al. [1985 and 1994] reported irregularity structures and their frequency spectra from polar cap derived measurements at Thule using 250 MHz transmissions from quasi-stationary satellites. They also reported phase and intensity scintillation variations for several years. These are compared to observations in this study and interpreted in section 6.2.2.

A digital ionosonde operating in Qaanaaq (located approximately 100 km north of Thule Air Base) provided relevant measurements until the second half of August 2014. This data provides a good overlap with our GNSS-TEC measurements (more details on TEC are presented later this section). Based on the ionosonde measurements, bottomside electron density (N_e) profiles can be reconstructed while the topside is modeled with a fitted Chapman profile. Measurements were collected every 15 minutes. Ionosonde-derived N_e profiles can be compared to TEC measurements after integration. More details on this method can be found in Durgonics et al. [2017].

The polar cap north (PCN) index [Vennerstrøm et al., 1991] is computed from single-station magnetic measurements (ground-based magnetometer) located in Thule. The variations and values of PCN index indicate energy input changes into the polar cap region [Durgonics et al., 2017]. Larger variations and values are expected during geomagnetic storms and there is also seasonal dependence, which will be discussed in Section 6.2.2.2. PCN values were acquired from the Polar Cap Magnetic Index website (*http://pcindex.org/*), which is maintained by the Arctic and Antarctic Research Institute and the Technical University of Denmark, DTU Space.

In this study, EUV flux measurements from NASA's Solar Radiation and Climate Experiment (SORCE) satellite [Fröhlich, 2016] were employed, which was launched on 25 January 25 2003. SORCE collects continuous measurements of the sun's total solar irradiance (TSI) and spectral solar irradiance (SSI) and carries four observational instruments on board: Total Irradiance Monitor (TIM), Solar Stellar Irradiance Comparison Experiment (SOLSTICE), Solar Irradiance Monitor (SIM), and soft X-ray Ultraviolet Photometer System (XPS). Because SORCE data contains gaps from time to time, we complemented the EUV measurements with F10.7 solar radio flux data. The SORCE instruments together provide measurements of the full-disk spectral solar irradiance (SSI) from 0.1 nm to 2400 nm, but the frequency range between 34 to 115 nm is not covered. The resolution of the SSI measurements from 115 nm to 310 nm is 1 nm, from 310 nm to 2400 nm is varying from 1 to 34 nm. The irradiance data represents measurements at a mean solar distance of 1 astronomical unit (AU) with units of $W/m^2/nm$. The SORCE data can be acquired from the University of Boulder Colorado website (*http://lasp.colorado.edu/home/sorce/data/*). The F10.7 data was acquired from the Space Physics Data Facility (SPDF) website (*https://omniweb.gsfc.nasa.gov/form/dx1.html*).

The TEC values were calculated from the Thule-based GNSS receiver (THU3) using an ionospheric single-layer model [e.g., Mannucci et al., 1999]. The possible IPPs coordinates from this station location can range from approximately 150°W to 10°E geographic longitudes and 63°N to 90°N geographic latitudes using a 10° elevation cutoff angle (Figure 6.1). The 1 Hz sampled data acquired from the station were processed by Jet Propulsion Laboratory's Global Ionospheric Maps (JPL GIMs). For more details on JPL GIM see, e.g., Vergados et al., [2016]. The outputs include VTEC values and their IPP coordinates and the data was down-sampled to 5 minutes. The VTEC values were then further processed to obtain mean VTEC (MVTEC) values [Durgonics et al., 2017] for a total period of four years: 2012, 2013, 2014, and 2015. MVTEC values represent a single

value measured in TEC units (TECU, 1 TECU = 10^{16} electrons m^{-2}) over the station and are calculated as the mean of all the observed VTEC values for a given epoch. This single value can be interpreted as a low-pass filtered, "smoothed" ionosphere single layer which removes smaller ionospheric irregularities and effectively represents the overall trend in ionization in the region. Changes in MVTEC are more likely to be the result of solar ionization or other large scale phenomena (e.g., N_2 upwelling due to atmospheric heating as a result of a geomagnetic storm) than studying individual VTEC values. Note that due to the fact that VTEC was down-sampled to a 5 minutes data rate from the original 1 Hz GNSS data, all the MVTEC time-series also have one value every 5 minutes. In the case of the polar cap region, this type of down-sampling is generally not justified due to possible rapid changes in, for example, convection speeds, but in this specific case we found it suitable due to the duration of the study.

Figure 6.1 shows the approximate geographic area that where the IPPs can be present. Every IPP arc represents a line where a signal path from a given GPS satellite intersects the ionosphere single layer model shell while it is observable from the Thule site. At any given epoch there can be typically 10 to 12 IPPs. Each VTEC value at these IPPs at a given epoch contributes to MVTEC with the same weight.

Figure 6.2 reveals a number of characteristic features in the four annual MVTEC time-series. The annual curves are similar but the amplitudes vary. The winter months' minima are present between each year, after which there is a steady rise in TEC during the spring. The TEC values decrease throughout the summer and approach minimum again in the winter. The highest TEC values and the highest diurnal amplitudes can be found during the spring of 2014.

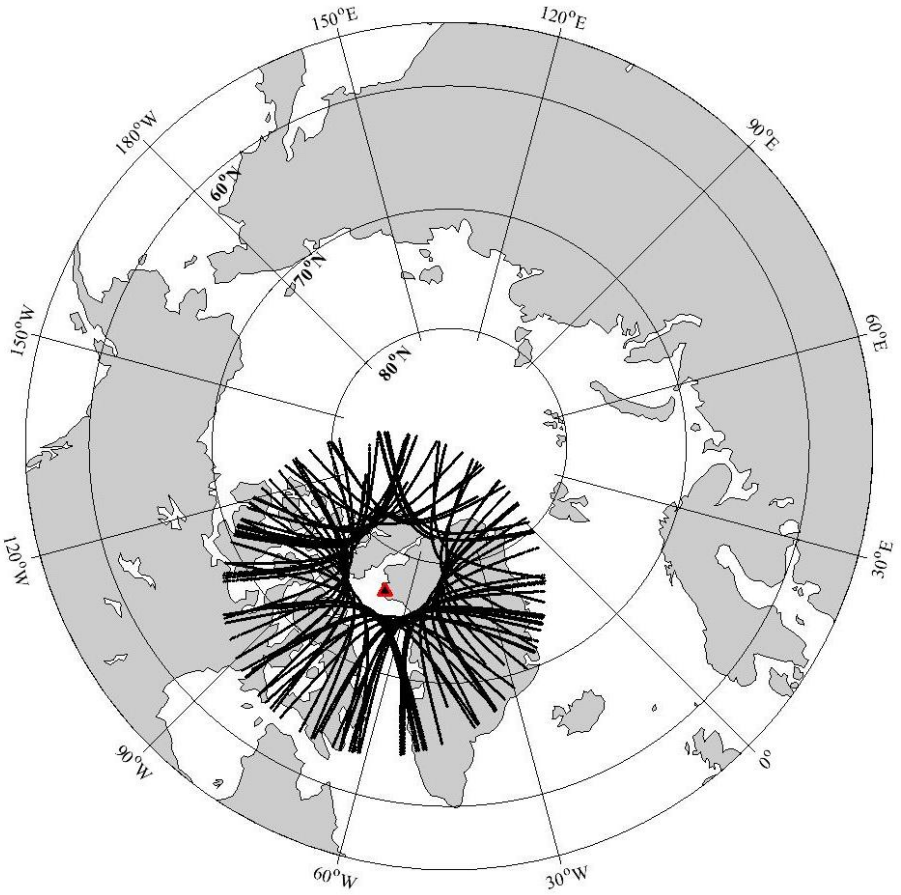

Figure 6.1 Thule GNSS station location and IPP coverage of the derived data.

6.2.2 Results

The MVTEC and 115 nm SSI variations for four consecutive years (2012, 2013, 2014, and 2015) are shown in Figure 6.2. These four years represent the peak of Solar Cycle 24 with two local sunspot number peaks in 2013 and 2015.

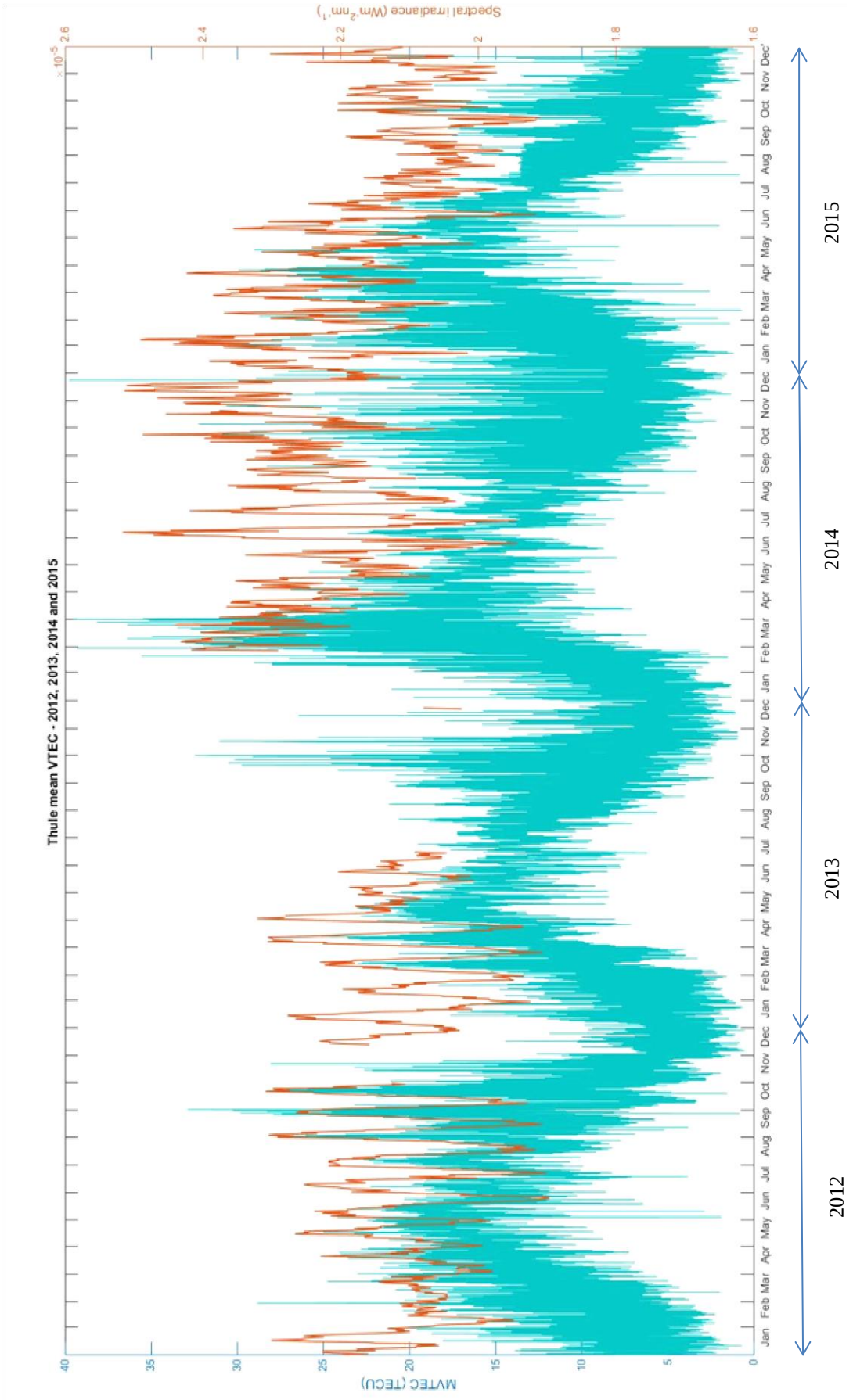

Figure 6.2 5-minute resolution MVTEC time-series and hourly 115 nm SSI time-series for the years of 2012, 2013, 2014, and 2015.

The TEC values vary most in the weeks around the equinoxes; they vary more during winters, but seem to be smoother during summer months. In addition to the diurnal variations there is an approximately 27-day period that can be most clearly observed during the summer, but it is also present throughout the entire year. During such a 27-day period the MVTEC can change 10 to 15 TECUs. Since MVTEC is less sensitive to local irregularities than large-scale solar-ionization-induced changes, this means that the source of this 27-day anomaly is possibly solar originated. Note that the Thule-based MVTEC does not cover all the longitudes of the entire polar cap at any given time, but it essentially covers all of its latitudes over Greenland and north-eastern Canada. Because of this spatial limitation, the MVTEC time-series in Figure 6.2 captures diurnal variations in addition to the longer term changes.

In addition to the diurnal changes there is a variation that occurs typically twice a day. This variation is caused by the plasma convection related to the **E**x**B** drift in the polar cap. Longer term changes, in addition to the 27-day one, that can be seen in Figure 6.2 are seasonal variations discussed above, while the longest ones span across years. The seasonal changes are caused by Earth's orbit around the sun and its rotational tilt. The longest period variations are solar cycle related and can be correlated to solar spot number statistics. The Fourier spectrum of the MVTEC time-series clearly reveals each of these typical frequencies (see Section 6.2.2.4). Figure 6.2 also shows the 115 nm solar spectral irradiance time-series to allow comparison with the MVTEC changes (see Section 6.2.2.3). Note that there is a large data gap in 2013, but the existing data reveals significant correlation to the 27-day TEC variations.

6.2.2.1 Interpretation of the MVTEC Time-Series and Related Observations

To interpret an MVTEC time-series one has to take into account the factors that are essentially biases or artifacts of the derivation of this value. These factors may make MVTEC vary in time even if the ionosphere itself is rather calm. In an ideal case the number of observed satellites would be constant and the spatial distribution of the IPPs would be uniform. In reality this is, of course, not the case. Satellites are ascending and descending (their signals are appearing and disappearing), the GNSS receiver may lose lock, and the GNSS satellite orbits and satellite orbital periods influence the IPP locations in a non-ideal way. Nevertheless, MVTEC has proven to be a robust, reliable observable for ionospheric studies (see, e.g., Durgonics et al., [2017]).

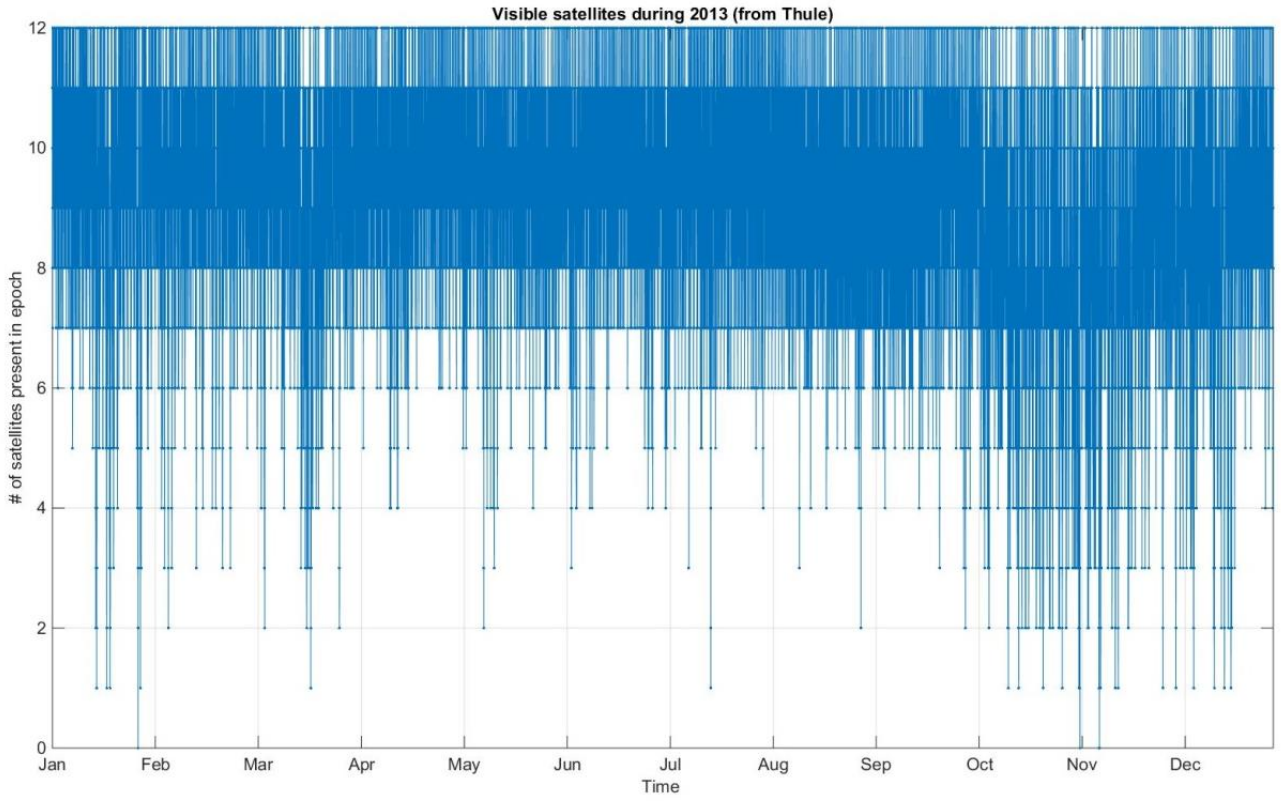

Figure 6.3 Number of observed satellites from Thule in 2013. There is a decrease in observed satellites around the equinoxes indicating increased ionospheric and geomagnetic activity during equinoctial months. Non-equinox anomalies are probably related to geomagnetic storm activity.

Figure 6.3 demonstrates how the number of observed satellites changes throughout a year according to the GNSS receiver in Thule. At high-latitudes, it is well-known that loss of lock may occur during geomagnetic storms and other disturbed times when ionospheric scintillations are significant (e.g., Prikryl et al., [2016]). These events are usually relatively short lived, however Figure 6.3 represents longer term effects that last for weeks or even months (seasonal effects). During the equinoctial months the number of observed satellites are generally lower than during the summer months. This may indicate increased geomagnetic and ionospheric activities (as a result of the increased number of loss-of-lock events in ground receivers) that can potentially produce more polar patches (see, e.g., Section 1.3) and the make the TOI appear more frequently. Around equinoxes, the entire deep polar cap ionosphere is more disturbed, while during the summer it is more calm and smooth.

Figure 6.4 shows more details of the MVTEC time-series by focusing on shorter time periods. There are noticeable differences between winter months, equinoctial months, and summer months. The polar ionosphere has variability around equinoxes. It has somewhat high variability but a low base value during winter and lowest short-term variability and somewhat high values during summer. Throughout the summer months the ionization is gradually decreasing, but superimposed on this decreasing trend there is an approximately 27-day fluctuation of around 10-15 TECU. This fluctuation is present throughout the year but less apparent when the diurnal variability masks it, e.g., near equinoxes.

To validate the MVTEC values obtained from Thule, data from 35 GNET stations were processed using Bernese 5.0 software (for details about how Bernese computes VTEC values see, e.g., Dach et al. [2007]). The Bernese software computes VTEC values in a regular grid, and the obtained values were averaged to obtain a similar quantity to MVTEC. The comparison of the Thule MVTEC and the Bernese-computed average VTEC can be seen in Figure 6.5.

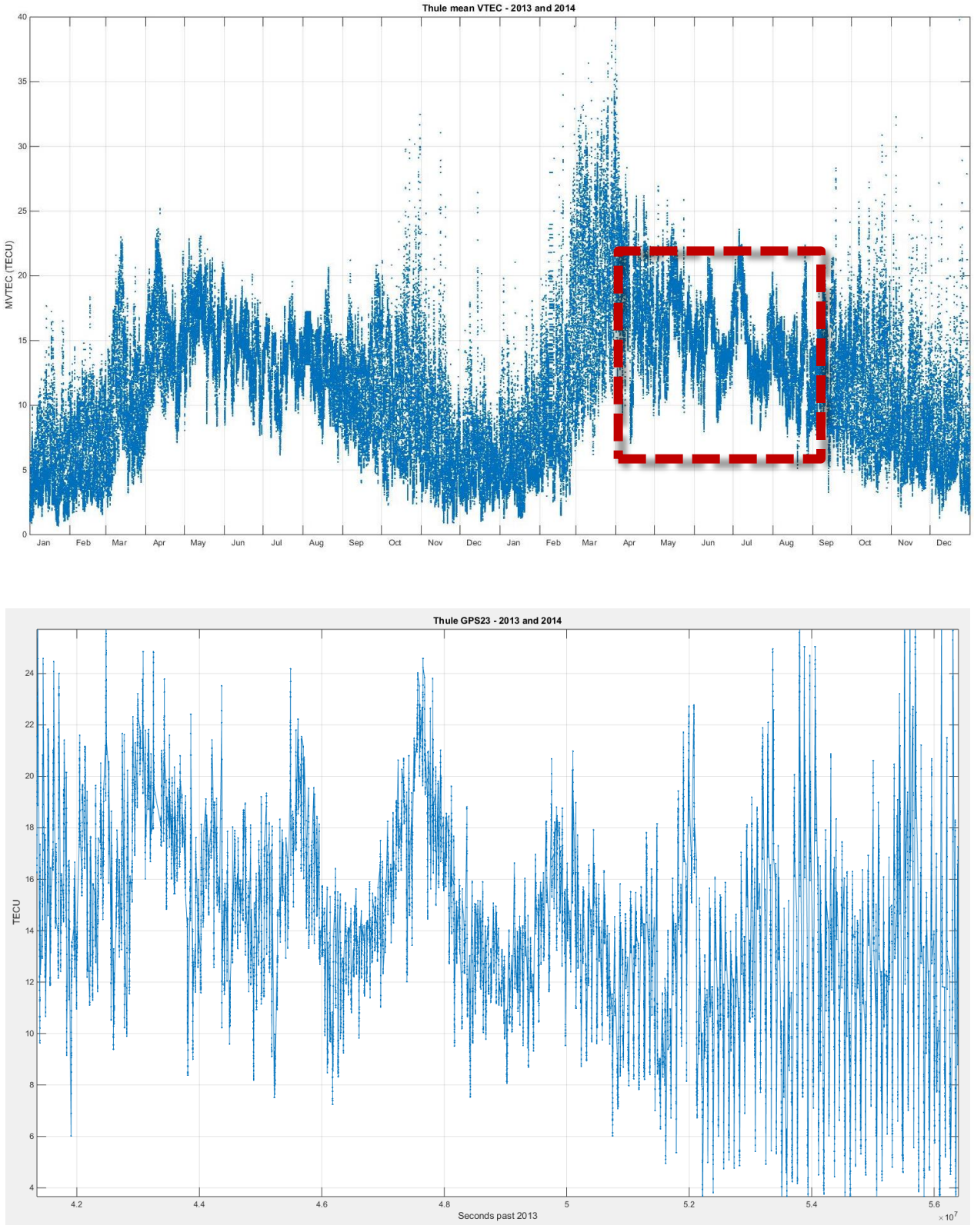

Figure 6.4 (top) MVTEC time-series of 2013 and 2014. **(bottom)** MVTEC time-series showing only the summer of 2014.

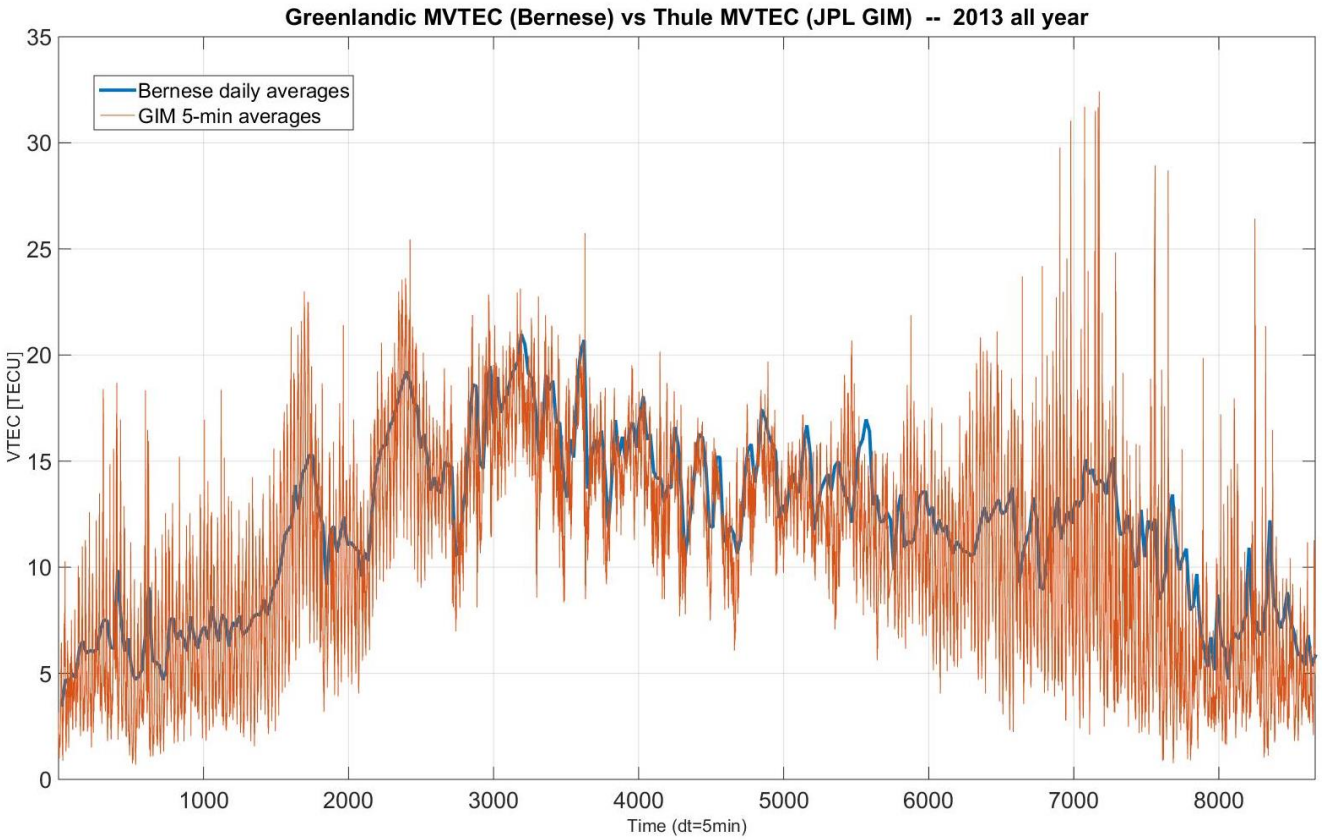

Figure 6.5 Comparison of two differently computed MVTEC time-series of the same data.

Figure 6.5 reveals a surprisingly good match between the two independently computed electron densities. Note that the Bernese output has a time resolution of 1 hour, while the JPL GIM data has 5-minute resolution. Because of this, the Bernese time-series (blue line) is more smooth than the JPL GIM time-series (red line). Smaller irregularities and faster variations do not appear in the Bernese output.

6.2.2.2 Relation of MVTEC Time-Series to Geomagnetic Indices and Digital Ionosonde Measurements

The relationship between MVTEC time-series, critical frequency profiles, and various geomagnetic indices were analyzed in this section in detail. It was also attempted to use digital ionosonde derived electron density data to obtain information about the altitudes where the most prominent changes are occuring. Note that the relationship between the critical frequency (f_c) and maximum plasma number density ($N_{e,max}$) is given by $f_c = 9\sqrt{N_{e,max}}$ (see Reinisch et al. [2009] and references therein). MVTEC and the integrated critical frequency are later compared , which reveals significant correlation.The comparison of MVTEC with Dst and AE does not indicate any significant relation (Figure 6.6). The MVTEC wavelet decomposition clearly shows the diurnal variations, but the comparison is also inconclusive (see Section 6.2.2.4). Next, MVTEC was compared with the PCN-index (Figure 6.7). The PCN-index shows unique features unrelated to the MVTEC features, featuring higher amplitudes during summer months and lower amplitudes during winter months Another comparison was carried out with digital ionosonde derived vertical N_e profiles, and these can be seen in Figures 6.8a, 6.8b, and 6.8c. These three digital ionosonde critical frequency plots reveal geomagnetic storms occuring during the relevant months (June, July, and August of 2014) as in Chapter 3. Futhermore, the 27-day MVTEC variations appear as F layer ionization enhancement. Additionally, the digital ionosonde critical frequency profiles were integrated and compared with with the MVTEC time-series (Figure 6.9), which revealed significant correlation. This serves as another independent measurement that validates the use of MVTEC as a measure of ionospheric electron density variations. The digital ionosonde critical frequency profiles and plots (Figures 6.8a, 6.8b, 6.8c, 6.10, and 6.11) were made using the SAO Explorer software (*http://ulcar.uml.edu/SAO-X/SAO-X.html*) and the related Dst time-series were taken from the

World Data Center for Geomagnetism, Kyoto website (*http://wdc.kugi.kyoto-u.ac.jp/dst_realtime/presentmonth/*).

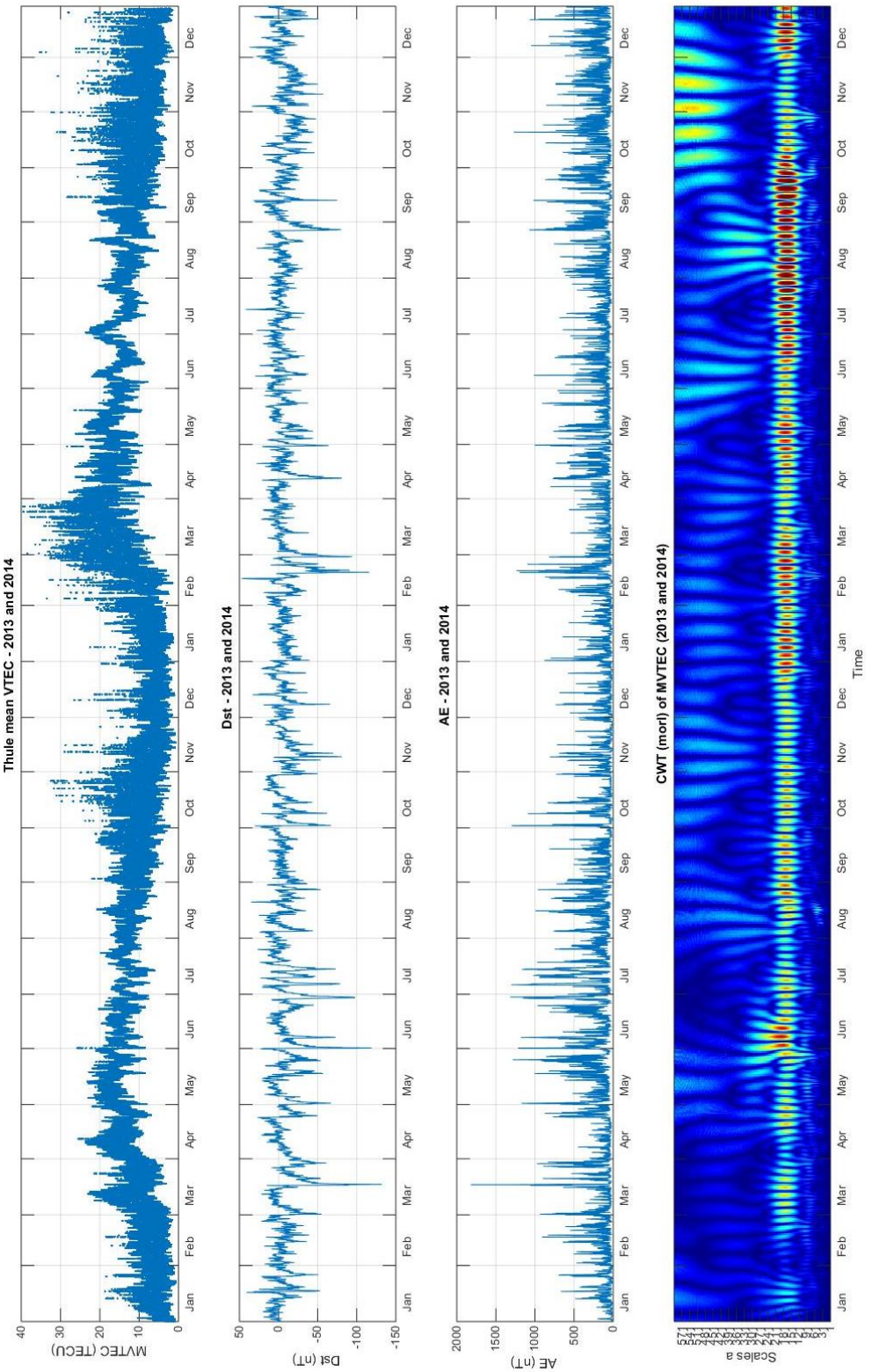

Figure 6.6 Comparison of MVTEC and its wavelet decomposition and geomagnetic indices (Dst and AE).From top to bottom panels: MVTEC, Dst. AE. and MVTEC wavelet decomposition using Morlet wavelet.

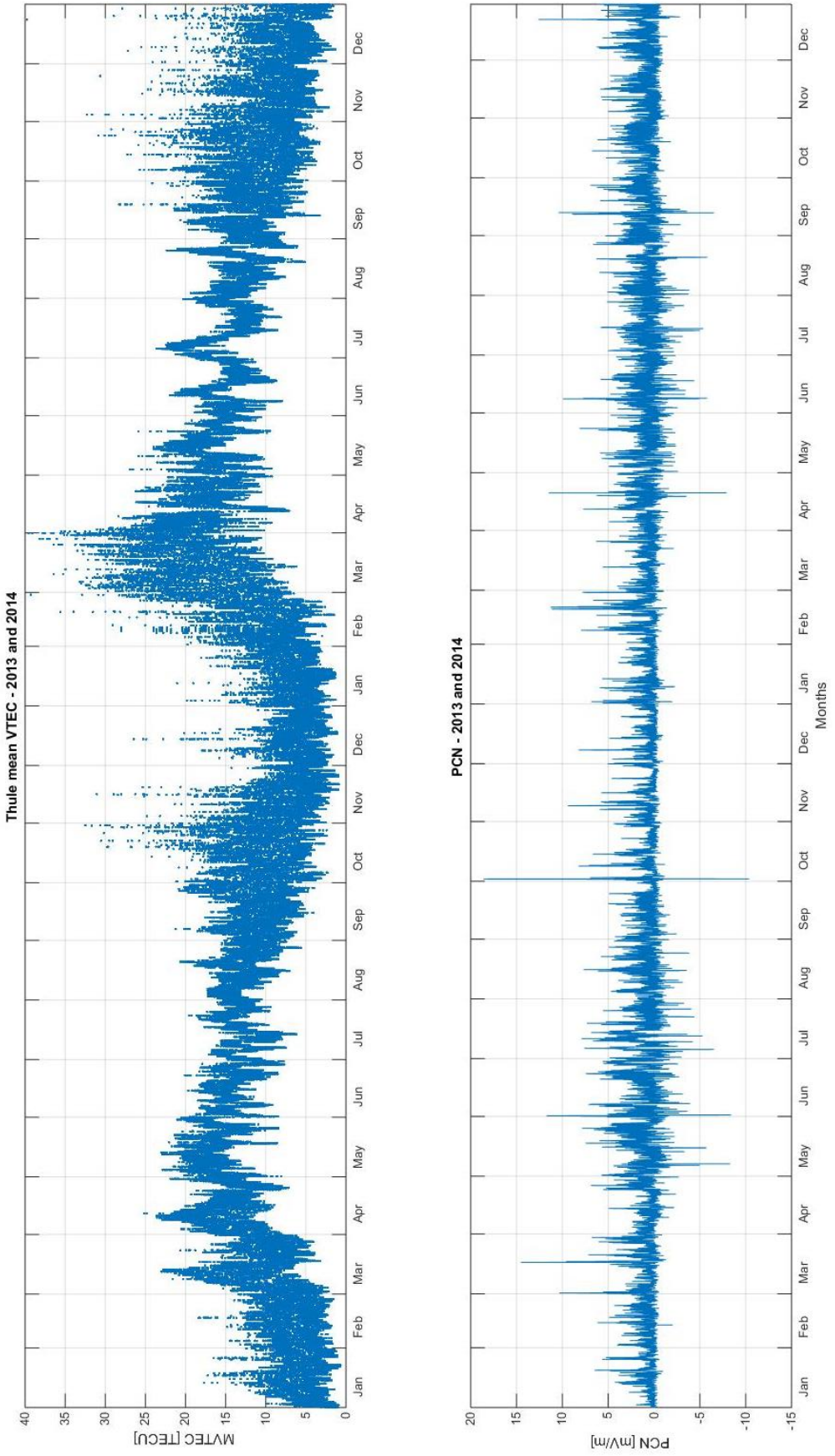

Figure 6.7 MVTEC time-series and PCN time-series for 2013 and 2014.

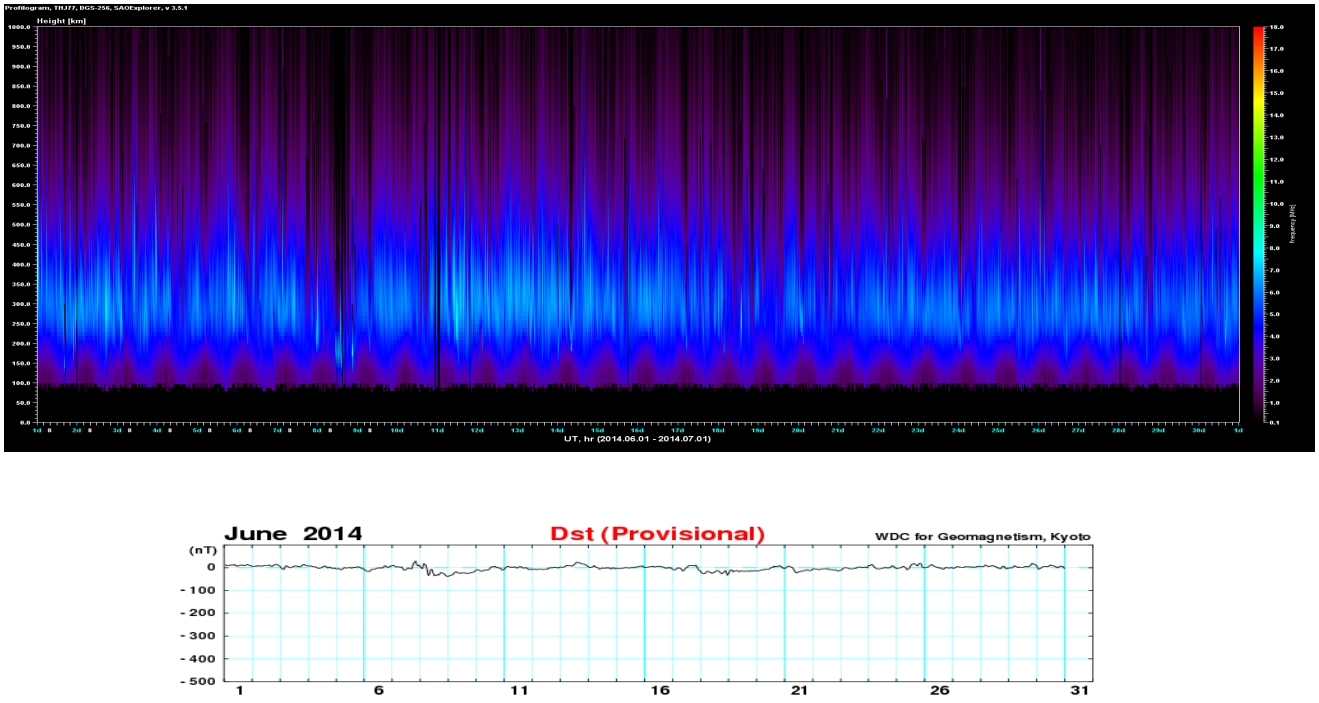

Figure 6.8a Digital ionosonde profiles and concurrent Dst time-series for June 2014 (larger resolution top panel image is available in Appendix VIII).

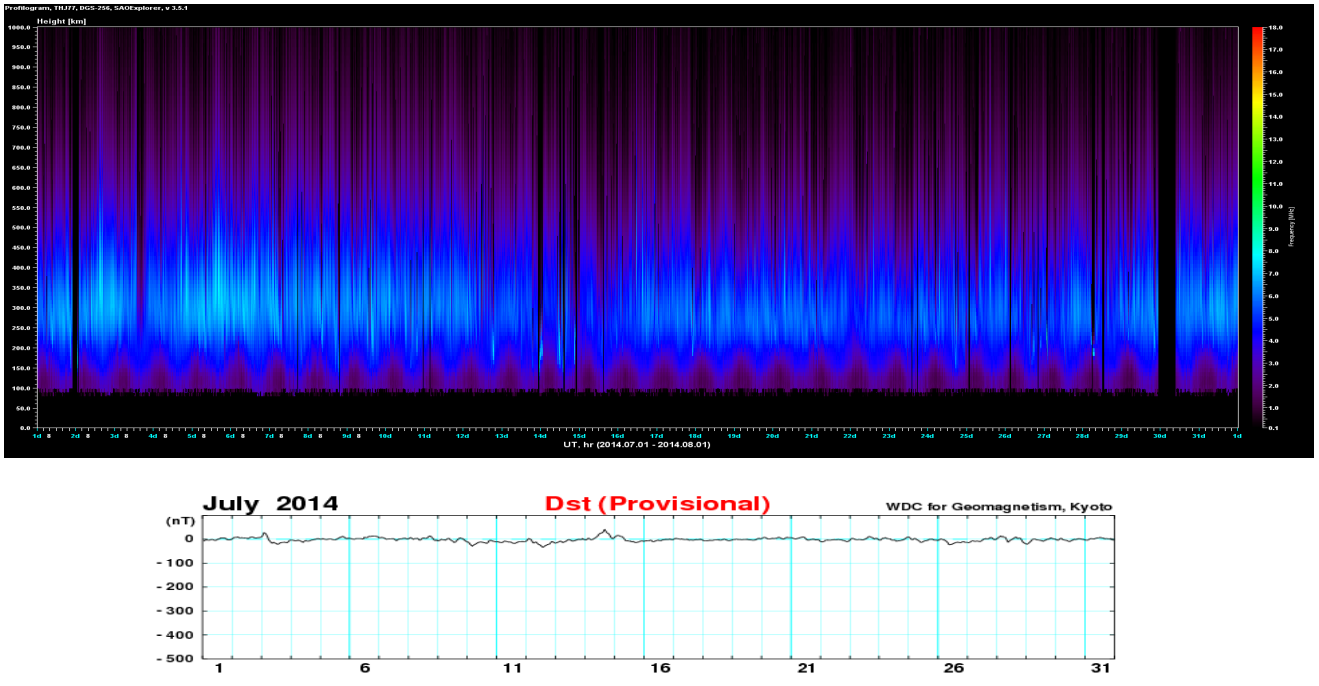

Figure 6.8b Digital ionosonde profiles and concurrent Dst time-series for July 2014.

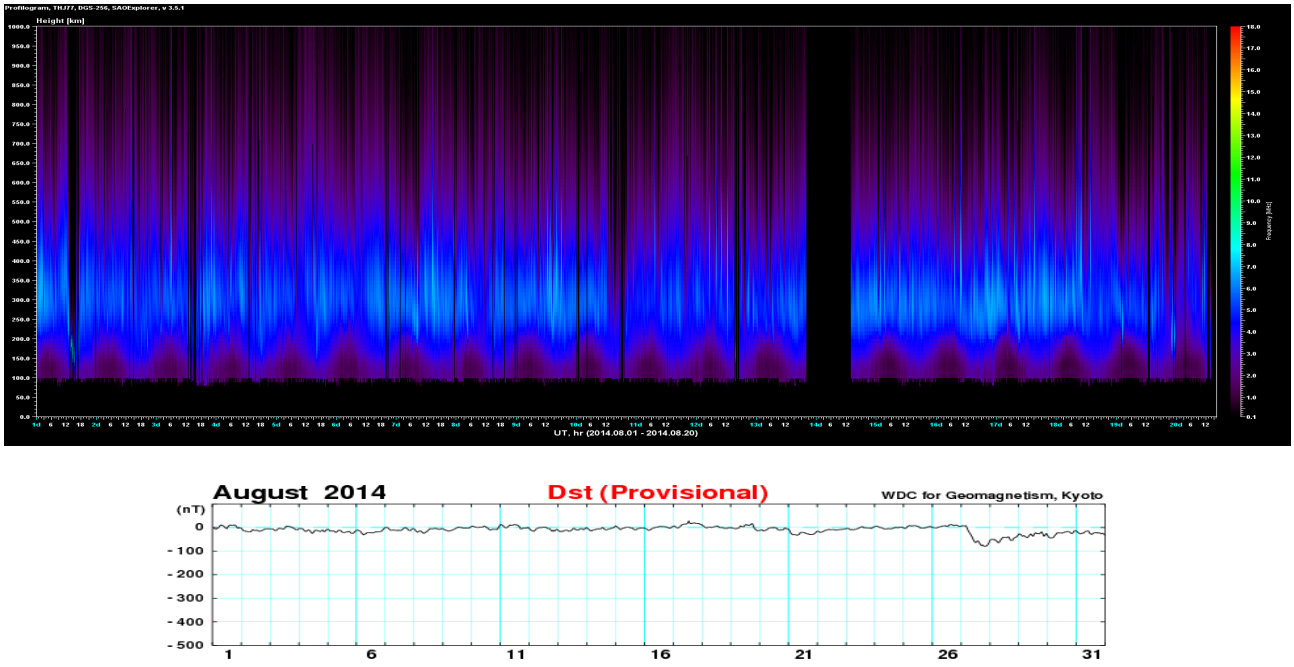

Figure 6.8c Digital ionosonde profiles and concurrent Dst time-series for August 2014.

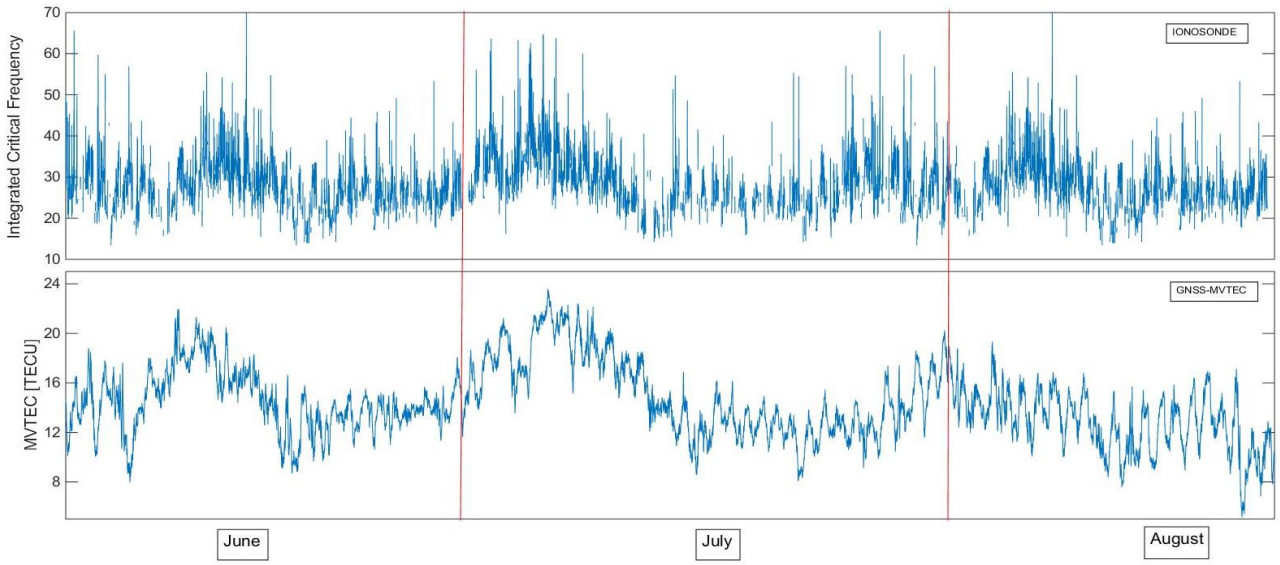

Figure 6.9 Validation of integrated digital ionosonde profile data against MVTEC.

Figures 6.10 and 6.11 clearly demonstrate at what altitudes the 27-day fluctuations (seen in Figure 6.4, bottom) occur in the ionosphere, from the digital ionosonde data. This is the F region where

atomic oxygen is the dominant species. Knowing the dominant species and where the bulk of the ionization occurs allows for an estimation of the required minimum energy to cause the TEC anomaly that is shown in Figure 6.4 (bottom), which is further discussed in Section 6.2.3.

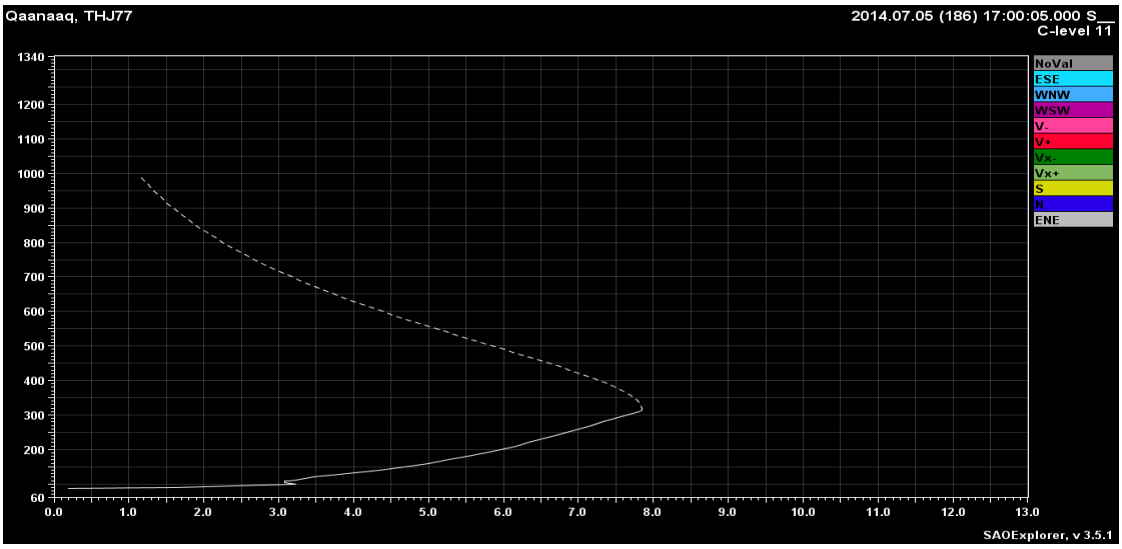

Figure 6.10 Digital ionosonde derived vertical N_e profile during high EUV irradiance during the 27-day variation's maximum enhancement.

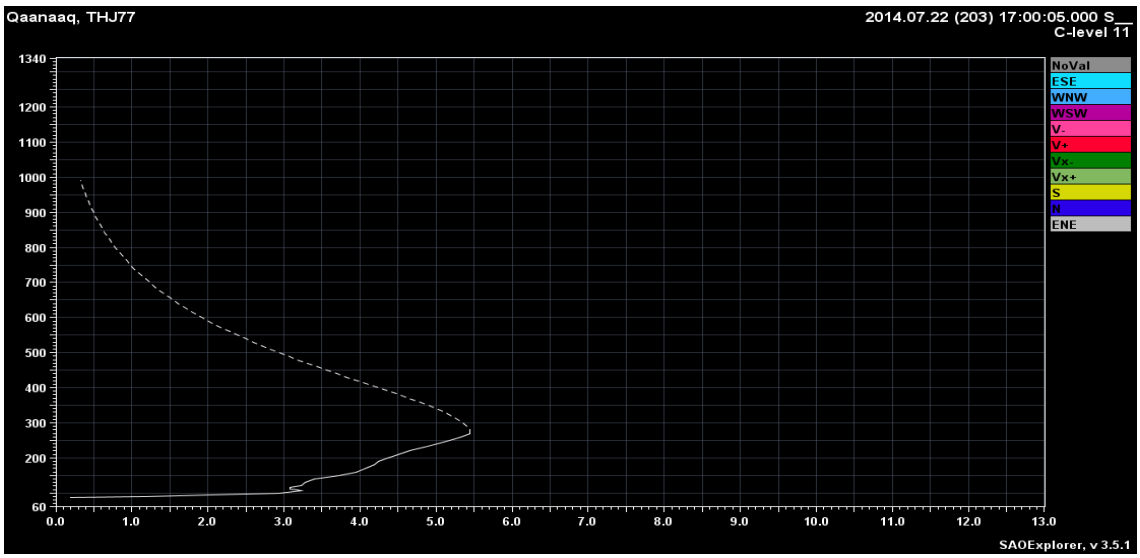

Figure 6.11 Digital ionosonde derived vertical N_e profile during low EUV irradiance during the 27-day variation's minimum enhancement.

6.2.2.3 Dependency of MVTEC Time-Series on Solar Irradiance

As it has been shown in previous chapters, solar EUV radiation plays a fundamental role in the formation of Earth's ionosphere. In addition to direct photo-ionization it also creates the conducting E layer, which plays an imporant role in the polar cap ionosphere dynamics as it consists of a highly conducting horizontal layer that can short circuit vertical geomagnetic field lines [Vickrey and Kelley, 1982]. Furthermore, solar EUV radiation can also induce thermal winds via solar heating and other effects. In this section, the dependency of MVTEC time-series on solar EUV radiation is studied. Note that solar wind related phenomena such as, CMEs can also cause geomagnetic disturbances, but the current focus is on EUV-driven processes)

The full SORCE mission plot can be seen in Figure 6.12, which shows TSI and thus includes the whole measured spectrum. TSI is measured in units of W/m^2 and it is an excellent indicator of solar cycle activity [Coddington et al., 2015]. As it was shown in Section 1.4, solar EUV radiation is the main driver of ionization in the F-region of the ionosphere, therefore the relevant wavelengths should be further explored. More specifically, the focus is on atomic oxygen photoionization (the dominant F region species) so only photons with 91.2 nm or shorter wavelength are relevant, as photons with less energy cannot ionize O. Therefore, instead of TSI we must focus on SSI and more specifically on the 91.2 nm or shorter wavelengths. Unfortunately, the shortest UV wavelength measured by SORCE is 115 nm, however a number of UV wavelengths were selected in the range of 115-350 nm, in addition to higher wavelengths (up to 1000 nm). Time-series of solar irradiance at these selected wavelengths are shown in Figure 6.13..

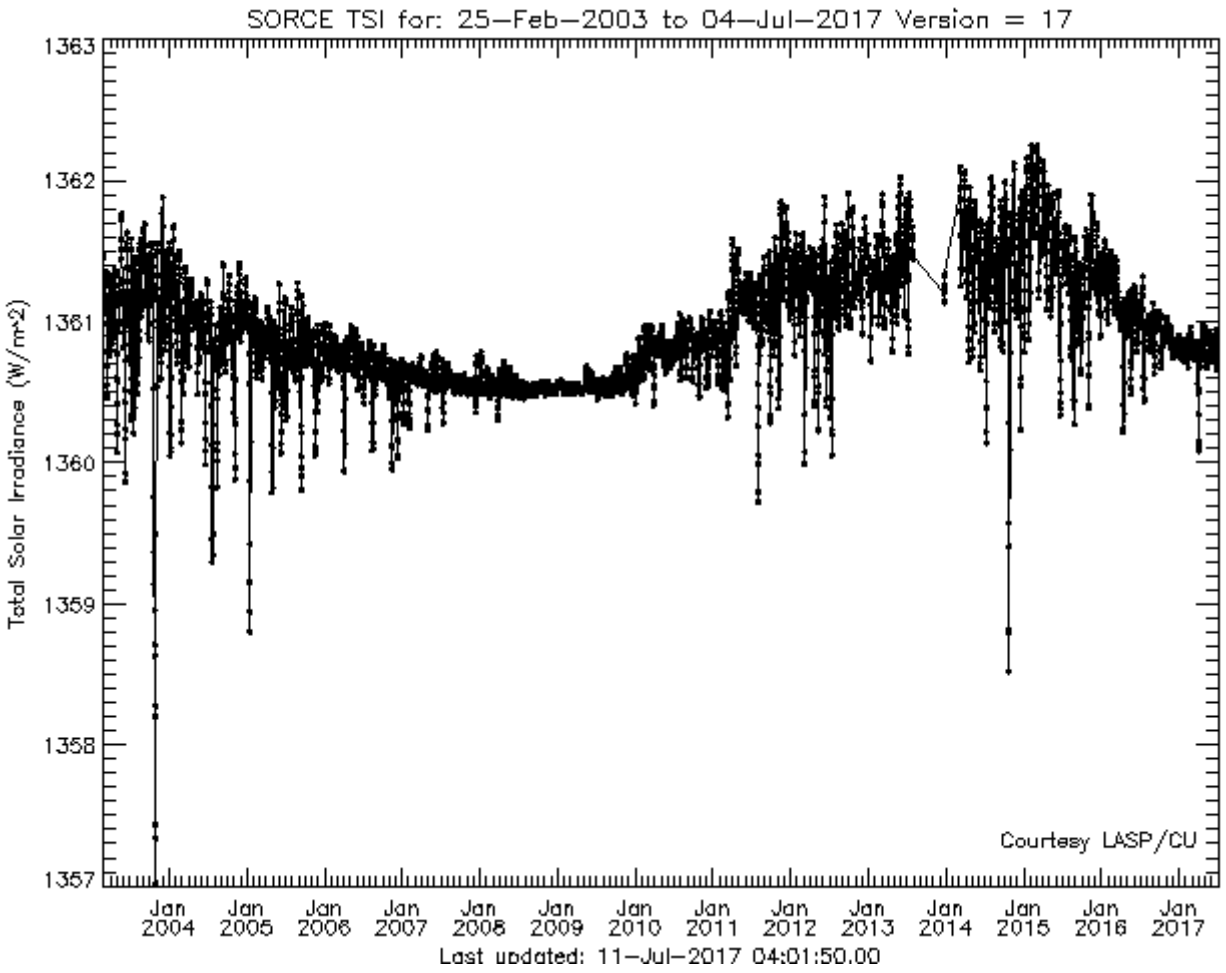

Figure 6.12 Total solar irradiance measured by SORCE showing data for the entire mission. The data shows clear correlation with solar cycle activity.

(From http://lasp.colorado.edu/data/sorce/total_solar_irradiance_plots/images/tim_level3_tsi_24hour_640x480.png)

In Figure 6.13, it is apparent that not all wavelengths have the same variability in solar irradiance versus time, and if compared with the ~27-day MVTEC data anomalies (Figure 6.4), one can conclude that correlation is only significant in the UV and shorter wavelengths. Figure 6.14 focuses on the summer of 2014 (compare it with Figure 6.4) at 115.5 nm which is the closest wavelength in the EUV band required to the atomic oxygen first ionization and shows clear solar rotation related fluctuations.

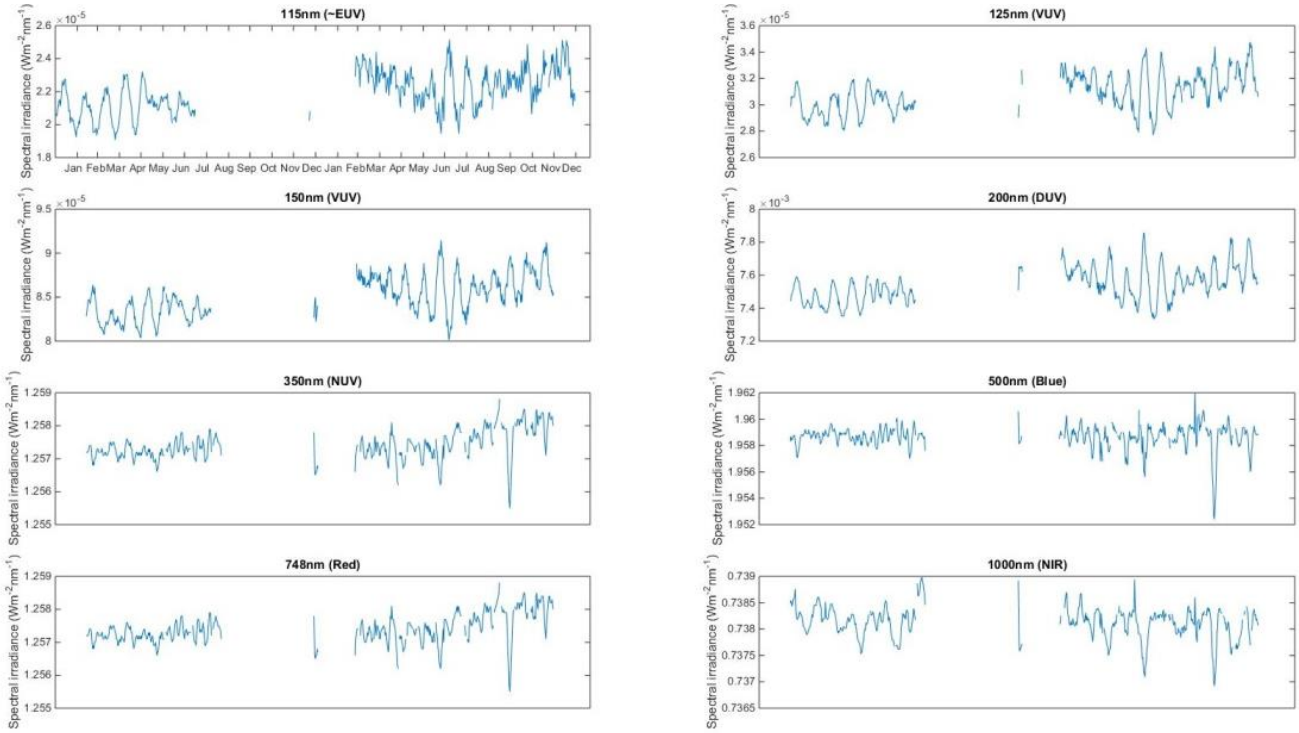

Figure 6.13 Solar spectral irradiances at various wavelengths measured by SORCE during 2013 and 2014. The spectral study reveals that quasi 27-day variations are present in the EU spectra, but not in the visible or longer wavelength bands.

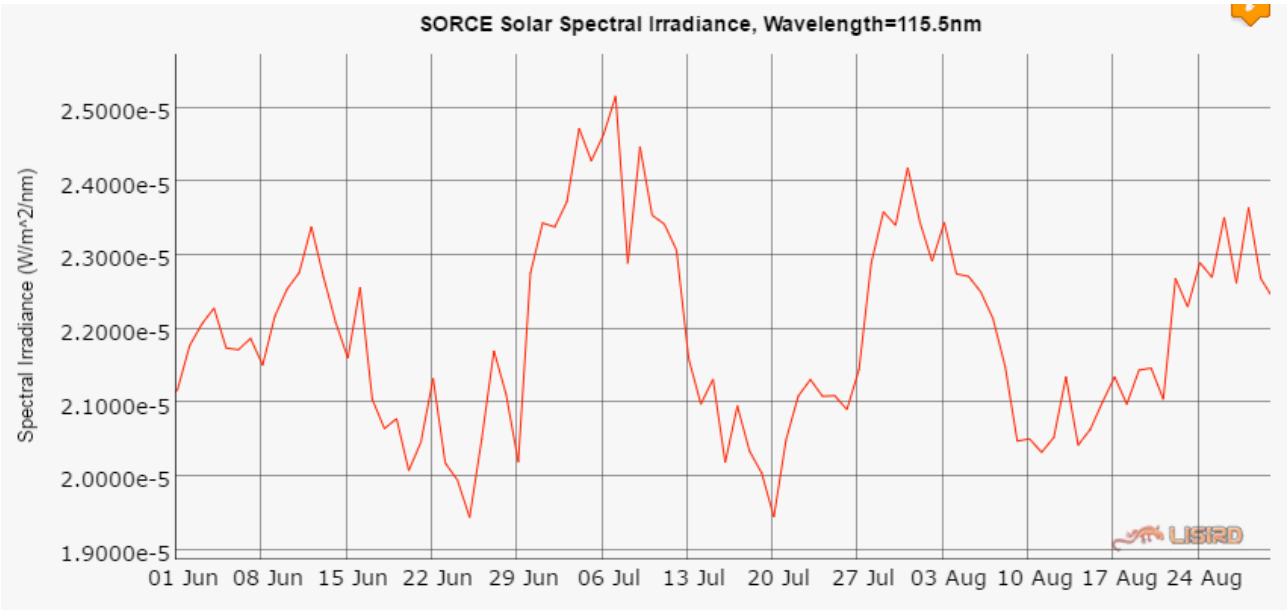

Figure 6.14 Spectral irradiance data acquired from SORCE showing the same variability as the MVTEC time-series during the summer of 2014 (see also Figure 6.4 (bottom)).

The possible connection between the SSI fluctuations and the MVTEC 27-day anomalies is discussed later in this chapter.

6.2.2.4 MVTEC Decomposition

The MVTEC time-series (Figures 6.2 and 6.4) was also analyzed using wavelet (Figure 6.6) and Fourier analyses (Figures 6.17 and 6.18) [Pinsky, 2002]. The goal of the wavelet and Fourier analyses was to identify the different drivers in the MVTEC data because certain influences can easily mask others when one only looks at the raw results. This is especially true for the equinoctial months where diurnal variations can be very large. This is still a work in progress but for the sake of completeness, it was included in this chapter. A detailed description of the employed mathematical tools in the Fourier and wavelet analyses can be found in Pinsky [2002].Since the MVTEC measures the superposition of various effects (diurnal, storm-related disturbances, seasonal etc.), with each having their own variability and reoccurrence, it would be useful to determine which are the most energetic frequencies and waveforms. The time-scales include interannual, annual, seasonal, sub-seasonal, diurnal, sub-diurnal, and even shorter storm or sub-storm (in the auroral region) related disturbances in the observed electron density.

Interannual changes can be related to long-term solar changes and solar cycles. Annual and seasonal changes are essentially related to earth's rotational axis' tilt relative to the direction of the sun [e.g., Russell and McPherron, 1973], and atmospheric heating induced secondary effects [e.g., Durgonics et al., 2017]. The so called sub-seasonal TEC anomalies are discussed later in this chapter, these are apparent in the polar cap ionosphere, but their presence at lower latitudes is not yet known. Diurnal changes are mainly resulting from Earth's rotation, while the even shorter sub-diurnal changes are

typically driven by geomagnetic storms or other disturbances that usually do not have a periodicity and may occur randomly.

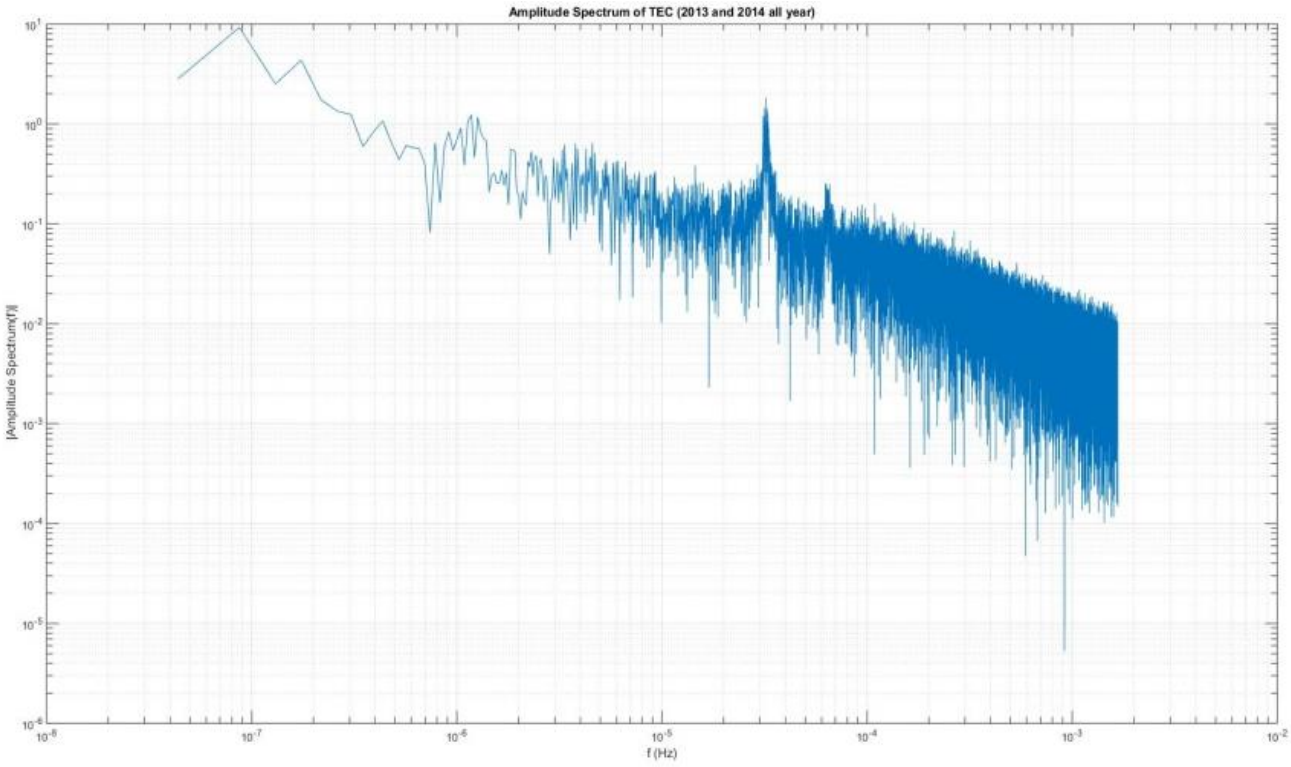

Figure 6.15 MVTEC Fourier spectra computed from 2-years of data (2013-2014).

In Figure 6.6 (bottom; wavelet analysis) it is clearly visible that the diurnal frequency is very dominant around equinoxes and in winter, but almost disappears during the summer. The reason behind this phenomenon will be discussed in the next section. The Fourier spectra (Figures 6.15 and 6.16 for the full two years and monthly for 2014, respectively) clearly show the diurnal peak and an approximately 8-12 hour half-day peak, but the ~27-day TEC anomaly is not apparent.

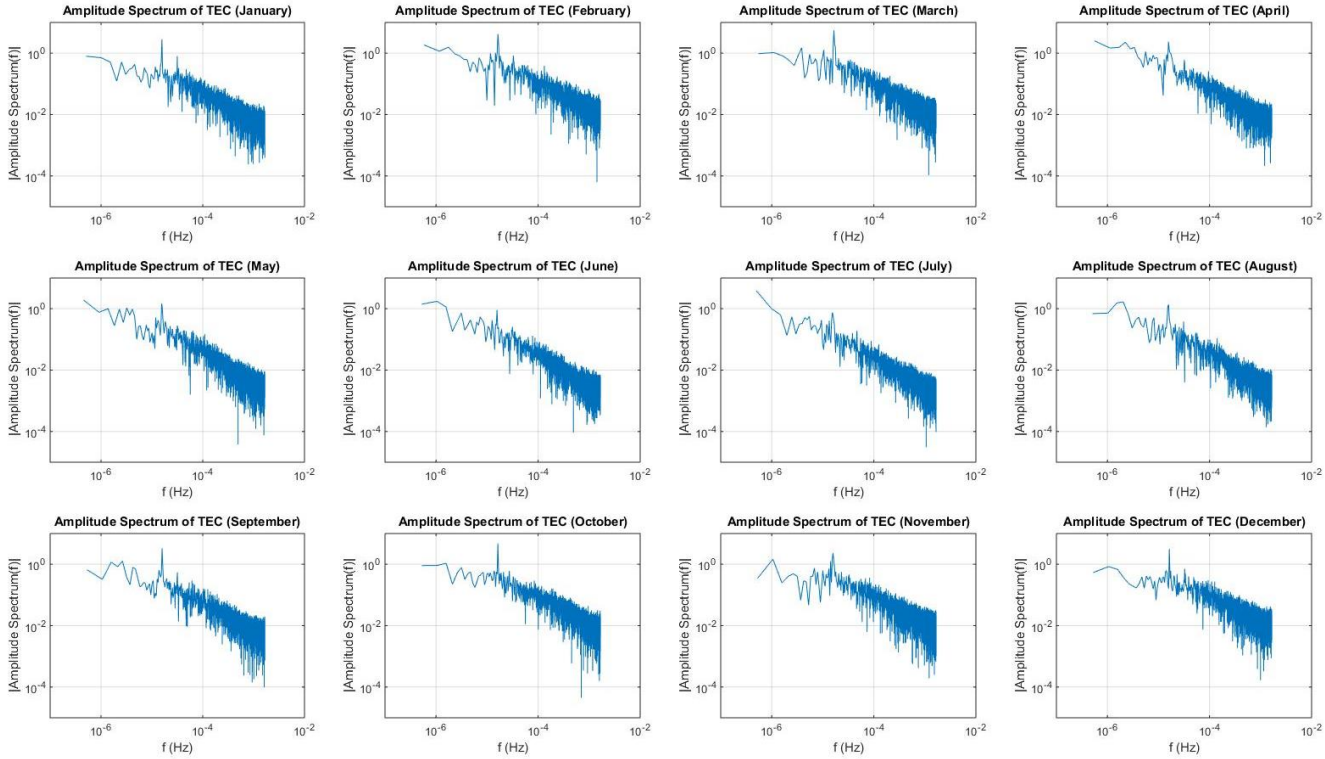

Figure 6.16 Monthly MVTEC Fourier spectra from 2014.

6.2.3 Discussion

Three distinct causes behind the features of the MVTEC time-series (Figure 6.2) were found in this study and further discussed below: (1) solar wind, (2) solar EUV (and higher frequency) radiation, and finally (3) a combination of solar EUV and E-layer-related causes.

(1) Russel and McPherron [1973] discussed in detail the semiannual variation of geomagnetic activity due to the varying angle between the southward component of the IMF with the magnetosphere. The exact mechanism and detailed discussion of the Russel-McPherron-effect is out of the scope of this work, but briefly, they used the relationship between the solar equatorial (GSEQ) [Coleman, 1966], solar ecliptic (GSE) [Russel, 1971], and the solar magnetospheric (GSM) coordinate system [Hirshberg and Colburn, 1969; Arnoldy, 1971] to infer that the semiannual

variation arises from the "varying probability of a southward component occuring in solar magnetospheric coordinates due to the changing orientation of the solar magnetospheric coordinate system relative to the solar equatorial system". This implies that the deposited energy is dependent on the angle between earth's rotational axis and the solar wind which is causing the semiannual anomalies. The semiannual variation of geomagnetic activity described in their study is likely to be responsible for the highly disturbed MVTEC time-series segment around equinoctial months. The enormous amount of energy that is required for the extra ionization of the polar cap ionosphere must be solar in origin due to the lack of other known potential energy input sources. The approximate lower energy threshold to uniformly raise polar cap ionization by ~10 TECU is around $\sim 10^{13}$ J. This was calculated using a series of simplifying assumptions: pure atomic O atmosphere (the most probable species in the F region), uniform density (obtained from the MVTEC), neglecting all other interactions and losses, and spherical sector geometry. During the disturbed weeks (compared to the solstitial months) approximatey 40% more solar wind energy (including e.g., HSSs, shocks, CMEs) is being deposited into the magnetosphere. This extra energy will also cause increased disturbances in the ionosphere via magentosphere-ionosphere coupling mechanisms, resulting in the MVTEC features observed around equinoxes. Note that the exact physical mechanism of the propagation of this extra deposited energy into the polar cap ionosphere that is inferred by Russel and McPherron [1973] and the calculations presented here requires further studies. These studies could potentially use solar wind parameter data (e.g., B_z) SuperDARN convection and potential maps combined with GNSS-derived TEC maps, Swarm measurements, and other available satellite and ground-based observation techniques.

(2) There are other features in the MVTEC time-series (Figures 6.2 and 6.4) that still cannot be explained merely by solar wind and magnetosphere interactions (see Figures 6.6 and 6.7). These are the solar irradiance driven variations. Some of these are obvious, for example, one would expect

that during summer months the polar cap ionosphere would receive more ionizing radiation, therefore higher TEC values would be observed. Futhermore, there is a time period when the sun is always above the horizon of the polar cap region, thereby causing continuous (although with varying incident angle) ionization all day. If one assumes that the only factors affecting MVTEC are those described above, a quasi-sinusiodal MVTEC time-series can be assumed throughout the year with the peak during summer and lowest values during the winter months. Figures 6.2, 6.4, and 6.5 reveal a somewhat different picture. Some of the observed anomalies can likely be attributed to the Russel-McPherron effect discussed earlier, but other anomalies possibly have a different driver.

The period of the MVTEC anomalies appear to be around just a few days less than a month which could potentially indicate good correlation with the 27-day solar rotation. For details about the differential rotation of the sun see, e.g., Beck [2000] and later in this Section. To validate that this 27 day electron density variation is present in other independent measurements as well, data acquired from the Qaanaaq digital ionosonde was employed. During the summer months (June, July, and August) of 2014 (Figures 6.8a, 6.8b, and 6.8c) critical frequency profiles were caculated. Figures 6.10 and 6.11 demonstrate how the profiles differ during a specific 27 day electron density maximum and minimum. The results indicate that the overwhelming portion of the ionization is occuring in the F_2 region (note that another viable method to determine vertical N_e profiles could be to employ RO data from polar orbiting satellites) and that the 27 day variation can be observed in the digital ionosonde data as well.

Figure 6.19 demonstrates the connection/correlation between the number of sunspots to the observed solar EUV spectral irradiance. While a model strictly considering only total solar irradiance does not explain the 27-day anomaly, the EUV portion of the solar irradiance correlates well with the MVTEC. This correlation is significant, furthermore it is also clear that other effects must also be present since the sunspot numbers do not account for all the variations in EUV.

Nevertheless, using the aforementioned observations, one can infer that the ~27-day MVTEC variations are solar rotation dependent. More specifically, as the sun rotates, Earth's ionosphere will receive varying amount of ionizing radiation depending partially on the number of existing sunspots. Kitchatinov [2011] discussed the phenomenon of solar differential rotation. The summary of solar differential rotation is the following, different latitudes of the solar surface rotate with different periods, the period of rotation is shortest (~24.47 days) around the solar equator and longest (~35 days) close to the poles. This implies that the sunspots also rotate differentially.

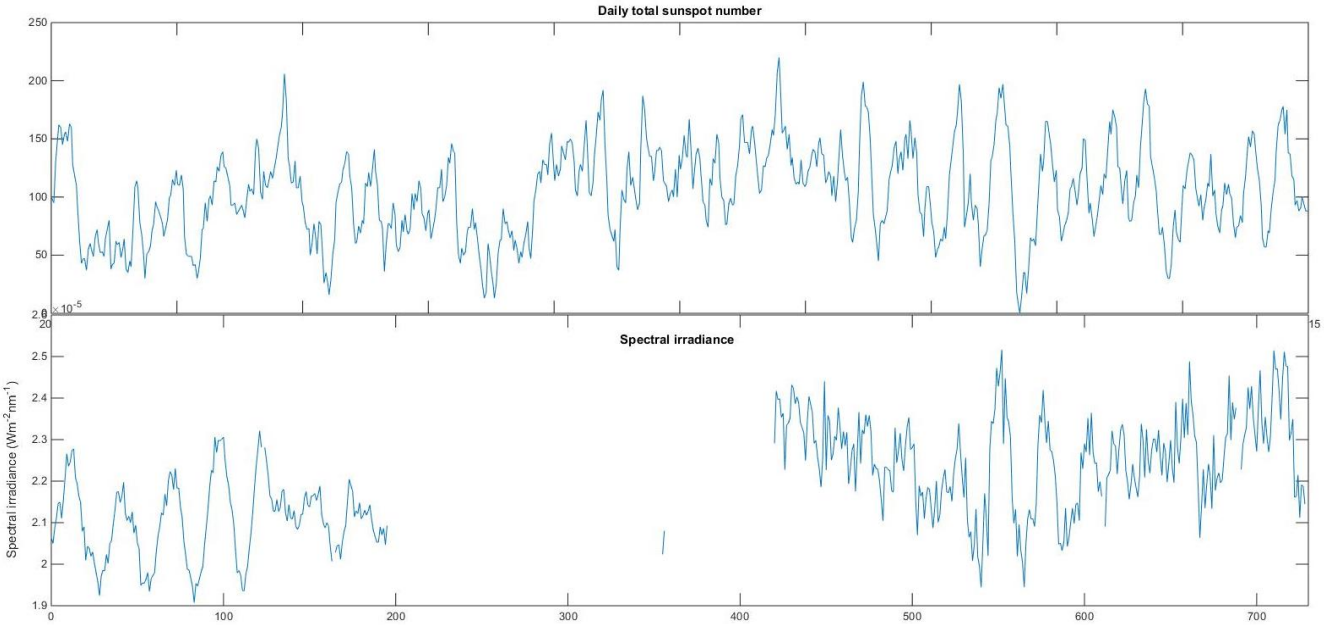

Figure 6.19 Correlation between daily total sunspot numbers and solar EUV spectral irradiance during 2013 and 2014. The x-axis is time in days from the first day of 2013.

(3) The third phenomenon is also fundamentally solar EUV-induced, but there is a significant secondary effect is also at play which is related to polar cap E layer. Therefore (3) is discussed separately from (2). The theory proposed here is based on a modeling effort made by Vickrey and Kelley [1982]. This model (referred to here as Horizontally Structured F region Plasma Decay

Model or FPDM) attempts to explain by what physical mechanisms the polar cap (and also the auroral) F layer structures decay, including the effects of a conducting E layer.

Both the highly structured F layer and the conducting E layer are ubiquitous features of the Arctic ionosphere (although most of what is written here may be valid for both polar caps and auroral regions, the data presented here obtained solely from the Arctic region, therefore there will be no claims about the Antarctic ionosphere in this work) and are fundamental features of the FPDM. These ionospheric structures and other large-scale, high-latitude ionospheric phenomena have been described by many authors, e.g., Pedersen et al. [1998], Prikryl et al. [2016], and Durgonics et al. [2017]. These include TOI, polar patches, polar holes, ionization troughs, auroral ionization enhancements, electron/ion temperature hotspots. The occurrence of these features and their exact characteristics depend on several factors, e.g., convection patterns, local time, season, IMF/solar wind parameters, and even the solar cycle [Schunk and Nagy, 2009]. It is also important to note that the Arctic ionosphere is obviously not a closed system and there can be significant plasma transport from midlatitudes. This midlatitude originated plasma can be transported antisunward into and across the polar cap which occurs mainly during southward IMF when there is a two-cell convection pattern present in the polar cap [Zou et al., 2014]. The source of this plasma can be storm enhanced density (SED) plumes. SED plumes are observed between the post-noon and pre-midnight sectors and are essentially distinct regions of enhanced plasma densities. SEDs have been studied by several authors [e.g., Coster et al., 2007; Zou et al., 2014; Liu et al., 2016] but not yet completely understood and are out of the scope of the current work.

The detailed mathematical derivation of FPDM can be found in Vickrey and Kelley [1982] but a short summary is presented here. Some simplifying assumptions are made: (a) The E layer is treated as a uniform, conducting medium (this is a good approximation for a summer polar cap ionosphere) by employing the height-integrated Pedersen conductivity, $\sum_P^E$. (b) $N_e(z, \boldsymbol{r}, t)$ can be mathematically

separated into *Z(z)N(**r**, t)*, where the ***r*** vector is perpendicular to the magnetic field **B. B** is assumed to be vertical in the polar cap. (c) **E** is independent of altitude, ***z***, due to the sufficiently high vertical conductivity. (d) Quasi neutrality is valid, that is $N_e = N_i = N$. Using these assumptions and introducing the ion and electron continuity equations, Vickrey and Kelley [1982] derive the equation for the relationship between **E** and density gradient ∇N, which also includes the effects of the conducting E layer:

$$\boldsymbol{E}(\boldsymbol{r},t) = \left[\frac{q_i(D_{i\perp}-D_{e\perp})}{\sum_i^F+\sum_e^F+\sum_P^E}\right]\nabla_\perp N(r,t), \tag{6.1}$$

where $\sum_i^F$ is the height-integrated ion conductivity, $\sum_e^F$ is the height-integrated electron conductivity, q_i is the species charge, $D_{i\perp}$ is the ion ambipolar diffusion coefficient, and $D_{e\perp}$ is the electron ambipolar diffusion coefficient. $\perp$ represents a perpendicular orientation relative to the magnetic field. The ambipolar diffusion coefficients are calculated from the diffusion tensors. Ambipolar diffusion arises when the polarization electric field (this occurs when a force is trying to separate the ions from the electrons) does not allow more than a slight charge separation between ions and electrons in the ionospheric plasma and thus the ions and electrons move together under the influence of acting external forces.

In case of an insulating E layer (e.g., in the winter-time polar cap) Equation (6.1) can be simplified and takes the form of:

$$\boldsymbol{E}_{winter}(\boldsymbol{r},t) = \frac{K_B T_i}{q_i}\frac{\nabla_\perp N(r,t)}{N}, \tag{6.2}$$

where K_B is the Boltzmann constant and T_i is the ion temperature [Vickrey and Kelley, 1982; Schunk and Nagy, 2009]. One is now able to compare the FPDM predictions with the MVTEC observations (Figure 6.2 and 6.4). It is expected that according to Equations 6.1 and 6.2 there would be different ionospheric features observed during winter (when the polar cap is essentially void of

solar photoionization or photoionization is significantly decreased), summer (when the polar cap ionosphere is sunlit constantly or during most of the day), and finally there should be some transition period around the equinoxes when the effect described in Russel and McPherron [1973] is also occuring.

During winter, the highly conducting E layer is generally not present in the polar cap and 10 km scale size patches (irregularities) can survive diffusion decay for days, which is more than enough time to convect through the polar cap several times. At 1 km scale size the decay rate is two order of magnitudes faster, which effectively means hours of survival at most. Even at smaller scale sizes (around hundreds of meters), the diffusion is so fast (even with insulating E layer) that these scale sizes should not be present in the observations. However, small scale size structures have been observed, implying a contribution from other processes that are not included in the FPDM [Vickrey and Kelley, 1982]. Comparing the results expected from the model with the observations, very high MVTEC variations can be identified during the winter months in Figure 6.2 which occur due to fast-propagating patches that are present at most times and are not fast decaying. Note that MVTEC is only sensitive to larger scale-size structures which decay very slowly during winter according to FPDM.

In addition to the FPDM model predictions, a closely related phenomenon described by Basu et al. [1987] should be discussed in the same context. During summer or anytime when flux tubes move into a sunlit sector, the lower-density structures (holes) between patches (enhancements) will be "filled in" by photoionization, and provided there is enough time for this process, it should reach a common plasma number density [Vickrey and Kelley, 1982; Basu et al., 1987]. Basu et al. [1987] used amplitude scintillation data acquired from Thule at 250 MHz and found an equivalent phenomenon. To justify this equivalence, it is necessary to understand the relations between amplitude scintillations and TEC variations. It is known from Pi et al. [2013], Jacobsen [2014] and

Durgonics et al. [2017] that amplitude scintillations exhibit a non-linear correlation with ROTI (which is another scintillation index that is calculated differently). ROTI is calculated from L1 and L2 observables, similar to how TEC is calculated (for the exact equations see, e.g., Jacobsen [2014]). Therefore, when there are high variations in the MVTEC data, it can also be expected that the scintillations are also strong in that region, or more precisely along the same signal path. And thus is it valid to use the findings in Basu et al. [1987], where it is described that due to this "filling in" photoionization effect, the summer polar cap ionosphere always shows diminished scintillations, while during equinoctial weeks it is 10 times as likely to occur. Basu et al. [1987] found that statistically, the highest scintillations occur just after the equinoxes, but they remain consistently high throughout the whole winter. This may imply that the Russel-McPherron effect has an even larger impact on the polar cap scintillations than the slowed decay due to the insulating E layer.

6.2.4 Summary

Three distinct phenomena have been discussed in this work that could explain the main features of a set of 4-year regional electron density observations obtained from the Thule GNSS site deep in the Arctic region. The key results are briefly summarized below. These are original contributions and have not been explored before this study.

(1) Russel-McPherron effect: the high MVTEC variability near the equinoxes is due to the 40% increased energy input from the solar wind into the magnetosphere during these times. The increased energy injection consequently results in increased ionospheric disturbances in the Arctic ionosphere.

(2) SSI EUV-related 27-day fluctuations: there is an approximately 27-day fluctuation with an amplitude of 10-15 TECU in the MVTEC data throughout the studied years. These fluctuations are more apparent during the summer when the ionosphere is smooth due to the "filling in" effect caused by the constant solar photoionization. The fluctuations correlate with solar EUV, F10.7, and sunspot numbers, indicating that solar rotation plays an essential role in the process.

(3) E layer conductance dependent diffusion model, FPDM: During the summer the MVTEC time-series are significantly less variable than during the winter or equinox times. These results can be interpreted using the FPDM model developed by Vickrey and Kelley [1982]. During the summer, the F layer cross-field plasma diffusion rate is increased when there is an underlying conductive E layer. During the winter, the insulating E layer slows the F layer plasma decay rate, thereby allowing F layer structures to survive significantly longer and thus cause higher variability in MVTEC.

CHAPTER 7

CROSS-VALIDATION OF TEC DATA PRODUCTS

7.1 Introduction

This chapter contains an abridged version of a technical note that was prepared for the Space Situational Awareness (SSA) program of European Space Agency (ESA) by Per Høeg and Tibor Durgonics. Its goal is to support the European independent utilization of and access to space for research and services, through timely and quality data, information, services and knowledge regarding the environment, the threats, and the sustainable exploitation of space. The present text is shortened; some specific parts are omitted, and it focuses on the scientific applications rather than the technical details. The goal is to give the reader an overview about the newest approach to TEC map validation. The scientific background and technological details behind 2D TEC maps are described in, e.g., Chapter 2 and Chapter 3.

TEC map validation is a fundamental issue when it comes to space weather activities at agencies such as NASA and ESA. Map errors are typically given in root mean square (RMS) maps attached to the TEC data products, but these metrics do not answer the question of how close these maps are to physical reality. There have been attempts of such cross-validations before. For example Hernandez-Pajares et al. [2008] approached this problem by statistical means using several years of data. In this work, a different approach was employed where specific geomagnetic events were

focused upon, and the variation between different data products was studied in terms of how they describe calm and disturbed times. The users of these TEC maps are often interested in ionospheric corrections, but they also have to be aware of how reliable these products are and which are the most reliable.

7.2 Objectives and Approaches of the TEC validation

TEC maps are empirical, or parameterized, or tomographic representations of large-scale TEC based on regional observations. The cross-validation is performed by comparing the obtained ESA's Ionospheric Weather Center data products (*http://swe.ssa.esa.int/ionospheric-weather*) with results from the IGS and the CODE database (*ftp://cddis.gsfc.nasa.gov/gnss/products/ionex/*) for the same periods. The comparisons were performed for (1) a one month-period during equinoctial conditions at northern hemispherical latitudes (March 1 – March 31, 2015) and (2) a one-month validation during winter conditions (October 15 – November 15, 2015). The geophysical conditions for the chosen periods cover quiet, moderate and disturbed conditions. In period (1) we have maximum Dst of -200 nT, and Kp larger than 8 with large negative B_z of 20 nT. In period (2) we have maximum Dst of 100 nT, and Kp larger than 5 with large negative B_z values.

The validation is about the strength of the correctness of an output or geophysical parameter, while verification addresses the truth and accuracy of the observable. The test procedures will contain comparisons of the above-mentioned dataset, so the validation approach will identify resemblances and discrepancies in the data products (cell differences, standard deviations, biases, and dilution of precision). The validation is based on a correlation scheme for sub-regional areas. To minimize the assessment of the outcome only extreme differences, averages, standard deviations, and biases were considered. This will be complemented by a geophysical analysis of spatial and temporal changes.

Conclusions of the cross-validation exercise are presented in the last chapter of the report, highlighting development requirements, as outcome of the campaign, providing a set of guidelines for users, indicating recommended products under given sets of geophysical conditions.

7.3 Data Products for the Cross-Validation

TEC maps are typically given in IONEX format with a few exceptions (the IONEX format description can be found at: *https://igscb.jpl.nasa.gov/igscb/data/format/ionex1.pdf*). The ESA TEC map data products are listed in the below table, including their internal numbering. They differ not only in coverage area, temporal, and spatial resolution, but also in the applied background models, input data, and mapping approaches. Some TEC maps are generated near real-time (NRT), while others are a-posteriori analysis. Also forecast products are available. The most important product parameters are listed in the next Table 7.1.

The IGS and CODE TEC data products are both global with a 2.5-degree latitudinal and 5-degree longitudinal grid. Their single-layer shell height is 450 km and using a *cos(z)* type mapping function similarly to the ESA products.

ID	Coverage [Long.; Lat.]	Spatial resolution [Long.; Lat.] Degrees	Temporal resolution	Type	Background models
I.101	[30W-50E; 30N-72N]	[2; 2]	NRT	Current	NTCM-EU
I.102	[30W-50E; 30N-72N]	[2; 2]	1 hour	Forecast	-
I.103a	[180W-180E; 90S-90N]	[5; 2.5]	NRT	Current	NTCM-GL
I.103b	[180W-180E; 90S-90N]	[5; 2.5]	NRT	Current	NTCM-GL
I.104	[180W-180E; 90S-90N]	[5; 2.5]	1 hour	Forecast	-
I.107	[10W-40E; 50N-80N]	[1; 1]	NRT	Current	None
I.117	[10W - 40E; 35N - 55N]	[1; 1]	NRT	Current	TaD

Table 7.1 Important parameters of some example ESA TEC map data products.

7.4 Description of the Geophysical Conditions

The month of March 2015 was chosen for identifying how well the ESA data products are in accordance with similar global data products from other international entities during an event that primarily is quiet to moderately disturbed with one major severe period (CME + HSS). This month starts having quiet conditions in the ionosphere, which suddenly changes for a three-day period into a strongly disturbed situation (see Table 7.2 and Figure 7.1). After the severe event a standard decay is observed, which returned to a normal situation for the rest of the month.

Dates in March, 2015	Disturbance level	Specifics
1 – 16	Normal (Kp < 3)	From March 15 and onwards B_z turns negative.
17 – 18	Severe (5 < Kp < 8)	Kp increase from 3 to 8 at 4:00 UT on March 17. Strong proton events March 16 – 17.
19 - 24	Moderate (Kp < 5)	From March 20, the event decays to a Kp of 3.
25 – 31	Normal (Kp < 3)	

Table 7.2 Outline of the major conditions in the ionosphere and solar wind for the month of March 2015.

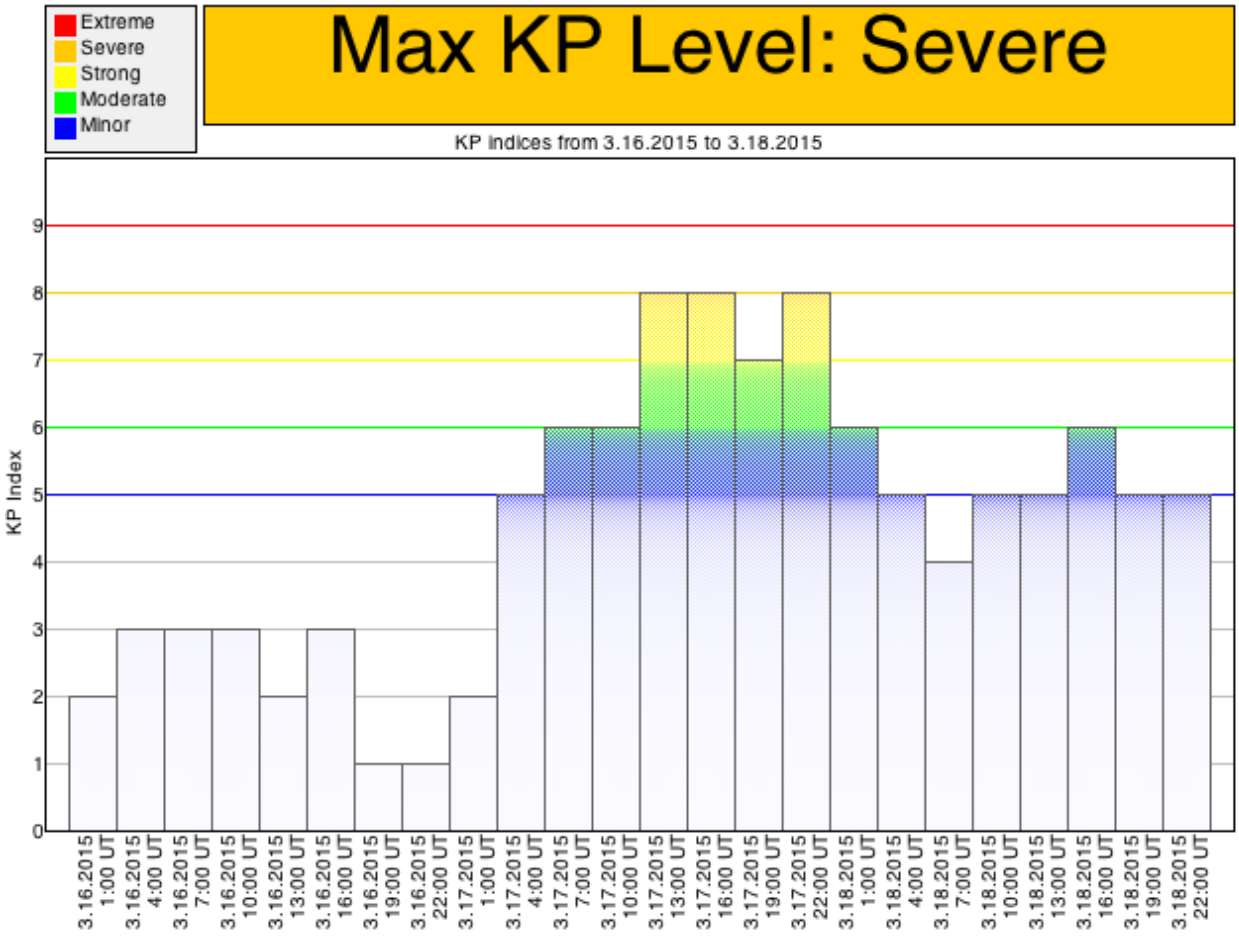

Figure 7.1 Plot for Kp index for the severely disturbed period of the ionosphere-magnetosphere system. The time window from onset to peak disturbance is less than 9 hours.

This period, ranging from October 15 until November 15, consists of a basically quiet period (Kp < 3) overlaid by three minor to moderate disturbed periods (November 3rd – 4th, 6th – 7th, and 10th) where Kp reaches 5 to 6 (See Figure 7.3).

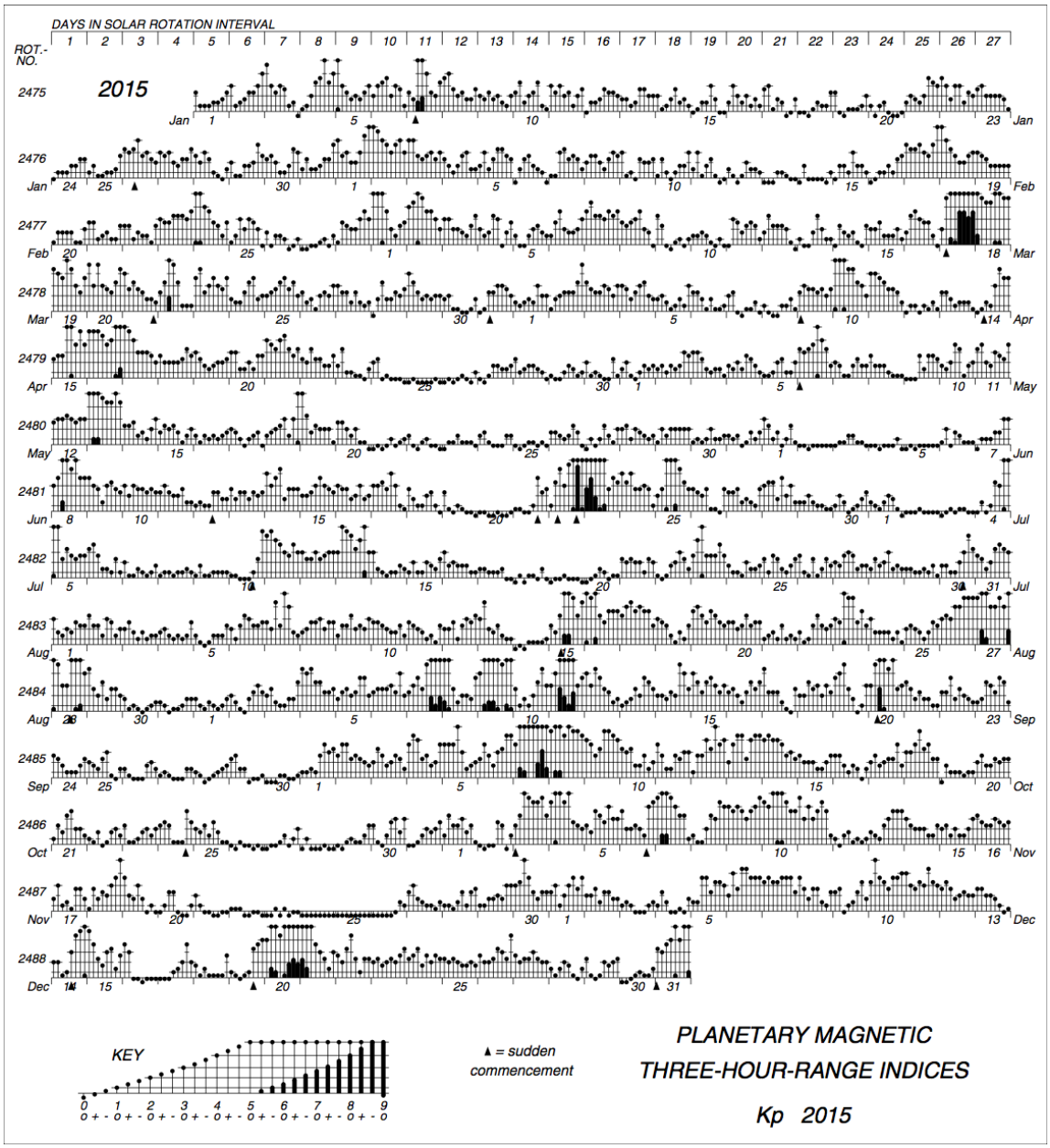

Figure 7.3 Planetary magnetic Kp index for 2015, covering the two chosen periods in 2015 for the cross-validation analysis project (source: *http://wdc.kugi.kyoto-u.ac.jp/kp/index.html*).

The three events in the period are driven by HSS's and CME's of short duration (less than 9 hours). But they all give rise to expanded polar cap regions of magnetic open-field lines.

7.5 Cross-Validation Results

The VTEC maps from ESA, CODE, and IGS are all retrieved from networks of ground GNSS-receiver measurements of STEC. The observed STEC variations are normally very precise and better than 0.1 TECU. The data are obtained through combined code and carrier phase observations. Raw data are pre-processed for removing cycle-slips, satellite position and satellite orbit errors, and antenna phase center offset. The L1-L2 bias estimation of STEC leads to the computing of the delay code bias of the GNSS satellites used in the observations for that specific station. VTEC is then estimated for each single station through a mapping function procedure. The station set of STEC measurements are interpolated to form the station VTEC at that instance in time. The delay code bias is normally larger at lower and equatorial latitudes due to the higher electron density in the height profile of the day-time ionosphere. Other studies have shown that the biases applied at different centers are rather constant and driven by their retrieval procedure. The differences are in the range of 1-2 TECU. Figure 7.4 shows a difference map computed as a pixel-by-pixel difference between ESA and an external data product. Computationally it is done as, e.g., $TEC^{a}_{x,y}$ - $TEC^{b}_{x,y}$, where *a* and *b* are two different maps and *x,y* are pixel coordinates covering all latitude and longitude values. The pixel-by-pixel difference method requires the two maps to have the same grid resolution. When the maps had different grids the less dense grid was interpolated and sampled at the denser grid points and the subtraction can be done after this step, see Figure 7.5. Note that this grid matching technique will not improve the information content of any map; it is simply a computational way to make the map subtraction possible.

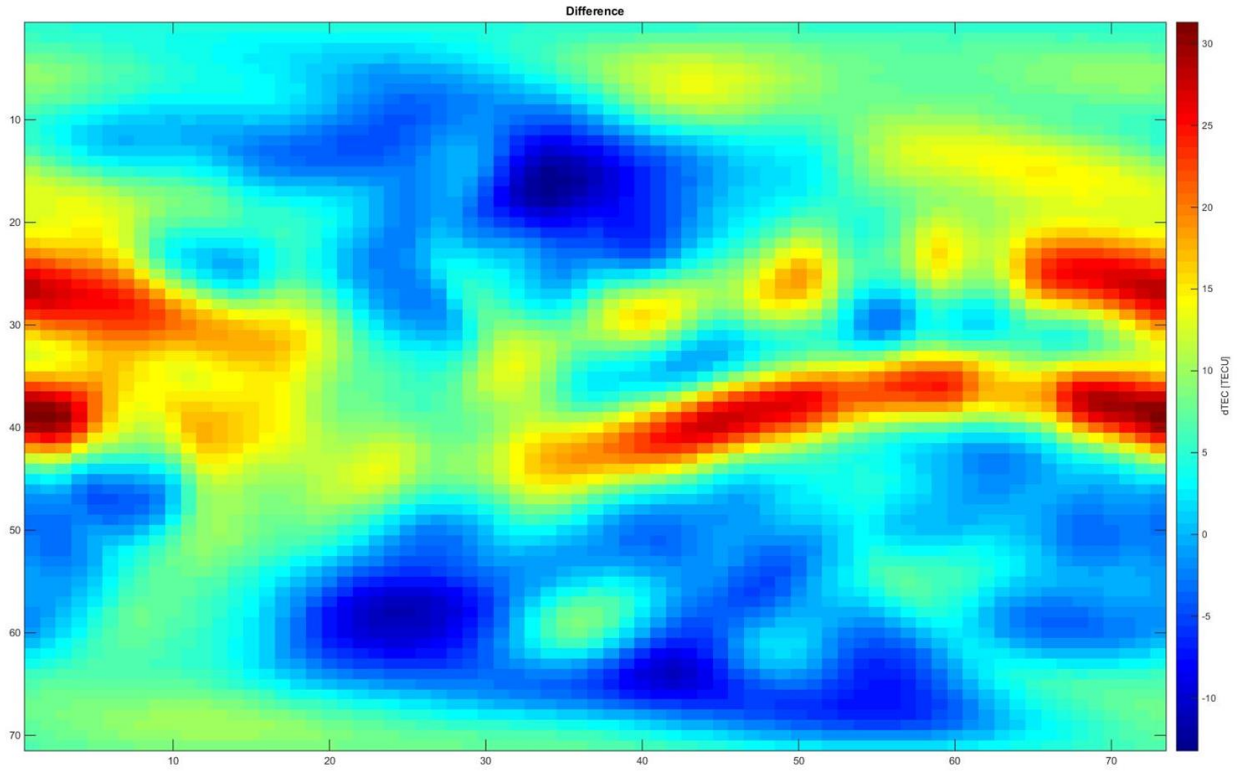

Figure 7.4 Raw global TEC difference map computed from ESA and IGS data products.

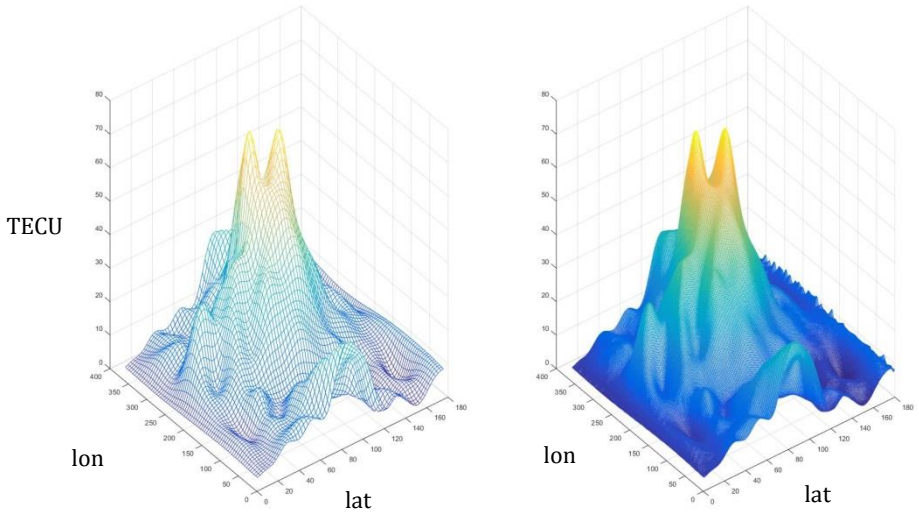

Figure 7.5 (left) Original global data grid 5-degree by 2.5-degree. **(right)** The new and interpolated data grid with 1-by-1-degree resolution.

The data in this study represent a more global view of the geophysical conditions with a two-hour resolution. This can be clearly identified when focusing on the CME event of March 17, 2015 (marked by a red vertical line in Figure 7.6). The number of outlier data increased during the event, while the mean difference did not change, indicating that regional changes are more important in the onset phase of a CME.

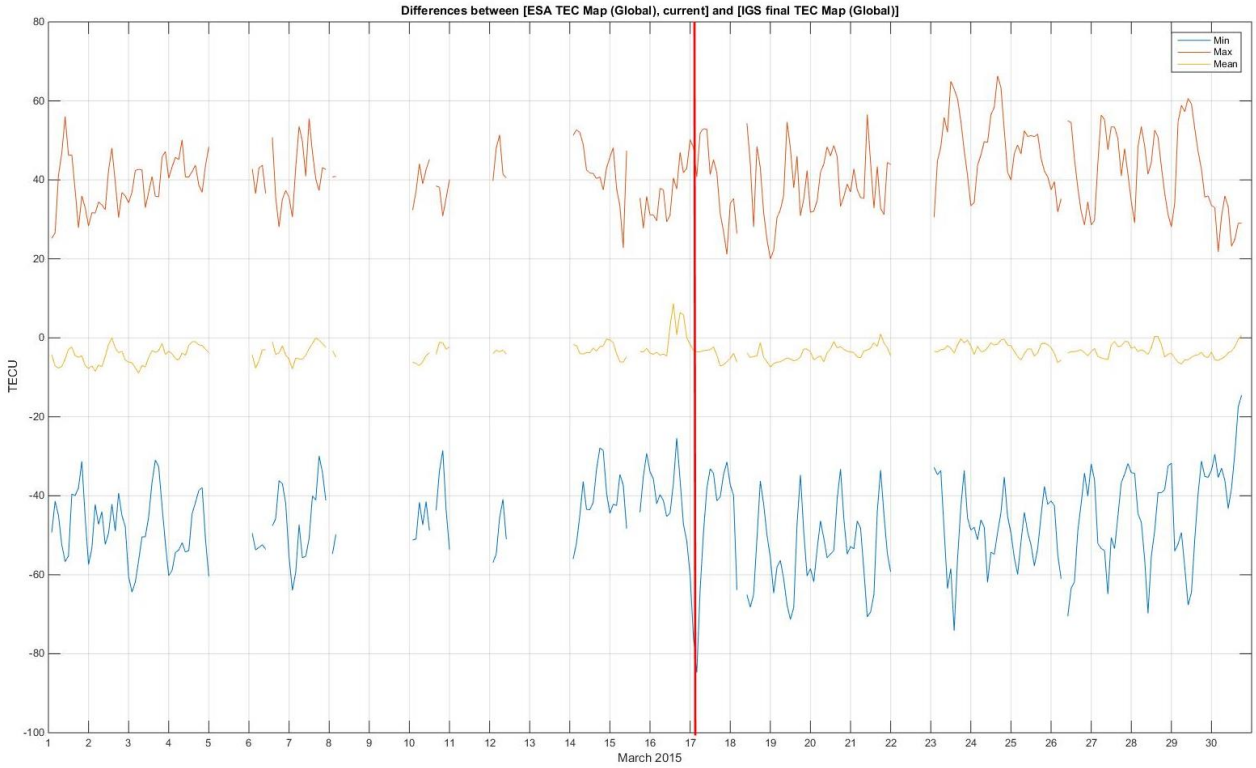

Figure 7.6 Difference plot between ESA(I.103a) and IGS data for the month of March 2015. The red and blue curves mark the envelope of the differences, while the yellow curve depicts the mean of all differences for that instance in time.

Note that this was reversed for the conditions on March 16, which leads up to the March 17 event. This may be because data are not observed over the oceans and that the ESA data products tend to present more clearly the phenomena monitored in the European sector. Figure 7.7 shows new and

interesting information about the characteristics of the difference density distribution functions. The bulk of the global observations are within 7.5% of the mean difference. This is the dominant scenario, especially during quiet and normal conditions. While during the build-up of the severe event on March 16-17, 2015, quite different and peaked distributions are observed with larger offset to the average mean of the month (4.3 TECU). On March 16, 2015, a sinusoidal movement is seen, indicating that the preliminary phase of the severe disturbance does start over Europe, but gradually the effect is transferred to the magnetosphere and ionosphere giving rise to TEC changes over Europe during a period of less than 12-hour period.

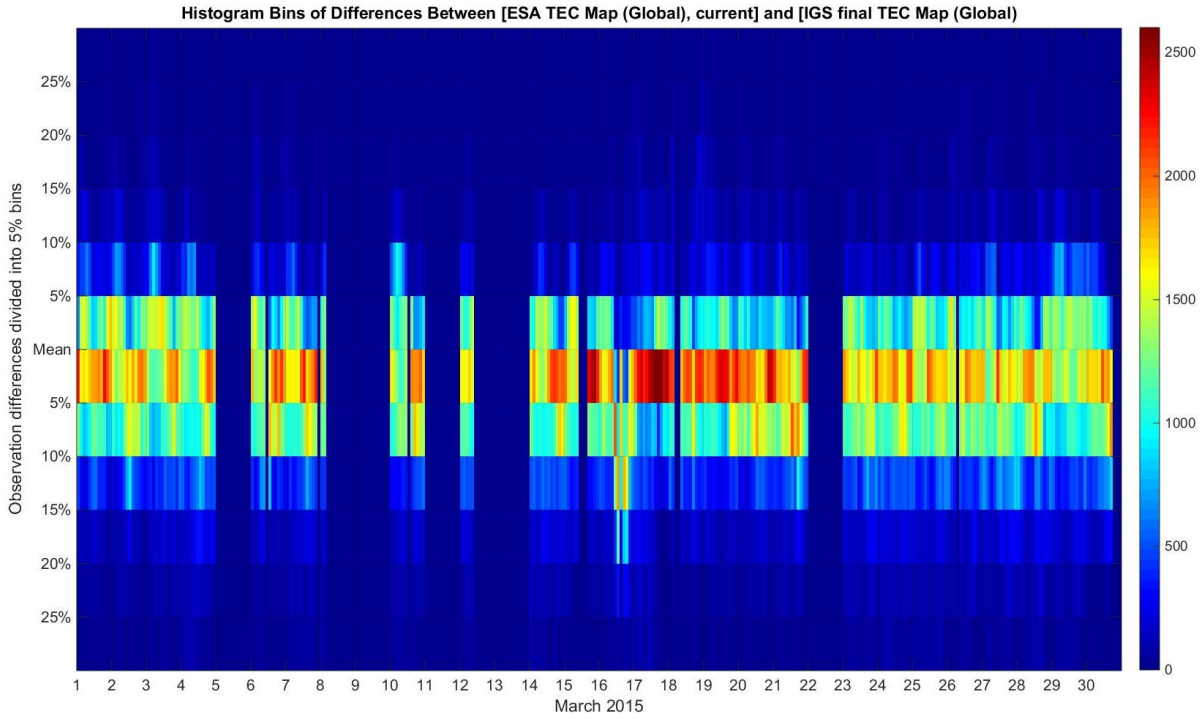

Figure 7.7 Spectral density distribution of number of occurrence of TEC differences from the mean value in 5% bins with one hour resolution for the month of March 2015. The differences, TEC [ESA(I.103a) – IGS], are absolute and range from zero to more than 2500 observations per time interval. All distribution functions in the plot are therefore comparable for all events of the month.

Right after the CME hits the magnetosphere/ionosphere system of the Earth the distribution becomes very spike-like around 2.5 TECU from the mean value (see Figure 7.7) with small spread in the differences. This may indicate that the IGS combined dataset dominate the observed differences. In the decay phase of the severe disturbance (after March 17, 2015) a distribution of spread materializes, which resembles the conditions during normal and quiet situations.

Figure 9.8 shows the bias variation for the whole month. The linear trend has a slope of close to zero, and is therefore negligible. So, a bias of 4.2 - 4.3 TECU between the two dataset is a good estimator of the differences between the retrievals for the two centers (ESA and IGS).

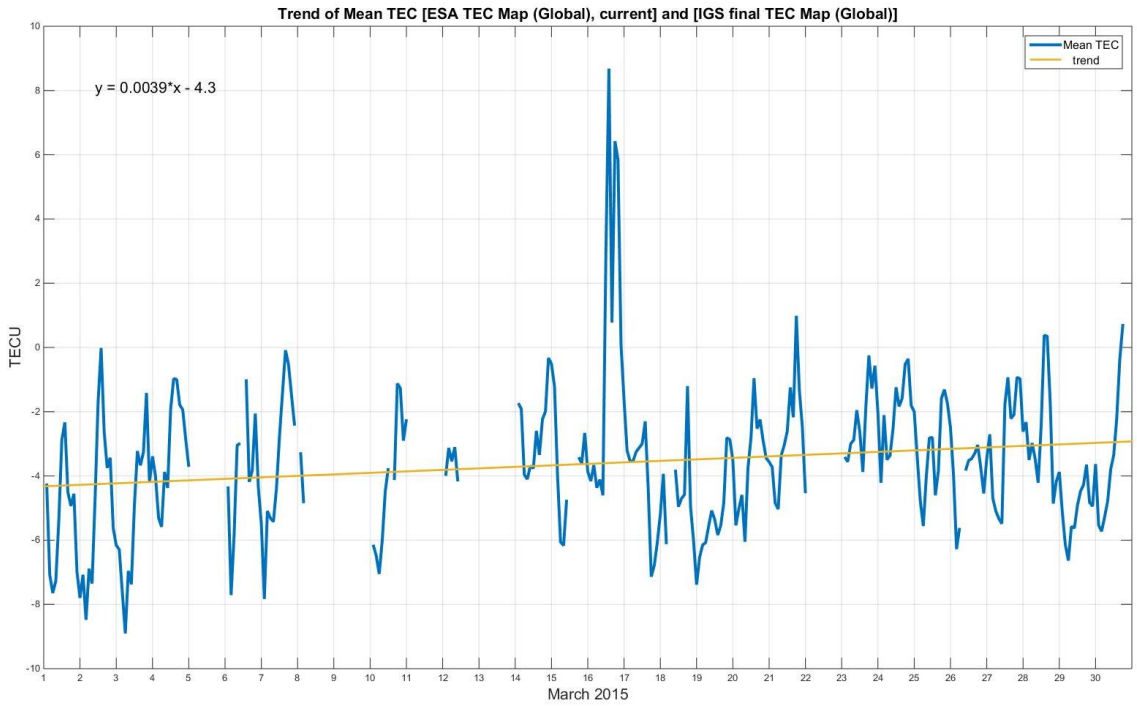

Figure 7.8 Trend plot of the bias for the month of March 2015. The blue line depicts the hourly biases, and the yellow line is the linear trend line.

The residuals with respect to a constant bias of 4.3 TECU is given in Figure 7.9. Most of the variations are related to regional TEC changes caused by ionosphere/magnetosphere impacts that for the majority are linked to the solar wind changes. The largest residuals are directly linked to CME and HSS impinging the magnetosphere of the Earth.

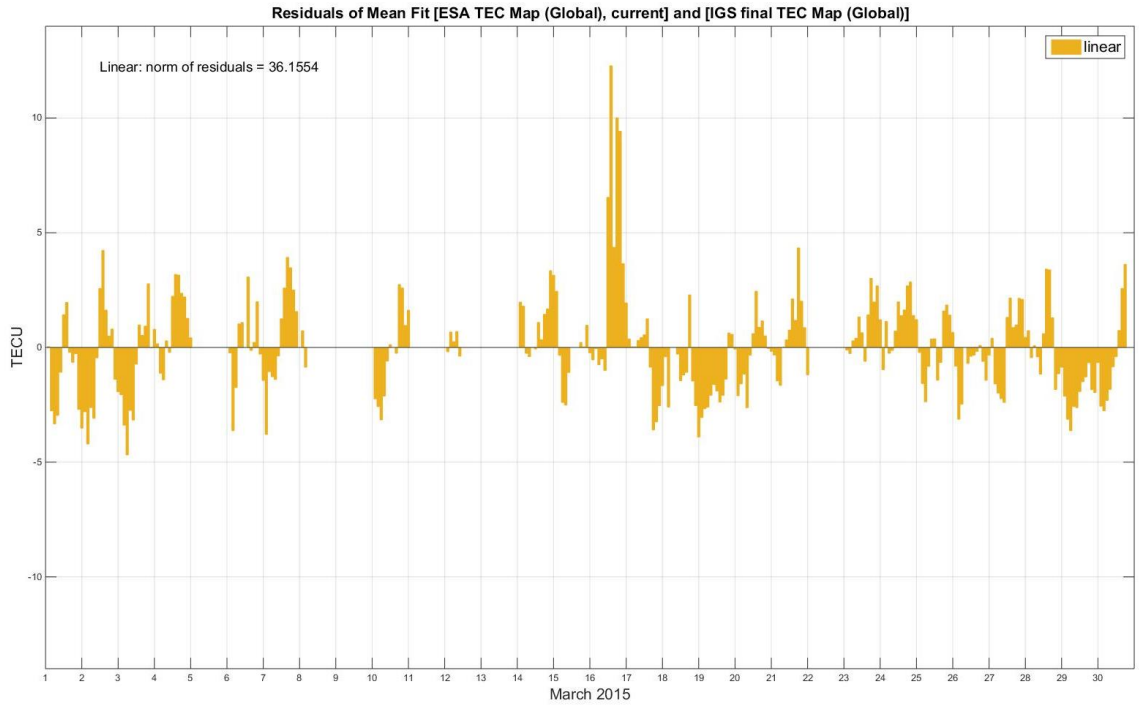

Figure 7.9 Residual of the mean with a time resolution of one hour in the data and a grid cell-size in degrees of (longitude, latitude) = (5.0, 2.5).

7.6 Conclusions and Summary

The data approach in this study represents a global view of the geophysical conditions with a one-hour resolution, which is different from the comparisons of center datasets with satellite observations of TEC. This is emphasized in the CME event of March 17, 2015 (Figure 9.6). The

number of outlier data increased during the event, while the mean difference did not change, indicating that regional changes are more important in the onset phase of a CME. A conclusion that only be done from the approach in this study or when applying satellite observations originating from regions directly impacted by the build-up phase of the CME.

Figure 7.7 displays new and interesting information about the characteristics of the difference density distribution functions. Approximately 80% of the global observations are within 7.5 % of the mean difference. Especially during quiet and normal conditions this is the dominant scenario.

During severe disturbed conditions, peaked difference distributions are observed with larger offset to the average mean of 4.3 TECU. On March 16, 2015, a sinusoidal movement is seen, indicating that the preliminary phase of the severe disturbance does start over Europe, but gradually the effect is transferred to the magnetosphere and ionosphere giving rise to TEC changes over Europe during a period of 6 to 10 hours.

Right after the CME hits the magnetosphere/ionosphere system of the Earth the distribution becomes very spike-like around 2.5 TECU from the mean value (see Figure 7.6) with small spread in the differences. This may indicate that the IGS dataset dominate the observed differences. In the decay phase of the severe disturbance (after March 17, 2015) the distribution becomes wider with a larger spread, resembling the conditions during normal and quiet situations.

Other studies have given variations between the center (ESA, CODE, IGS, and JPL) data products of VTEC and satellite JASON data in the range of 0.2 – 3.7 TECU [Hernandez-Pajares et al., 2008]. The approach in the validation here is limited by the fact that the satellite data does not represent all grid-cells globally with a time resolution of one hour, but are linked to a limited number of grid-cells represented by the footprint swath of the satellite. The results in this study give variations in the range of 2.6 to 4.3 TECU.

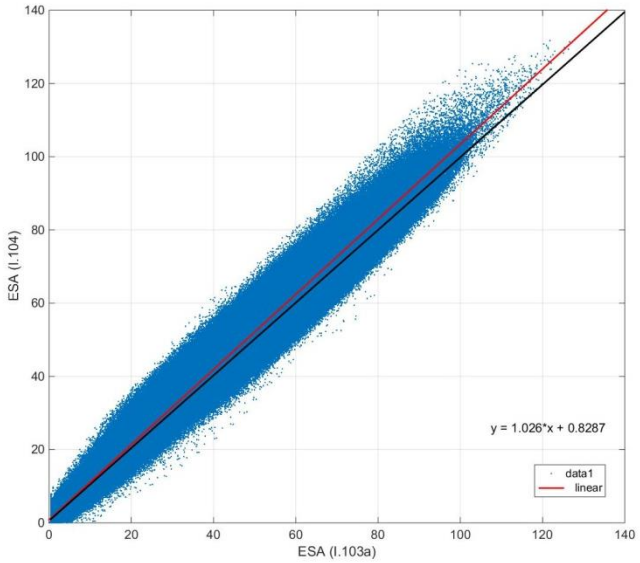

Figure 7.10 Scatter plot of all global data for the month of March 2015 comparing the ESA 1-hour forecast TEC map [ESA(I.104)] with the ESA global and current dataset [ESA(I.103a)] for the same instance in time.

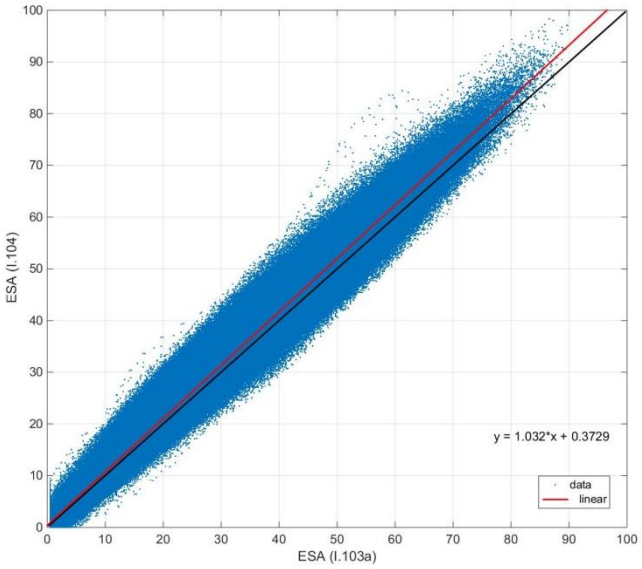

Figure 7.11 Scatter plot of all global data for the period October-November 2015. The comparison consists of the ESA 1-hour forecast TEC data product [ESA(I.104)] with the ESA global and current dataset [ESA(I.103a)] for the same instance in time.

Figure 7.10 depicts the comparison of 1-hour forecasts data [ESA(I.104)] with the ESA current data set [ESA(I.103a)] for all latitudes and longitudes globally. The scatter plot reveals the overall situation during severely disturbed conditions for an extended period, where maximum TEC values range up 130 TECU.

Figure 7.11 shows the statistical data spread for the same two data products during quiet to moderately disturbed conditions in the October-November period of 2015. The maximum TEC values reach 95 TECU. Table 7.3 summarizes the main statistics.

2015	**ESA(I.117) - ESA(I.101) [TECU]**	
	Mean	**Standard deviation**
March	2.2-2.5	1.0-1.7
October - November	0.9-1.5	0.4-0.6

Table 7.3 Averaged European TEC differences between ESA(I.117) and ESA(I.101). The former represents results from the TaD model driven by digital ionosonde data.

The model forecasting technique works well below the error limitations and assumptions of the method during quiet to moderate disturbed conditions. However, during severe conditions the TEC errors double, having standard deviations of up to three times the values observed during quiet conditions. The main cause for this is related to the fact that the observations of the model originate from only four digital ionosonde stations sensing only the European sector.

CHAPTER 8

COMPARISON OF HIGH-LATITUDE IONOSPHERIC PROCESSES DURING HSS AND ICME-INDUCED GEOMAGNETIC STORMS

8.1 Introduction

In Chapter 3 the focus was on ICME-induced geomagnetic storms and their effects on the Arctic ionosphere. The question then arises: are these effects the same for a HSS-induced [Meng et al., 2016] storm as well and if there are differences what can we say about them? Both ICMEs and HSSs originate from the sun and they both inject energy into geospace, but they are also results of fundamentally different physical processes and might impact the Arctic ionosphere differently.

In this chapter, VTEC maps inferred from Greenlandic GNSS stations (Figure 8.1) are used for the first time to investigate differences in ionospheric disturbances caused by HSSs and ICMEs. Section 8.2 introduces the observational and mapping techniques. The comparison of the effects of ICME and HSS storms has not been explored in detail in the Arctic ionosphere. TEC mapping reveals a pronounced negative main storm phase and significantly decreased polar patch formation due to increased atmospheric heating. The negative phase is similar to the one described in Durgonics et al. [2017], but the energy input rate is fundamentally different. Section 8.3 describes briefly the physical mechanisms of ICMEs and HSSs, and Section 8.4 discusses the obtained results.

An additional small study was conducted on the day following the HSS event (4 November 2015), where a solar radio burst (SRB) caused anomalies in European and Greenlandic air navigation. Appendix IV contains relevant data and a brief analysis of this particular event.

8.2 Observations and Mapping Technique

Figure 8.1 demonstrates the GNSS ground stations used for the TEC mapping. In Durgonics et al. [2017], use of these 18 ground stations proved sufficient for identifying TOI and large-scale polar patches over the Greenland sector. As the goal here is to compare ICME and HSS ionospheric effects the station selection was kept the same, thus all the obtained TEC maps are directly comparable to the study in Chapter 3 without having to take into account different map resolutions.

Figure 8.2 shows the computed TEC map for ~21:10 UTC, 18 February 2014, which was a particular ICME-related event. RINEX files from the 18 GNSS ground stations were collected. The data processing procedure and the algorithms employed were the same as those described in Section 3.2.1 (see also Figure 3.1).

Figure 8.3 shows a TEC map for ~11:50 UTC, 3 November 2015, which was a particular HSS-related event. From a technical point of view there is no difference between the data processing and mapping between the two different kinds of events. Therefore only geophysical drivers make up the TEC differences for the two events. The interpretation of the observed differences is given in Section 8.4.

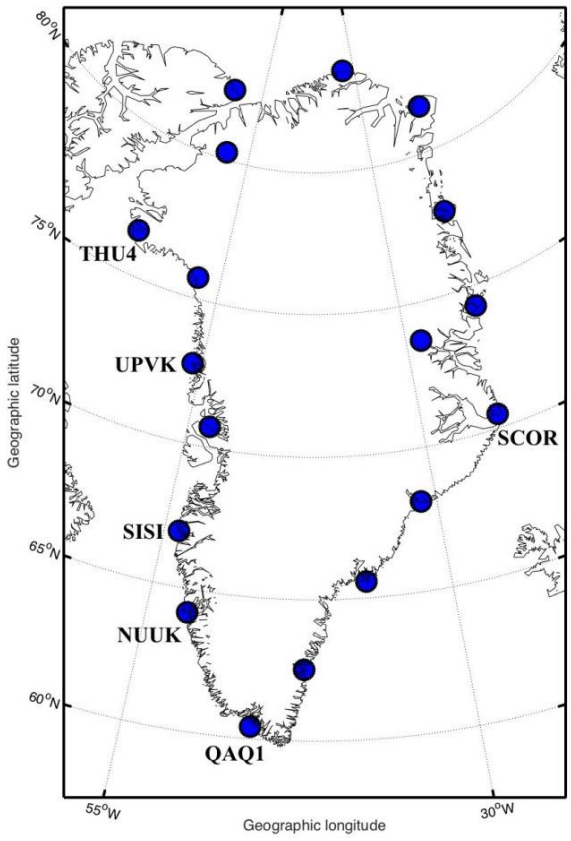

Figure 8.1 The 18 GNET stations that were used for the TEC mapping with the 4-digit names of the most important stations.

8.3 Comparison of ICME-Induced and HSS-induced Storms

An example of a larger ICME-driven ionospheric storm is the 19 February 2014, highly complex, multiphase storm, which had the largest impact on the Dst index that year (see Chapter 3 and Durgonics et al. [2017]). This geomagnetic storm was the result of two powerful Earth-directed ICMEs. Figure 8.2 shows TEC map generated from GNSS data obtained during that event. A schematic of the structure of an interplanetary ICME can be seen in Figure 8.4. An ICME can occur with or without a preceding solar flare in the solar corona. The energy release that composes the

ICME is associated with coronal magnetic reconnection, which is a sudden rearrangement of the solar magnetic field lines in the corona [Carley et al., 2012; Schunk and Nagy, 2009]. An ICME is essentially magnetized plasma consisting of protons and electrons propagating with typical speeds of 30-3000 km/s or even larger and carrying mass in the order of 10^{12} kg.

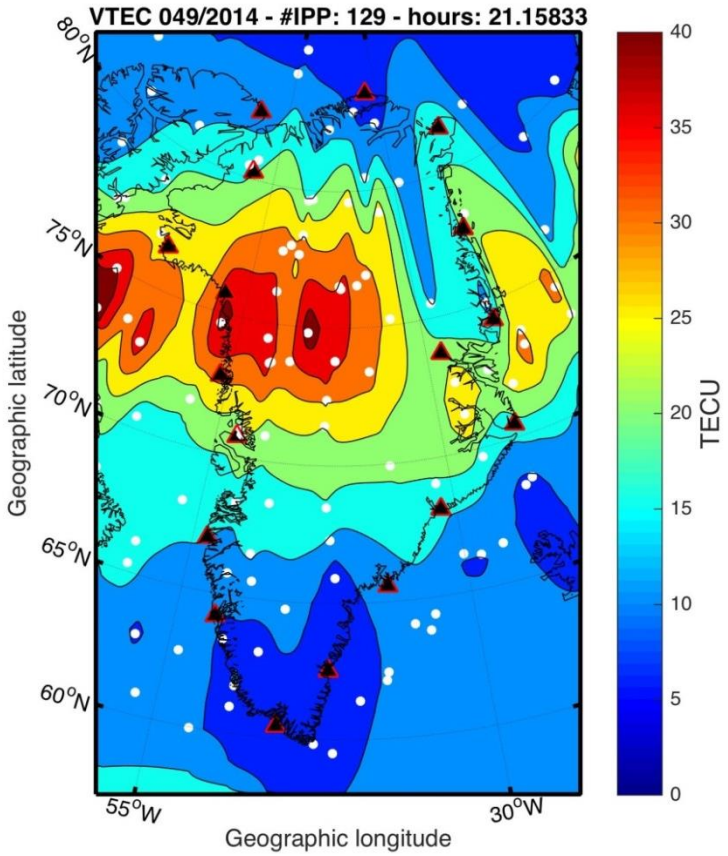

Figure 8.2 TEC map showing polar patch structures in the polar cap during an ICME-related event (the white dots mark the IPP locations).

A detailed discussion of the ICME triggering mechanism is beyond the scope of this work, however there are several theories existing in the literature (e.g., Howard [2011]; Chen and Shibata [2000]). For the purpose of ionospheric research, the most important factor is whether the ICME is Earthward-directed or not.

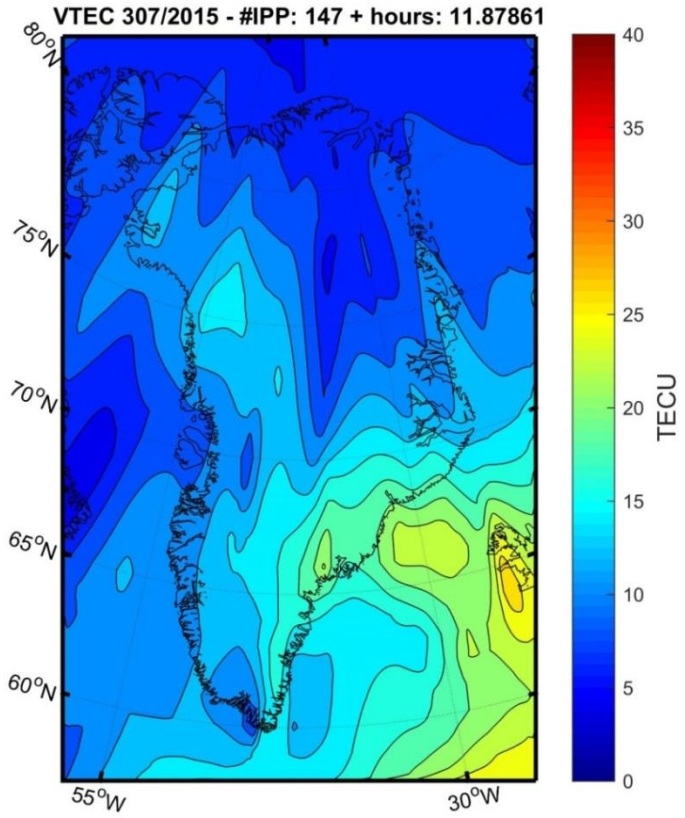

Figure 8.3 TEC map showing polar patch structures in the polar cap during a HSS-related event.

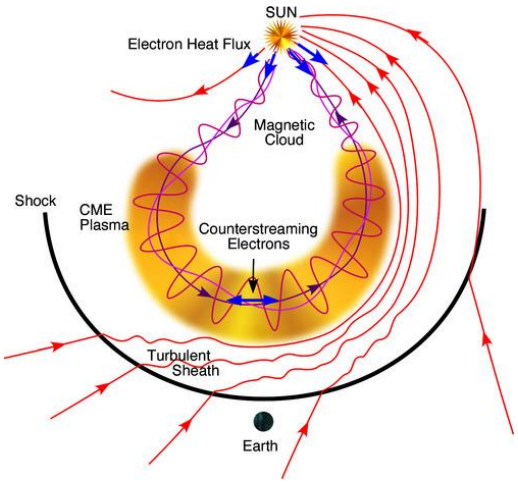

Figure 8.4 Presents a schematic about our current understanding of the complex structure of an interplanetary CME. (Courtesy of Deborah Eddy and Thomas Zurbuchen. From: https://ase.tufts.edu/cosmos/view_picture.asp?id=910)

The ICME-magnetosphere interaction can typically be observed by a sudden change in the Dst index. From that point on, there are a large number of complex processes which signal the beginning of a geomagnetic storm. Some important ICME-related solar wind parameters for the 19 February 2014 storm are shown in Figure 8.5.

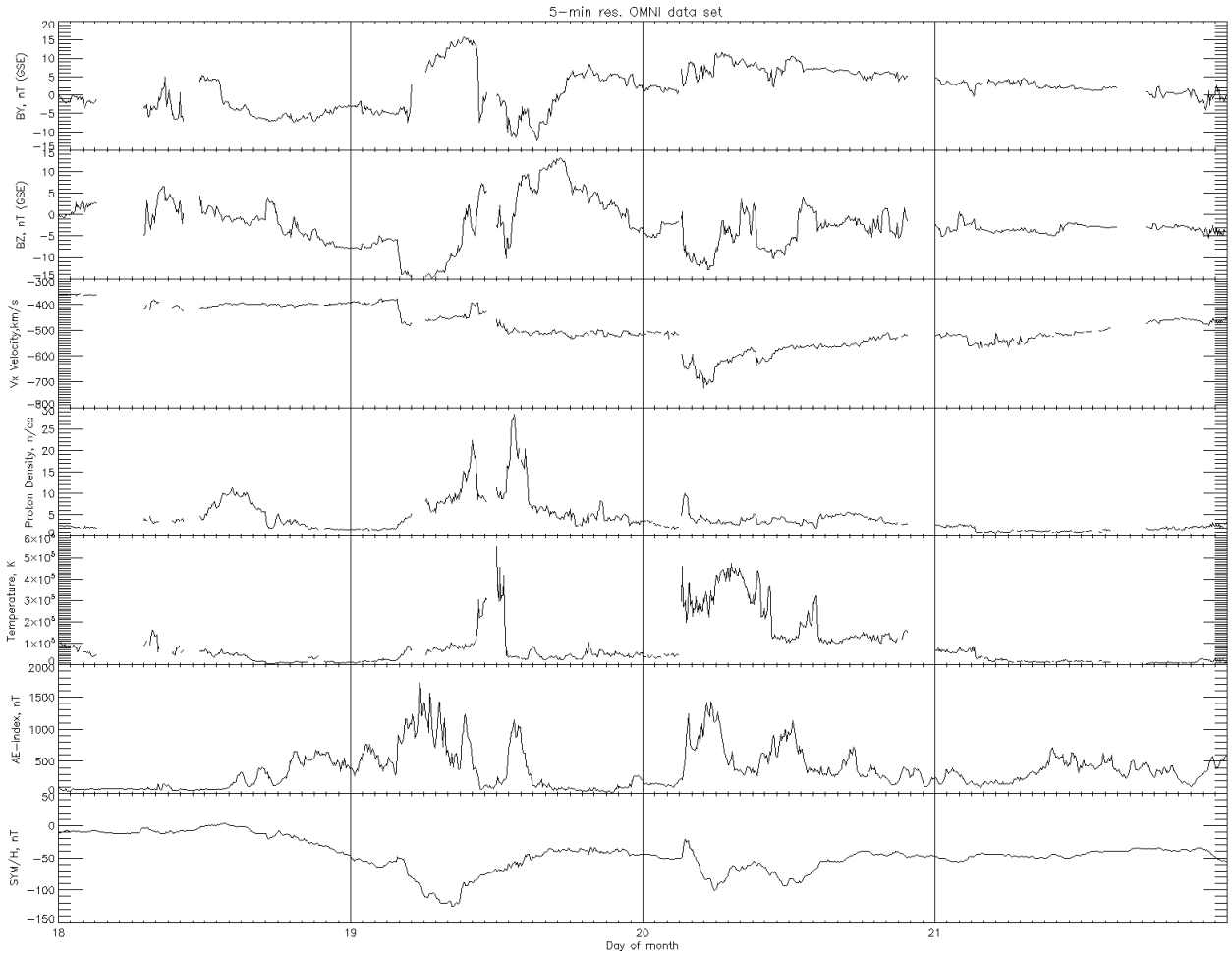

Figure 8.5 Relevant ICME-related solar wind parameter observations obtained from OMNI. Day of ICME arrival: 19 February 2014.

HSSs also propagate in the background solar wind, but they originate from coronal holes and they can be active for a longer time and even return and hit geospace again after a solar rotation. A schematic of a HSS can be seen in Figure 8.6 with expected, theoretical solar wind parameter

changes as the HSS passes the observer. Observation-based, HSS-induced solar wind parameters for the 3 November 2015 storm can be seen in Figure 8.7. The comparison of the typical features in both cases can lead to the identification whether it is an ICME or a HSS-type of disturbance that is occurring, if the source is not otherwise known.

Coronal holes appear as darker areas on the solar corona when observed in EUV or x-ray wavelengths. As in the case of ICME triggering mechanisms, the detailed description of the coronal hole formation is beyond the scope of this work, but it is enough to consider that these regions correspond to open solar field lines and higher speed solar wind. This stream of faster solar wind will wrap around the sun in a spiral as a result of the solar rotation, see Figure 8.6. The more energetic solar wind associated with HSSs will inject extra energy into the magnetosphere and can result in a geomagnetic storm and associated ionospheric disturbances [Pizzo, 1978].

The HSS-driven ionospheric storm on 3 November 2015 was a larger event that was followed on the next day by an ICME (and an associated SRB; see Appendix IV). One of the important differences between Figure 8.5 and 8.7.can be seen in the behavior of the IMF components. In the HSS case, B_z and B_y tend to change sign and fluctuate which will result in sudden electric field changes [Borovsky et al., 2006].

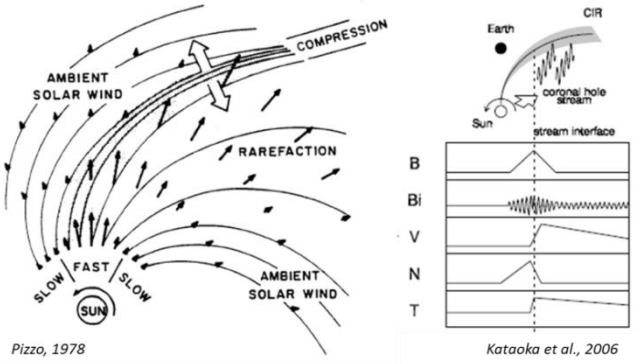

Figure 8.6 shows the interplanetary structure of a HSS (after Pizzo [1978]) and its typical signatures in solar wind parameter data (after Kataoka et al. [2006]).

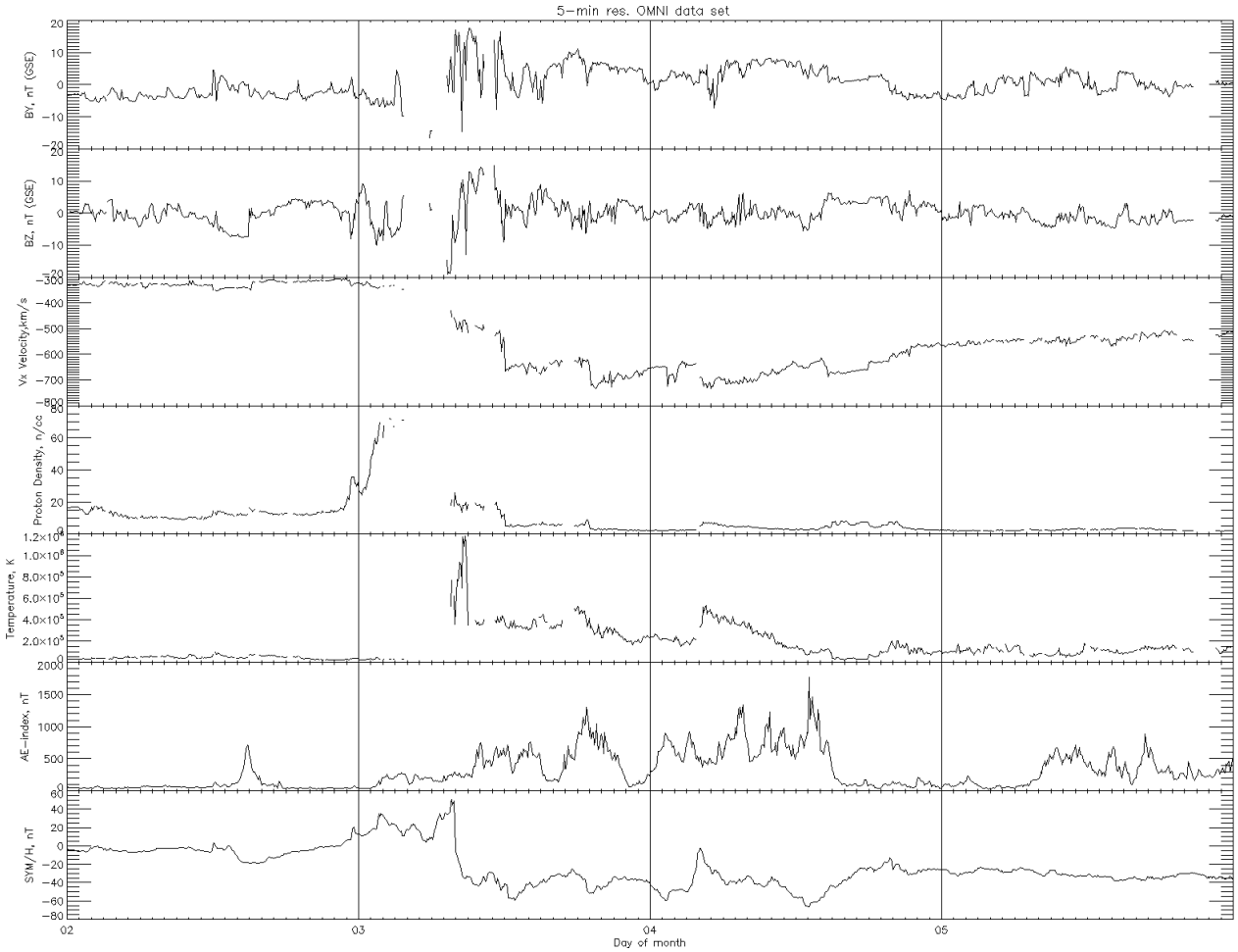

Figure 8.7 Relevant HSS-related solar wind parameter observations obtained from OMNI. Day of HSS arrival: 3 November 2015.

8.4 Results

Figure 8.8 shows the polar cap north index (or PCN) time-series for the ICME and HSS-related disturbances (more details on the PC-index can be found in, e.g., Vennerstrøm et al. [1991], and in Chapter 3 and Chapter 6 in this dissertation). The red dotted line indicated by **A** shows the HSS arrival time and the blue dashed line **B** marks the ICME arrival time. The most striking feature is the fundamental difference between the rates of energy deposition of the two phenomena.

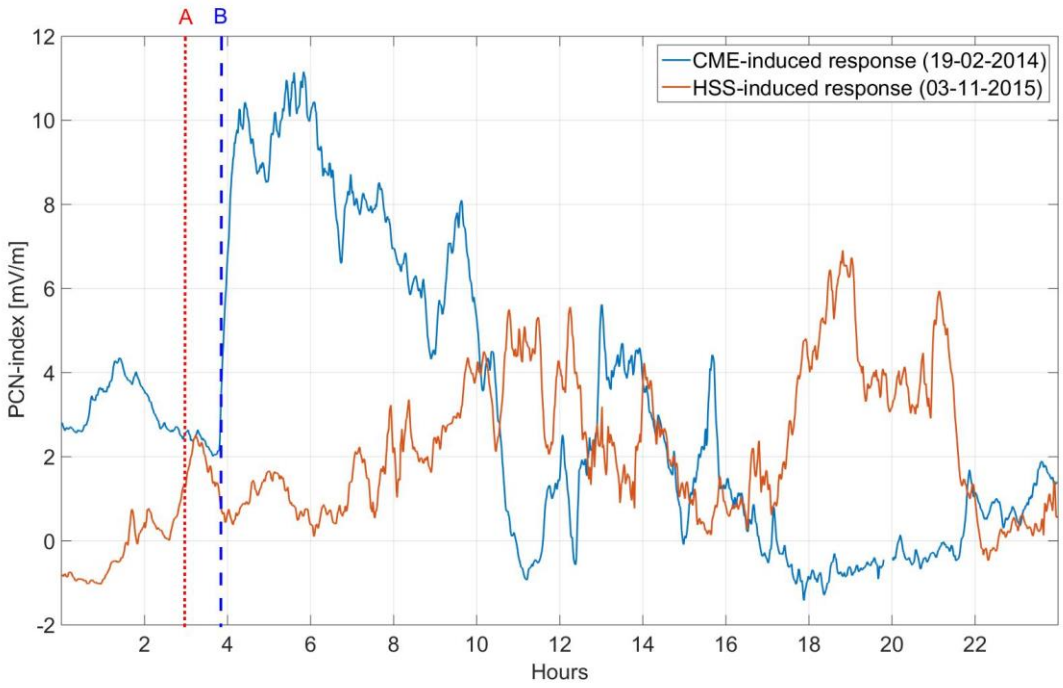

Figure 8.8 PCN time-series for the corresponding ICME and HSS-related disturbances.

The ICME related PCN value rises almost instantly after the ICME hits Earth at around 04:00 UTC, then the first block of disturbance decays before noon. Around noon a second positive block follows which lasts for several hours. The main portion of the energy input for that day is injected into the polar cap in 6 to 8 hours.

Conversely, the HSS related PCN value rises gradually and relatively slowly throughout the day with a small (~2 mV/m) spike just after Earth arrival around 03:00 UTC.

By comparing Figure 8.5 and 8.7, one can see that during HSS-related storms, the B_z component tends to fluctuate and changes sign frequently, unlike during ICME-related storms when there is typically a longer negative phase following the initial positive spike. During downward (negative) B_z times, a well-structured double cell convection structure forms in the polar cap ionosphere which can lead to TOI formation and increased plasma transport from midlatitudes [Brekke, 2013; Schunk

and Nagy, 2009]. There is a much more complex structure when the B_z is upwards (positive). One can observe 4-cell or even more complex configurations, and the exact physical description of such periods are still not complete [Schunk and Nagy, 2009]. From these facts it can be hypothesized that an ICME-induced geomagnetic storm is more favorable for TOI and polar patch formation than the HSS-induced ones. Unfortunately, this is hard to verify observationally due to the negative TEC phase that typically follows the onset of a geomagnetic storm in the Arctic ionosphere [Durgonics et al., 2017]. This phenomenon itself can suppress patch formation for days during the storm recovery period.

The electron density depletion during ICME-related storms was discussed in detail in Chapter 3. In order to get a better understanding of how this ionospheric depletion manifests during HSS-induced storms, Figure 8.9 shows 2 days of observations from 3 different latitudes in Greenland: deep polar cap, auroral oval – polar cap boundary, and the equatorward edge of the auroral zone. The blue lines show the day before the HSS hit and the red is the day of the event. This storm occurred during winter, which means the deep polar cap is in darkness during the whole day and one should not expect diurnal TEC variations, therefore the electron density depletion should have little to no effect here (Figure 8.9 top) as there is no well-developed ionosphere present.

At Thule (THU4) (Figure 8.9, top), the observations the day before the storm show a very small diurnal variation but significant patch-activity throughout the entire day. The source of the patch forming plasma is the cross-polar-cap convection. These winter time patches in the polar cap ionosphere tend to survive for a longer time (even days) due to the lack of a highly conducting E layer (see Chapter 6 for a detailed discussion on this subject).

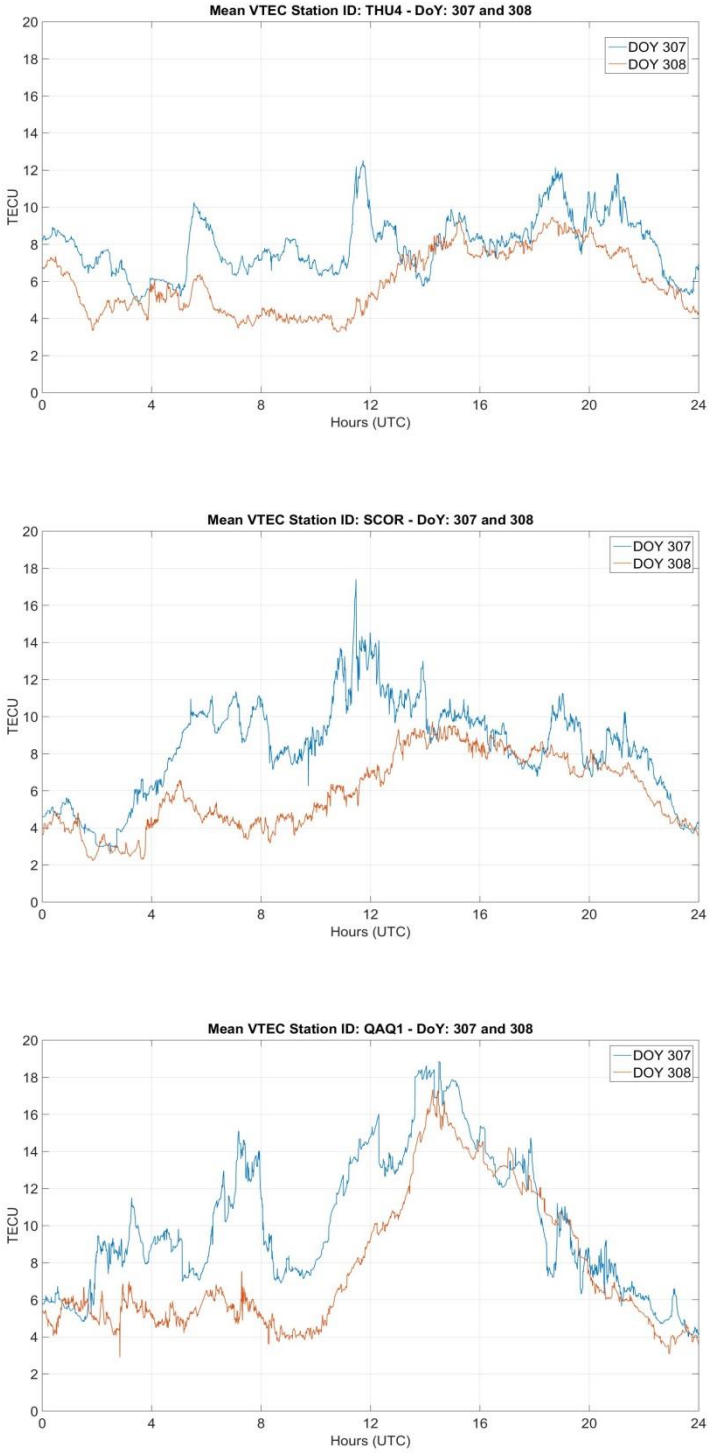

Figure 8.9 MVTEC time-series for the day of the HSS arrival and the following day for a polar cap (THU4), an auroral oval (SCOR), and a station which is at the equatorward edge of the auroral zone (QAQ1). See also Figure 8.1.

On the storm day there is an apparent depletion, however the patches are not present anymore with the amplitudes and frequencies that existed the day before.

In Qaqortoq (QAQ1) (Figure 8.9, bottom) there is a significant diurnal cycle present before the storm day with large patches/TOI signatures. Similarly to the other two latitudes, the patches are not very significant after the storm onset, but the daytime photoionization-related TEC peak is just barely suppressed.

8.5 Summary

In this chapter ionospheric effects of HSS and ICME-driven storms at high-latitudes were compared. There were similarities and also differences observed in the development of the storms. (1) Both type of storms exhibited a clear negative phase, which resulted in an increase of TOI breaking down into patches and a decrease in patch formation in general throughout the Greenland sector. The negative phase developed as the PCN-index started to increase indicated energy input into the polar cap. (2) The rate of PCN increase was clearly different for the two types of storms. (3) The impact of the physical processes responsible for the negative phase have less pronounced impact on the diurnal TEC variations than on patch formation.

Storm influences on airborne navigation at high-latitudes were also investigated and assessed in order to determine the possible cause of the radio communication disturbances. This effort may lead to a better understanding of the phenomenon and might help develop communication hardware that is more resistant to such effects.

CHAPTER 9

CONCLUSIONS AND RECOMMENDATIONS FOR FUTURE WORK

This final Chapter offers a short summary of the research topics including the description of the target of the research. This is followed by the final conclusions and future recommendations for each of the presented studies in Chapters 2 to 8.

9.1 Conclusions and Recommendations for Future Work

Earth's ionosphere and particularly the Arctic ionosphere is a highly complex physical system. The spatial extent of this system is described by the horizontal boundary where the open geomagnetic field lines turn into closed field lines and the vertical boundary, which spans from around 60 km altitude up to 1000 km or higher. The horizontal boundary forms an oval shape which constantly shifts with time. For practical TEC applications, the vertical boundary is as high as GPS satellite orbits (~20,200 km). This massive volume contains an open physical system with the constantly changing background geomagnetic field and electric field, with continuous energy input and output via the magnetosphere and neutral atmosphere. The ionosphere is strongly coupled to the magnetosphere and the atmosphere via electric fields, friction, precipitation, and different field

aligned currents (FACs), such that they affect each other continuously. This in sum gives rise to high-latitude ionospheric dynamics.

One of the main goals of this dissertation was to demonstrate how crucial it is to incorporate several different measurements to understand this complex region. In addition to new types of observations, there is a need for new indices that can better describe the state of the ionosphere. TEC and scintillation indices like S_4 and σ_ϕ are the oldest, most established indices the scientific community uses to characterize the ionosphere. More recently, ROTI was introduced as a third scintillation index; however others have also been developed such as derivative-of-ROTI (DROTI). The future focus should be on a different approach: a spectral approach. Spectral scintillation indices have a more profound connection to plasma phenomena and appear very promising. While these indices have existed for decades, they are still not very well understood. There are case studies about them, but there is still no generally applicable spectral scintillation index (see also Appendixes V and VI) in use today [Umeki et al., 1977; Yeh and Liu, 1982].

TEC should be revisited as well. It is a powerful tool and well-established but it is not without its limitations. Firstly, it is an integrated measurement; therefore it does not contain information about what is occurring in different regions along the signal path. An already known and exploited technique, GNSS-RO, can provide vertical electron density profiles. While this is also an integrated measurement, it gives very useful information about what is occurring in the tangent point. RO measurements can already be obtained via COSMIC, CASSIOPE and other satellites, thus combining these with TEC maps can provide further depth of understanding of the Arctic ionosphere (however while COSMIC and the planned COSMIC-2 mission are excellent tools for a wide variety of atmospheric research, their high-latitude coverage is very poor). Fortunately, in 2013, ESA launched the Swarm mission. Swarm consists of three satellites in polar orbits equipped with high-precision and high-resolution geomagnetic and electric field measurements, and it is

capable of providing data for topside TEC derivation. It allows the comparison of traditional, ground based GNSS-TEC measurements with topside TEC. This could allow (especially if combined with RO and ionosonde profiles) for a better understanding of the vertical structure of polar cap patch dynamics, patch decay, and the exploration of the relationship between TEC, magnetic fluctuations, conductivity, and FACs. Ground-based magnetic observation data can additionally be integrated. If TEC data could be complemented with all these aforementioned observations, it could potentially lead to much more precise TEC maps, even in areas where ground station coverage is poor or nonexistent [Olsen et al., 2016; Wu et al., 2015].

Another potential method to improve TEC maps is the further advancement of interpolation methods that are used to fill the gaps between IPP points. In Chapter 2 we found that Kriging interpolation is a very good candidate method. However, every institution that provides TEC maps currently approaches this differently. The interpolation does not have to be static, as it is possible to obtain some information about how the ionosphere may change in the near future from later magnetic local time (MLT) areas due to their eventual rotation into subsequent MLTs. For instance, if there is a good ground station coverage in an area (X) east of an area (Y) along the same latitude that has poor coverage, it is potentially possible to use the data over area X to forecast how the ionosphere will behave when that plasma arrives over area Y. The forecast quality will decrease with larger distance between area X and area Y, due to a higher probability that the plasma density will decay, enhance, or get convected into different latitudes.

Long term statistical studies are also crucial for a better understanding of the high-latitude ionosphere. In Chapter 3, we looked the three largest ICME-driven storms in 2014, but that is clearly not a large enough data set to draw final conclusions. There is sufficient data available from GNET stations to make a decade long study which would encompass ICME, HSS, and mixed storms and compare them. Is the prolonged negative TEC phase a universal feature or does it only

sometimes occur? Such a long-term statistical study could potentially improve air navigation and ship navigation in the Arctic area because strong scintillation times could be better forecasted. From the context of navigational applications, , the scintillation forecast is more important than the TEC forecast due to the cycle slips which typically occur during strong phase scintillations. This claim is also supported by the findings in Chapter 3.

Finally, one of the most important aspects of ionospheric research is to construct a computational model that could adequately represent, reproduce, and to some extent forecast the physical processes therein. There have been a number of attempts to build such models. Here we will briefly mention three of them. The first is the Global Assimilative Ionospheric Model (GAIM) [Wang et al., 2004]. GAIM is a global, 3D, time-dependent model which incorporates Kalman filter and 4DVAR approaches. It is capable of assimilating a number of observational data types but it does not contain a high-latitude physical model. The second is the Thermosphere-Ionosphere-Electrodynamics General Circulation Model (TIE-GCM) [Roble and Ridley, 1987; Qian et al., 2009]. TIE-GCM is a numeric simulation physics-based model of the upper atmosphere; it also includes high-latitude ionospheric physical and atmospheric chemical processes. And finally, there is the Global Ionosphere Thermosphere Model (GITM) [Ridley et al., 2006; Meng et al., 2016]. GITM is somewhat similar to TIE-GCM in its capabilities as it is also a 3D spherical model of the upper atmosphere and includes high-latitude physical and atmospheric chemical processes. Among these three models, as a preliminary study, we have used TIE-GCM to simulate the VTEC results found in Chapter 6. This is still very much a work in progress, but a ~27-day electron density fluctuation signature was identified in the model output, despite thatthe amplitude was significantly lower than in the TEC observations (3-5 TECU vs. 10-15 TECU). One of the more important recommendations for future work is to further explore the comparison between TIE-GCM TEC outputs and MVTEC observations in the polar cap, which could lead to further improvement in the

high-latitude physical model underlying TIE-GCM, and therefore lead to a better understanding of the underlying physical processes. Lastly, it is suggested to extend the comparison of TEC observations with GITM.

In summary, the studies presented in this dissertation achieved a greatly furthered understanding of the Arctic ionosphere. Nevertheless, a large amount of additional studies need to be conducted in order to have a full understanding of all the intricacies of this complex and dynamic geophysical system.

REFERENCES

Aarons, J. (1997), Global positioning system phase fluctuations at auroral latitudes, J. Geophys. Res., 102(A8), 17,219–17,231, doi:10.1029/97JA01118.

Aarons, J., B. Lin, M. Mendillo, K. Liou, and M. Codrescu (2000), Global Positioning System phase fluctuations and ultraviolet images from the Polar satellite, J. Geophys. Res., 105(A3), 5201–5213, doi:10.1029/1999JA900409.

Afraimovich E. L., Voyeikov S. V., Edemskiy I. K. and Yasyukevich Y. V., 2009, MHD nature of night-time MSTIDs excited by the solar terminator, Geophys. Res. Lett., 36.

Alfonsi, L., L. Spogli, G. De Franceschi, V. Romano, M. Aquino, A. Dodson, and C. N. Mitchell (2011), Bipolar climatology of GPS ionospheric scintillation at solar minimum, Radio Sci., 46, RS0D05, doi:10.1029/2010RS004571.

Amm, O., and A. Viljanen (1999), Ionospheric disturbance magnetic field continuation from the ground to the ionosphere using spherical elementary currents systems, Earth Planets Space, 51, 431–440, doi:10.1186/BF03352247.

Anderson, B. J., S.-I. Ohtani, H. Korth, and A. Ukhorskiy (2005), Storm time dawn-dusk asymmetry of the large-scale Birkeland currents, J. Geophys. Res., 110, A12220, doi:10.1029/2005JA011246 .

Aquino, M. A., Dodson, J. Souter, and T. Moore (2007), Ionospheric scintillation effects on GPS carrier phase positioning accuracy at auroral and sub-auroral latitudes, in Dynamic Planet, International Association of Geodesy Symposia, vol. 130, edited by M. Aquino, et al., pp.859–866, Springer, Berlin, doi:10.1007/978-3-540-49350-1_12 1.

Arnoldy, R. L. (1971), Signature in the interplanetary medium for substorms, J. Geophys. Res., 76(22), 5189-5201.

Astafyeva E. I., Afraimovich E. L., Oinats A. V., Yasukevich Yu. V. and Zhivetiev I. V., 2008, Dynamics of global electron content in 1998–2005 derived from global GPS data and IRI modeling, Adv. Space Res., 42, 763–769.

Astafyeva, E., Y. Yasyukevich, A. Maksikov, and I. Zhivetiev (2014), Geomagnetic storms, super-storms, and their impacts on GPS-based navigation systems, Space Weather, 12, 508–525, doi:10.1002/2014SW001072.

Barclay, L. (2003), Propagation of Radiowaves 2, The Institution of Engineering and Technology, London, U. K.

Basu, S., E. J. Weber, T. W. Bullett, M. J. Keskinen, E. MacKenzie, P. Doherty, R. Sheehan, H. Kuenzler, P. Ning, and J. Bongiolatti (1998),Characteristics of plasma structuring in the cusp/cleft region at Svalbard, Radio Sci., 33(6), 1885 –1899, doi:10.1029/98RS01597.

Basu, S., E. M. MacKenzie, S. Basu, E. Costa, P. F. Fougere, H. C. Carlson Jr., and H. E. Whitney (1987), 250 MHz/GHz scintillation parameters in the equatorial, polar, and auroral environments, IEEE J. Select. Areas Commun., 2(2), 102–115, doi:10.1109/JSAC.1987.1146533.

Basu, S., E. MacKenzie, and S. Basu (1988), Ionospheric constraints on VHF/UHF communications links during solar maximum and minimum periods, Radio Sci., 23, pp. 363-378, doi: 10.1029/RS023i003p00363.

Basu, S., S. Basu, E. MacKenzie, and H. E. Whitney (1985), Morphology of phase and intensity scintillations in the auroral oval and polar cap, Radio Sci., 20(3), 347–356, doi:10.1029/RS020i003p00347.

Basu, S., S. Basu, J. J. Sojka, R. W. Schunk, and E. MacKenzie (1995), Macroscale modeling and mesoscale observations of plasma density structures in the polar cap, Geophys. Res. Lett., 22(8), 881–884, doi:10.1029/95GL00467.

Basu, S., S. Basu, P. K. Chaturvedi, and C. M. Bryant Jr. (1994), Irregularity structures in the cusp/cleft and polar cap regions, Radio Sci., 29(1), 195–207, doi:10.1029/93RS01515.

Beck, J.G. (2000), A comparison of differential rotation measurements, Solar Physics, 191, 47, doi:10.1023/A:1005226402796.

Beckmann, P. and A. Spizzchino (1987), The Scattering of Electromagnetic Waves from Rough Surfaces, Artech House, Norwood, MA, USA.

Benzon, H. H. and S. Syndergaard (2013), Simulation of radio occultation measurements, Space Commun., vol. 22, no. 2–4, pp. 179-187, doi:10.3233/SC-130013.

Benzon, H.-H. and P. Hoeg (2015), Wave propagation simulation of radio occultations based on ECMWF refractivity profiles, Radio Sci., vol. 50, pp. 778-788, 2015, doi:10.1002/2015RS005649.

Besprozvannaya, A. S., Empirical modeling of the polar foF2 in the North-ern and Southern hemispheres, Adv. Space Res., 16 (1), 27–36, 1995.

Beyerle, G. and K. Hocke (2001), Observation and simulation of direct and reflected GPS signals in radio occultation experiments, Geophys. Res. Lett., vol. 28, no. 9, pp. 1895-1898.

Beyerle, G., K. Hocke, J. Wickert, T. Schmidt, C. Marquardt and C. Reigber (2002), GPS radio occultations with CHAMP: A radio holographic analysis of GPS signal propagation in the troposphere and surface reflections, J. Geophys. Res., vol. 107, no. D24, p. 4802, doi:10.1029/2001JD001402.

Bhattacharyya, A., T. L. Beach, S. Basu, and P. M. Kintner (2000), Nighttime equatorial ionosphere: GPS scintillations and differential carrier phase fluctuations, Radio Sci., 35(1), 209–224, doi:10.1029/1999RS002213.

Bilitza, D. (2001), International Reference Ionosphere 2000, Radio Sci., 36(2), 261–275, doi:10.1029/2000RS002432.

Bittencourt, J. A. (2004), Fundamentals of Plasma Physics, Springer, New York, U.S.A.

Blagoveshchenskii, D. V. (2013), Effect of Geomagnetic Storms (Substorms) on the Ionosphere: 1. A Review, Geomagn. Aeron., Vol. 53, No. 3, pp. 275-290, doi:10.1134/S0016793213030031.

Boashash, B. (2003), Time Frequency Signal Analysis and Processing: A Comprehensive Reference, Elsevier, Amsterdam, The Netherlands.

Bole, A., B. Dineley and A. Wall (2005), Radar and ARPA Manual, Elsevier, Amsterdam, The Netherlands.

Boots B. N., 1986, Voronoi (Thiessen) Polygons (Concepts and techniques in modern geography), GeoBooks, Norwich, UK.

Bothmer, V. and I. A. Daglis (2007), Space weather, physics and effects, Springer, Heidelberg, Germany.

Brekke, A., (2013), Physics of the Upper Polar Atmosphere, 2nd ed., Springer, Heidelberg, Germany.

Brekke, A., J. R. Doupnik, and P. M. Banks (1974), Observations of neutral winds in the auroral E region during the magnetospheric storm of August 3–9, 1972, J. Geophys. Res., 79(16), 2448–2456, doi:10.1029/JA079i016p02448.

Buonsanto, M. J. (1999), Ionospheric storms – A review, Space Science Reviews, 88, pp. 563-601, doi: 10.1023/A:1005107532631.

Camargo P. O., Monico J. F. G. and Ferreira L. D. D., 2000, Application of ionospheric corrections in the equatorial region for L1 GPS users, Earth Planets Space, 52, 1083–1089.

Cardellach E., C. O. Ao, M. de la Torre Juàrez and G. A. Hajj (2004), Carrier phase delay altimetry with GPS-reflection/occultation interferometry from low earth orbiters, Geophys. Res. Lett., vol. 31, p. L10402, doi:10.1029/2004GL019775.

Cardellach E., F. Fabra, O. Noguès-Correig, S. Oliveras, S. Ribò and A. Rius (2011), GNSS-R ground based and airborne campaigns for ocean, land, ice, and snow techniques: Application to the GOLD-RTR data sets, Radio Sci., vol. 46, p. RS0C04, doi:10.1029/2011RS004683.

Carley, E. P., R. T. J. McAteer, and P. T. Gallagher (2012), CORONAL MASS EJECTION MASS, ENERGY, AND FORCE ESTIMATES USING STEREO, The Astrophysical Journal, 752, 1.

Chakrabarty, D., M. S. Bagiya, S. V. Thampi, and K. N. Iyer (2012), Solar EUV flux (0.1-50 nm), F10.7 cm flux, sunspot number and the total electron content in the crest region of equatorial ionization anomaly during the deep minimum between solar cycle 23 and 24, Indian Journal of Radio and Space Physics, 41, pp. 110-120.

Chasovitin, Yu. K., A. V. Shirochkov, A. S. Besprozvannaya, T. L. Gulyaeva (1987), An empirical model for the global distribution of density, temperature and effective collision frequency of electrons in the ionosphere, Adv. Space Res., 7 (6), 49–52.

Chen, G., J. Xu, W. Wang, J. Lei, and A. G. Burns (2012), A comparison of the effects of CIR- and CME-induced geomagnetic activity on thermospheric densities and spacecraft orbits: Case studies, J. Geophys. Res., 117, A08315, doi:10.1029/2012JA017782.

Chen P. F. and K. Shibata (2000), An Emerging Flux Trigger Mechanism for Coronal Mass Ejections, The Astrophysical Journal, 545, 1.

Chen, Y., L. Liu, and W. Wan (2011), Does the F10.7 index correctly describe solar EUV flux during the deep solar minimum of 2007–2009? J. Geophys. Res., 116, A04304, doi:10.1029/2010JA016301.

Cherniak, I., I. Zakharenkova, and R. J. Redmon (2015), Dynamics of the high-latitude ionospheric irregularities during the 17 March 2015 St. Patrick's Day storm: Ground-based GPS measurements, Space Weather, 13, 585–597, doi:10.1002/2015SW001237.

Chisham, G., et al. (2007), A decade of the Super Dual Auroral Radar Network (SuperDARN): Scientific achievements, new techniques and future directions, Surv. Geophys., 28,33–109, doi:10.1007/s10712-007-9017-8.

Coddington, O., Lean, J.L., Pilewskie, P., Snow, M., Lindholm, D.: 2015, A solar irradiance climate data record, Bull. American Meteorological Soc. doi: 10.1175/BAMS-D-14-00265.1.

Coker, C., R. Hunsucker, and G. Lott (1995), Detection of auroral activity using GPS satellites, Geophys. Res. Lett., 22, 23, doi:10.1029/95GL03091.

Coleman, P. J., Jr. (1966), Variations in the interplanetary magnetic field: Mariner 2, 1, Observed properties, J. Geophys. Res., 7(23), 5509-5531.

Collins, M. D. (1992), A two way parabolic equation for acoustic backscattering in the ocean, J. Acoust. Soc. Amer., vol. 91, pp. 1357-1358.

Coster, A. J., M. J. Colerico, J. C. Foster, W. Rideout, and F. Rich (2007), Longitude sector comparisons of storm enhanced density, Geophys. Res. Lett., 34, L18105, doi:10.1029/2007GL030682.

Cousins, E. D. P., T. Matsuo, and A. D. Richmond (2015), Mapping high-latitude ionospheric electrodynamics with SuperDARN and AMPERE, J. Geophys. Res. Space Physics, 120, 5854–5870, doi:10.1002/2014JA020463.

Cressie, N. A. C., 1990, The Origins of Kriging, Mathematical Geology, 22, 239–252.

Dach R., Hugentobler U., Pierre F. and Michael M., 2007, User manual of the Bernese GPS Software Version 5.0, Swiss Astronomical Institute, Bern, Switzerland.

Dashkevich, Z.V., Ivanov, V.E., Sergienko, T.I. (2017), Physicochemical model of the auroral ionosphere, Cosmic. Res., 55: 88. https://doi.org/10.1134/S0010952517020022.

David, M., J. J. Sojka, R. W. Schunk, and A. J. Coster (2016), Polar cap patches and the tongue of ionization: A survey of GPS TEC maps from 2009 to 2015, Geophys. Res. Lett., 43, 2422–2428, doi:10.1002/2016GL068136.

Davies, K., (1990), Ionospheric Radio, Peter Peregrinus Ltd., London, UK.

Davis P. J. (1975), Interpolation and Approximation, Dover Publications, New York, U.S.A.

de Paula, E. R., O. F. Jonah, A. O. Moraes, E. A. Kherani, B. G. Fejer, M. A. Abdu, M. T. A. H. Muella, I. S. Batista, S. L. G. Dutra, and R. R. Paes (2015), Low-latitude scintillation weakening during sudden stratospheric warming events, J. Geophys. Res. Space Physics, 120, 2212–2221,doi:10.1002/2014JA020731.

Deng, Y., A. J. Ridley, and W. Wang (2008), Effect of the altitudinal variation of the gravitational acceleration on the thermosphere simulation, J. Geophys. Res., 113, A09302, doi:10.1029/2008JA013081.

Denton, M. H., J. E. Borovsky, R. M. Skoug, M. F. Thomsen, B. Lavraud, M. G. Henderson, R. L. McPherron, J. C. Zhang, and M. W. Liemohn (2006), Geomagnetic storms driven by ICME- and CIR-dominated solar wind, J. Geophys. Res., 111, A07S07, doi:10.1029/2005JA011436.

Dmitriev, A. V., and A. V. Suvorova (2012), Traveling magnetopause distortion related to a large-scale magnetosheath plasma jet: THEMIS and ground-based observations, J. Geophys. Res., 117, A08217, doi:10.1029/2011JA016861.

Doherty, P., A. Coster, and M. Murtagh (2004), Space weather effects of October– November 2003, GPS Solutions, 8(4), 267, doi:10.1007/s10291-004-0109-3.

Dubois G., 2000, How representative are samples in a sampling network?, J. Geogr. Inform. Decis. Anal., 4, 1-10.

Dungey, J. W. (1961), Interplanetary Magnetic Field and the Auroral Zones,Physical Review Letters, vol. 6, Issue 2, pp. 47-48.

Durgonics, T., A. Komjathy, O. Verkhoglyadova, E. B. Shume, H.-H. Benzon, A. J. Mannucci, M. D. Butala, P. Høeg, and R. B. Langley (2017), Multiinstrument observations of a geomagnetic

storm and its effects on the Arctic ionosphere: A case study of the 19 February 2014 storm, Radio Sci., 52, doi:10.1002/2016RS006106.

Durgonics, T., G. Prates, and M. Berrocoso (2014), Detection of ionospheric signatures from GPS-derived total electron content maps, Journal of Geodetic Science, Vol. 4, Issue 1, doi:10.2478/jogs-2014-0011.

Emmert, J. T., A. D. Richmond, and D. P. Drob (2010), A computationally compact representation of Magnetic-Apex and Quasi-Dipole coordinates with smooth base vectors, J. Geophy. Res., 115, A08322, doi:10.1029/2010JA015326.

Feldstein, Y. I. (1986), A quarter of a century with the auroral oval, Eos Trans. AGU, 67(40), 761–767, doi:10.1029/EO067i040p00761-02.

Feynman, J., and S. B. Gabriel (2000), On space weather consequences and predictions, J. Geophys. Res., 105(A5), 10543–10564, doi:10.1029/1999JA000141.

Fjeldbo, G., A. J. Kliore, and V. R. Eshleman (1971), The neutral atmosphere of Venus as studied with the Mariner V radio occultation experiment, Astron. J., 76, 123 – 140, doi:10.1086/111096.

Fjeldbo, G., and V. R. Eshleman (1969), Atmosphere of Venus as Studied with the Mariner 5 Dual Radio-Frequency Occultation Experiment, Radio Sci., 4(10), 879–897, doi:10.1029/RS004i010p00879.

Fong, C.-J., N. L. Yen, G.-S. Chang, K. Cook and P. Wilczynski (2014), Future low earth observation radio occultation mission: From research to operations, Proc. IEEE Aerosp. Conf., pp. 1-10.

Foster, J. C., A. J. Coster, P. J. Erickson, F. J. Rich, and B. R. Sandel (2004), Stormtime observations of the flux of plasmaspheric ions to the dayside cusp/magnetopause, Geophys. Res. Lett., 31, L08809, doi:10.1029/2004GL020082.

Foster, J. C., A. J. Coster, P. J. Erickson, J. M. Holt, F. D. Lind, W. Rideout, M. McCready, A. van Eyken, R. J. Barnes, R. A. Greenwald, and F. J. Rich (2005), Multiradar observations of the polar tongue of ionization, J. Geophys. Res., 110, A09S31, doi:10.1029/2004JA010928.

Fröhlich, C. (2016), Determination of time-dependent uncertainty of the total solar irradiance records from 1978 to present, J. of Space Weather & Space Climate, 6, A18, doi: doi.org/10.1051/swsc/2016012.

Fuller-Rowell, T. J., M. V. Codrescu, R. G. Roble, and A. D. Richmond (1997), How does the thermosphere and ionosphere react to a geo-magnetic storm?, in Magnetic Storm, Geophys. Monogr. Ser., vol. 98, pp. 203–205, AGU, Washin gton, D. C.

Georgiadou, Y., 1994, Modelling the ionosphere for an active control network of GPS stations, Delft, University of Technology, LGR - series: publications of the Delft Geodetic Computing Centre 7.

Gerard, J.-C., and D. Rusch (1979), The auroral ionosphere: Comparison of a time-dependent model with composition measurements, J. Geophys. Res., 84(A8), 4335–4340, doi:10.1029/JA084iA08p04335.

Ghamry, E., A. Lethy, T. Arafa-Hamed, and E. A. Elaal, A comprehensive analysis of the geomagnetic storms occurred during 18 February and 2 March 2014, NRIAG-JAG (2016) 5, 263–268, doi:10.1016/j.nrjag.2016.03.001.

Ghoddousi-Fard, R., and F. Lahaye (2016), Evaluation of single frequency GPS precise point positioning assisted with external ionosphere sources, Adv. Space Res., 57 , 2154–2166, doi:10.1016/j.asr.2016.02.017.

Ghoddousi-Fard, R., L. Nikitina, D. Danskin, and P. Prikryl (2015), Analysis of GPS phase rate variations in response to geomagnetic field perturbations over the Canadian auroral region, Adv. Space Res., 55(5), 1372–1381, doi:10.1016/j.asr.2014.12.021.

Ghoddousi-Fard, R., P. Héroux, D. Danskin, and D. Boteler (2011), Developing a GPS TEC Mapping Service over Canada, Space Weather, 9, S06D11, doi:10.1029/2010SW000621.

Ghoddousi-Fard, R., P. Prikryl, and F. Lahaye (2013), GPS phase difference variation statistics: A comparison between phase scintillation index and proxy indices, Adv. Space Res., 52, 1397–1405, doi:10.1016/ j.asr.2013.06.035.

Gibbons W. and Moreno T., 2003, The geology of Spain, Geological Society of London.

Giraud, A., and M. Petit (1978), Ionospheric Techniques and Phenomena, Geophysics and Astrophysics Monographs, 13, Springer.

Gonzalez, W. D., J. A. Joselyn, Y. Kamide, H. W. Kroehl, G. Rostoker, B. T. Tsurutani, and V. M. Vasyliunas (1994), What is a geomagnetic storm?, J. Geophys. Res., 99(A4), 5771–5792, doi:10.1029/93JA02867.

Greenwald, R. A., et al. (1995), DARN/SUPERDARN: A global view of the dynamics of high-latitude convection, Space Sci. Rev., 71, 761–796.

Gulyaeva, T.L., F. Arikan, and I. Stanislawska (2011), Inter-hemispheric imaging of the ionosphere with the upgraded IRI-Plas model during the space weather storms, Earth Planet Sp 63: 929. https://doi.org/10.5047/eps.2011.04.007.

Haaland, S., J. Reistad, P. Tenfjord, J. Gjerloev, L. Maes, J. DeKeyser, R. Maggiolo, C. Anekallu, and N. Dorville (2014), Characteristics of the flank magnetopause: Cluster observations, J. Geophys. Res. Space Physics, 119, 9019–9037, doi:10.1002/2014JA020539.

Hajj, G. A., and L. J. Romans (1998), Ionospheric electron density profiles obtained with the Global Positioning System: Results from the GPS/MET experiment, Radio Sci., 33(1), 175–190, doi:10.1029/97RS03183.

Hatch, R. R. (1982), The synergism of GPS code and carrier measurements, J. Geod., 57, pp. 207–208.

Haynes, W. M. (2012), CRC Handbook of Chemistry and Physics 93, CRC Press, Boca Raton, FL

Heelis, R. A. (1982), The polar ionosphere, Rev. Geophys., 20(3), 567–576, doi:10.1029/RG020i003p00567.

Hernandez-Pajares, M., Garcia-Fernàndez, M., Rius, A., Notarpietro, R., Engeln, A. v., Olivares-Pulido, G., Aragón-Àngel, À. and García-Rigo, A. (2017), Electron density extrapolation above F2 peak by the linear Vary-Chap model supporting new GNSS-LEO occultation missions. J. Geophys. Res. Space Physics., doi:10.1002/2017JA023876.

Hernandez-Pajares, M., J. M. Juan, J. Sanz, and R. Orus (2007), Second-order ionospheric term in GPS: Implementation and impact on geodetic estimates, J. Geophys. Res., 112, B08417, doi:10.1029/2006JB004707.

Hernandez-Pajares, M., Juan, J. M., Sanz, J., Orus, R., Garcia-Rigo, A., Feltens, J., Komjathy, A., Schaer, S. C., and Krankowsi, A. (2008), The IGS VTEC maps: a reliable source of ionospheric information since 1998, J. Geod., 83, 263–275, doi: 10.1007/s00190-008-0266-1.

Hirshberg, J. (1969), and D. S. Colburn, Interplanetary field and geomagnetic variations: A .unified view, Planet. Space Sci., 17, 1183-1206.

Hofmann-Wellenhof B., Lichtenegger H. and Collins J., 1994, GPS Theory and Practice (3rd ed.), Springer-Verlag. Vienna, Austria.

Holzworth, R. H., and C.-I. Meng (1975), Mathematical representation of the auroral oval, Geophys. Res. Lett., 2(9), 377–380, doi:10.1029/GL002i009p00377.

Horvath I. and Essex E. A., 2000, Investigating the midlatitude nighttime total electron content (TEC) enhancements and their relation to the low-latitude ionosphere at low sunspot numbers, Workshop on the Applications of Radio Science WARS 2000 (Beechworth, Australia), Melbourne, Australia.

Horvath, I. and Lovell, B. C. (2015), Investigating storm-enhanced density and polar tongue of ionization development during the 22 October 1999 great storm. J. Geophys. Res. Space Physics, 120: 1428–1444. doi: 10.1002/2014JA020598.

Horvath, I., and B. C. Lovell (2011), Storm-enhanced plasma density (SED) features, auroral and polar plasma enhancements, and rising topside bubbles of the 31 March 2001 superstorm, J. Geophys. Res., 116, A04307, doi:10.1029/2010JA015514.

Hosokawa, K., J. I. Moen, K. Shiokawa, and Y. Otsuka (2011), Decay of polar cap patch, J. Geophys. Res., 116, A05306, doi:10.1029/2010JA016297.

Hosokawa, K., T. Tsugawa, K. Shiokawa, Y. Otsuka, N. Nishitani, T. Ogawa, and M. R. Hairston (2010), Dynamic temporal evolution of polar cap tongue of ionization during magnetic storm, J. Geophys. Res., 115, A12333, doi:10.1029/2010JA015848.

Howard, T. (2011), Coronal mass ejections an introduction, Astrophysics and Space Science Library 376, Springer, doi:10.1007/978-1-4419-8789-1.

Huang Z. and Roussel-Dupré R., 2006, Total electron content (TEC) variability at Los Alamos, New Mexico: A comparative study: FORTE-derived TEC analysis, Radio Sci., 40.

Imber, S. M., S. E. Milan, and M. Lester (2013), The Heppner-Maynard boundary measured by SuperDARN as a proxy for the latitude of the auroral oval, J. Geophys. Res. Space Physics, 118, 685–697, doi:10.1029/2012JA018222.

Jacobsen, K. S. (2014), The impact of different sampling rates and calculation time intervals on ROTI values, J. Space Weather Space Clim., 4, 9, doi:10.1051/swsc/2014031.

Jacobsen, K. S., and M. Dähnn (2014), Statistics of ionospheri c disturbances and their correlat ion with GNSS 338 positioning errors at high latitudes, J. Space Weather Space Clim., 4, A27, doi:10.1051/swsc/2014024.

Jacobsen, K. S., and Y. L. Andalsvik (2016), Overview of the 2015 St. Patrick's day storm and its consequences for RTK and PPP positioning in Norway, J. Space Weather Space Clim., 6, A9, doi:10.1051/swsc/2016004.

Jacobsen, K. S. (2014), The impact of different sampling rates and calculation time intervals on ROTI values, J. Space Weather Space Clim., 4, A33, doi: 10.1051/swsc/2014031.

Jakowski N, M. M. Hoque, and C. Mayer (2011), A new global TEC model for estimating transionospheric radio wave propagation errors, J. Geod, 85, 12, pp. 965-974 doi:10.1007/s00190-011-0455-1.

Jayachandran, P. T., C. Watson, I. J. Rae, J. W. MacDougall, D. W. Danskin, R. Chadwick, T. D. Kelly, P. Prikryl, K. Meziane, and K. Shiokawa (2011), High-latitude GPS TEC changes associated with a sudden magnetospheric compression, Geophys. Res. Lett., 38, L23104, doi:10.1029/2011GL050041.

Jayachandran, P. T., et al. (2009), Canadian High Arctic Ionospheric Network (CHAIN), Radio Sci., 44, RS0A03, doi:10.1029/2008RS004046[printed 45(1), 2010].

Jensen, A. S., M. S. Lohmann, H.-H. Benzon and A. S. Nielsen (2003), Full spectrum inversion of radio occultation signals, Radio Sci., vol. 38, pp. 6-1-6-15, doi:10.1029/2002RS002,763.

Jin S. and Jin R. (2011), GPS Ionospheric Mapping and Tomography: A case study in a geomagnetic storm, Proceeding of IEEE International Geoscience and Remote Sensing Symposium, Vancouver, Canada, 1127–1130.

Jin, Y., J. I. Moen, and W. J. Miloch (2015), On the collocation of the cusp aurora and the GPS phase scintillation: A statistical study, J. Geophys. Res. Space Physics, 120, 9176–9191, doi:10.1002/2015JA021449.

Kamide, Y., and K. Kusano (2015), No major solar flares but the largest geomagnetic storm in the present solar cycle, Space Weather, 13,365–367, doi:10.1002/2015SW001213.

Kappenman, J. G. (2005), An overview of the impulsive geomagnetic field disturbances and power grid impacts associated with the violent Sun-Earth connection events of 29–31 October 2003

and a comparative evaluation with other contemporary storms, Space Weather, 3, S08C01, doi:10.1029/2004SW000128.

Kataoka, R., and Y. Miyoshi (2006), Flux enhancement of radiation belt electrons during geomagnetic storms driven by coronal mass ejections and corotating interaction regions, Space Weather, 4, S09004.

Kataoka, R., D. Shiota, E. Kilpua, and K. Keika (2015), Pileup accident hypothesis of magnetic storm on 17 March 2015, Geophys. Res. Lett., 42,5155–5161, doi:10.1002/2015GL064816.

Kaufmann, R. L., D. J. Larson, and C. Lu (1990), Mapping and distortions of auroral structures in the quiet magnetosphere, J. Geophys. Res., 95(A6), 7973–7994, doi:10.1029/JA095iA06p07973.

Kaufmann, R. L., D. J. Larson, and C. Lu (1990), Mapping and distortions of auroral structures in the quiet magnetosphere, J. Geophys. Res., 95(A6), 7973–7994, doi:10.1029/JA095iA06p07973.

Kelly, M. C. (1989), The Earth' Ionosphere: Plasma Physics and Electrodynamics, Academic Press, San Diego, Calif.

Kerr, D. E. (1951), Propagation of Short Radio Waves, Dover, New York, NY, USA

Kersley, L., S. E. Pryse, and N. S. Wheadon (1998), Amplitude and phase scintillation at high latitudes over northern Europe, Radio Sci., 23, 3, doi: 10.1029/RS023i003p00320.

Keskinen, M. J. (1984), The structure of the high-latitude ionosphere and magnetosphere, Johns Hopkins APL Technical Digest, vol. 5, Apr.-June 1984, p. 154-158.

Khazanov, G. V. (2011), Kinetic theory of the inner magnetospheric plasma, Springer-Verlag, New York, doi:10.1007/978-1-4419-6797-8.

Kinrade, J., C. N. Mitchell, N. D. Smith, Y. Ebihara, A. T. Weatherwax, and G. S. Bust (2013), GPS phase scintillation associated with optical auroral emissions: First statistical results from the geographic South Pole, J. Geophys. Res. Space Physics, 118, 2490–2502, doi:10.1002/jgra.50214.

Kintner, P. M., B. M. Ledvina, and E. R. de Paula (2007), GPS and ionospheric scintillations, Space Weather, 5, S09003, doi:10.1029/2006SW000260.

Kitchatinov, L. L. (2011), Solar differential rotation: origin, models and implications for dynamo, First Asia-Pacific Solar Physics Meeting ASI Conference Series, 2011, Vol. 2, pp 71-80.

Kivanç, Ö., and R. A. Heelis (1998), Spatial distribution of ionospheric plasma and field structures in the high-latitude F region, J. Geophys. Res., 103(A4), 6955–6968, doi:10.1029/97JA03237.

Knipp, D. J., et al. (2016), The May 1967 great storm and radio disruption event: Extreme space weather and extraordinary responses, Space Weather, 14, 614–633, doi:10.1002/2016SW001423.

Komjathy, A. (1997). Global Ionospheric Total Electron Content Mapping Using the Global Positioning System. Ph.D. dissertation, Department of Geodesy and Geomatics Engineering Technical Report No. 188, University of New Brunswick, Fredericton, New Brunswick, Canada, 248 pp. (http://www2.unb.ca/gge/Pubs/TR188.pdf).

Komjathy, A. A.J. Mannucci, L. Sparks, and A. Coster (2005b). ”The Ionospheric impact of the October 2003 Storm Event on WAAS.” GPS Solutions, (9). pp. 41-50.

Komjathy, A., L. Sparks, B. D. Wilson, and A. J. Mannucci (2005a), Automated daily processing of more than 1000 ground-based GPS receivers for studying intense ionospheric storms, Radio Sci., 40, RS6006, doi:10.1029/2005RS003279.

Kullen, A., J. A. Cumnock, and T. Karlsson (2008), Seasonal dependence and solar wind control of transpolar arc luminosity, J. Geophys. Res., 113, A08316, doi:10.1029/2008JA013086.

Kuttler, J. R. and G. D. Dockery (1991), Theoretical description of the parabolic approximation/Fourier split-step method of representing electromagnetic propagation in the troposphere, Radio Sci., vol. 26, no. 2, pp. 381-393.

Lastovicka J. (2002), Monitoring and forecasting of ionospheric space weather effects of geomagnetic storms, J. Atmos. Sol.–Terr. Phys., Vol. 64, pp. 697–705, doi:10.1016/S1364-6826(02)00031-7.

Laundal, K. M., et al. (2015), Birkeland current effects on high-latitude ground magnetic field perturbations, Geophys. Res. Lett., 42, 7248–7254,doi:10.1002/2015GL065776.

Le, G., C. T. Russell, and K. Takahashi (2004), Morphology of the ring current derived from magnetic field observations, Ann. Geophys., 22, pp. 1267-1295, doi:10.5194/angeo-22-1267-2004.

Le, G., G. Lu, R. J. Strangeway, and R. F. Pfaff Jr., Strong interplanetray magnetic field By-related plasma convection in the ionosphere and cusp field-aligned currents under northward interplanetary magnetic field conditions, J. Geophys. Res., 107(A12), 1477, doi:10.1029/2001JA007546, 2002.

Le, G., G. Lu, R. J. Strangeway, and R. F. Pfaff Jr., Strong interplanetray magnetic field By-related plasma convection in the ionosphere and cusp field-aligned currents under northward

interplanetary magnetic field conditions, J. Geophys. Res., 107(A12), 1477, doi:10.1029/2001JA007546, 2002.

Leick A., 1995, GPS Satellite Surveying (2nd ed.), John Wiley & Sons, Hoboken, NJ, U.S.A.

Li, G., B. Baiqi Ning, Z. Ren, and L. Lianhuan Hu (2010), Statistics of GPS ionospheric scintillation and irregularities over polar regions at solar minimum, GPS Solut., doi:10.1007/s10291-009-0156-x.

Liemohn, M. W., J. U. Kozyra, M. F. Thomsen, J. L. Roeder, G. Lu, J. E. Borovsky, and T. E. Cayton (2001), Dominant role of the asymmetric ring current in producing the stormtime Dst*, J. Geophys. Res., 106(A6), 10883–10904, doi:10.1029/2000JA000326.

Liu, J., T. Nakamura, L. Liu, W. Wang, N. Balan, T. Nishiyama, M. R. Hairston, and E. G. Thomas (2015), Formation of polar ionospheric tongue of ionization during minor geomagnetic disturbed conditions, J. Geophys. Res. Space Physics, 120, 6860–6873, doi:10.1002/2015JA021393.

Liu, J., W. Wang, A. Burns, X. Yue, S. Zhang, Y. Zhang, and C. Huang (2016), Profiles of ionospheric storm-enhanced density during the 17 March 2015 great storm, J. Geophys. Res. Space Physics, 121, 727–744, doi:10.1002/2015JA021832.

Liu, W. W. (2005), Canadian space environment program and international living with a star, Adv. Space Res., 35(1), 51–60, doi:10.1016/j.asr.2004.09.011.

Lockwood, M., M. J. Owens, L. A. Barnard, S. Bentley, C. J. Scott, and C. E. Watt (2016), On the origins and timescales of geoeffective IMF, Space Weather, 14, 406–432, doi:10.1002/2016SW001375.

Lockwood, M., M. J. Owens, L. A. Barnard, S. Bentley, C. J. Scott, and C. E. Watt (2016), On the origins and timescales of geoeffective IMF, Space Weather, 14, 406–432, doi:10.1002/2016SW001375.

Lognonné P., Artrub J., Garcia R., Crespona F., Ducica V., Jeansouc E. et al., 2006, Ground-based GPS imaging of ionospheric postseismic signal, Planet. Space Sci., 54, 528–540.

Lu, G., A. D. Richmond, H. Lühr, and L. Paxton (2016), High-latitude energy input and its impact on the thermosphere, J. Geophys. Res. Space Physics, 121, 7108–7124, doi:10.1002/2015JA022294.

Lu, J. Y., Z.-Q. Liu, K. Kabin, H. Jing, M. X. Zhao, and Y. Wang (2013), The IMF dependence of the magnetopause from global MHD simulations, J. Geophys. Res. Space Physics, 118, 3113–3125, doi:10.1002/jgra.50324.

MacDougall, J. W., and P. T. Jayachandran (2007), Polar patches: Auroral zone precipitation effects, J. Geophys. Res., 112, A05312, doi:10.1029/2006JA011930.

Maini, A. K. and V. Agrawal (2011), Satellite Technology: Principles and Applications, John Wiley, Chichester, United Kingdom.

Mann, I. R., et al. (2008), The upgraded CARISMA magnetometer array in the THEMIS era, Space Sci. Rev., 141(1–4), 413–451, doi:10.1007/s11214-008-9457-6.

Mannucci, A. J., B. A. Iijima, U. J. Lindqwister, X. Q. Pi, L. J. Sparks, and B. D. Wilson (1999), GPS and ionosphere, in Review of Radio Science 1996–1999, edited by W. Ross-Stone, pp. 625–665 , Wiley-IEEE Press, New York, isbn:978-0-7803-6003-7.

Mannucci, A. J., B. D. Wilson, D. N. Yuan, C. H. Ho, U. J. Lindqwister, and T. F. Runge (1998), A global mapping technique for GPS-derived ionospheric total electron content measurements, Radio Sci., 33(3), 565–582, doi:10.1029/97RS02707.

Mannucci, A. J., B. D. Wilson, D. N. Yuan, C. H. Ho, U. J. Lindqwister, and T. F. Runge (1998), A global mapping technique for GPS-derived ionospheric total electron content measurements, Radio Sci., 33(3), 565–582.

Mannucci, A.J., Iijima, B.A., Lindqwister, U.J., Pi, X.Q., Sparks, L.J., Wilson, B.D., (1999), GPS and ionosphere. In: Ross-Stone, W. (Ed.), Review of Radio Science 1996-1999, Wiley-IEEE Press, New York, ISBN: 978-0-7803-6003-7, pp. 625-665.

Matsushita, S., Ionospheric F2 behavior at conjugate places in low latitudes, Radio Sci., 3 (7), 658–667, 1968.

Matsushita, S., Ionospheric F2 behavior at conjugate places in low latitudes, Radio Sci., 3 (7), 658–667, 1968.

Matuura, N. (1972), Theoretical models of ionospheric storms, Space Sci. Rev., 13, 1, pp. 124-189, doi:10.1007/BF00198166.

Mavromichalaki, H., M. Papailiou, S. Dimitrova, E. S. Babayev, P. Loucas (2012), Space weather hazards and their impact on human cardio-health state parameters on Earth, Nat Hazards, 64: 1447, https://doi.org/10.1007/s11069-012-0306-2.

Meier, R., Crowley, G., Strickland, D.J., Christensen, A.B., Paxton, L.J., Morrison, D., Hackert, C.L., (2005), First look at the 20 November 2003 superstorm with TIMED/GUVI: comparisons with a thermospheric global circulation model. J. Geophys. Res. 110, A09S41, http://dx.doi.org/10.1029/2004JA010990.

Mende, S., S. Harris, H. Frey, V. Angelopoulos, C. Russell, E. Donovan, B. Jackel, M. Greffen, and L. Peticolas (2008), The THEMIS array ofground-based observatories for the study of auroral substorms, Space Sci. Rev., 141, 357–387, doi:10.1007/s11214-008-9380-x.

Mendillo, M. (2006), Storms in the ionosphere: Patterns and processes for total electron content, Rev. Geophys., 44, RG4001, doi:10.1029/2005RG000193.

Mendillo, M., and J. A. Klobuchar (2006), Total electron content: Synthesis of past storm studies and needed future work, Radio Sci., 41, RS5S02, doi:10.1029/2005RS003394.

Meng, X., J. A. Mannucci, O. Verkhoglyadova and T. Bruce (2016), On forecasting ionospheric total electron content responses to high-speed solar wind streams, J. Space Weather Space Clim., 6, doi:https://doi.org/10.1051/swsc/2016014.

Middleton, H. R., S. E. Pryse, A. G. Wood, and R. Balthazor (2008), The role of the tongue-of-ionization in the formation of the poleward wall of the main trough in the European post-midnight sector, J. Geophys. Res., 113, A02306, doi:10.1029/2007JA012631.

Middleton, H. R., S. E. Pryse, L. Kersley, G. S. Bust, E. J. Fremouw, J. A. Secan, and W. F. Denig (2005), Evidence for the tongue of ionization under northward interplanetary magnetic field conditions, J. Geophys. Res., 110, A07301, doi:10.1029/2004JA010800.

Misra P., and P. Enge (2011), Global Positioning System, Signals, Measurements, and Performance, Revised 2nd Edition, Ganga-Jamuna Press.

Moen, J., K. Oksavik, L. Alfon si, Y. Daabakk, V. Romano, and L. Spogli (2013), Space weather challenges of the polar cap ionosphere, J. SpaceWeather Space Clim., 3, A02, doi:10.1051/swsc/2013025.

Moen, J., N. Gulbrandsen, D. A. Lorentzen, and H. C. Carlson (2007), On the MLT distribution of F region polar cap patches at night, Geophys. Res. Lett., 34, L14113, doi:10.1029/2007GL029632.

Morioka, A., et al. (2011), On the simultaneity of substorm onset between two hemispheres, J. Geophys. Res., 116, A04211, doi:10.1029/2010JA016174.

Mushini, S., C., E. Donovan, P. T. Jayachandran, R. B. Langley, P. Prikryl, and E. Spanswick (2014), On the relation between auroral 'scintillation' and 'phase without amplitude' scintillation: Initial investigations, IEEE Conference Publications, 2014 XXXIth URSI, DOI:10.1109/URSIGASS.2014.6929726.

Nava, B., P. Coisson and S. M. Radicella (2008), A new version of the NeQuick ionosphere electron density model, J. Atmos. Solar-Terr. Phys., vol. 70, no. 15, pp. 1856-1862, doi:10.1016/j.jastp.2008.01.015.

Okabe A., Boots B., Sugihara K. and Chiu S. N., 2000, Spatial Tessellations – Concepts and Applications of Voronoi Diagrams (2nd ed.), John Wiley.

Oksavik, K., C. van der Meeren, D. A. Lorentzen, L. J. Baddeley, and J. Moen (2015), Scintillation and loss of signal lock from poleward moving auroral forms in the cusp ionosphere, J. Geophys. Res. Space Physics, 120, 9161–9175, doi:10.1002/2015JA021528.

Oksavik, K., V. L. Barth, J. Moen, and M. Lester (2010), On the entry and transit of high-density plasma across the polar cap, J. Geophys. Res., 115, A12308, doi:10.1029/2010JA015817.

Oliveira, D. M., Zesta, E., Schuck, P. W., & Sutton, E. K. (2017). Thermosphere global time response to geomagnetic storms caused by coronal mass ejections. Journal of Geophysical Research: Space Physics, 122. https://doi.org/10.1002/2017JA024006.

Olsen, L. (2005), Ocean reflection interference in low elevation GPS measurements, Jun. 6–8, 2005, Elsinore, Denmark

Olsen, N., C. Stolle, R. Floberghagen, G. Hulot, A. Kuvshinov (2016), Special issue "Swarm science results after 2 years in space", Earth, Planets and Space (ISSN: 1343-8832), 68, 1, pp. 1-3, DOI:http://dx.doi.org/10.1186/s40623-016-0546-6.

Orús R., Hernández-Pajares M., Juan J. M. and Sanz J., 2003, Ionospheric effects on precise navigation at regional and continental scales over Europe, ISPRS International workshop, Castelldefels, Spain.

Ostgaard, N., S. B. Mende, H. U. Frey, J. B. Sigwarth, A. Asnes, and J. M. Weygand, Auroral conjugacy studies based on global imaging, J. Atmos. Sol-Terr. Phys, 69 (3), 249–255, doi:10.1016/j.jastp.2006.05.026,2007.

Ouzounov D., Pulinets S., Romanov A., Romanov A., Tsybulya K., Davidenko D. et al., 2011, Atmosphere-Ionosphere Response to the M9 Tohoku Earthquake Revealed by Joined Satellite and Ground Observations. Preliminary results. Earthq. Sci., 24, 557- 564.

Paláncz B., Völgyesi L., Zaletnyik P. and Kovács L., 2006, Extraction of Representative Learning Set from Measured Geospatial Data, 7th International Symposium of Hungarian Researchers on Computational Intelligence, Budapest, Hungary.

Park, C. G. (1976), Downward mapping of high-latitude ionospheric electric fields to the ground, J. Geophys. Res., 81(1), 168–174, doi:10.1029/JA081i001p00168.

Pavelyev, A. G. (2011), Analytical model of bistatic reflections and radio occultation signals, Radio Sci., vol. 46, p. RS1009, doi:10.1029/2010RS004434.

Paxton, L. J., D. Morrison, Y. Zhang, H. Kil, B. Wolven, B. S. Ogorzalek, D. C. Humm, and C.-I. Meng (2002), Validation of remote sensing products produced by the Special Sensor Ultraviolet Scanning Imager (SSUSI)—A far-UV imaging spectrograph on DMSP F16, Proc. SPIE, 4485, 338.

Paxton, L.J., A. B. Christensen, D. Morrison et al., 2004, GUVI: a hyperspectral imager for geospace. Proc. SPIE Int. Soc. Opt. Eng. 5660, 227–240, doi:10.1117/12.579171.

Pedatella, N. M., J. M. Forbes, A. Maute, A. D. Richmond, T.-W. Fang, K. M. Larson, and G. Millward (2011), Longitudinal variations in the F region ionosphere and the topside ionosphere-plasmasphere: Observations and model simulations, J. Geophys. Res., 116, A12309, doi:10.1029/2011JA016600.

Pedersen, T. R., B. G. Fejer, R. A. Doe, and E. J. Weber (1998), Incoherent scatter radar observations of horizontal F region plasma structure over Sondrestrom, Greenland, during polar cap patch events, Radio Sci., 33(6), 1847–1866, doi:10.1029/98RS01702.

Pedersen, T., B. Fejer, R. Doe, and E. Weber (2000), An incoherent scatter radar technique for determining two-dimensional horizontal ionization structure in polar cap F region patches, J. Geophys. Res., 105, 10,637–10,655.

Perrone L., Korsunova L. P. and Mikhailov A. V., 2010, Ionospheric precursors for crustal earthquakes in Italy, Ann. Geophys., 28, 941–950.

Pfaff, R. F., M. C. Kelley, B. G. Fejer, E. Kudeki, C. W. Carlson, A. Pedersen, and B. Hausler (1984), Electric field and plasma density measurements in the auroral electrojet, J. Geophys. Res., 89(A1), 236–244, doi:10.1029/JA089iA01p00236.

Phillips, O. M. (1957), On the generation of waves by turbulent wind, J. Fluid Mech., vol. 2, pp. 417-445.

Pi, X., A. J. Mannucci, B. Valant-Spaight, Y. Bar-Sever, L. J. Romans, S. Skone, L. Sparks, and G. Martin Hall (2013), Observations of Global and Regional Ionospheric Irregularities and Scintillation Using GNSS Tracking Networks, Proceedings of the ION 2013 Pacific PNT Meeting, Honolulu, Hawaii, April 2013, pp. 752-761.

Pi, X., A. J. Mannucci, U. J. Lindqwister, and C. M. Ho (1997), Monitoring of global ionospheric irregularities using the Worldwide GPS Network, Geophys. Res. Lett, 24(18), 2283–2286, doi:10.1029/97GL02273.

Ping J., Matsumoto K., Kono Y., Saito A., Shum C., Heki K. and Kawano N., 2002, Regional ionosphere map over Japanese Island, Earth Planets Space, 54, 13–16.

Ping J., Matsumoto K., Kono Y., Saito A., Shum C., Heki K. and Kawano N., 2003, Monitoring the Middle and Small Scale TEC Variations over Japanese Islands by GEONET, International Workshop on GPS Meteorology, Tsukuba, Japan.

Pinsky, M. A. (2002), Introduction to Fourier Analysis and Wavelets, Brooks/Cole series in advanced mathematics, Pacific Grove, CA, USA.

Pizzo, V. (1978), A three-dimensional model of corotating streams in the solar wind, 1. Theoretical foundations, J. Geophys. Res., 83(A12), 5563–5572.

Press, W. H., B. P. Flannery, S. A. Teukolsky and W. T. Vetterling (1992), FFT of Real Functions, Sine and Cosine Transforms. § 12.3 in Numerical Recipes in FORTRAN: The Art of Scientific Computing 2, pp. 504-515, Cambridge Univ. Press, Cambridge, U.K.

Prikryl, P., et al. (2013b), An interhemispheric comparison of GPS phase scintillation with auroral emission observed at South Pole and from DMSP satellite, Ann. Geophys., (2, R0216), 56, doi:10.4401/ag-6227.

Prikryl, P., Ghoddousi-Fard, R., Thomas, E. G., Ruohoniemi, J. M., Shepherd, S. G., Jayachandran, P. T., Danskin, D. W., Spanswick, E., Zhang, Y., Jiao, Y., and Morton, Y. T. (2015b), GPS phase scintillation at high latitudes during geomagnetic storms of 7–17 March 2012 – Part 1: The North American sector, Ann. Geophys., 33, 637-656, doi:10.5194/angeo-33-637-2015.

Prikryl, P., P. T. Jayachandran, R. Chadwick, and T. D. Kelly (2015a), Climatology of GPS phase scintillation at northern high latitudes for the period from 2008 to 2013, Ann. Geophys., 33, 531–545, doi:10.5194/angeo-33-531-2015.

Prikryl, P., P. T. Jayachandran, S. C. Mushini, and I. G. Richardson (2014), High-Latitude GPS phase scintillation and cycle slips during high speed solar wind streams and interplanetary coronal mass ejections: A superposed epoch analysis, Earth Planets Space, 66, 62,doi:10.1186/1880-5981-66-62.

Prikryl, P., P. T. Jayachandran, S. C. Mushini, and R. Chadwick (2011a), Climatology of GPS phase scintillation and HF radar backscatter for the high-latitude ionosphere under solar minimum conditions, Ann. Geophys., 29, 377–392, doi:10.5194/angeo-29-377-2011.

Prikryl, P., R. Ghoddousi-Fard, B. S. R. Kunduri, E. G. Thomas, A. J. Coster, P. T. Jayachandran, E. Spanswick, and D. W. Danskin (2013a), GPS phase scintillation and proxy index at high latitudes during a moderate geomagnetic storm, Ann. Geophys., 31, 805–816, doi:10.5194/angeo-31-805-2013.

Prikryl, P., R. Ghoddousi-Fard, J. M. Ruohoniemi, and E. G. Thomas (2015c), GPS phase scintillation at high latitudes during two geomagneticstorms, in Auroral Dynamics and Space Weather, edited by Y. Zhang and L. J. Paxton, Wiley Publ, Hoboken, N. J.

Prikryl, P., R. Ghoddousi-Fard, L. Spogli, C. N. Mitchell, G. Li, B. Ning, P. J. Cilliers, V. Sreeja, M. Aquino, M. Terkildsen, P. T. Jayachandran, Y. Jiao, Y. T. Morton, J. M. Ruohoniemi, E. G. Thomas, Y. Zhang, A. T. Weatherwax, L. Alfonsi, G. De Franceschi, and V. Romano (2015), GPS phase scintillation at high latitudes during geomagnetic storms of 7–17 March 2012 – Part 1: The North American sector, Ann. Geophys., 33, 637-656, doi:10.5194/angeo-33-637-2015.

Prikryl, P., Spogli, L., Jayachandran, P. T., Kinrade, J., Mitchell, C. N., Ning, B., Li, G., Cilliers, P. J., Terkildsen, M., Danskin, D. W., Spanswick, E., Donovan, E., Weatherwax, A. T., Bristow, W. A., Alfonsi, L., De Franceschi, G., Romano, V., Ngwira, C. M., and Opperman, B. D. L. (2011b), Interhemispheric comparison of GPS phase scintillation at high latitudes during the magnetic-cloud-induced geomagnetic storm of 5–7 April 2010, Ann. Geophys., 29, 2287-2304, doi:10.5194/angeo-29-2287-2011.

Prikryl, R. Ghoddousi-Fard, J. M. Weygand, A. Viljanen, M. Connors, D. W. Danskin, P. T. Jayachandran, K. S. Jacobsen, Y. L. Andalsvik, E. G. Thomas, J. M. Ruohoniemi, T. Durgonics, K. Oksavik, Y. Zhang, E. Spanswick, M. Aquino, and V. Sreeja (2016), GPS phase scintillation at high latitudes during the geomagnetic storm of 17–18 March 2015, J. Geophys. Res. Space Physics, 121, 10,448–10,465, doi:10.1002/2016JA023171.

Prölls, G. W. (1995), Ionospheric F-Region Storms, In Handbook of Atmospheric Electrodynamics, Vol. 2 (ed. Volland), CRC Press/Boca Raton, pp. 195-248.

Prölls, G. W., L. H. Brace, H. G. Mayer, G R. Carignan, T. L. Killeen, and J. A. Klobuchar (1991), Ionospheric storm effects at subaruroral latitudes: A case study, J. Geophys. Res., 96, 2, pp. 1275-1288.

Pulinets S. and Boyarchuk K., 2004, Ionospheric Precursors of Earthquakes, Springer, Berlin, Germany.

Pulkkinen, A., S. Lindahl, A. Viljanen, and R. Pirjola (2005), Geomagnetic storm of 29–31 October 2003: Geomagnetically induced currents and their relation to problems in the Swedish high-voltage power transmission system, Space Weather, 3, S08C03, doi:10.1029/2004SW000123.

Qian, L., S. C. Solomon, and T. J. Kane (2009), Seasonal variation of thermospheric density and composition, J. Geophys. Res., 114, A01312, doi:10.1029/2008JA013643.

Reinisch, B. W., I. A. Galkin, G. M. Khmyrov, A. V. Kozlov, K. Bibl, I. A. Lisysyan, G. P. Cheney, X. Huang, D. F. Kitrosser, V. V. Paznukhov, Y. Luo, W. Jones, S. Stelmash, R. Hamel, J. Grochmal (2009), New Digisonde for research and monitoring applications, Radio Sci., 44, RS0A24, doi:10.1029/2008RS004115.

Richmond and Lu, 2000 Richmond, A. D., and G. Lu (2000), Upper-atmospheric effects of magnetic storms: A brief tutorial, J. Atmos. Sol. Terr. Phys., 62 , 1115–1127.

Richmond, A. D., and S. Matsushita (1975), Thermospheric response to a magnetic substorm, J. Geophys. Res., 80(19), 2839–2850, doi:10.1029/JA080i019p02839.

Ridley, A. J., Y. Deng, and G. Toth. (2006), The Global Ionosphere-Thermosphere Model (GITM). J. Atmos. Solar-Terrestr. Phys. 68, 839-864.

Rino, C. L. (1979), A power law phase screen model for ionospheric scintillation: 1. Weak scatter, Radio Sci., 14(6), 1135–1145, doi:10.1029/RS014i006p01135.

Rius, A., J. M. Aparicio, E. Cardellach, M. Martin-Neira and B. Chapron (2002), Sea surface state measured using GPS reflected signals, Geophys. Res. Lett., vol. 29, no. 23, p. 2122, doi:10.1029/2002GL015524.

Roble, R. G., and E. C. Ridley (1987), An auroral model for the NCAR thermospheric general circulation model (TGCM), Annales Geophys., 5A, 369-382.

Rodger, A. S, R. J. Moffett, and S. Quegan (1992), The role of ion drift in the formation of ionization troughs in the mid- and high-latitude ionosphere–A review, Journal of Atmospheric and Terrestrial Physics, Vol. 54, No. 1, pp. 1-30, doi:10.1016/0021-9169(92)90082-V.

Rodríguez-Zuluaga, J., S. M. Radicella, B. Nava, C. Amory-Mazaudier, H. Mora-Páez, and K. Alazo-Cuartas (2016), Distinct responses of the low-latitude ionosphere to CME and HSSWS: The role of the IMF Bz oscillation frequency, J. Geophys. Res. Space Physics, 121, 11,528–11,548, doi:10.1002/2016JA022539.

Rotwell, P. (1962), Charged particles in the Earth's magnetic field and the ionospheric F2-layer, J. Phys. Soc. Jpn, 17, Suppl. 1, 263–267.

Ruf, C. (2013), CYGNSS: Enabling the future of hurricane prediction, IEEE Geosci. Remote Sens. Mag., vol. 1, no. 2, pp. 52-67, doi:10.1109/MGRS.2013.2260911.

Ruohoniemi, J. M., and R. A. Greenwald (2005), Dependencies of high-latitude plasma convection: Consideration of interplanetary magnetic field, seasonal, and universal time factors in statistical patterns, J. Geophys. Res., 110, A09204, doi:10.1029/2004JA010815.

Russell, C. T. (1971), Geophysical coordinate transformations, Cosmic Electrodynamics, 2(2), 184-196.

Russell, C. T., and R. L. McPherron (1973), Semiannual variation of geomagnetic activity, J. Geophys. Res., 78(1), 92–108, doi:10.1029/JA078i001p00092.

Schaer S., Gurtner W. and Feltens J., 1998, WernerIONEX: The IONosphere Map EXchange Format Version 1, Proceedings of the IGS AC Workshop, Darmstadt, Germany.

Schunk, R. and A. Nagy (2009), Ionospheres Physics, Plasma Physics, and Chemistry, 2nd ed., Cambridge University Press, Cambridge, UK.

Serban, A. I., O. I. Geicu, and F. Serban (2016), Geophysicochemical model of an ionospheric auroral gyroscope, Earth and Space Science, 3, 15–33, doi:10.1002/2015EA000145.

Shue, J.-H., and J.-K. Chao (2013), The role of enhanced thermal pressure in the earthward motion of the Earth's magnetopause, J. Geophys. Res. Space Physics, 118, 3017–3026, doi:10.1002/jgra.50290.

Shume, E. B., Komjathy, A., Langley, R. B., Verkhoglyadova, O., Butala, M. D. and Mannucci, A. J. (2015), Intermediate-scale plasma irregularities in the polar ionosphere inferred from GPS radio occultation. Geophys. Res. Lett., 42: 688–696. doi: 10.1002/2014GL062558.

Shume, E. B., P. Vergados, A. Komjathy, R. B. Langley, and T. Durgonics (2017), Electron number density profiles derived from radio occultation on the CASSIOPE spacecraft, Radio Sci., 52, doi:10.1002/2017RS006321.

Sibson, R., 1981, A brief description of natural neighbor interpolation (Chapter 2), in V. Barnett. Interpreting Multivariate Data, pp. 21–36, John Wiley, Chichester, UK.

Skone, S. and V. Hoyle (2005), Canadian GPS Network for Ionosphere Monitoring (CANGIM), GPS Solut, 9, 59, https://doi.org/10.1007/s10291-004-0117-3.

Skone, S., and M. de Jong (2000), The impact of geomagnetic substorms on GPS receiver performance, Earth Planets Space, 52, 1067–1071,doi:10.1186/BF03352332.

Skone, S., and M. E. Cannon (1999), Ionospheric effects on differential GPS applications during auroral substorm activity, J. ISPRS, 54(4),279–288, doi:10.1016/S0924-2716(99)00017-9.

Skone, S., F. Man, F. Ghafoori, and R. Tiwari (2008), Investigation of scintillation characteristics for high latitude phenomena, ION GNSS 2008,Session D5, Savannah, GA, 16-19 September 2008.

Spogli, L., L. Alfonsi, G. De Franceschi, V. Romano, M. H. O. Aquino, and A. Dodson (2009), Climatology of GPS ionospheric scintillations over high and midlatitude European regions, Ann. Geophys., 27, 3429–3437, doi:10.5194/angeo-27-3429-2009.

Sreeja, V., and M. Aquino (2014), Statistics of ionospheric scintillation occurrence over European high latitudes, J. Atmos. Sol. Terr. Phys., 120,doi:10.1016/j.jastp.2014.09.003.

Sreeja, V., T. K. Pant, L. Jose, and S. Ravindran (2011), Westward electric field penetration to the dayside equatorial ionosphere during the main phase of the geomagnetic storm on 22 July 2009, J. Geophys. Res., 116, A03303, doi:10.1029/2010JA016013.

Steele, D. P., and L. L. Cogger (1996), Polar patches and the “tongue of ionization”, Radio Sci., 31(3), 667–677, doi:10.1029/96RS00369.

Stern, D. P. (1977), Large-scale electric fields in the Earth's magnetosphere, Rev. Geophys., 15(2), 156–194, doi:10.1029/RG015i002p00156.

Takahashi H., Costa S., Otsuka Y., Shiokawa K., Monico J. F. G. and Paula E., 2014, Diagnostics of equatorial and low latitude ionosphere by TEC mapping over Brazil, Adv. Space Res., doi: 10.1016/j.asr.2014.01.032.

Tatarskii, V. I. (1961), Wave Propagation in a Turbulent Medium, McGraw-Hill, New York, NY, USA.

Taylor G. and Blewit G., 2006, Intelligent positioning - GIS-GPS unification, Wiley, England.

Teunissen, P.J.G. and O. Montenbruck (Eds.) (2017), Springer Handbook of Global Navigation Satellite Systems, Springer, Cham, Switzerland.

Thomas, E. G., J. B. H. Baker, J. M. Ruohoniemi, L. B. N. Clausen, A. J. Coster, J. C. Foster, and P. J. Erickson (2013), Direct observations of the roleof convection electric field in the formation of a polar tongue of ionization from storm enhanced density, J. Geophys. Res. Space Physics, 118, 1180–1189, doi:10.1002/jgra.50116.

Thomas, E. G., K. Hosokawa, J. Sakai et al. (2015), Multi-instrument, high-resolution imaging of polar cap patch trans-portation, Radio Sci., 50, 904–915, doi:10.1002/2015RS005672.

Titheridge, J. E., and M. J. Buonsanto (1983), Annual variations in the electron content and height of the F layer in the Northern and Southern hemispheres, related to neutral composition, J. Atmos. Solar Terr. Phys., 45(10), 683–696; http:// dx.doi.org/10.1016/S0021-9169(83)80027-0.

Toffoletto, F. R., and T. W. Hill (1989), Mapping of the solar wind electric field to the Earth's polar caps, J. Geophys. Res., 94(A1), 329–347, doi:10.1029/JA094iA01p00329.

Tsurutani, B. T. and W. D. Gonzalez, (1997), The Interplanetary Causes of Magnetic Storms: A Review, in Magnetic Storms (eds B. T. Tsurutani, W. D. Gonzalez, Y. Kamide and J. K. Arballo), American Geophysical Union, Washington, D. C.. doi: 10.1029/GM098p0077.

Tsurutani, B. T., et al. (2006), Corotating solar wind streams and recurrent geomagnetic activity: A review, J. Geophys. Res., 111, A07S01, doi:10.1029/2005JA011273.

Umeki, R., C. H. Liu, and K. C. Yeh (1977), Multifrequency spectra of ionospheric amplitude scintillations, J. Geophys. Res., 82(19), 2752–2760, doi:10.1029/JA082i019p02752.

Ungan B. U. and J. T. Johnson (2000), Time statistics of propagation over the ocean surface: A numerical study, IEEE Trans. Geosci. Remote Sens., vol. 38, no. 4, pp. 1626-1634.

Unglaub, C., Ch. Jacobi, G. Schmidtke, B. Nikutowski, and R. Brunner (2011), EUV-TEC proxy to describe ionospheric variability using satellite-borne solar EUV measurements: First results, Advances in Space Research, Volume 47, Issue 9, p. 1578-1584, doi:10.1016/j.asr.2010.12.014.

van der Meeren, C., K. Oksavik, D. A. Lorentzen, M. T. Rietveld, and L. B. N. Clausen (2015), Severe and local ized GNSS scintillation at the poleward edge of the nightside auroral oval during intense substorm aurora, J. Geophys. Res. Space Physics, 120, 10,607–10,621,doi:10.1002/2015JA021819.

van der Meeren, C., K. Oksavik, D. Lorentzen, J. I. Moen, and V. Romano (2014), GPS scintillation and irregularities at the front of an ionization tongue in the nightside polar ionosphere, J. Geophys. Res. Space Physics, 119, 8624–8636, doi:10.1002 /2014JA020114.

Vennerstrøm, S., E. Friis-Christensen, O. A. Troshichev, and V. G. Andersen (1991), Comparison between the polar cap index, PC, and the auroral electrojet indices AE, AL, and AU, J. Geophys. Res., 96(A1), 101–113, doi:10.1029/90JA01975.

Vergados, P., A. Komjathy, T. F. Runge, M. D. Butala, and A. J. Mannucci (2016), On the characterization of the impact of GLONASS observables on the receiver bias, Radio Sci., 51, 1010–1021, doi:10.1002/2015RS005831.

Verkhoglyadova, O. P., Komjathy, A., Mannucci, A. J., Mlynczak, M. G., Hunt, L. A., & Paxton, L. J. (2017). Revisiting ionosphere-thermosphere responses to solar wind driving in superstorms of November 2003 and 2004. Journal of Geophysical Research: Space Physics, 122. https://doi.org/10.1002/2017JA024542.

Verkhoglyadova, O.P., B. T. Tsurutani, A. J. Mannucci, M. G. Mlynczak, L. A. Hunt, and L. J. Paxton (2014), Ionospheric TEC, thermospheric cooling and Σ[O/N2] compositional changes during the 6–17 March 2012 magnetic storm interval (CAWSES II), J. Atmos. Sol.-Terr. Phys., Vol 115–116,, spp. 41–51, doi:10.1016/j.jastp.2013.11.009.

Vickrey, J. F., and M. C. Kelley (1982), The effects of a conducting E layer on classical F region cross-field plasma diffusion, J. Geophys. Res., 87(A6), 4461–4468, doi:10.1029/JA087iA06p04461.

Volland, H. (1978), A model of the magnetospheric electric convection field, J. Geophys. Res., 83(A6), 2695–2699, doi:10.1029/JA083iA06p02695.

Wait, J. R. (1963), Review of mode theory of radio propagation in terrestrial waveguides, Rev. Geophys., vol. 1, pp. 481-505.

Wang, C., G. Hajj, X. Pi, I. G. Rosen, and B. Wilson (2004), Development of the Global Assimilative Ionospheric Model, Radio Sci., 39, RS1S06, doi:10.1029/2002RS002854.

Watson, C., P. T. Jayachandran, and J. W. MacDougall (2016), GPS TEC variations in the polar cap ionosphere: Solar wind and IMF dependence, J. Geophys. Res. Space Physics, 121, 9030–9050, doi:10.1002/2016JA022937.

Wei, Y., Z. Pu, M. Hong et al. (2009), Westward ionospheric electric field perturbations on the dayside associated with substorm processes, J. Geophys. Res., 114, A12209, doi:10.1029/2009JA014445.

Weygand, J. M., and S. Wing (2016), Comparison of DMSP and SECS region-1 and region-2 ionospheric current boundary, J. Atmos. Sol. Terr. Phys., 143-144,8–13, doi:10.1016/j.jastp.2016.03.002.

Weygand, J. M., O. Amm, A. Viljanen, V. Angelopoulos, D. Murr, M. J. Engebretson, H. Gleisner, and I. Mann (2011), Application and validationof the spherical elementary currents systems technique for deriving ionospheric equivalent currents with the North American and Greenland ground magnetometer arrays, J. Geophys. Res., 116, A03305, doi:10.1029/2010JA016177.

Wickert, J. (2014,)Innovative remote sensing using the international space station: GNSS reflectometry with GEROS, Proc. IEEE Int. Geosci. Remote Sens. Symp., pp. 1-4.

Wild, J. A., Milan, S. E., Owen, C. J., Bosqued, J. M., Lester, M., Wright, D. M., Frey, H., Carlson, C. W., Fazakerley, A. N., and Rème, H. (2004), The location of the open-closed magnetic field line boundary in the dawn sector auroral ionosphere, Ann. Geophys., 22, 3625-3639, doi:10.5194/angeo-22-3625-2004.

Willson, R. C. and H. S. Hudson (1991), The Sun's luminosity over a complete solar cycle, Nature. 351 (6321): 42–4, doi:10.1038/351042a0.

Wu, K., C. Su, and Y. Chu (2015), Improvement of GPS radio occultation retrieval error of E region electron density: COSMIC measurement and IRI model simulation. J. Geophys. Res. Space Physics, 120, 2299–2315. doi: 10.1002/2014JA020622.

Wu, Q., T. J. Rosenberg, L. J. Lanzerotti, C. G. Maclennan, and A. Wolfe (1991), Seasonal and diurnal variations of the latitude of the westward auroral electrojet in the nightside polar cap, J. Geophys. Res., 96 (A2), 1409–1419; doi:10.1029/90JA02379.

Yau, A. W., A. Howarth, A. White, G. Enno, and P. Amerl (2015) Imaging and Rapid-Scanning Ion Mass Spectrometer (IRM) for the CASSIOPE e-POP Mission, Space Sci. Rev., 189, pp. 41-63, doi: 10.1007/s11214-015-0149-8.

Yau, A.W., and H.G. James (2015), CASSIOPE Enhanced Polar Outflow Probe (e-POP) Mission Overview, Space Sci. Rev. doi: 10.1007/s11214-015-0135-1.

Yeh, K. C. and C-H. Liu (1982), Radio wave scintillations in the ionosphere, Proceedings of the IEEE, 70, 4, pp. 324-360, doi:10.1109/PROC.1982.12313.

Yeo, K. L., N. 201A. Krivova, S. K. Solanki and K. H. Glassmeier (2014), Reconstruction of total and spectral solar irradiance from 1974 to 2013 based on KPVT, SoHO/MDI, and SDO/HMI observations, A&A, Vol. 570, doi:10.1051/0004-6361/201423628.

Zavorotny, V. U. and A. G. Voronovich (2000), Scattering of GPS signals from the ocean with wind remote sensing application, IEEE Trans. Geosci. Remote Sens., vol. 38, no. 2, pp. 951-964.

Zesta, E., Boudouridis, A., Weygand, J. M., Yizengaw, E., Moldwin, M. B. and Chi, P. (2016) Interhemispheric Asymmetries in Magnetospheric Energy Input, in Ionospheric Space Weather: Longitude and Hemispheric Dependences and Lower Atmosphere Forcing (eds T. Fuller-Rowell, E. Yizengaw, P. H. Doherty and S. Basu), John Wiley & Sons, Inc., Hoboken, NJ, USA. doi: 10.1002/9781118929216.ch1.

Zhang, Q.-H., B.-C. Zhang, J. Moen, M. Lockwood, I. W. McCrea, H.-G. Yang, H.-Q. Hu, R.-Y. Liu, S.-R. Zhang, and M. Lester (2013), Polar cap patch segmentation of the tongue of ionization in the morning convection cell, Geophys. Res. Lett., 40, 2918–2922, doi:10.1002/grl.50616.

Zhang, Y., and L. J. Paxton (2008), An empirical Kp-dependent global auroral model based on TIMED/GUVI FUV data, J. Atmos. Sol. Terr. Phys., 70, 1231–1242, doi:10.1016/j.jastp.2008.03.008.

Zhang, Y., Paxton, L.J., Morrison, D., Wolven, B., Kil, H., Meng, C.-I., Mende, S.B., Immel, T.J., (2004), O/N2 changes during 1–4 October 2002 storms: IMAGE SI-13 and TIMED/GUVI observations. J. Geophys. Res. 109, A10308, http://dx.doi.org/10.1029/2004JA010441.

Zou, S., M. B. Moldwin, A. J. Ridley, M. J. Nicolls, A. J. Coster, E. G. Thomas, and J. M. Ruohoniemi (2014), On the generation/decay of the storm-enhanced density plumes: Role of the convection flow and field-aligned ion flow, J. Geophys. Res. Space Physics, 119, 8543–8559, doi:10.1002/2014JA020408.

APPENDIX I: AGU's Radio Science journal cover page from January 2017 featuring one of the figures (top) and figure caption (bottom) from Study 2.

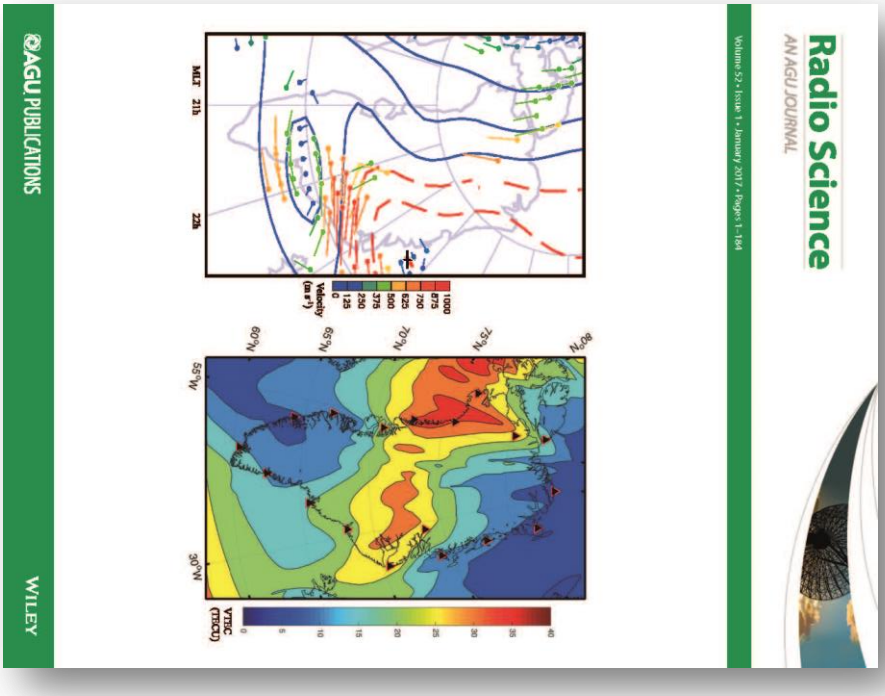

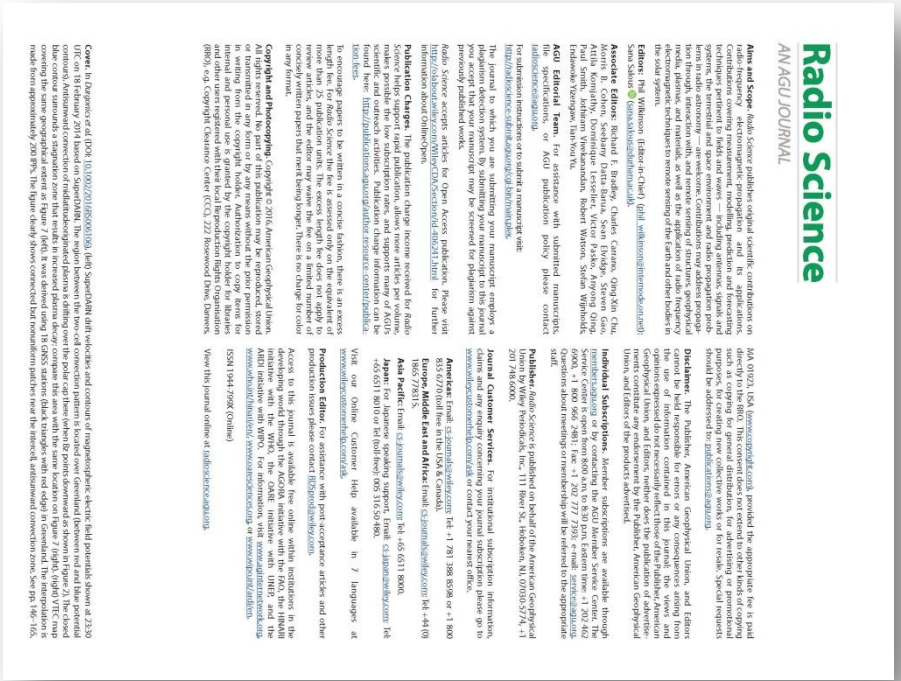

APPENDIX II: Hatch filter script (Matlab)

```
function [ Phatch ] = HatchFilter( P, L, BigN, NoOfBlocks )
%This function implements the Hatch filter

LengthOfArr=length(P);
count=0;

for jj=1:NoOfBlocks
    count=count+1;
    Phat(count)=P(count);
    for ii=2:BigN
        k=ii;
        if(k<BigN)
            n=k;
        else
            n=BigN;
        end
        count=count+1;
        Phatch (count) = (1/n)*P(count) + ((n-1)/n)*( Phatch (count-1) +
L(count) - L(count-1));
    end
end

DataLeftOver=LengthOfArr-(BigN*NoOfBlocks);
if(DataLeftOver>0)
    count=count+1;
    Phatch(count)=P(count);
    for ii=2:DataLeftOver
        k=ii;
        if(k<BigN)
            n=k;
        else
            n=BigN;
        end
        count=count+1;
        Phatch(count) = (1/n)*P(count) + ((n-1)/n)*( Phatch(count-1) + L(count)
- L(count-1));
    end
end

end
```

APPENDIX III: STEC calculating script (Matlab)

```
function [STECbasedOnP,STECbasedOnLFirstCal] =
CalOfTEC(SaveStartIndx,SaveEndIndx,TimeInSec,L1,L2,P1,P2,FreqL1,FreqL2,Fs,clight
,RecDCBBias,DCBBias,SatNo,outerpos6)

StartIndx = SaveStartIndx;
EndIndx = SaveEndIndx;

konst=9.52437;

LI=L1(StartIndx:EndIndx)-L2(StartIndx:EndIndx);
PI=P2(StartIndx:EndIndx)-P1(StartIndx:EndIndx);
bI=LI-PI;
%%
%START FILTERING
Fc=Fs/2;
Fn=0.1*1.5 *(Fs/50); % Scale relative to 50 Hz case CHECK
Wn=Fn/Fc;
[z,p,k] = butter(6,Wn,'low');
[sos,g] = zp2sos(z,p,k);      % Convert to SOS form
if (length(bI)<=261) %          The filter needs more than 261 ponts
    FiltbI = bI;
else
    FiltbI = filtfilt(sos,g,bI);
end
%END FILTERING
%%
SCALB=60-10;SCALB=SCALB*10^-9*clight*0;
NEGBIAS=-1;
STECbL=LI+SCALB-clight*NEGBIAS*(RecDCBBias+DCBBias(SatNo))*10^-9;
STECbP=PI+SCALB-clight*NEGBIAS*(RecDCBBias+DCBBias(SatNo))*10^-9;
STECbLAndbI=LI+SCALB-FiltbI-clight*NEGBIAS*(RecDCBBias+DCBBias(SatNo))*10^-9;
BigC=40.3082; %se doc
ScaleConst=(1/BigC)*10^-16*(FreqL1^2*FreqL2^2/(FreqL1^2-FreqL2^2));%cal in TECU
STECCorrected=ScaleConst*STECbLAndbI;
f=figure(9112);
subplot(3,1,1)
plot(TimeInSec(StartIndx:EndIndx),STECbL,'b',TimeInSec(StartIndx:EndIndx),STECbP
,'r',TimeInSec(StartIndx:EndIndx),STECbLAndbI,'g')
legend('TEC based on carrier phase','TEC based on code range','TEC based on
corrected carrier phase')
xlabel('Time (s)')
ylabel('TEC (m)')
grid on
subplot(3,1,2)
plot(TimeInSec(StartIndx:EndIndx),bI,'b',TimeInSec(StartIndx:EndIndx),FiltbI,'r'
)
legend('Ambiguity','Filtered ambiguity')
xlabel('Time (s)')
ylabel('Ambiguity (m)')
grid on
subplot(3,1,3)
plot(TimeInSec(StartIndx:EndIndx),STECCorrected,'b')
```

```
legend('TEC scaled to TEC units')
xlabel('Time (s)')
ylabel('TEC (TEC-unit)')
grid on
set(f,'OuterPosition',outerpos6)

% TEC calculation option 1
STECbasedOnLFirstCal=STECCorrected;

% Look at Hatch filteret data
BigN=100;
NoOfBlocks = floor( ((EndIndx-StartIndx)+1)/BigN );
PI=P2(StartIndx:EndIndx)-P1(StartIndx:EndIndx);
LI=L1(StartIndx:EndIndx)-L2(StartIndx:EndIndx);

[ PHatch ] = HatchFilter( PI, LI, BigN, NoOfBlocks );

% Moving average filter
npoints=88;
b = ones(1,npoints)/npoints; % n points point averaging filter
if (length(PHatch)<=261) %the filter needs more than 261 ponts
    filtPHatch = PHatch;
else
    filtPHatch = filtfilt(b,1,PHatch);
end

figure(898999)
plot(TimeInSec(StartIndx:EndIndx),PHatch,'b',TimeInSec(StartIndx:EndIndx),filtPH
atch,'r')
grid on
legend('Phat','FiltPhat')
xlabel('Time (s)')
ylabel('Phat FiltPhat (m)')

STECbasedOnP=konst*(filtPHatch-clight*NEGBIAS*(RecDCBBias+DCBBias(SatNo))*10^-
9);

end
```

APPENDIX IV: Solar Radio Burst results

IV.1 Solar Radio Burst and Ray Tracing During the 4 November 2015 Event

This appendix contains data related to Chapter 8. It describes an interesting phenomenon that occurred one day after the HSS hit. Figure IV.10 displays a spectrogram observed on 4 November 2015 at the Glasgow, Scotland site of the e-Callisto solar spectrometer international network (*http://www.e-callisto.org/*). Similar signatures were present at the same times throughout some European sites as well. The SRB was observed the day following the 3 November 2015 HSS-related ionospheric disturbances described in Chapter 8. This SRB disturbed the inflight airport ground radars and the airplane landing receivers in Thule, northern Greenland.

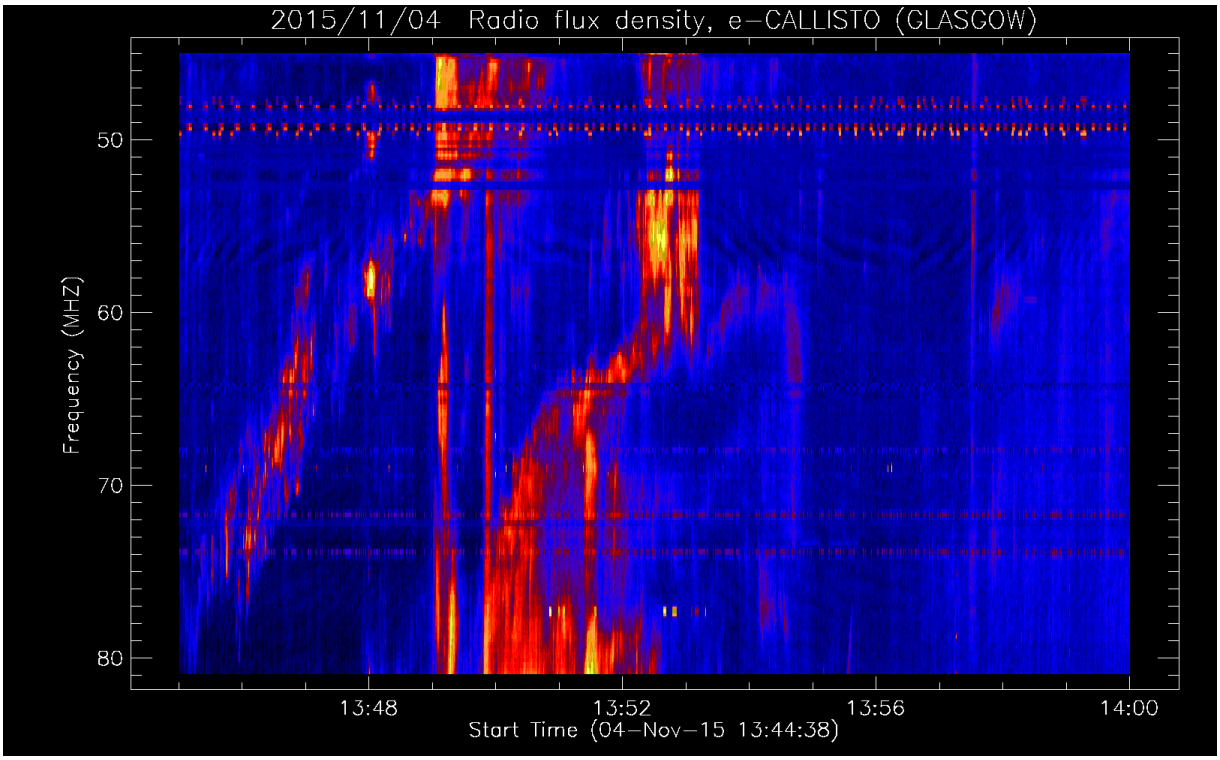

Figure IV.1 The spectrogram shows the initial detections of a SRB [Knipp et al., 2016], which started at approximately 13:40 UTC on 3 November 2015 and continued for hours.

IV.2 Proposed Questions

(1) Were these disturbances related to the HSS-induced ionospheric storm?

(2) At the latitude of Thule, the Sun never rises above the horizon during the days of the storm. Therefore how could air navigation be impacted by solar-originated phenomena?

IV.3 Facts about the Airport Base

The direction of the Thule AFB runway with North is: *85 degrees*.

The geographical coordinates of the runway in degrees are: *(lat, long) = (76.53, -68.73).*

The localizer frequency of the inflight radar system is: *109.5 MHz.*

IV.4 Time of Incidence for the Received Erroneous Localizer Signal

Event time: *14:45 UTC (11:45 LT).*

Elevation of the sun:

Local time:	*7:00*	*11:45*	*13:00*
Elevation:	*-15.95*	*-2.87*	*-1.81*
Azimuth:	*89.18*	*157.49*	*175.55*

IV.5 The Sunlit Ionosphere for the Period of November 3-4, 2015

The F-region (300 km) is sunlit in the period: *7-20 LT (6:30-20:00 LT)*

The bottom of the E-region (100 km) is sunlit in the period: *9-18 LT (8:30-18:00 LT)*

The E-region (100 km) of the ionosphere is sunlit for angles larger than -*10.1 degrees*, and the F-region is sunlit for angles larger than -*17.3 degrees*.

IV.6 Raytracing of the Localizer Frequency for Plasma Frequencies from 10 to 15 MHz

Radio bursts (less than 190 MHz) will (for elevation angles larger than -3 degrees) be reflected in the E- and F-region of the ionosphere.

Radio bursts (less than 115 MHz) will (for elevation angles between -5 and -3 degrees) be reflected in the E- and F-region of the ionosphere.

IV.7 Conclusions of the Ray Tracing Study

The disturbance was not related to the 3 November 2015 HSS event. It was caused by a SRB on the following day. It is possible to have solar radio bursts (of 109.5 MHz) that impact the ground antenna/cables/wave-guide and the airplane localizer radio.

APPENDIX V: Extra figures – Spectral Indices #1

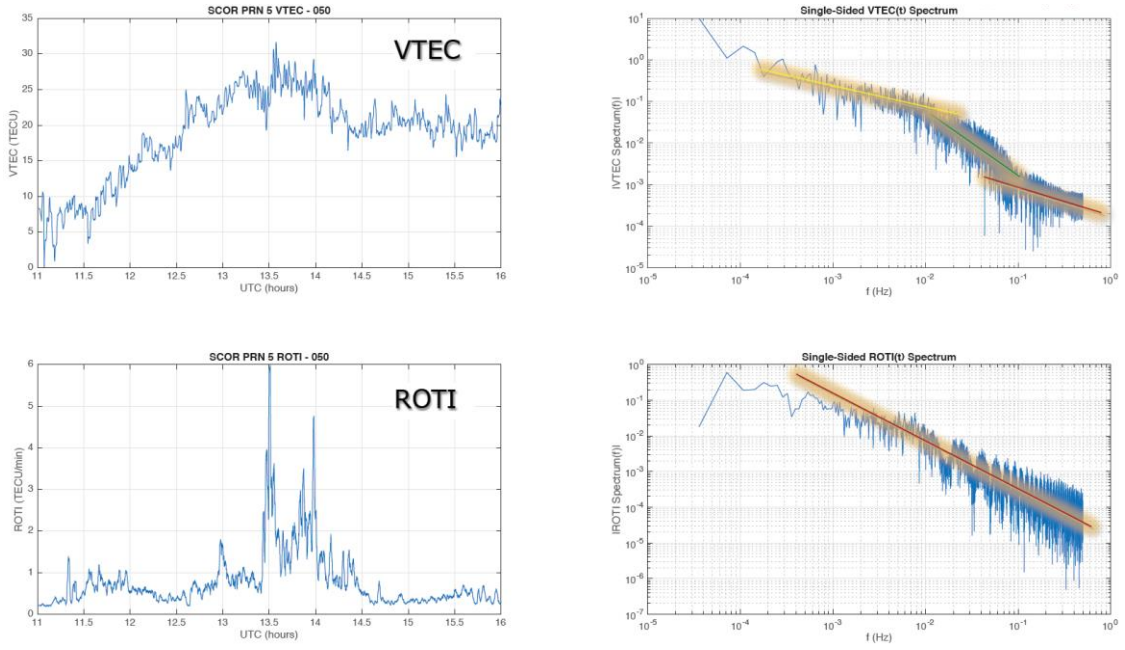

Figure V.1 (left panels) Example of VTEC and ROTI time-series observed from a polar cap station (Scorebysund) during disturbed times on 19 February 2014. **(right panels)** The spectra of the corresponding VTEC and ROTI time-series with the VTEC spectrum showing multiple high-frequency angles.

APPENDIX VI: Extra figures – Spectral Indices #2

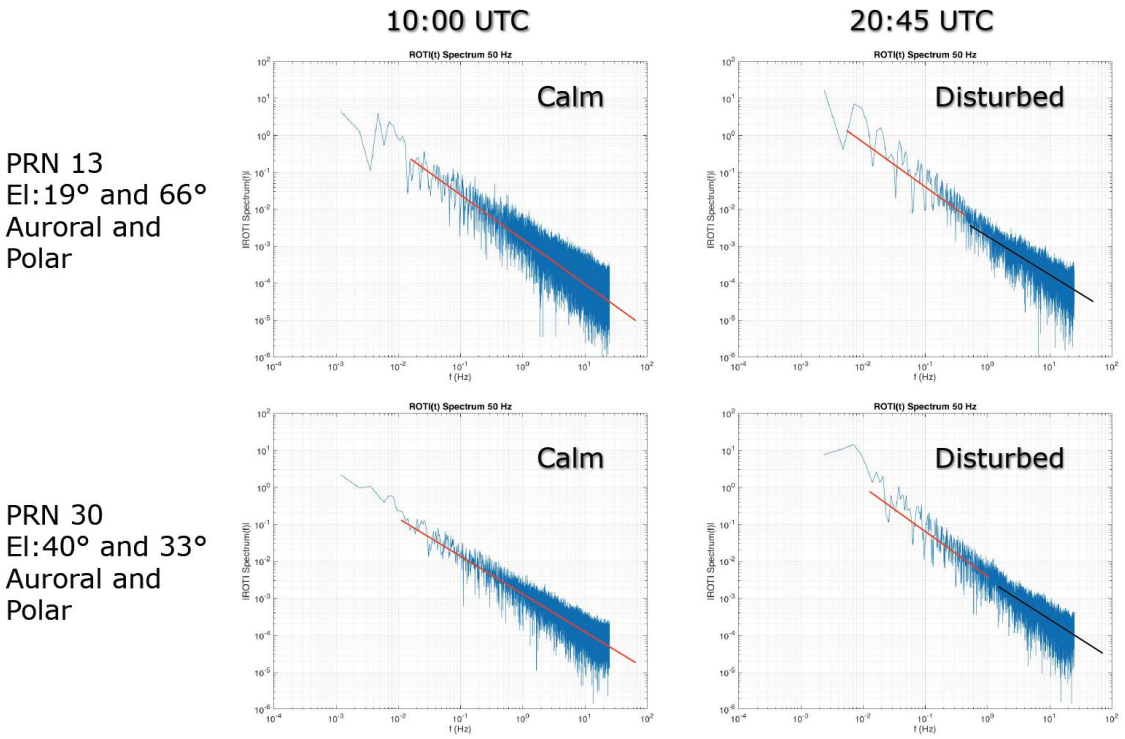

Figure VI.1 ROTI spectra high-frequency tails under different conditions during the 3 November 2015 geomagnetic storm.

APPENDIX VII: GNET stations (2017)

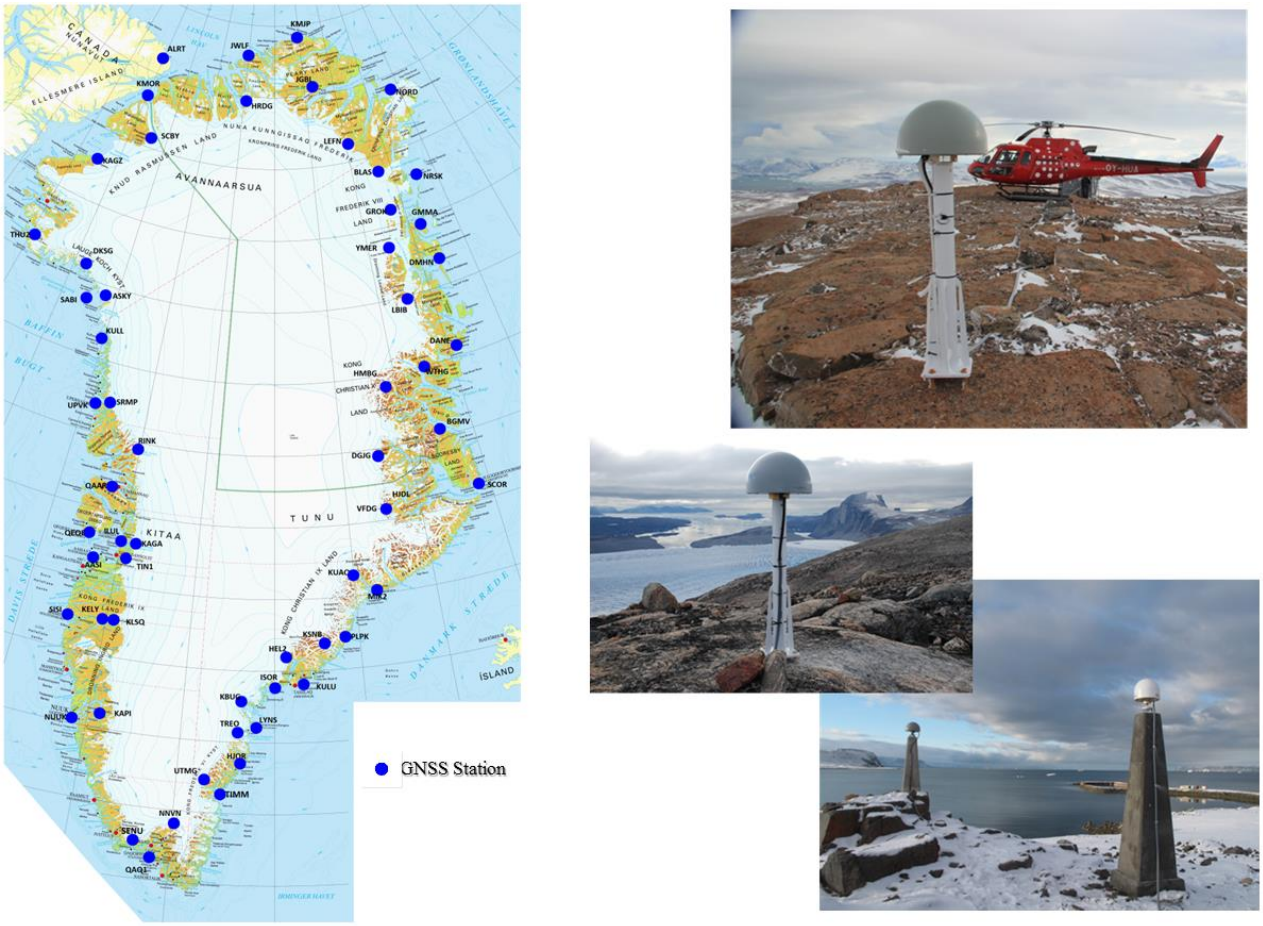

Figure VII.1 The state of GNET in the first half of 2017 with 62 stations (photos are courtesy of Finn Bo Madsen, DTU Space).

APPENDIX VIII: Critical frequency profile plots.

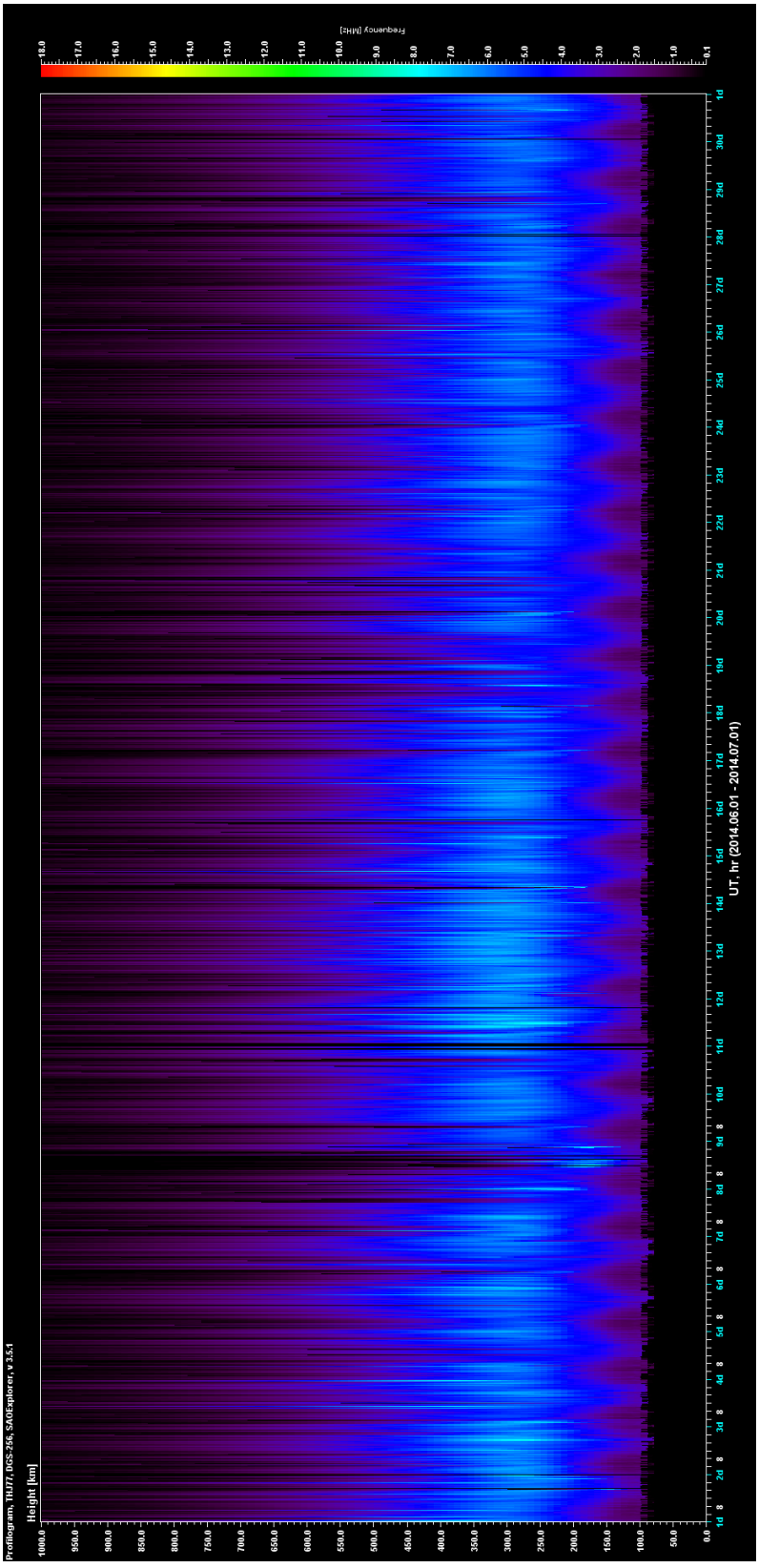

Figure VIII.1 Digital ionosonde-derived critical frequency profiles for June 2014 (large resolution version of Figure 6.8a)

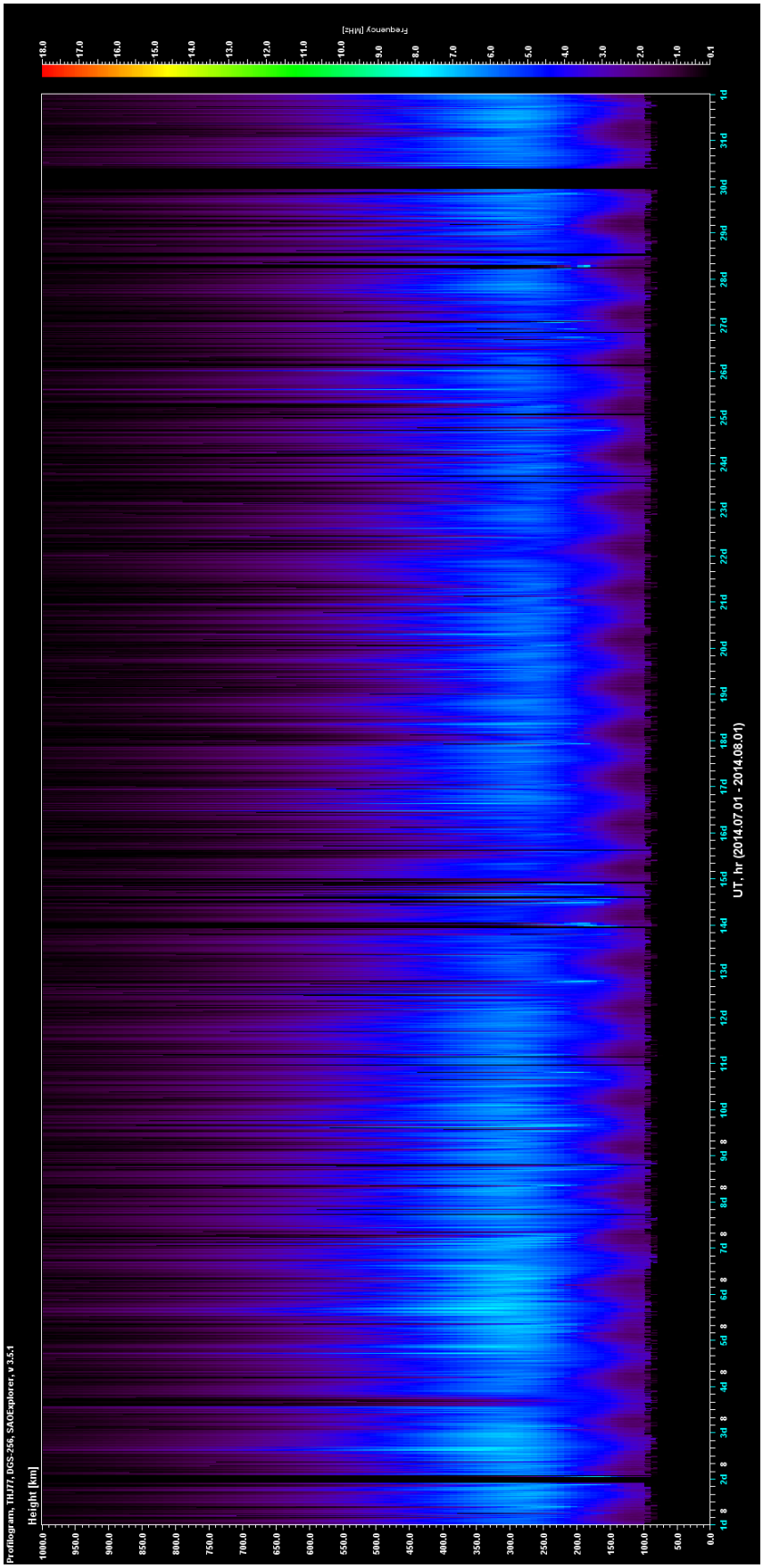

Figure VIII.2 Digital ionosonde-derived critical frequency profiles for July 2014 (large resolution version of Figure 6.8b)

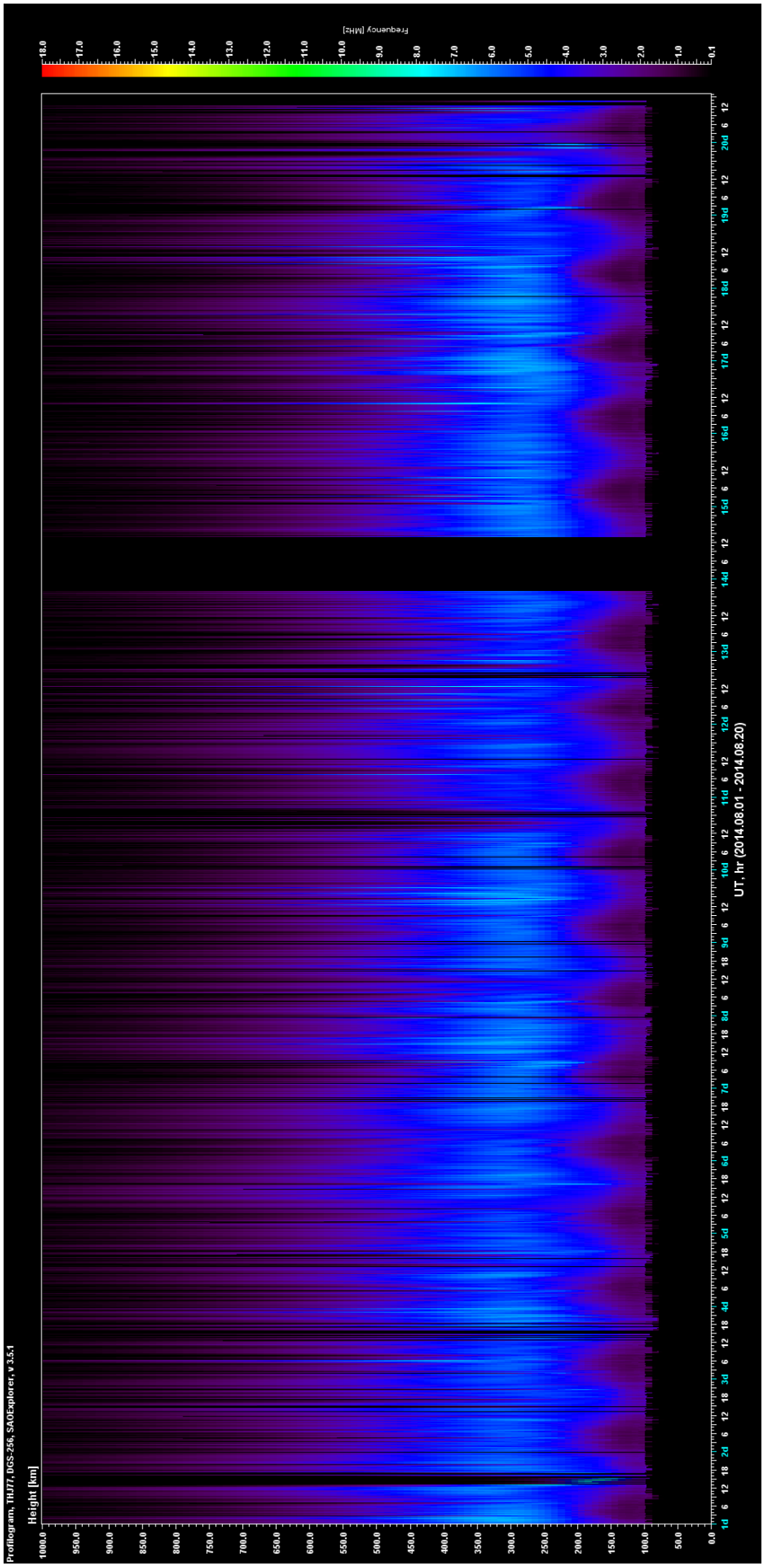

Figure VIII.3 Digital ionosonde-derived critical frequency profiles for August 2014 (large resolution version of Figure 6.8c)

APPENDIX IX: Conference participations during the Ph.D. (first author abstracts only)

Analysis of High-Latitude Ionospheric Processes During HSS and CME-Induced Geomagnetic Storms

Conference poster	AGU Fall meeting 2016
Country	United States
City	San Francisco
Period	12/12/2016 → 16/12/2016
Internet address	http://orbit.dtu.dk/files/128493452/AGU2016poster_Analysis_of_High_Latitude_Ionospheric_Processes_During_the_Nov_2015_HSS_and_CME_Induced_Geomagnetic_Storm_TiborDurgonics_etal.pdf

Authors:

Durgonics, Tibor (*Geodesy, National Space Institute, Technical University of Denmark*), Komjathy, Attila (*NASA Jet Propulsion Laboratory, United States*), Verkhoglyadova, Olga (*NASA Jet Propulsion Laboratory, United States*), Høeg, Per (*Geodesy, National Space Institute, Technical University of Denmark*), and Paul, Ashik (*University of Calcutta, India*).

Multi-Instrument Observations of Geomagnetic Storms in the Arctic Ionosphere

Conference talk	2016 Beacon Satellite Symposium
Location	The Abdus Salam International Centre for Theoretical Physics
Country	Italy
City	Trieste
Period	27/06/2016 → 01/07/2016
Internet address	http://orbit.dtu.dk/files/123360065/BSS16_Abstract_Durgonics.pdf

Authors:

Durgonics, Tibor (*Geodesy, National Space Institute, Technical University of Denmark*), Komjathy, Attila (*NASA Jet Propulsion Laboratory, United States*), Verkhoglyadova, Olga (*NASA Jet Propulsion Laboratory, United States*), Shume, Esayas B. (*NASA Jet Propulsion Laboratory, United States*), von Benzon, Hans-Henrik (*Geodesy, National Space Institute, Technical University of Denmark*), J. Mannucci, Anthony (*NASA Jet Propulsion Laboratory, United States*), D. Butala, Mark (*University of Illinois at Urbana-Champaign, United States*), Høeg, Per (*Geodesy, National Space Institute, Technical University of Denmark*), and B. Langley, Richard (*University of New Brunswick, Canada*).

GNSS-based Observations and Simulations of Spectral Scintillation Indices in the Arctic Ionosphere

Conference talk	2015 AGU Fall Meeting
Country	United States
City	San Francisco
Period	14/12/2015 → 18/12/2015
Internet address	https://agu.confex.com/agu/fm15/meetingapp.cgi/Paper/69428

Authors:

Durgonics, Tibor (Geodesy, National Space Institute, Technical University of Denmark), Hoeg, Per (Geodesy, National Space Institute, Technical University of Denmark), von Benzon, Hans-Henrik (Geodesy, National Space Institute, Technical University of Denmark), and Komjathy, Attila (NASA Jet Propulsion Laboratory, United States).

Regional Arctic observations of TEC gradients and scintillations

Conference poster	European Geosciences Union General Assembly 2015
Location	Austria Center Vienna
Country	Austria
City	Vienna
Period	12/04/2015 → 17/04/2015
Internet address	http://orbit.dtu.dk/files/107186357/EGU2015_12564_1_Abstract.pdf

Authors:

Durgonics, Tibor (Geodesy, National Space Institute, Technical University of Denmark), Høeg, Per (Geodesy, National Space Institute, Technical University of Denmark), von Benzon, and Hans-Henrik (Geodesy, National Space Institute, Technical University of Denmark).

Relations between Arctic large-scale TEC changes and scintillations over Greenland

Conference talk	2014 AGU Fall Meeting
Country	United States
City	San Francisco, CA
Period	15/12/2014 → 19/12/2014
Internet address	http://orbit.dtu.dk/files/107186218/AGU_Fall2014_Abstract.pdf

Authors:

Durgonics, Tibor (Geodesy, National Space Institute, Technical University of Denmark), Høeg, Per (Geodesy, National Space Institute, Technical University of Denmark), and von Benzon, Hans-Henrik (Geodesy, National Space Institute, Technical University of Denmark).

This dissertation is submitted for the degree of
Doctor of Philosophy on November 3, 2017.

Tibor Durgonics
National Space Institute, DTU Space
Technical University of Denmark
Kgs. Lyngby, Denmark
www.space.dtu.dk

Elektrovej 328
DK-2800 Kgs. Lyngby
Tel +45 45259500
Fax +45 45259575

ISBN 978-87-91694-39-4
ISSN -